Growth Kinetics, Thermodynamics, and Phase Formation of group-III and IV oxides during Molecular Beam Epitaxy

Dissertation

zur Erlangung des akademischen Grades
Doctor rerum naturalium (Dr. rer. nat.)
im Fach Physik

von M. Sc. Phys. Patrick Vogt

Präsidentin der Humboldt-Universität zu Berlin:
Prof. Dr.-Ing. Dr. Sabine Kunst

Dekan der Mathematisch-Naturwissenschaftlichen Fakultät:
Prof. Dr. Elmar Kulke

Gutachter:

(i) Prof. Dr. Henning Riechert
(ii) Prof. Dr. W. Ted Masselink
(iii) Prof. Dr. James S. Speck

Eingereicht am 14. März 2017
Tag der mündlichen Prüfung am 9. Juni 2017

Für meine Grossmutter

Für ihre Weisheit. Für ihr Vertrauen. Für ihre Liebe.

Zusammenfassung

Wachstumkinetik, Thermodynamik, und Phasenformierung von Gruppe-III und IV Oxiden während der Molekularstrahlepitaxie

Die vorliegende Arbeit präsentiert eine erste umfassende Wachstumsstudie, und erste quantitative Wachstumsmodelle, von Gruppe-III und IV Oxiden synthetisiert mit sauerstoffplasmaunterstützter Molekularstrahlepitaxie (MBE). Diese entwickelten Modelle beinhalten kinetische und thermodynamische Effekte. Die erworbenen Erkenntnisse sind auf fundamentale Wachstumsprozesse in anderen Syntheseverfahren übertragbar, wie zum Beispiel der Laserdeposition oder metallorganische Gasphasenepitaxie.

Die Wachstumsraten und Desorptionsraten werden `in-situ` mit Laser-Reflektometrie bzw. Quadrupol-Massenspektrometrie (QMS) bestimmt. Es werden die transparenten halbleitenden Oxide Ga_2O_3, In_2O_3 und SnO_2 untersucht. Es ist bekannt, dass sich das Wachstum von Gruppe-III und IV Oxiden, aufgrund der Existenz von Suboxiden, fundamental von anderen halbleitenden Materialien unterscheidet. Es stellt sich heraus, dass die Wachstumsrate der untersuchten binären Oxide durch die Formierung und Desorption von Suboxiden flussstöchiometrisch und thermisch limitiert ist. Es werden die Suboxide Ga_2O für Ga_2O_3, In_2O für In_2O_3 und SnO für SnO_2 identifiziert. Ein Suboxid ist ein untergeordneter Oxidationszustand, und es wird gezeigt, dass die untersuchten Oxide über einen Zwei-Stufen-Prozess gebildet werden: vom Metall zum Suboxid, und weiterer Oxidation vom Suboxid zum thermodynamisch stabilen festen Metalloxid. Dieser Zwei-Stufen-Prozess ist die Basis für die Entwicklung eines ersten quantitativen, semiempirschen MBE-Wachstumsmodells für binare Oxide die Suboxide besitzen. Dieses Model beschreibt und erklärt die gemessenen Wachstumsraten und Desorptionsraten. Es wird die Kinetik und Thermodynamik des ternären Oxidsystems $(In_xGa_{1-x})_2O_3$ untersucht. Die gemittelten Einbauraten von In und Ga in ein makroskopisches Volumen von $(In_xGa_{1-x})_2O_3$ Dünnschichten werden `ex-situ` mit energiedispersiver Röntgenspektroskopie gemessen. Diese Einbauraten werden systematisch analysiert und im Rahmen kinetischer und thermodynamischer Grenzen beschrieben. Es wird gezeigt, dass Ga den In-Einbau in $(In_xGa_{1-x})_2O_3$ aufgrund seiner stabileren Ga–O Bindungen thermodynamisch verhindert. In diesen Zusammenhang wird ein neuer katalytisch-tensidischer Effekt des In auf den Einbau von Ga gefunden. Eine Folge dieses katalytisch-tensidischen Effektes ist die Formierung der thermodynamisch, metastabilen hexagonalen ε-Ga_2O_3 phase mit sehr hoher Kristallqualität. Ein thermodynamisch induziertes, kinetisches Wachstumsmodel für $(In_xGa_{1-x})_2O_3$ wird entwickelt, mit dem sich alle makroskopischen Metall-Einbauraten und Desorptionsraten vorhersagen lassen. Mögliche $(In_xGa_{1-x})_2O_3$ Strukturen gewachsen mit MBE werden mittels Röntgenkristallographie bestimmt. Mit Hilfe der Röntgenstrukturanalyse wird ein erster makroskopischer Ansatz zur Bestimmung der mikroskopischen In Konzentration χ in möglichen $(In_\chi Ga_{1-\chi})_2O_3$ Phasen hergeleitet. Es werden Löslichkeitsgrenzen von In bzw. Ga in monoklinem und kubischem $(In_\chi Ga_{1-\chi})_2O_3$ bestimmt.

Stichwörter:

Transparente halbleitende Oxide, Suboxide, Wachstumskinetik, Thermodynamik, Modellelierung, Katalysator, Tensid, Molekularstrahlepitaxie.

Abstract

Growth kinetics, thermodynamics, and phase formation of group-III and IV oxides during molecular beam epitaxy

The present thesis presents a first comprehensive growth investigation and first quantitative growth models of group-III and IV oxides synthesized by oxygen plasma-assisted molecular beam epitaxy (MBE). The developed models include kinetic and thermodynamic effects. The obtained findings are generally valid for fundamental growth processes in other growth techniques, such as pulsed laser deposition and metal-organic vapor phase-epitaxy.

The growth rates and desorption rates are measured `in-situ` by laser reflectometry and quadrupole mass spectrometry (QMS), respectively. The binary transparent semiconducting oxides Ga_2O_3, In_2O_3, and SnO_2 are investigated. It is known that the growth of group-III and IV oxides is fundamentally different as compared to other semiconductor compounds and due to the existence of suboxides. It is found that the growth rate of the binary oxides investigated is flux-stoichiometrically and thermally limited by the formation and desorption of their respective suboxide. These suboxides are identified as Ga_2O for Ga_2O_3, In_2O for In_2O_3, and SnO for SnO_2. A suboxide is a lower oxidation state, and it is shown, that the investigated oxides grow via a two-step oxidation process. That means, all metal oxidizes to the suboxide, and the suboxide can be further oxidized to the thermodynamic stable solid metal-oxide. This two-step oxidation process is the basis for the development of a first quantitative semi-empirical MBE growth model which predicts and explains the measured growth rates and desorption rates, for binary oxides possessing suboxides. The kinetics and thermodynamics of the ternary oxide system $(In_xGa_{1-x})_2O_3$, grown by MBE, is investigated. The average In and Ga incorporation rates into a macroscopic volume of $(In_xGa_{1-x})_2O_3$ are measured `ex-situ` by energy dispersive X-ray spectroscopy. These incorporation rates are systematically analyzed and explained in the framework of kinetic and thermodynamic limitations. It is shown that Ga thermodynamically inhibits the incorporation of In into $(In_xGa_{1-x})_2O_3$ due to its stronger Ga–O bonds. In this context, a new catalytic-surfactant effect of In on the formation of Ga_2O_3 is found. As a consequence of this catalytic-surfactant effect the metastable hexagonal ε-Ga_2O_3 with very high crystal quality is formed. A thermodynamically induced kinetic growth model for $(In_xGa_{1-x})_2O_3$ MBE is developed. It predicts all macroscopic metal incorporation rates and desorption rates. Possible $(In_xGa_{1-x})_2O_3$ phases grown by MBE are investigated by X-ray crystallography. By means of X-ray diffraction analysis, a first macroscopic approach to determine the microscopic In concentration χ in possible $(In_\chi Ga_{1-\chi})_2O_3$ phases is derived. The solubility limits of In and Ga in monoclinic and cubic $(In_\chi Ga_{1-\chi})_2O_3$ phases, respectively, are identified.

Keywords:

Transparent semiconducting oxides, suboxides, growth kinetics, thermodynamics, modeling, catalyst, surfactant, molecular beam epitaxy.

Parts of this work have been published

in journals (in reverse chronological order):

- P. Vogt and O. Bierwagen

  Kinetics versus thermodynamics of the metal incorporation in molecular beam epitaxy of $(In_xGa_{1-x})_2O_3$

  APL Mater. **4**, 086112 (2016)

- P. Vogt and O. Bierwagen

  Comparison of the growth kinetics of In_2O_3 *and* Ga_2O_3*, and their suboxide desorption during plasma-assisted molecular beam epitaxy*

  Appl. Phys. Lett. **109**, 062103 (2016)

- P. Vogt and O. Bierwagen

  Reaction kinetics and growth window for plasma-assisted molecular beam epitaxy of Ga_2O_3*: Incorporation of Ga vs.* Ga_2O *desorption*

  Appl. Phys. Lett. **108**, 072101 (2016)

- P. Vogt, A. Trampert, M. Ramsteiner, and O. Bierwagen

  Domain matching epitaxy of cubic In_2O_3 *on r-plane sapphire*

  Phys. Stat. Solidi (a) **212**, 1433 (2015) (Editor's Choice)

- P. Vogt and O. Bierwagen

  The competing oxide and suboxide formation in metal-oxide molecular beam epitaxy

  Appl. Phys. Lett. **106**, 081901 (2015)

- R. Schewski, G. Wagner, M. Baldini, D. Gogova, Z. Galazka, T. Schulz, T. Remmele, T. Markurt, H. v. Wenckstern, M. Grundmann, O. Bierwagen, P. Vogt, and M. Albrecht

  Epitaxial stabilization of pseudomorphic α*-*Ga_2O_3 *on sapphire (0001)*

  Appl. Phys. Express **8**, 011101 (2014)

AT CONFERENCES AND WORKSHOPS AS A PRESENTER
(IN REVERSE CHRONOLOGICAL ORDER):

- P. Vogt and O. Bierwagen

  Kinetics and thermodynamics of binary and ternary oxides during molecular beam epitaxy

  DPG Spring Meeting (national), Dresden 2017, Germany, invited talk

- P. Vogt and O. Bierwagen

  Modeling the metal incorporation during MBE growth of the oxide semiconductors Ga_2O_3, In_2O_3, and their alloy $(In_xGa_{1-x})_2O_3$

  MBE 2016 — 19$^{\text{th}}$ International Conference on Molecular Beam Epitaxy (international), Montpellier 2016, France, contributed talk

- P. Vogt and O. Bierwagen

  Metal incorporation and reaction kinetics for the molecular beam epitaxial growth of $(In_xGa_{1-x})_2O_3$

  DPG Spring Meeting (national), Regensburg 2016, Germany, contributed talk

- P. Vogt and O. Bierwagen

  Metal incorporation and reaction kinetics for the molecular beam epitaxial growth of β-Ga_2O_3 and $(In_xGa_{1-x})_2O_3$

  1$^{\text{st}}$ International Workshop on Gallium Oxide and Related Materials (international), Kyoto 2015, Japan, late-news talk

- P. Vogt and O. Bierwagen

  Comprehensive growth kinetics study of the group-III sesquioxide β-Ga_2O_3

  DPG Spring Meeting (national), Berlin 2015, Germany, contributed talk

- P. Vogt and O. Bierwagen

  Molecular beam epitaxial growth of transparent semiconducting III-oxides: growth kinetics and epitaxial relations

  Transparent Conductive Oxides — Fundamentals and Applications (international), Leipzig 2014, Germany, keynote talk

- P. Vogt and O. Bierwagen

  `In-situ` growth kinetics studies of Ga_2O_3, In_2O_3, and SnO_2

  German MBE Workshop (national), Darmstadt 2015, Germany, contributed talk

AT CONFERENCES, WORKSHOPS, AND INSTITUTIONS AS A CONTRIBUTOR (IN REVERSE CHRONOLOGICAL ORDER):

- P. Vogt and O. Bierwagen
  Thermodynamics and suboxide kinetics governing the metal incorporation during molecular beam epitaxy of Ga_2O_3, In_2O_3, and their alloy
  EMRS Fall meeting (international), Warsaw 2016, Poland, contributed talk
- P. Vogt and O. Bierwagen
  Modeling the metal incorporation during MBE growth of the oxide semiconductors Ga_2O_3, In_2O_3, and their alloy $(In_xGa_{1-x})_2O_3$
  German-Japanese Gallium Oxide Technology Meeting (international), 2016 Berlin, Germany, invited talk
- O. Bierwagen, P. Vogt, *et al.*
  Single crystalline Ga_2O_3 and In_2O_3: fundamentals of the growth by molecular beam epitaxy and the gas sensor application
  EMRS Spring meeting (international), Lille 2016, France, invited talk
- O. Bierwagen, P. Vogt, *et al.*
  The transparent semiconducting oxides SnO_2, Ga_2O_3, and In_2O_3: MBE growth, morphology, and electrical properties
  Materials Research Outreach Program, Santa Barbara 2015, USA, invited talk
- O. Bierwagen and P. Vogt
  In-situ investigation of the growth kinetics during oxide plasma-assisted molecular beam epitaxy: oxide vs. suboxide formation
  MRS Fall meeting (international), Boston 2015, USA, contributed talk
- O. Bierwagen, P. Vogt, *et al.*
  The transparent semiconducting oxides SnO_2, Ga_2O_3, In_2O_3: understanding the MBE growth and transport properties
  EMRS Fall meeting (international), Warsaw 2014, Poland, invited talk
- O. Bierwagen, P. Vogt, *et al.*
  Epitaxial growth, doping, and electron transport of the semiconducting oxides In_2O_3, Ga_2O_3, and SnO_2
  International Conference on Solid State Devices and Materials (international), Tsukuba 2014, Japan, invited talk

Contents

Glossary

Parameters, variables, and index families are written in *italics*, e.g., $\sum_{i=1}^{n} o_i$ with running index i. Indices used as terms are written in normal font, e.g., activation energy E_a with index a for activation. Vectors are written in **bold**. Names, companies, theories, new terms, and definitions are introduced in sans serif. Accentuations in the text are given in `typewriter`. Hyperlinks are highlighted in blue.

Table lists variables and parameters frequently used in this thesis, introduces their names, a short explanation, and their units.

Symbol	Name → Explanation	Unit
R	reactant → substance consumed via a chemical reaction	N_R
P	product → substance formed via a chemical reaction	N_P
$\mathcal{R}$	reaction rate → speed of a chemical reaction	$N_{R,P}\,\mathrm{nm}^{-2}\,\mathrm{s}^{-1}$
$\theta_{R,P}$	surface density of R, P → number of R, P per unit area	$N_{R,P}\,\mathrm{nm}^{-2}$
$\dot{\theta}_{R,P}$	time derivative of $\theta_{R,P}$ → change of $\theta_{R,P}$ per unit time	$N_{R,P}\,\mathrm{nm}^{-2}\,\mathrm{s}^{-1}$
o	partial reaction order → exponent in θ_R^o	none
$\mathcal{O}$	total reaction order → $\sum_{i=1}^{n} = o_i$	none
k	reaction rate constant → quantifies $\mathcal{R}$	$(N_{R,P}\,\mathrm{nm}^{-2})^{1-\mathcal{O}}\,\mathrm{s}^{-1}$
E_a	activation energy → minimum kinetic energy required for R to react	eV
G	Gibbs free energy → thermodynamic potential suitable for chemical reactions	eV
ΔG	Gibbs free energy of formation → energy change of G between R and P	eV
$\Delta G^\ddagger$	Gibbs free energy of activation → energy change between R and activated complex	eV
$\Delta S^\ddagger$	entropy of activation → entropy change between R and activated complex	$\mathrm{eV\,K}^{-1}$

Symbol	Name → Explanation	Unit
T_G	growth temperature → growth surface temperature	°C
p_Me	beam equivalent pressure (BEP) → relative Me (Ga, In, Sn) particle flux	Torr
Φ_Me	metal flux → Me rate supplied from effusion cell	$\mathrm{Å\,s^{-1}}$
ϕ_Me	metal flux → Me atoms supplied from effusion cell	$N_\mathrm{Me}\,\mathrm{nm^{-2}\,s^{-1}}$
Φ_{O_2}	oxygen flux → total O flux supplied from research grade	SCCM
Φ_O^*	activated oxygen flux → atomic O or excited O_2 rate	$\mathrm{Å\,s^{-1}}$
ϕ_O^*	activated oxygen flux → atomic O or excited O_2 flux	$N_\mathrm{O}\,\mathrm{nm^{-2}\,s^{-1}}$
$\phi_\mathrm{O}^{*,\mathrm{eff}}$	effective activated oxygen flux → caused by the different oxidation efficiencies of the Me	$N_\mathrm{O}\,\mathrm{nm^{-2}\,s^{-1}}$
ϕ_j^des	desorbing species → species j that is not incorporated during growth	$N_j\,\mathrm{nm^{-2}\,s^{-1}}$
Γ	binary growth rate → film growth rate	$\mathrm{Å\,s^{-1}}$
γ	binary growth rate → Me incorporation rate during binary growth	$N_j\,\mathrm{nm^{-2}\,s^{-1}}$
ρ	pseudo-binary growth rate → binary Me incorporation rate during ternary growth	$N_j\,\mathrm{nm^{-2}\,s^{-1}}$
D_Me	decomposition rate → negative γ	$N_j\,\mathrm{nm^{-2}\,s^{-1}}$
r_Me	Me-to-O flux ratio → $r_\mathrm{Me} = \phi_\mathrm{Me}/\phi_\mathrm{O}^*$	none
X	nominal alloy concentration → $X = \phi_\mathrm{Me1}/(\phi_\mathrm{Me1} + \phi_\mathrm{Me2})$	none
x	layer Me concentration → macroscopic Me concentration for ternary compound	none
χ	alloy composition → microscopic In concentration in $(\mathrm{In}_\chi\mathrm{Ga}_{1-\chi})_2\mathrm{O}_3$	none
$\mathscr{R}$	re-oxidation rate → In re-oxidation rate using it as catalyst for Ga_2O_3 formation	none

1. Introduction

Spanning from insulators to superconductors, metal-oxides are a materials-class with the widest tunability of physical properties and the most abundant materials in the Earth's crust. Their properties are strikingly different compared to conventional semiconductors such as silicon or group-III nitrides, e.g. with respect to their electronic structure. Hence, metal-oxides are a class of materials with very high potential for a new generation of electronic and optoelectronic devices.

Metal-oxides have been used, e.g., as transparent (semi)conducting oxides (T(S)COs) and are well established in industry, like tin dioxide SnO_2, indium sesquioxide In_2O_3, or their alloy indium-tin-oxide (ITO). They have been mass-produced over a long period of time and used for (opto)electronic devices such as photovoltaics [43], transparent contact electrodes for flat panel displays [27], or used as active gas sensor materials [11]. The electronic characteristics of these materials can be easily controlled from semi-insulating by acceptor doping to (semi)conductivity by donor doping or annealing. A rather new material compared to the well established T(S)COs is gallium sesquioxide Ga_2O_3, a TSO when doped with donors. It possesses the second widest band gap of $\sim 5\,\mathrm{eV}$ among semiconductors (after that of diamond) and is transparent deep into the ultra-violet (UV) regime of light. Ga_2O_3 has a very high expected $\sim 8\,\mathrm{MV\,cm^{-1}}$ [55] and already demonstrated breakdown field of $\sim 3.8\,\mathrm{MV\,cm^{-1}}$ [50], thus, is a very promising material for high-power electronic devices. Alloying these compounds, for example Ga_2O_3 and In_2O_3 to $(In_xGa_{1-x})_2O_3$, allows to expand the range of their potential applications such as wavelength-tunable UV detectors, enables band gap engineering, and the growth of heterostructures [46].

Despite their several device applications of the established T(S)COs many fundamental material properties remain uninvestigated. In contrast, within the sophistication of device functioning and operation, the need of improved and controlled material properties has been increased. For this reason, a precise understanding of the growth of these materials is necessary since most of the material properties are set during their synthesis. Molecular beam epitaxy (MBE) is a suitable growth technique to enable the study of fundamental material properties due to its ultra-high vacuum growth environment and the use of very pure source materials for growth. These factors minimize the impurity levels in the grown layers. An epitaxial crystal growth process like MBE is a dynamic phenomenon, hence, the consideration of the growth kinetics as well as the thermodynamics of a growing thin film is essential.

In this context, the purpose of this work is the understanding of the reaction kinetics and thermodynamics during binary and ternary oxide MBE of Ga_2O_3, In_2O_3, $(In_xGa_{1-x})_2O_3$, and SnO_2 on the macroscopic scale.

This work serves as a systematic, comprehensive, and quantitative growth investigation of these compounds, unveils their fundamental chemistry and reaction mechanisms, presents a new catalytic-surfactant effect of In on the formation of Ga_2O_3, studies different polymorphs of Ga_2O_3 and $(In_\chi Ga_{1-\chi})_2O_3$, investigates the miscibility of Ga_2O_3 and In_2O_3 into $(In_xGa_{1-x})_2O_3$, and determines the microscopic In and Ga solubility in possible $(In_\chi Ga_{1-\chi})_2O_3$ phases.

This thesis is organized as follows:

(2) Chapter two introduces the crystal structures and main material properties of Ga_2O_3, In_2O_3, their alloy $(In_xGa_{1-x})_2O_3$, and SnO_2.

(3) Chapter three focuses on the experimental methods used for this thesis. It presents the growth technique, oxygen plasma-assisted MBE, by which all samples have been grown, `in-situ`, and `ex-situ` material characterization methods. A quantitative calibration of all MBE growth parameters is given.

(4) Chapter four gives a brief introduction about the reaction kinetics and thermodynamics needed for the data analysis given in chapters 5 and 6. It introduces the mathematical background for the derivation of the kinetic models presented in these chapters.

(5) Chapter five deals with the reaction kinetics (major part) and thermodynamics (minor part) of binary oxide MBE. The metal incorporation and desorption is presented and their origin explained. A first quantitative growth model of oxides possessing suboxides is derived. The reaction mechanisms of Ga_2O_3, In_2O_3, and SnO_2 as well as the formalism that enables a prediction of the growth and desorption rates for all oxides possessing suboxides are outlined.

(6) Chapter six discusses the reaction kinetics and thermodynamics of the ternary compound $(In_xGa_{1-x})_2O_3$. It presents the growth rates as a function of growth temperature, different In-to-(In+Ga) flux ratios, and (In+Ga)-to-O flux ratios. In order to compare the results with the binary growth kinetics and thermodynamics pseudo-binary growth rates are extracted. A new catalytic-surfactant effect of In on the formation of Ga_2O_3 is found and explained. A first quantitative kinetic model for the macroscopic In and Ga incorporation into $(In_xGa_{1-x})_2O_3$ is derived.

(7) Chapter seven presents studies of different polymorphs of $(In_\chi Ga_{1-\chi})_2O_3$. A macroscopic method to determine the microscopic In concentration χ in different $(In_\chi Ga_{1-\chi})_2O_3$ phases by X-ray diffraction is derived. Crystal structure studies on the metastable ε-Ga_2O_3, stabilized by In, is presented.

The main scientific results are presented in chapters 5, 6, and 7.

2. Group-III and IV oxides

This chapter introduces the binary oxides Ga_2O_3, In_2O_3, and SnO_2 investigated in this thesis. It presents the electrical and optical properties, their crystal structures. The alloy $(In_xGa_{1-x})_2O_3$ is briefly introduced. All investigated compounds are transparent (semi)conducting oxides when doped. Some material properties of Ga_2O_3, In_2O_3, and SnO_2 are collected in Tab. 2.1.

2.1. Gallium sesquioxide — Ga_2O_3

The unique property of Ga_2O_3 is its large band gap of $E_g \sim 4.7\,\mathrm{eV}$ [57]. For this reason, Ga_2O_3 remains transparent into the deep ultra-violet (UV) regime of light and makes it a promising material for optoelectronic devices in the deep-UV regime [88]. It has been used as a material for high temperature gas sensors [42], but its most attractive feature is its potential for being a material for high-power electronics with higher breakdown voltage — expected breakdown electric field of $\sim 8\,\mathrm{MV\,cm^{-1}}$ [55] — and efficiency than its counterparts, e.g. silicon carbide (SiC) or gallium nitride (GaN) [57]. First single-crystalline Ga_2O_3 metal-semiconductor field effect transistors (MESFETs) have been reported by Higashiwaki *et al.* [55].

Stoichiometric Ga_2O_3 is an insulator. Possible n-type conductivity has been attributed to donor impurities such as hydrogen (H) or silicon (Si) [119]. Intentionally doping Ga_2O_3 with the shallow donors Sn [104] or Si [124] causes n-type semiconductivity with electron densities n up to $\sim 10^{19}\,\mathrm{cm^{-1}}$. In this thesis, $Ga_2O_3/Al_2O_3(0001)$ were doped with Sn up to a concentration of $\sim 4 \times 10^{19}\,\mathrm{cm^{-1}}$ without measurable n-type conductivity by capacitance-voltage-measurements. All Sn-doped Ga_2O_3 films were grown in the excess of O, therefore, the missing n-type conductivity might be due Ga vacancies which act as compensating acceptors [67], for the Sn donors.

Another advantage of Ga_2O_3 is the availability of bulk crystals grown by the Czochralski [47, 113], floating zone [123], and edge-defined film-fed [2] growth methods. Bulk Ga_2O_3 may be also used as substrate for other semiconductors like GaN [122], for instance, combining transparency and semiconductivity deep into the UV regime of light.

2.1.1. Crystal phases of Ga_2O_3

Various studies about crystal structures and morphologies of Ga_2O_3 grown by MBE [56, 87, 90, 103, 117] and other epitaxial growth techniques like metal-organic vapor phase epitaxy (MOVPE) [129], metal-organic vapor phase deposition (MOCVD) [34], or chemical vapor deposition (CVD) [108] have been performed.

Material	Space-group	Band gap (eV)	Conductivity	Dopants
Ga_2O_3	C2/m	4.5–4.9 [57]	n-type	Sn [104], Si [124], H [119]
In_2O_3	I$a\bar{3}$	2.7–2.9 [13]	n-type	Sn [17], Mg [16]
SnO_2	P4_2/mnm	3.6 [39]	n-type	Ga [14], In [133], Sb [132]

Table 2.1.: Collection of some material properties of Ga_2O_3, In_2O_3, and SnO_2. The energies for the band gaps correspond to the fundamental one at room temperature. Dopants may be acceptors or donors.

Five different polymorphs of Ga_2O_3 are known, called: α, β, γ, δ, and ε-phase [102, 137]. The thermodynamically most stable phase is the monoclinic one — called: β-Ga_2O_3; unit-cell shown in Fig. 2.1. Other meta-stable phases of Ga_2O_3 occurring during epitaxy are a rhombohedral (space-group: R$\bar{3}$c) — called: α-Ga_2O_3 [69, 108] and a hexagonal phase (space-group: P6_3mc) — called ε-Ga_2O_3. The ε-phase is synthesized using In as a catalyst in this thesis (chapter 7). Oshima *et al.* recently grew ε-Ga_2O_3 by means of halide vapor phase epitaxy (HVPE) [91], and Boschi *et al.* grew it by MOCVD and atomic layer deposition (ALD) [24]. The cubic defective-spinel γ-Ga_2O_3 phase has been synthesized by Oshima *et al.* utilizing CVD [89].

β-Ga_2O_3

Figure 2.2 (a) shows the XRD pattern of a Ga_2O_3 layer doped with Sn grown on Al_2O_3(0001). The Sn concentration was measured by Lutz Kirste[1] and calibrated using secondary ion mass spectrometry (SIMS) as 4×10^{19} Sn-atoms cm^{-3}. This measurement reveals that β-Ga_2O_3 grows phase-pure in ($\bar{2}$01)-direction for Sn-doping up to at least 4×10^{19} Sn-atoms cm^{-3}. On-axis X-ray rocking curve measurements (ω-scan, explanation given in the appendix A.4) of the ($\bar{2}$01)-peak showed a full-width-at-half-maximum (FWHM) of $\omega \sim 1°$ (not shown). This quite large mosaicity of β-Ga_2O_3($\bar{2}$01)/Al_2O_3(0001) has also been reported in literature [117] and is referred to the large lattice mismatch between substrate and layer in in-plane direction and six possible rotational domains. The in-plane crystalline orientation was analyzed by ϕ-scans of off-axis diffraction peaks (explanation given in the appendix A.4) of the substrate (Al_2O_3) and layer (Ga_2O_3) and is depicted in Figs. 2.2 (b)$_1$ and (b)$_2$, respectively. The epitaxial relation between Al_2O_3(0001) and β-Ga_2O_3($\bar{2}$01) is reported in Ref. [49].

α-Ga_2O_3

Studies on α-Ga_2O_3 were made in collaboration with the group of Martin Albrecht and Günter Wagner (Institute of Crystal Growth (IKZ), Berlin, Germany) and Marius Grundmann (University of Leipzig (UL), Leipzig, Germany). In this study, Ga_2O_3 was grown on Al_2O_3(0001) by MBE (this work), pulsed laser depostion (PLD) (UL), and MOVPE (IKZ). Investigations by transmission electron microscopy (TEM) revealed the presence of a three-monolayer thick ($\sim$ 1 nm) pseudomorphically grown α-Ga_2O_3/Al_2O_3(0001). On

[1] Fraunhofer Institut für Angewandte Festkörperphysik, Tullastraße 72, 79108 Freiburg, Germany.

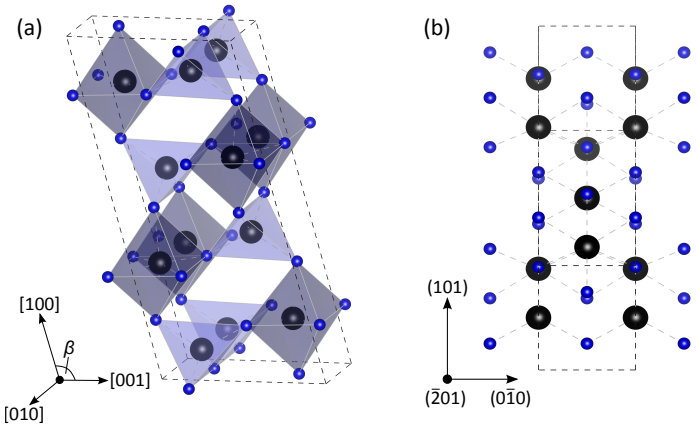

Figure 2.1.: (a) Unit-cell (black dashed line) of monoclinic Ga_2O_3 (crystal space-group: $C2/m$) with lattice parameters $a = 12.21\,\text{Å}$, $b = 3.04\,\text{Å}$, $c = 5.80\,\text{Å}$, and $\beta = 103.83°$ [1]. Polyhedra indicating the octahedral and tetrahedral sites are depicted as light black and light blue, respectively. (b) Projection of the $(\bar{2}01)$-growth surface — the usual growth direction of β-Ga_2O_3 on $Al_2O_3(0001)$. Ga and O atoms are drawn in black and blue, respectively.

top of the α-Ga_2O_3 layer, plastically relaxed β-Ga_2O_3 grew in the form of rotational domains. This α-Ga_2O_3 layer formed for all three growth techniques. This work has been published by Schewski *et al.* [105].

2.2. Indium sesquioxide — In_2O_3

In contrast to Ga_2O_3, In_2O_3 is a well established material in industry when doped with Sn to indium-tin-oxide (ITO). It is used as a transparent contact electrode for flat panel displays [27], solar cells [112], or active gas sensor material [10].

In_2O_3 condensed in its perfect crystal structure is an insulator. However, unintentionally doped In_2O_3 becomes semiconductive by doubly charged O vacancies and H interstitials occurring during growth acting as donors [13]. The carrier concentration caused by O-deficiency in the In_2O_3 crystal may be further increased by post-growth annealing in reduced atmosphere [33]. The bulk resistivity of In_2O_3 can be controlled over nine orders of magnitude from $\sim 10^{-4}\,\Omega\,\text{cm}$ (highly Sn-doped) [17] up to $\sim 10^{5}\,\Omega\,\text{cm}$ (highly Mg-doped) [16].

2.2.1. Crystal phases of In_2O_3

Crystallographic studies on In_2O_3 grown by MBE were carried out and are reported in Refs. [17, 18, 81, 128, 138]. Other epitaxial growth techniques in order to grow In_2O_3, such as PLD [28, 111], solid-source electron cyclotron resonance [63], or MOCVD [130, 139] are used.

Figure 2.3 plots the thermodynamically most stable phase of In_2O_3 — bixbyite In_2O_3. (a) Depicts a quarter of the unit-cell in slightly tilted (010)-projection. In this thesis,

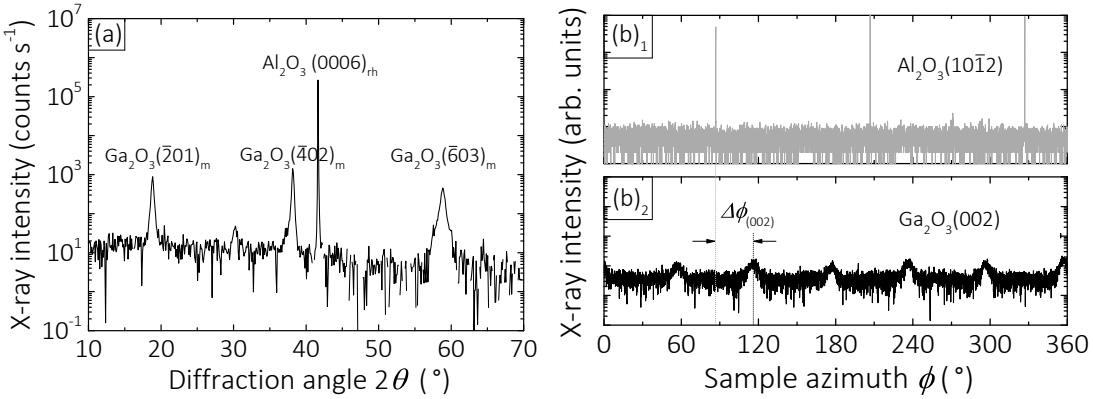

Figure 2.2.: (a) X-ray intensity as a function of the diffraction angle 2θ obtained by a XRD ω-2θ scan showing the crystal phases of $Ga_2O_3/Al_2O_3(0001)$. $(b)_1$ and $(b)_2$ Plot the X-ray intensity as function of the sample azimuth ϕ of the asymmetric $(10\bar{1}2)$-peak of the substrate and (002)-peak of the Ga_2O_3 layer, respectively. The growth and Sn cell temperatures, Ga as well as O fluxes were $T_G = 600\,°C$, $T_{Sn} = 600\,°C$, $\phi_{Ga} = 2.1\,Ga\,nm^{-2}\,s^{-1}$, and $\phi^*_O = 9.8\,O\,nm^{-2}\,s^{-1}$, respectively.

various In_2O_3 layer were grown on different substrates for growth kinetics studies and alloy growth of $(In_xGa_{1-x})_2O_3$ (chapters 6 and 7). Crystal structure data of In_2O_3 are presented in chapter 7. On $Al_2O_3(0001)$, In_2O_3 grows textured with rotational domains in (111)-growth direction and single-crystalline with anti-phase domains [58] on yttrium-stabilized zirconia (YSZ) [15, 101]. Studies on the surface morphologies are reported in Refs. [15, 101] and the epitaxial relation of $In_2O_3(111)/Al_2O_3(0001)$ has been published in Ref. [138].

2.2.2. Domain matching epitaxy of cubic In_2O_3 / $Al_2O_3(10\bar{1}2)$

In this thesis, the non-trivial full epitaxial relationship of bixbyite $In_2O_3(110)/Al_2O_3(10\bar{1}2)$ was determined. A low-mismatch coincidence lattice of In atoms from the film and O atoms from the substrate rationalizes this epitaxial relation by domain-matched epitaxy. This work has been published by Vogt *et al.* [128]. The samples for this study were grown by Oliver Bierwagen at the University of California, Santa Barbara, United States of America, in the group of James S. Speck.

2.3. Indium-gallium sesquioxide — $(In_\chi Ga_{1-\chi})_2O_3$

Combining the material properties of the binary compounds, e.g. by alloying In_2O_3 and Ga_2O_3 to $(In_\chi Ga_{1-\chi})_2O_3$, allows band gap engineering ranging from 2.7 to 4.7 eV, and enables the growth of heterostructures for applications such as power transistors or deep UV detectors.

Systematic studies on the average In concentration x in a macroscopic volume of $(In_xGa_{1-x})_2O_3$ and the microscopic In concentration χ in different phases of $(In_\chi Ga_{1-\chi})_2O_3$ are presented in chapters 6 and 7, respectively.

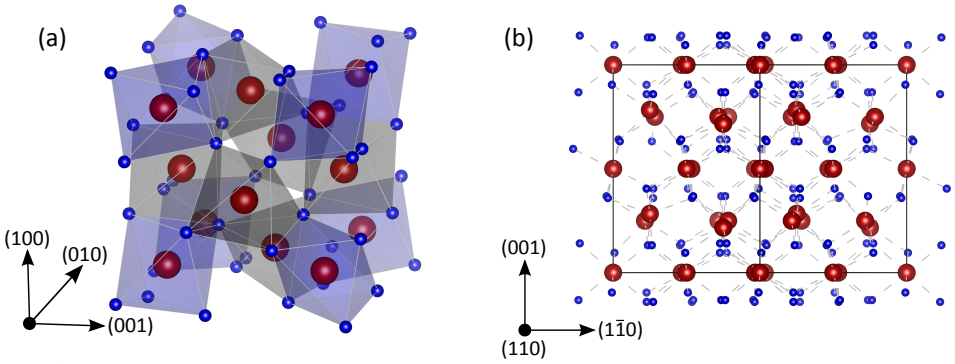

Figure 2.3.: (a) A quarter of the unit-cell of bixbyite In_2O_3 (space-group: I$a\bar{3}$) with lattice parameters $a = b = c = 10.12$ Å [79]. Symmetric and asymmetric octahedral sites are depicted in blue and gray, respectively. (b) Projection of the (110)-surface of bixbyite In_2O_3. Its surface unit-cell is shown as a solid black line. In and O atoms are drawn in red and blue, respectively.

2.4. Tin di-oxide — SnO_2

For decades SnO_2 has been used as a gas sensing material [11]. Its bulk resistivity may be controlled by antimony (Sb) [132] and In [133] doping in a range of $\sim 10^{-4}\,\Omega$cm to $\sim 10^{4}\,\Omega$cm. Structural investigations of epitaxially grown rutile SnO_2 by MBE or CVD, for instance, are reported in Refs. [115–117, 134] and [74], respectively.

The main focus of this thesis is the investigation of the growth kinetics, thermodynamics, and their modeling as presented in chapters 5 and 6. Hence, no systematic investigation on SnO_2 phase formation was performed. The growth kinetics of SnO_2 were performed on $Al_2O_3(10\bar{1}2)$ substrates. White *et al.* determined the epitaxial relationship between $Al_2O_3(10\bar{1}2)$ and SnO_2 (grown by MBE), which is out-of-plane $SnO_2(101)/Al_2O_3(10\bar{1}2)$ [134]. Figures 2.4 (a) and (b) show the unit-cell of rutile SnO_2 and its (101)-surface, respectively.

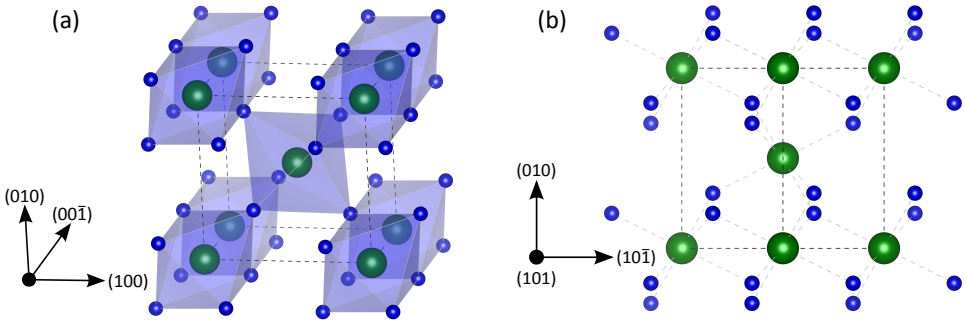

Figure 2.4.: (a) Unit-cell of rutile SnO_2 (space-group: $P4_2/mnm$) with lattice parameters $a = b = 4.74$ Å and $c = 3.19$ Å [23]. (b) Surface of SnO_2 projected along (101)-direction. Sn and O atoms are shown in green and blue, respectively.

3. Growth of group-III and IV oxides by O plasma-assisted MBE

This chapter introduces the synthesis method: oxygen (O) plasma-assisted oxide molecular beam epitaxy (MBE), by which all samples presented in this thesis have been grown. A brief introduction of the MBE growth chamber used for this thesis is given. The `in-situ` and `ex-situ` characterization techniques are introduced. A calibration of the growth chamber, i.e., a calibration of the metal (Me) and O fluxes as well as the substrate temperature which equals the growth temperature T_G is presented. A newly developed sample preparation technique that allows the growth of In-bonded samples at very high-T_G for very long growth times is explained.

3.1. Basics of molecular beam epitaxy

MBE is a crystal growth method for thin- and ultra-thin oxide films with thicknesses on the nanometer scale. The advantage of MBE for thin film growth is that the growth may take place in ultra-high vacuum (UHV). This UHV environment is achieved by using a diaphragm, turbomolecular, cryo, and ionpump. A cryopanel, cooled with liquid nitrogen around the substrate heater and effusion cells, is used to remove condensable contaminants, such as water H_2O or carbon dioxide CO_2. The base-pressure of the growth chamber is on the order of $p_{GC} \sim 10^{-10}$ Torr.

Using an UHV growth environment has three main advantages: (i) the atomic or molecular species propagating line-of-sight from the sources (the Me effusion cells and O plasma source, Fig. 3.1) to the target (a high-quality single crystal: the substrate, Fig. 3.1). (ii) It suppresses the presence of impurities in the growth chamber, hence, their incorporation into the crystal. (iii) It facilitates the use of `in-situ` characterization techniques such as line-of-sight quadrupole mass spectrometry (QMS) and reflection high-energy electron diffraction (RHEED). Both techniques are indicated in Fig. 3.1 and discussed briefly in section 3.2. Another advantage of MBE is all chemicals used during growth are desired constituents of the growing crystal (surfactants[1] excluded) resulting in a defined surface reaction chemistry. This is in contrast to other epitaxial growth techniques such as metal-organic vapor phase epitaxy (MOVPE) [8, 9] where Trimethylmetal, H_2O, and O_2 as precursors for Me incorporation are needed. All these advantages enable the study of crystal growth fundamentals like the reaction kinetics of a growing material, a main part of this thesis.

The MBE is equipped with a laser reflectometry set-up that allows the `in-situ` mea-

[1] A surface active agent is a substance that may improve the crystal quality of a growing material while `not` necessarily being incorporated into the crystal.

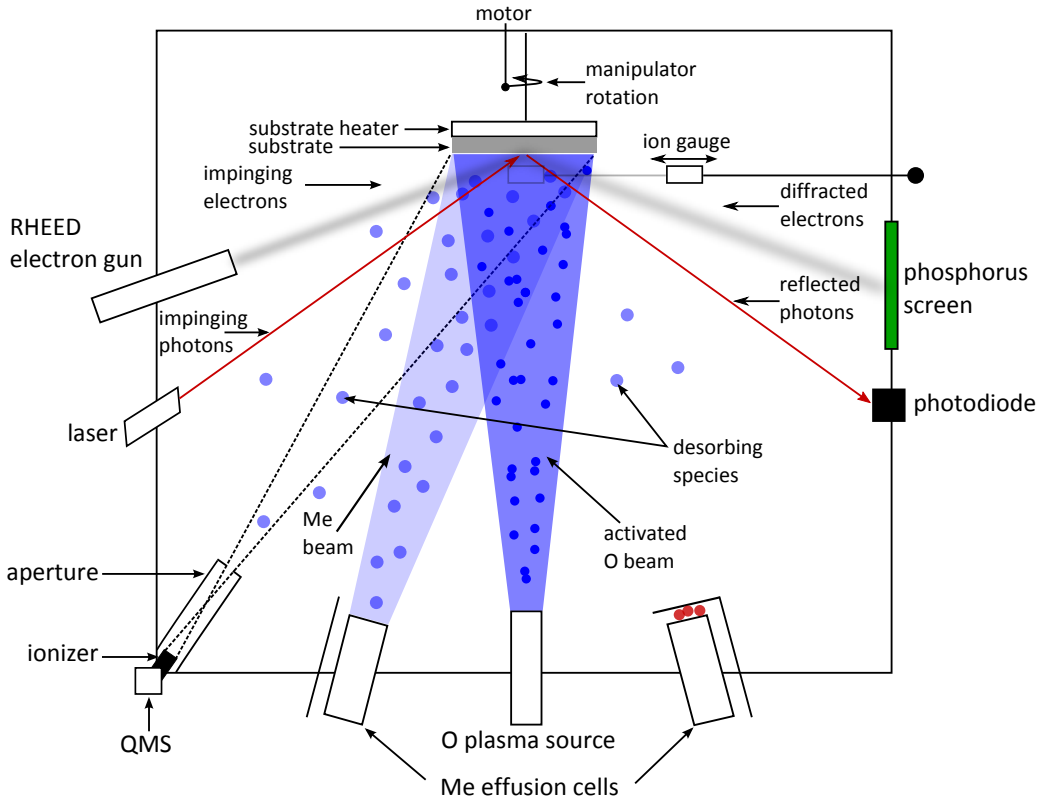

Figure 3.1.: Schematic of the MBE growth chamber used for this thesis. The species fluxes from the Me effusion cells and O plasma source, the substrate and substrate heater, as well as all installed `in-situ` analysis methods are drawn. Chamber, devices, and number of species are not to scale. A technical drawing of the growth chamber is depicted in the appendix A.1 delivered by CreaTec GmbH.

surement of the growth rate, a QMS that allows to monitor the desorbing flux from the substrate `in-situ`, and RHEED, an `in-situ` surface analysis method by means of electron diffraction. All devices are schematically drawn in Fig. 3.1.

Standard shuttered hot-lip effusion cells are used to evaporate liquid In, Ga, and Sn (7N purity). The beam equivalent pressure (BEP) which is proportional to the Me particle flux is measured `in-situ` by a nude filament ion gauge positioned at the substrate location. A radio frequency (RF) O plasma source with mass flow controller supplies active O flux from the research-grade O_2 gas Φ_{O_2} (6N purity). A heating filament to heat the substrate up to $T_G \sim 900\,°C$ is installed. A motor outside the growth chamber is mounted to rotate the substrate for homogeneous layer growth and homogeneous substrate heating.

3.2. Methodology

The `in-situ` and `ex-situ` characterization methods needed for the analysis of the grown samples are briefly introduced in this section.

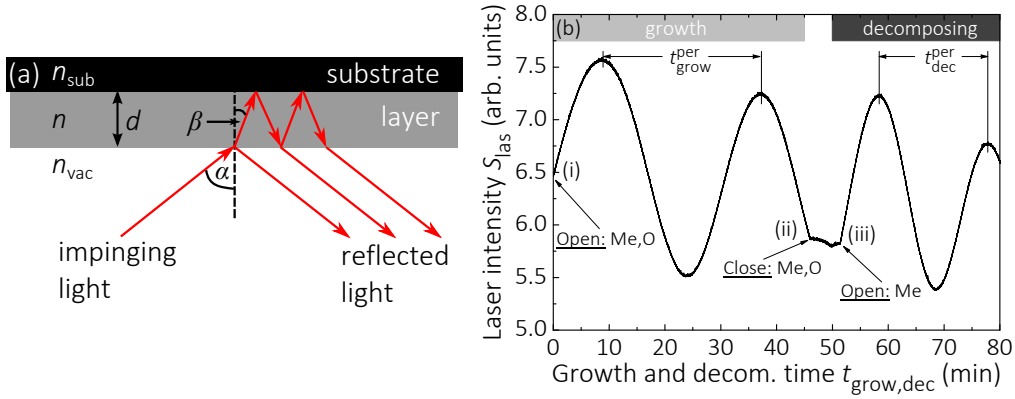

Figure 3.2.: (a) Depicts the principle of the measurement using laser reflectometry. (b) Detected laser signal S_{las} while growing and decomposing a layer as a function of time t. The layer was $Ga_2O_3(\bar{2}01)/Al_2O_3(0001)$. Position (i) indicates the start of growth, (ii) its end, and (iii) refers to the start of layer decomposition.

3.2.1. In-situ monitoring techniques

This subsection describes the laser reflectometry set-up as it was installed during this thesis. The design follows the one of Marcin Siekacz [109]. The operating principles of the QMS [62, 96] and RHEED [26, 60] are briefly discussed.

Laser reflectometry

In order to measure the growth rate Γ and decomposition rates D_{Me} of the metal-oxide layers a laser reflectometry set-up was built and installed. The term 'decomposition rate' corresponds to a negative Γ, i.e. a reduction of the layer thickness. Figure 3.2 (a) schematically shows the principle of the laser reflectometry set-up with laser light impinging on the growth surface. The used laser has a wavelength of $\lambda_{las} = 650\,nm$. For heteroeptitaxial growth this method is suitable to measure Γ due to the occurring thin-film interference of the laser light when propagating through the growing layer and being reflected between two boundaries: the layer and substrate boundary (interface) and the layer and vacuum boundary. This method cannot be applied for homoepitaxial growth because the substrate and growing layer posses the same refractive indices. In Fig. 3.2 (b) a measurement of the laser intensity while growing and decomposing a Ga_2O_3 layer is shown. A reduction of the layer (i.e. a negative Γ) can be seen by the amplitude change of the laser signal between growth and decomposition by comparing points (ii) and (iii). A sketch of the developed circuit that enables the read-out of the used laser by a photodiode is given in appendix A.2.

The condition for constructive interference for a layer thickness d is fulfilled when the difference between the optical paths of two interfering beams equals an integer multiple of λ_{las}. At which d the beams constructively interfere depends on λ_{las}, the angle between the impinging laser light and the normal of the growth surface α (Fig. 3.2), the refractive index of the growing material n, and the refractive index in vacuum $n_{vac} = 1$. At the used

growth chamber, the laser is positioned at port '16' (see technical drawing in appendix, Fig. A.1), thus, $\alpha = 60\,^{\circ}$.

For each material, d can be calculated by using and combining Bragg's law [25] with Snell's law [21] as

$$d = \Gamma t^{\mathrm{per}}_{\mathrm{grow}} = \frac{\lambda_{\mathrm{las}}}{2\,n}\left(\cos\left(\arcsin\left(\sin(\alpha)\,n^{-1}\right)\right)\right)^{-1} = -D_{\mathrm{Me}}\,t^{\mathrm{per}}_{\mathrm{dec}} \tag{3.1}$$

with $t^{\mathrm{per}}_{\mathrm{grow}}$ and $t^{\mathrm{per}}_{\mathrm{dec}}$ referring to one oscillating period for growth and decomposition, respectively, as depicted in Fig. 3.2 (b). The minus sign on the right-hand side refers to a reduction of the layer.

The refractive indices for β-Ga_2O_3, rutile SnO_2, bixbyite In_2O_3 and the used substrate α-Al_2O_3 (space-group: $R\bar{3}c$) are $n_{Ga_2O_3} = 2.00 \pm 0.05$ [110], $n_{SnO_2} = 2.0 \pm 0.02$ [39], $n_{In_2O_3} = 2.02$ [40], and $n_{Al_2O_3} = 1.70 \pm 0.03$ [136], respectively. The error takes the anisotropy of the crystal structure, and the dependence of n on the crystal orientation, into account. Inserting the values for $n_{Ga_2O_3}$, n_{SnO_2}, and n_{SnO_2} in Eq. (3.1) gives a layer thickness per oscillation period for Ga_2O_3, SnO_2, and In_2O_3 of $d_{Ga_2O_3} = (175 \pm 5)\,\mathrm{nm}$, $d_{SnO_2} = (175 \pm 3)\,\mathrm{nm}$, and $d_{In_2O_3} = 173\,\mathrm{nm}$, respectively. Figures 3.3 (a) and (c) show the `in-situ` measured oscillations by laser reflectometry while growing Ga_2O_3 and the `ex-situ` measured thickness of the same layer measured by SEM, respectively. The growth rate for this sample obtained by laser reflectometry was $3.1\,\text{Å}\,\mathrm{s}^{-1}$ resulting in a oscillation period of $t^{\mathrm{per}}_{\mathrm{growth}} = 1956\,\mathrm{s}$ with obtained layer thickness $d_{Ga_2O_3} = (606 \pm 7)\,\mathrm{nm}$. The `ex-situ` determination by SEM yields a layer thickness of $d_{Ga_2O_3} = (610 \pm 5)\,\mathrm{nm}$. Within their accuracy limits both methods yield the same result.

For $(In_xGa_{1-x})_2O_3$ growth the refractive indices and resulting layer thicknesses are calculated using a linear interpolation of d depending on x, i.e

$$d_{(In_xGa_{1-x})_2O_3}(x) = x\,d_{In_2O_3} + (1-x)\,d_{Ga_2O_3}\quad , \tag{3.2}$$

with the macroscopic In concentration x measured by EDX in a macroscopic layer volume of $\sim 4\,\mu\mathrm{m}^3$. As an example, the laser reflectometry signal and measured thickness by SEM of an $(In_{0.57}In_{0.43})_2O_3$ layer is shown in Figs. 3.3 (b) and (d), respectively. The measured Γ for this sample was $2.15\,\text{Å}\,\mathrm{s}^{-1}$. The oscillation period in this case was $t^{\mathrm{per}}_{\mathrm{growth}} = 840\,\mathrm{s}$. Multiplying it with Γ gives a layer thickness of $(In_{0.57}In_{0.43})_2O_3$ per period of $d_{(In_{0.57}Ga_{0.43})_2O_3} = 177\,\mathrm{nm}$. Inserting $x = 0.57$, $d_{Ga_2O_3}$, and $d_{In_2O_3}$ in Eq. (3.2) gives an interpolated thickness of $(174 \pm 5)\,\mathrm{nm}$. Within the error limits of laser reflectometry and calculated d, the `in-situ` determination of Γ for $(In_xGa_{1-x})_2O_3$ layers using laser reflectometry yields reliable results.

Line-of-sight quadrupole mass spectroscopy

QMS was used to monitor the desorbing species that are not incorporated during growth. It is commonly used for residual gas analysis in vacuum chambers. In the last decades, QMS has become an important `in-situ` tool for studying the growth and surface kinetic processes of MBE [41, 65, 66].

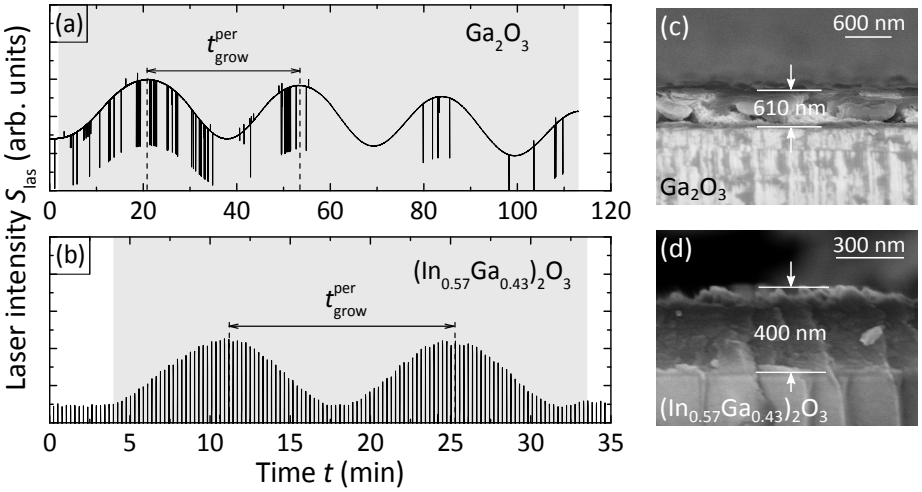

Figure 3.3.: (a) and (b) Variation of the measured laser intensity S_{las} while growing Ga_2O_3 and $(In_{0.57}Ga_{0.43})_2O_3$, respectively, as a function of time t. Gray areas indicate the total growth time. (c) and (d) Thickness of the same layers as shown in (a) and (b), respectively, measured by Anne-Kathrin Bluhm (PDI, Berlin) using SEM.

The principle of the QMS as it is mounted at the MBE growth chamber is drawn in Fig. 3.1. The aperture in front of the ionizer of the quadrupole serves as a filter so that only species desorbing from the substrate are detected. After a precise Me flux ϕ_{Me} calibration (subsection 3.3) this aperture allows to monitor desorption rates ϕ_j^{des} of species j quantitatively, and thus, the growth rate by $\gamma = \phi_{Me} - \phi_j^{des}$ (in $N_j\,nm^{-2}\,s^{-1}$). Besides that, T_G was calibrated by QMS as explained in subsection 3.3.3. A calibration of the QMS used for this thesis is given in the appendix A.5.

Reflection high-energy electron diffraction

RHEED is a surface sensitive characterization and analysis technique that allows studying the growth mode of the epilayer [86], possible surface reconstructions [59], Γ by measuring RHEED oscillations [51], or surface kinetics [99], `in-situ`.

An electron gun built by Createc GmbH[2] was used, supplying electrons with kinetic energy of $E_{kin} = 20\,keV$ impinging on the growth surface at gracing incidence $< 2°$. The electrons are only scattered by atoms of the topmost atomic layers of the sample and are detected with a phosphor screen placed in the diffracted beam path (schematic Fig. 3.1). These electrons may be described as planar waves with incident and diffracted wave vectors $\mathbf{k}_i$ and $\mathbf{k}_d$, respectively. Constructive interference occurs when the difference of the norm of $||\mathbf{k}_i||$ and $||\mathbf{k}_d||$ equals a multiple integer n of translation of the crystal lattice in reciprocal space:

$$||\mathbf{K}|| = ||\mathbf{k}_d|| - ||\mathbf{k}_i|| = n\left(\frac{2\pi}{||\mathbf{a}||}\right) , \tag{3.3}$$

with the norm of lattice vector in real space $||\mathbf{a}|| \equiv a$. With $E_{kin} = 20\,keV$ the electrons have wave-like behavior with de Broglie wavelength of $\lambda_{deB} = 0.62\,Å$. That means, $\lambda_{deB} < a$

[2] Adress: Createc GmbH, Industriestraße 9, 74391 Erligheim, Germany

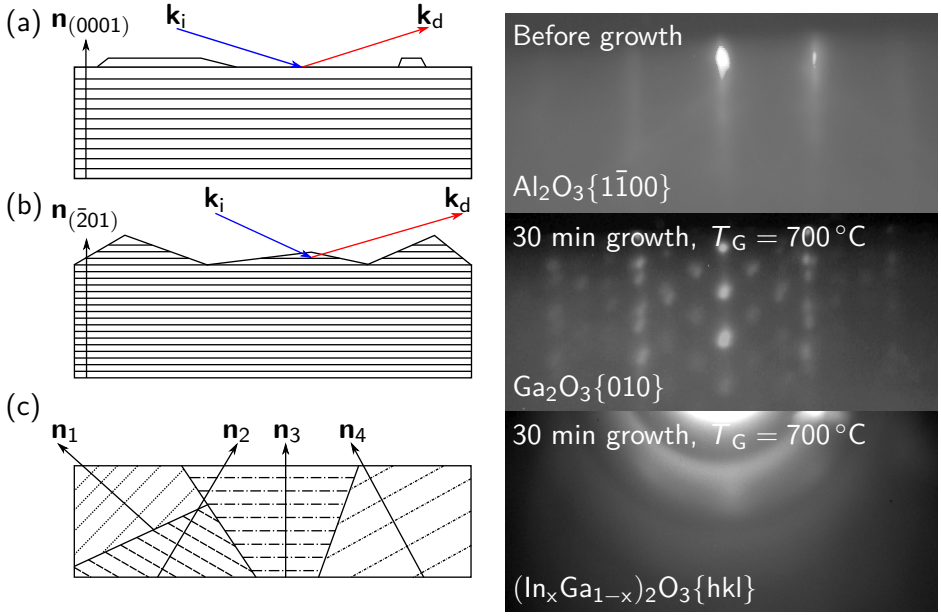

Figure 3.4.: Sketch of the correspondence between surface morphology and resulting RHEED pattern. (a) Left: sketch of a sapphire substrate with (0001) out-of-plane direction. Right: RHEED pattern showing its surface with azimuth $\{1\bar{1}00\}$ before growth after O plasma cleaning. (b) Left: sketch of a $Ga_2O_3(\bar{2}01)$ layer. Right: RHEED pattern of a grown Ga_2O_3 layer depicting the $\{010\}$ planes. (c) Left: sketch of a polycrystalline surface consisting of In_2O_3, Ga_2O_3, and $(In_\chi Ga_{1-\chi})_2O_3$ crystallites. Right: 'smeared-out' electron pattern diffracted from a polycrystalline surface.

for all investigated structures in this thesis, thus, there is always a reciprocal wave vector $||\mathbf{K}||$ that satisfies condition (3.3).

In this thesis, RHEED was used to monitor the crystallinity and surface morphology before, during and after growth. Figure 3.4 (a) shows an O plasma-treated $Al_2O_3(0001)$ surface before growth in in-plane direction $\{1\bar{1}00\}$. A streaky RHEED pattern indicates a smooth surface since the condition for constructive interference, Eq. (3.3), is fulfilled for laterally equidistant reciprocal lattice spacings $||\mathbf{K}||$. (b) Depicts a rough $Ga_2O_3(\bar{2}01)$ surface with azimuth $\{010\}$ after growth. Impinging a rough surface, the electrons may penetrate deeper into the sample (sketch in Fig. 3.4 (b)). Therefore, they can be diffracted by several lattice planes, and thus, out-of-plane diffraction occurs resulting in a spotty RHEED pattern. (c) Shows a $(In_\chi Ga_{1-\chi})_2O_3\{hkl\}$ surface after growth. The nominal In-to-(In+Ga) flux ratio was $X = \phi_{In}/(\phi_{In} + \phi_{Ga}) = 0.46$. The rings indicate a polycrystalline surface consisting of differently oriented grains with different microscopic In concentrations χ. These different directions are denoted by different vectors $\mathbf{n}_i$ and undefined Miller indices $\{hkl\}$. Since this surface possesses crystallites with different In and Ga concentrations, χ was left as a parameter. Rings are observed because for each grain a $||\mathbf{K}||$ exists that contributes to the RHEED pattern. An amorphous surface would result in a diffuse halo produced by electrons diffracted from a surface without any structure.

3.2.2. `Ex-situ` characterization techniques

Various material characterization techniques were used to investigate the crystal and electronic properties of the grown materials.

For the investigation of the crystal structure X-ray diffraction (XRD) [80] is used. The basic principle of XRD and its different scanning modes used for this thesis are given in the appendix A.4. The morphology of the samples are measured by means of atomic force microscopy (AFM) [12] and scanning electron microscopy (SEM) [100]. The macroscopic Me composition of $(In_xGa_{1-x})_2O_3$ is identified by energy dispersive X-ray spectroscopy (EDX) [61] in a SEM. Transport and electronic properties of the samples are investigated by current-voltage (I-V) and capacitance-voltage (C-V) measurements [93, 98] (no data shown).

All mentioned techniques are described in several books and papers (as cited) and will not be discussed. If necessary, experimental details for a mentioned technique will be given when the corresponding data is shown.

3.3. Calibration of the MBE growth chamber

In order to understand the reaction kinetics of a growing layer it is crucial to know the number of atoms or molecules reaching the growth surface, the number of atoms or molecules that are incorporated into the crystal, and the number of atoms or molecules desorbing off the growth surface during growth.

In this section, a calibration of all MBE growth parameters, i.e. particle Me flux ϕ_{Me} (Me = Ga, In, Sn), particle O flux during binary growth ϕ^{*}_{O}, 'effective' particle O flux during ternary growth $\phi^{*,\mathrm{eff}}_{\mathrm{O}}$, and surface growth temperature T_{G}, is given.

3.3.1. Metal fluxes

In order to determine the supplied ϕ_{Me} prior to growth the Me BEP p_{Me} is measured `in-situ` by a nude filament ion gauge, positioned at substrate location. The BEP is calibrated by measuring it at different effusion cell temperatures, T_{ec}, and fitting the obtained values as a function of T_{ec} by an Arrhenius plot (not shown). The calibration procedure follows the one as developed at the PDI (code for the EPIC software given in the appendix A.3). Since the BEP is an auxiliary quantity it has to be converted into quantitative reliable fluxes. This is because: (i) each Me effusion cell is mounted at different ports of the growth chamber, and therefore, each Me has a different impinging angle between the ion gauge and its normal to the ground (Figs. 3.1 and A.1), resulting in different measured atomic Me fluxes for each cell. (ii) Each Me has a specific ionization cross sectional factor that has to be multiplied with the measured BEP. The current measured by the ion gauge used for this calibration is normed to an equivalent nitrogen particle flux.

The Me fluxes were calibrated by measuring Γ in the O-rich growth regime, i.e. in the excess of O. In order to assure that all Me supplied was oxidized to the desired metal-oxide and incorporated into the layer, (i) `in-situ` QMS monitoring to detect potential desorbing

species from the growth surface (at too high T_G) and (ii) `ex-situ` SEM measurements that identify possible Me droplets on the growth surface (at too low T_G) were performed. In this case, the BEP is proportional to Γ and can be converted into reliable growth rate units. The relation between p_{Me} in Torr and Γ in Å/s (equaling Φ_{Me} in Å/s in this case) is for Ga, In, and Sn:

$$p_{Ga} = 3.3 \times 10^{-7}\,\text{Torr} \mathrel{\hat{=}} 1.0\,\text{Å}\,\text{s}^{-1} = \Phi_{Ga}\ , \tag{3.4}$$

$$p_{In} = 5.7 \times 10^{-7}\,\text{Torr} \mathrel{\hat{=}} 1.0\,\text{Å}\,\text{s}^{-1} = \Phi_{In}\ , \tag{3.5}$$

$$p_{Sn} = 2.8 \times 10^{-7}\,\text{Torr} \mathrel{\hat{=}} 1.0\,\text{Å}\,\text{s}^{-1} = \Phi_{Sn}\ , \tag{3.6}$$

respectively. The obtained growth rate units are still relative quantities depending on the structure of the measured layer. They are converted into particle flux units by taking the different phases of Ga_2O_3, In_2O_3, and SnO_2 for the determination of the atomic Ga, In, and Sn flux, respectively, into account.

First, Φ_{Me} is multiplied by the cation density ρ_{Me} of the specific compound,

$$\phi_{Me} = \Phi_{Me}\,\rho_{Me}\ . \tag{3.7}$$

The obtained values are collected in Tab. 3.1. Second, the `relative` Me particle flux ϕ_{Me}^{BEP} obtained by measuring p_{Me} is calculated by kinetic theory of gases

$$\phi_{Me}^{BEP} = C \times \left(\frac{p_{Me}^2}{2\,\pi\,m_{Me}\,k_B\,T_{Me}} \right)^{\frac{1}{2}}\ . \tag{3.8}$$

The pre-factor $C = 10^{-18}\,\text{Pa}\,\text{Torr}^{-1}$ serves as a conversion factor in order to obtain ϕ_{Me}^{BEP} in $\text{Me}\,\text{nm}^{-2}\,\text{s}^{-1}$. The mass of the element and its temperature (similar to effusion cell temperature) are denoted as m_{Me} and T_{Me}, respectively. Third, the 'effective' sensitivity factor of the Me I_{Me} is determined by the ratio of Eqs. (3.7) and (3.8), i.e.

$$I_{Me} = \frac{\phi_{Me}}{\phi_{Me}^{BEP}}\ . \tag{3.9}$$

This sensitivity factor connects the `in-situ` measured relative Me flux ϕ_{Me}^{BEP} (i.e, the BEP) with the actual ϕ_{Me} impinging the growth surface.

The standard deviation of I_{Me}, $\sigma_{I_{Me}}$, is calculated for independent variables as

$$\sigma_{I_{Me}} = \sqrt{\sum_{v\,=\,\phi_{Me},\,p_{Me},\,T_{Me}} \left(\frac{\partial I_{Me}}{\partial v} \right)^2 \sigma_v^2}\ , \tag{3.10}$$

with standard deviation σ_v of variable v. The standard deviation of ϕ_{Me} is assumed to be $\sigma_{\phi_{Me}} = 0.03\,\phi_{Me}$. It originates from the laser reflectometry set-up by which ϕ_{Me} was calibrated (e.g. an impinging laser deviating from α), and by the read out of Γ using its software. For p_{Me} the standard deviation is estimated as $\sigma_{p_{Me}} = 0.05\,p_{Me}$. It can be caused by different background pressures in the growth chamber. This, in turn, causes a different sensitivity of the ion gauge on the measured p_{Me}. For the Me temperature T_{Me} the standard deviation is approximated as $\sigma_{T_{Me}} = 0.05\,T_{Me}$. It is an estimation of the real temperature of the Me atoms and the one measured by the thermo-couple mounted at the corresponding effusion cell. With this calibration the atomic or molecular incorporation rate into the crystal and its desorption rate can be quantitatively compared to ϕ_{Me}. All factors and the obtained $I_{Me} \pm \sigma_{I_{Me}}$ are tabulated in Tab. 3.1.

Compound	space-group	p_{Me} (10^{-7} Torr)	Φ_{Me} $\left(\frac{\text{Å}}{\text{s}}\right)$	$\phi_{\mathrm{Me}}^{\mathrm{BEP}}$ $\left(\frac{\text{Me}}{\text{nm}^2\,\text{s}}\right)$	ϕ_{Me} $\left(\frac{\text{Me}}{\text{nm}^2\,\text{s}}\right)$	I_{Me}	$\sigma_{I_{\mathrm{Me}}}$
Ga_2O_3	$C2/m$	3.30	1.0	0.42	3.8	9.1	0.67
In_2O_3	$Ia\bar{3}$	5.67	1.0	0.60	3.1	5.2	0.40
SnO_2	$P4_2/mnm$	2.77	1.0	0.24	4.2	17.5	1.22

Table 3.1.: Conversion factors for the `in-situ` measured BEP p_{Me} into growth rate and particle flux units. The Ga, In, and Sn cell temperatures were $T_{\mathrm{Ga}} = 820\,^{\circ}\mathrm{C}$, $T_{\mathrm{In}} = 800\,^{\circ}\mathrm{C}$, and $T_{\mathrm{Sn}} = 1100\,^{\circ}\mathrm{C}$, respectively.

3.3.2. Oxygen fluxes

In order to grow the investigated metal-oxides, activated O species are needed, and obtained by a RF plasma source. The used source for this thesis is a SVTA-RF-4.5 O plasma source built by SVT Associates[3]. This device is designed to break the O bonds in order to supply activated O_2 or atomic O.

Figure 3.5 shows the calibration of the O RF plasma source. (a) Depicts the minimum P_{rf} needed for a given $\Phi_{\mathrm{O_2}}$ to sustain the plasma, and gives information about lower limits of O atoms supplied for growth. (b) Plots Γ of Ga_2O_3 as a function of $\Phi_{\mathrm{O_2}}$. For $\Phi_{\mathrm{Ga}} = 1.6\,\text{Å}\,\mathrm{s}^{-1}$ the minimum $\Phi_{\mathrm{O_2}}$ needed for Ga_2O_3 formation is 0.3 SCCM with $P_{\mathrm{rf}} = 300\,\mathrm{W}$. This is due to the O-deficiency induced Ga_2O desorption in the Ga-rich regime as explained in chapter 5, section 5.1.

Now, a quantitative calibration of the activated particle O flux for each binary metal-oxide $\phi_{\mathrm{O}}^{*,\mathrm{Me}}(P_{\mathrm{rf}})$ is given. This calibration already contains scientific results but has to be anticipated. However, the physics and chemistry behind the data will only be discussed in chapter 5. Figures 3.6 (a), (b). and (c) plot Γ of Ga_2O_3, In_2O_3, and SnO_2 as a function of Φ_{Ga}, Φ_{In}, and Φ_{Sn}, respectively. The peak in all figures represents the stoichiometric growth condition for the supplied $\Phi_{\mathrm{O_2}}$. At this peak, with respect to the stoichiometry of the perfect crystal, the same amount of Me and O atoms are provided on the growth surface and are incorporated. With these measurements, $\Phi_{\mathrm{O_2}}$ may be converted into growth rate units. The conversion for of the activated of flux $\Phi_{\mathrm{O}}^{*,\mathrm{Me}}$ in growth rate units for each compound is:

$$\Phi_{\mathrm{O}}^{*,\mathrm{Ga}}(P_{\mathrm{rf}} = 300\,\mathrm{W}) = 1.7\,\text{Å}\,\mathrm{s}^{-1} \mathrel{\hat{=}} \Phi_{\mathrm{O_2}} = 1.0\,\mathrm{SCCM}\,, \tag{3.11}$$

$$\Phi_{\mathrm{O}}^{*,\mathrm{In}}(P_{\mathrm{rf}} = 200\,\mathrm{W}) = 1.9\,\text{Å}\,\mathrm{s}^{-1} \mathrel{\hat{=}} \Phi_{\mathrm{O_2}} = 0.5\,\mathrm{SCCM}\,, \tag{3.12}$$

$$\Phi_{\mathrm{O}}^{*,\mathrm{Sn}}(P_{\mathrm{rf}} = 300\,\mathrm{W}) = 1.8\,\text{Å}\,\mathrm{s}^{-1} \mathrel{\hat{=}} \Phi_{\mathrm{O_2}} = 0.5\,\mathrm{SCCM}\,. \tag{3.13}$$

Assuming that the number of activated O atoms increases linearly with $\Phi_{\mathrm{O_2}}$ and P_{rf} the active O fluxes are extrapolated and normalized for $\Phi_{\mathrm{O_2}} = 1.0\,\mathrm{SCCM}$ and $P_{\mathrm{rf}} = 300\,\mathrm{W}$.

[3] SVT Associates, Eden Prairie, Minnesota 55344, USA.

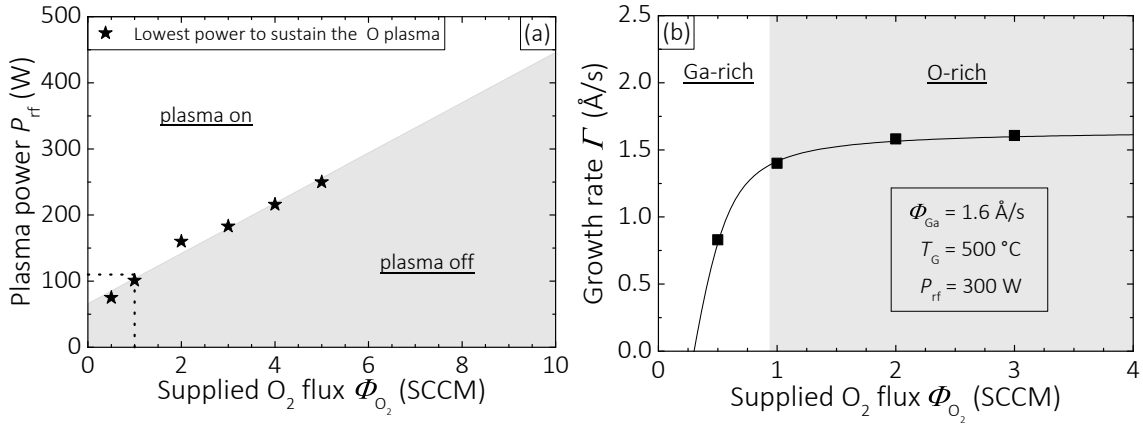

Figure 3.5.: (a) Phase diagram of the O plasma source used in this thesis. The minimum plasma power P_{rf} needed to sustain the plasma as a function of the supplied O_2 flux Φ_{O_2} is plotted. (b) Depicts the growth rate Γ of Ga_2O_3 as a function of Φ_{O_2}. The lines are guides to the eye.

The results are:

$$\Phi_{\mathrm{O}}^{*,\mathrm{Ga}}(P_{\mathrm{rf}} = 300\,\mathrm{W}) = 1.7\,\text{Å}\,\mathrm{s}^{-1} \mathrel{\hat{=}} \Phi_{\mathrm{O}_2} = 1.0\,\mathrm{SCCM}\,, \tag{3.14}$$

$$\Phi_{\mathrm{O}}^{*,\mathrm{In}}(P_{\mathrm{rf}} = 300\,\mathrm{W}) = 5.7\,\text{Å}\,\mathrm{s}^{-1} \mathrel{\hat{=}} \Phi_{\mathrm{O}_2} = 1.0\,\mathrm{SCCM}\,, \tag{3.15}$$

$$\Phi_{\mathrm{O}}^{*,\mathrm{Sn}}(P_{\mathrm{rf}} = 300\,\mathrm{W}) = 3.6\,\text{Å}\,\mathrm{s}^{-1} \mathrel{\hat{=}} \Phi_{\mathrm{O}_2} = 1.0\,\mathrm{SCCM}\,. \tag{3.16}$$

The conversion from growth rate units into atomic O flux units for each crystal structure is done in a similar way as presented for ϕ_{Me}.

First, the respective 'effective' active O flux for the used metal $\phi_{\mathrm{O}}^{*,\mathrm{Me}}$ is multiplied by the O atom density per unit-cell $\rho_{\mathrm{O}}^{\mathrm{Me}}$,

$$\phi_{\mathrm{O}}^{*,\mathrm{Me}} = \Phi_{\mathrm{O}}^{*,\mathrm{Me}}\,\rho_{\mathrm{O}}^{\mathrm{Me}}\,. \tag{3.17}$$

The values are collected in Tab. 3.2. To determine the fraction of provided O species that can contribute to growth, it is assumed that each O_2 molecule is cracked by RF in the O plasma source. The resulting O particle flux $\phi_{\mathrm{O}}^{\mathrm{BEP}}$, obtained by measuring the O BEP p_{O}, is calculated by kinetic theory of gases,

$$\phi_{\mathrm{O}}^{\mathrm{BEP}} = 2C \times \left(\frac{p_{\mathrm{O}}^2}{2\,\pi\,m_{\mathrm{O}}\,k_{\mathrm{B}}\,T_{\mathrm{O}}}\right)^{\frac{1}{2}}\,. \tag{3.18}$$

The conversion factor C is the same as introduced in Eq. (3.8). The total oxidation efficiency $J_{\mathrm{O}}^{\mathrm{Me}}$ that connects $\phi_{\mathrm{O}}^{\mathrm{BEP}}$ and $\phi_{\mathrm{O}}^{*,\mathrm{Me}}$ is determined by the ratio of Eqs. (3.17) and (3.18),

$$J_{\mathrm{O}}^{\mathrm{Me}} = \frac{\phi_{\mathrm{O}}^{*,\mathrm{Me}}}{\phi_{\mathrm{O}}^{\mathrm{BEP}}}\,. \tag{3.19}$$

The results are collected in Tab. 3.2.

The factor $J_{\mathrm{O}}^{\mathrm{Me}}$ is a combination of the cracking efficiency of the used plasma source η_{OPla}, a possible cracking of excited O_2-molecules on the growth surface by the supplied

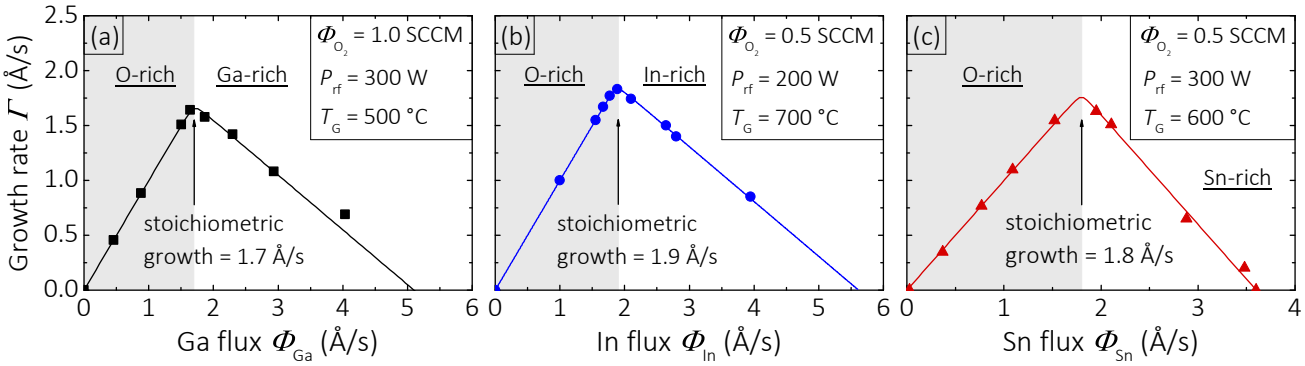

Figure 3.6.: (a), (b), and (c) depict the binary growth rates Γ as a function of the respective Me flux $\Phi_{\mathrm{Ga,In,Sn}}$ of Ga_2O_3 (squares), In_2O_3 (discs), and SnO_2 (triangles), respectively. The lines are guides to the eye.

Me adatoms, and the specific oxidation potential of the used Me. A potential kinetic interpretation for the different $J_{\mathrm{O}}^{\mathrm{Me}}$ is given in chapter 5, subsection 5.2.2. An upper limit for η_{OPla} at $P_{\mathrm{rf}} = 300\,\mathrm{W}$, i.e. how many O_2 molecules are indeed broke by the RF is $\eta_{\mathrm{OPla}} \leq J_{\mathrm{O}}^{\mathrm{Ga}}$.

Due to the different $J_{\mathrm{O}}^{\mathrm{Me}}$, for ternary growth the 'effective' atomic O flux available on the growth surface $\phi_{\mathrm{O}}^{*,\mathrm{eff}}$ for each nominal alloy concentration $X = \phi_i/(\phi_i + \phi_j)$ (with i, j = Ga, In, Sn and $i \neq j$) has to be interpolated using equation:

$$\boxed{\phi_{\mathrm{O}}^{*,\mathrm{eff}} = \phi_{\mathrm{O}}^{\mathrm{BEP}} \left(X\, J_{\mathrm{O}}^{i} + (1 - X)\, J_{\mathrm{O}}^{j} \right)} \quad . \tag{3.20}$$

The determination of $\phi_{\mathrm{O}}^{*,\mathrm{eff}}$ is needed to understand the kinetics and thermodynamics during $(In_xGa_{1-x})_2O_3$ MBE presented in chapter 6.

The standard deviation for $J_{\mathrm{O}}^{\mathrm{Me}}$, $\sigma_{J_{\mathrm{O}}^{\mathrm{Me}}}$ (for independent variables), is calculated as

$$\sigma_{J_{\mathrm{O}}^{\mathrm{Me}}} = \sqrt{\sum_{v\,=\,\phi_{\mathrm{O}}^{*,\mathrm{Me}},\,\phi_{\mathrm{Me}},\,T_{\mathrm{O}}} \left(\frac{\partial J_{\mathrm{O}}^{\mathrm{Me}}}{\partial v} \right)^2 \sigma_v^2} \quad . \tag{3.21}$$

Here, $\sigma_{\phi_{\mathrm{O}}^{*,\mathrm{Me}}} = 0.03\,\phi_{\mathrm{Me}}$ (same argument as given for $\sigma_{\phi_{\mathrm{Me}}}$). The standard deviation of p_{O}, $\sigma_{p_{\mathrm{O}}} = 0.01\,p_{\mathrm{O}}$, is much smaller as the analogon for ϕ_{Me} since $p_{\mathrm{O}} \sim p_{\mathrm{GC}}$. Therefore, fluctuations of p_{O} are very small. The uncertainty in O temperature T_{O} is assumed as $\sigma_{T_{\mathrm{O}}} = 0.05\,T_{\mathrm{O}}$, and takes parasitic heating by the surrounding Me effusion cells into account.

3.3.3. Growth temperature

In order to obtain reproducible results for the layers grown by MBE a calibration of T_{G} is essential. Direct physical T_{G} measurements were used to measure the temperature offset between the growth surface and the thermo-couple T_{TC}, i.e., $\Delta T = T_{\mathrm{TC}} - T_{\mathrm{G}}$.

Compound	space-group	$\phi_{\mathrm{O}}^{\mathrm{BEP}}$ $\left(\frac{\mathrm{O}}{\mathrm{nm^2\,s}}\right)$	$\Phi_{\mathrm{O}}^{*,\mathrm{Me}}$ $\left(\frac{\text{Å}}{\mathrm{s}}\right)$	$\rho_{\mathrm{O}}^{\mathrm{Me}}$ $\left(\frac{\mathrm{O}}{\mathrm{nm^3}}\right)$	$\phi_{\mathrm{O}}^{*,\mathrm{Me}}$ $\left(\frac{\mathrm{O}}{\mathrm{nm^2\,s}}\right)$	$J_{\mathrm{O}}^{\mathrm{Me}}$	$\sigma_{J_{\mathrm{O}}^{\mathrm{Me}}}$
Ga_2O_3	$C2/m$	102	1.7	57.5	9.8	0.096	0.004
In_2O_3	$Ia\bar{3}$	102	5.7	47.0	26.8	0.263	0.012
SnO_2	$P4_2/mnm$	102	3.6	84.0	30.2	0.296	0.014

Table 3.2.: Conversion factors for the supplied O flux and its maximum atomic incorporation into the crystal for an O BEP of 1×10^{-5} Torr, plasma power $P_{\mathrm{rf}} = 300$ W, and O plasma cell temperature of 22 °C (equaling laboratory temperature).

Reliable T_{G} measurements are an issue in MBE since the heating of the substrate and its surface by the heating filament is not homogeneous. This issue can be partly overcome by rotating the sample during growth. Rotating the sample has two advantages: (i) it allows a more homogeneous substrate heating, and (ii) a more uniform reactant distribution on the growth surface delivered by the Me effusion cells and O plasma source impinging in different angles on the growth surface (Fig. 3.1). In addition to substrate rotation, the wafers used for growth were back side sputter coated with titanium and a boron nitride (BN) plate between the heating filament and wafer was used to further improve heat distribution on the growth surface, i.e., reducing the T_{G}-gradient.

The thermo-couple used in this thesis is C-type made of a tungsten (W) - rhenium (Rh) alloy ($W_{0.74}Rh_{0.26}$), that allows temperature measurements in the high-T_{G} range of T_{TC} up to 2300 °C. The heating filament is made of pure W due to its high melting point and low vapor pressure leading to less impurity contamination in the grown layers caused by the heating filament. Another effect that hampers precise T_{G}-calibration is the heating of the growth surface by the heat radiation from the effusion cells during growth. This is the case when the effusion cell temperature is higher than T_{G}, and mostly valid for the growth rate studies presented in this thesis.

The growth temperature was calibrated by one fix-point temperature obtained by melting aluminum (Al) on a sapphire substrate. At $T_{\text{Al-melt}} = 660\,^{\circ}\mathrm{C} = T_{\mathrm{G}}$ Al starts melting [22] at a background pressure in the growth chamber of $p_{\mathrm{GC}} \sim 10^{-9}$ Torr. Once Al starts melting the RHEED pattern of crystalline Al disappears and a diffuse halo appears due to the scattering of electrons on amorphous Al. The T_{TC} measured at this point can be compared with $T_{\text{Al-melt}} = T_{\mathrm{G}}$ and usually has an offset of $\Delta T = T_{\mathrm{TC}} - T_{\mathrm{G}}$. The offset ΔT may have different origins: (i) the position of the thermo-couple, i.e., how close it is to the heating filament, (ii) different heat conductivities of the used substrates when there are different materials, (iii) the age of the BN plate, (iv) different substrate holders.

After ΔT is obtained, a second method was used to calibrate T_{G}. By this method [53], the adsorption temperature of Ga, T_{ads}, on the growth surface at given ϕ_{Ga} is measured. Here, the total desorption of Ga is detected by QMS at sufficiently high T_{G}. Once the vapor pressure caused by the substrate equals the vapor pressure of the impinging Ga — while slowly decreasing T_{TC} — the detected Ga signal starts decreasing. This onset of Ga adsorption at given ϕ_{Ga} and T_{TC} may be compared with the Ga vapor pressure curve [35] in order to obtain the relative growth temperature $T_{\mathrm{TC}} = T_{\mathrm{ads}}$. This relative temperature can be measured before each growth cycle and T_{G} reproduced.

With the calibration of all MBE growth parameters ϕ_{Me}, $\phi_{\mathrm{O}}^{*,\mathrm{Me}}$ (also $\phi_{\mathrm{O}}^{*,\mathrm{eff}}$), and T_{G}, the data obtained and models derived in this thesis shall be reproducible (within the error limits) in all MBE growth chambers.

3.4. Sample preparation — In-bonding

The grown films for data obtained and presented in chapters 6 and 7 were grown on substrates that were In-bonded to a Si carrier wafer. Here, In acts as glue and provides a good thermal contact.

The In-bonding technique allows the simultaneous growth of a material on different substrates under 'identical' growth conditions. However, the issue concerning In-bonded samples is that In melts and evaporates at T_{G} used for the studies presented. Consequently, the sample may drop off the carrier wafer due to In out-diffusion at elevated T_{G} after a limited growth time t_{grow} and fells into the growth chamber. The fall of the sample has two major disadvantages: (i) the sample (usually) cannot be used for systematic data analysis since the moment when the sample drops off is (usually) unknown. (ii) Depending on the position the sample is glued on the Si carrier substrate, the rotation speed of the manipulator, and position of the effusion cell(s), it may happen that the sample fells into the crucible of the effusion cell, which, in turn, cannot be used for growth anymore. As a consequence, this may lead to an undesired opening of the growth chamber.

For these reasons, a special preparation technique was developed during this thesis that allows the growth of In-bonded samples at very high-T_{G} and arbitrarily long t_{grow} without a sample drop during growth or sample transfer. Figure 3.7 shows an example of samples that were In-bonded: (a) before growth (a) and (b), (c) post growth.

First, the samples are In-bonded on a new or used Si carrier wafer, in a way, that the area of the Si wafer covered by In is larger than the size of the sample (Fig. 3.7 (a)). In order for the sample to stick on the carrier wafer it is moved on a small amount of In melted by a heating plate. The temperature of the heating plate is too high when In starts oxidizing (becomes golden-brown) with the O species in air. The sample bonds to the carrier wafer once the force needed to move the sample appreciable increases. In the example shown in Fig. 3.7, the Si wafer is a used one as can be seen by thin-films interferences of light waves in films emerged during a previous growth cycle. The In glue appears in 'metallic' gray. Second, the Si wafer with the bonded sample is loaded into the load-lock chamber of the MBE and heated so that water may desorb off the sample. The set temperature shall be above the water desorption temperature and below the In melting temperature at given pressure in the load-lock chamber. Third, after water desorption, the sample is moved to growth position. Fourth, the thermo-couple temperature T_{TC} of the substrate heater is being increased to the desired T_{G} starting from $T_{\mathrm{TC}} = 100\,^{\circ}\mathrm{C}$. During this process, the O plasma is turned on at the beginning of substrate heating. Due to the O plasma the In which is not covered by the sample oxidizes to In_2O_3 — dark areas in post-growth samples shown in Figs. 3.7 (b) and (c). The O plasma also oxidizes the In being directly at the edge of the sample, as depicted in Fig. 3.7 (c). Here, the shape of the sample is still visible after growth and removing it.

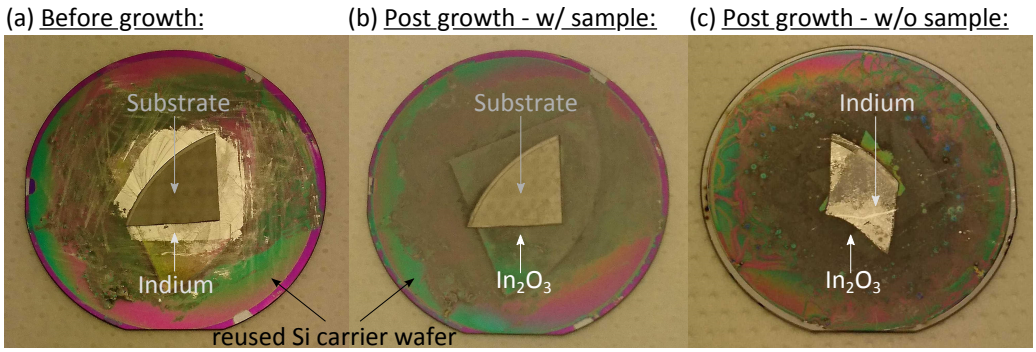

Figure 3.7.: Samples grown by a new developed In-bonding technique. (a) Shows a substrate bonded by In ('metallic' gray) on a reused Si carrier wafer before growth. (b) Depicts the same sample after growth. The metallic In is oxidized to In_2O_3. (c) After removing the sample the In below the sample is still present and metallic after growth. The area covered by In has the shape of the removed sample indicating that In hardly diffuses below the substrate. This sample was not the same as shown in (a) and (b).

Since In_2O_3 is temperature stable under MBE growth conditions up to $\sim 1500\,^{\circ}C$ it does not decompose for all T_G used in this thesis. This preparation technique has two advantages: (i) the high melting or decomposition temperature of In_2O_3 during MBE allows the growth of In-bonded samples at very high-T_G, e.g., in order to achieve high-quality crystals. (ii) The In below the sample cannot diffuse out, since blocked by In_2O_3 at the sample's edge (Fig. 3.7 (c)), and therefore, arbitrarily long growth cycles and very high-T_G can be performed.

After growth all In is oxidized as shown in Fig. 3.7 (b). After removing the sample from the Si carrier substrate the metallic In which was below the sample is still present, Fig. 3.7 (c). This illustrates the third advantage of this method, (iii): since the In below the substrate cannot diffuse, the heat contact between Si carrier wafer and substrate remains almost constant resulting in a more stable growth surface temperature. This is not the case when In is diffusing during growth. In the case of In diffusion, the heat resistance between substrate and carrier wafer increases with t_{grow}, thus, the surface growth temperature decreases.

4. Theory

This chapter introduces the theoretical background needed to explain the thermodynamics and kinetics of chemical reactions, contributing to the Me incorporation and desorption, as well as their respective kinetic growth models presented in chapters 5 and 6. It deals with the theoretical treatment of simple chemical reactions, their reaction rates, and rate laws. Large parts of the thermodynamics and chemical kinetics shown in this chapter can be found in literature [6, 97].

A chemical reaction is defined as the interaction between reactants R_i, that results in the formation of new chemical compounds, the products P_j. Two major factors determine the reaction rate of a chemical reaction: (i) the thermodynamic one that describes whether a reaction occurs spontaneously or not. This factor can be described by a thermodynamic potential, that is minimized when a system reaches chemical equilibrium: the Gibbs free energy G (section 4.2). (ii) The kinetic factor that describes how fast or likely a chemical reaction may occur: the reaction rate constant k (section 4.3).

4.1. Chemical equations and reaction rates

An elementary chemical reaction with n reactants R_i forming m products P_j reads as

$$\sum_{i=1}^{n} r_i \, R_i(a) \xrightarrow{k} \sum_{j=1}^{m} p_j \, P_j \, (a,\, g,\, s) \tag{4.1}$$

with a, g, s denoting the adsorbate, gaseous, and solid phase, respectively. The stoichiometric coefficients of R_i and P_j are r_i and p_j, respectively. In this thesis, r_i and p_j are given in number of atoms or molecules of the corresponding species. Reaction (4.1) can be described by the reaction rate

$$\mathcal{R} = -\frac{1}{r_i}\dot{\theta}_{\mathrm{R}_i} = +\frac{1}{p_j}\dot{\theta}_{\mathrm{P}_j} \tag{4.2}$$

with surface densities of R_i, P_j, and their partial derivatives with respect to time, $\partial_t\theta_{\mathrm{R}_i} = \dot{\theta}_{\mathrm{R}_i}$ and $\partial_t\theta_{\mathrm{P}_j} = \dot{\theta}_{\mathrm{P}_j}$, respectively. During MBE, growth takes place on a heated substrate (chapter 3, section 3.1), and is assumed to be a two-dimensional process. For this reason, all θ are given in $N_{R,P}\,\mathrm{nm}^{-2}$. The minus and plus signs in Eq. (4.2) refer to consumption and formation of R_i and P_j, respectively.

As an example, the simplest chemical reaction described in this thesis is the desorption of a species from a growth surface. In this case, reaction (4.1) reads as

$$r\,R\,(a) \xrightarrow{k_{\mathrm{des}}} r\,P(g) \tag{4.3}$$

with $n = m = 1$ and the reaction rate constant for R desorption k_{des}. In this special case $R = P$ and $r = p$. The reaction rate for the desorption reaction is given by

$$\mathcal{R}_{\mathrm{des}} = -\frac{1}{r}\,\dot{\theta}_{\mathrm{R}} = \frac{1}{p}\,\dot{\theta}_{\mathrm{P}}\ . \tag{4.4}$$

The minus sign refers to the loss of R from the growth surface.

4.2. Thermodynamics

Each macroscopic (closed) physical system tends to minimize its energy and maximize its entropy. The state satisfying this tendency is called thermodynamic equilibrium. A thermodynamic potential that describes this behavior for chemical reactions is the Gibbs free energy G and reads as

$$G(T, P, N) = H(S, P, N) - TS\ \ , \tag{4.5}$$

with: temperature T, enthalpy H, pressure P, number of reactants N, and entropy S. Under growth conditions used in this thesis, the total change of G under isothermal-isobaric conditions is given by

$$\Delta G = \Delta H - T\Delta S\ . \tag{4.6}$$

The change of H, ΔH, is referred to the change of the kinetic and potential energy of the system due to mass or heat transfer. For example, a change in number of reactants N_{R_i} of species i changes the chemical potential of the system.

The enthalpy and entropy of formation at given temperature $H(T)$ and $\Delta S(T)$, respectively, are calculated as

$$\Delta H(T) = \Delta H_{T_0} + \int_{T_0}^{T_{\mathrm{G}}} \mathrm{d}T\, C_P(T) \tag{4.7}$$

and

$$\Delta S(T) = \Delta S_{T_0} + \int_{T_0}^{T_{\mathrm{G}}} \mathrm{d}T\, \left(\frac{C_P(T)}{T}\right)\ , \tag{4.8}$$

respectively. The enthalpy and entropy of formation at room temperature T_0 are denoted as ΔH_{T_0} and ΔS_{T_0}, respectively. The heat capacity at constant P can be expressed as

$$C_P(T) = a + b\,10^{-3}\,T + c\,10^{6}\,T{-}2 + d\,10^{-6}\,T^2 \tag{4.9}$$

with pre-factors a, b, c, and d. The values ΔH_{T_0}, ΔS_{T_0}, a, b, c, and d were taken from Ref. [19] and are collected for all species in Ga_2O_3, In_2O_3, and SnO_2, in Tab. B.1 (appendix B). The Gibbs free energy of formation, ΔG, can be calculated as the sum of all Gibbs free energies of formation of the products, $\sum_j \Delta G_{P_j}$, minus the sum of all Gibbs free energies of formation of the reactants, $\sum_i \Delta G_{R_i}$, and their corresponding stoichiometric coefficients, i.e.,

$$\Delta G = \sum_{j=1}^{m} p_j\,\Delta G_{P_j} - \sum_{i=1}^{n} r_i\,\Delta G_{R_i}\ . \tag{4.10}$$

4.3. Chemical kinetics

In chemical kinetics a rate law relates the reaction rate $\mathcal{R}$ to the surface concentration of the reactants θ_{R_i}, i.e., the higher θ_{R_i} the higher $\mathcal{R}$. As an example, the rate law for reaction rate (4.1) is:

$$\mathcal{R} = k \prod_{i=1}^{n} \theta_{\mathrm{R}_i}^{o_i} \, . \tag{4.11}$$

The power o_i describes the partial reaction order of reactant R_i and has to be determined from experiment. The total order of reaction $\mathcal{O}$ is the sum over all partial orders, i.e., $\mathcal{O} = \sum_{i=1}^{n} o_i$. The `kinetic factor` in this rate law is the reaction rate constant k.

4.3.1. Reaction rate constant

The T_{G}-dependence of a chemical reaction may be described in several ways. The first generally accepted formula was the Arrhenius equation [5],

$$k(T_{\mathrm{G}}) = A \exp\left(-\frac{E_{\mathrm{a}}}{k_{\mathrm{B}} T_{\mathrm{G}}}\right) \, , \tag{4.12}$$

where E_{a} and A are empirical quantities called activation energy and pre-exponential factor, respectively. The Boltzmann constant is denoted as k_{B}. This formulation of $k(T_{\mathrm{G}})$ includes the T_{G} influence on $\mathcal{R}$ for a chemical reaction. It is mainly determined by the Boltzmann factor $e^{-\frac{E_{\mathrm{a}}}{k_{\mathrm{B}} T_{\mathrm{G}}}}$, a probability factor that exponentially increases with increasing T_{G} and decreasing E_{a}.

According to collision theory of gases [72], A may be quantified as the collision number (i.e., the total number of collisions per unit time and volume) between two reactants R_i and R_k $(i \neq k)$, regarded as hard spheres. The chemical reactions of interest in this thesis start from the adsorbate phase, and therefore, the collision number $Z_{\mathrm{R}_i,\mathrm{R}_k}$ in the two-dimensional case between two adsorbed particles is calculated as [95]

$$Z_{\mathrm{R}_i,\mathrm{R}_k} = \theta_{\mathrm{R}_i} \theta_{\mathrm{R}_k} (r_{\mathrm{R}_i} + r_{\mathrm{R}_k}) v_{\mathrm{avg}} \tag{4.13}$$

with the radii of the reactants $r_{i,k}$ and their average velocity v_{avg} (calculated statistically by Maxwell-Boltzmann distribution [107]). Setting $A = Z \equiv Z_{\mathrm{R}_i,\mathrm{R}_k}$ would lead to an overestimation of $\mathcal{R}$, since, it takes into account that each collision of R_i and R_k leads to the formation of a product. This is usually not the case and the reactants must collide in a correct orientation. Therefore, a probability factor $\mathcal{P}$ which considers the asymmetry in directions that lead to a reaction is used. This probability may be determined as the ratio of the observed A and the calculated Z, i.e., $\mathcal{P} = A/Z \leq 1$ — called: steric factor. The modified Arrhenius equation using collision theory now reads as

$$k(T_{\mathrm{G}}) = A \exp\left(-\frac{E_{\mathrm{a}}}{k_{\mathrm{B}} T_{\mathrm{G}}}\right) = (\mathcal{P} \times Z) \exp\left(-\frac{E_{\mathrm{a}}}{k_{\mathrm{B}} T_{\mathrm{G}}}\right) \, . \tag{4.14}$$

In order to explain the obtained values of E_{a} and A presented in this thesis a modification of the Arrhenius equation by means of collision theory is not sufficient and a more sophisticated theory is needed.

Transition state theory

For many chemical reactions, a large discrepancy between the measured $\mathcal{R}$ and those calculated using collision formulas is observed [71]. A collision theory in which molecules are regarded as hard spheres is inadequate, hence, a refined theory was developed using a statistical mechanical approach: the transition state theory. It was mainly developed by Henry Eyring and is also called Eyring-theory. Here, $\mathcal{R}$ is calculated by focusing on the activated complexes, which lie on the saddle point or local minimum of the potential energy surface [38]. An activated complex can be understood as one (or several) intermediate configuration(s) that atoms or molecules pass trough in between the defined thermodynamic conditions of R_i and P_j.

The reaction rate constant according to Eyring's formulation reads as [38]

$$k = \left(\frac{k_\mathrm{B}\,T_\mathrm{G}}{h}\right) \exp\left(-\frac{\Delta G^\ddagger}{k_\mathrm{B}\,T_\mathrm{G}}\right) \mathcal{M}^{1-\mathcal{O}} \tag{4.15}$$

with Planck constant h. The factor $\mathcal{M}^{1-\mathcal{O}} = (N\,\mathrm{nm}^{-2})^{1-\mathcal{O}}$ depends on $\mathcal{O}$ and the total number of reactants N.

The Gibbs free energy of activation $\Delta G^\ddagger$ may be expressed in the same way as ΔG, i.e.,

$$\Delta G^\ddagger = \Delta H^\ddagger - T\Delta S^\ddagger\,, \tag{4.16}$$

where now, $\Delta H^\ddagger$ and $\Delta S^\ddagger$ denote the enthalpy and entropy of activation, respectively. The relation between $\Delta H^\ddagger$ in the latter equation and E_a in the Arrhenius equation (4.12) is [73]

$$\Delta H^\ddagger = E_\mathrm{a} - k_\mathrm{B}T_\mathrm{G}\ . \tag{4.17}$$

Transforming and inserting Eqs. (4.16) and (4.17) in (4.15) yields the expression of k that is used to discuss the model parameters obtained by the kinetic binary growth models in chapter 5,

$$k(T_\mathrm{G}) = B\exp\left(-\frac{E_\mathrm{a}}{k_\mathrm{B}\,T_\mathrm{G}}\right)\ . \tag{4.18}$$

The new pre-exponential factor B reads as

$$B = \left(\frac{k_\mathrm{B}\,T_\mathrm{G}}{h}\right) \exp\left(\frac{\Delta S^\ddagger}{k_\mathrm{B}} + 1\right) \mathcal{M}^{1-\mathcal{O}}\,. \tag{4.19}$$

The growth models derived in chapter 5 are macroscopic ones solved by a special approach. For this reason, a quantitative microscopic discussion of the pre-exponential factors obtained by these models is not possible, but shall be qualitatively described by means of the latter expression (4.19). A deeper insight into transition state theory is beyond the scope of this thesis, and the underlying microscopic formalism will not be discussed and justified.

5. Reaction kinetics and thermodynamics of binary group-III and IV oxides in MBE

In this chapter, the reaction kinetics and thermodynamics during MBE of Ga_2O_3, In_2O_3, and SnO_2 is given. It turns out, that on a macroscopic scale the reaction kinetics, i.e. the macroscopic Me incorporation and Me desorption during heteroepitaxially growth, does not depend on the crystal structure nor on the substrate on which the layer is grown.

In section 5.1 the Me incorporation and desorption as a function of all MBE growth parameters is presented. The origin of the decreasing growth rate γ at increasing Me flux ϕ_{Me} is explained and justified by several approaches. Decomposition of the metal-oxide layers by their respective Me is shown. Similarities and differences in the growth kinetics of Ga_2O_3, In_2O_3, and SnO_2 are given and explained. Large parts presented in this section are published in Refs. [125–127].

Section 5.2 gives a comprehensive understanding of the growth kinetics presented in section 5.1. The complex reaction mechanism of oxides is introduced and quantitatively described. Based on this reaction mechanism and the experimental data shown in section 5.1, a general kinetic growth model for oxide MBE is derived. It predicts the Me incorporation and desorption as a function of ϕ_{Me}, active O flux ϕ_{O}^{*}, and growth temperature T_{G}. By means of the resulting model parameters, the Me incorporation and desorption data presented in section 5.1 are kinetically explained.

5.1. Metal incorporation, suboxide formation, and layer decomposition

The growth rate γ of the compounds investigated was measured `in-situ` by laser reflectometry. The species desorption rates ϕ_j^{des} were monitored `in-situ` by QMS.

To exclude the effect of nucleation on the measured γ, a $\approx 20\,\mathrm{nm}$-thick nucleation layer was grown at $T_{\mathrm{G}} = 700\,^{\circ}\mathrm{C}$ and $\Phi_{\mathrm{O_2}}(P_{\mathrm{rf}} = 300\,\mathrm{W}) = 3\,\mathrm{SCCM}$ before the growth rate study. At this T_{G} and $\Phi_{\mathrm{O_2}}$ full Me incorporation is guaranteed for $\phi_{\mathrm{Me}} \approx 6\,\mathrm{Me\,nm^{-2}\,s^{-1}}$ (a common Me flux used for nucleation).

5.1.1. Metal incorporation as a function of metal flux

The γ-evolution of Ga_2O_3, In_2O_3, and SnO_2 when varying ϕ_{Me}, while keeping ϕ_{O}^{*} and T_{G} constant, are shown in Figs. 5.1 (a), (b), and (c), respectively. They are similar to

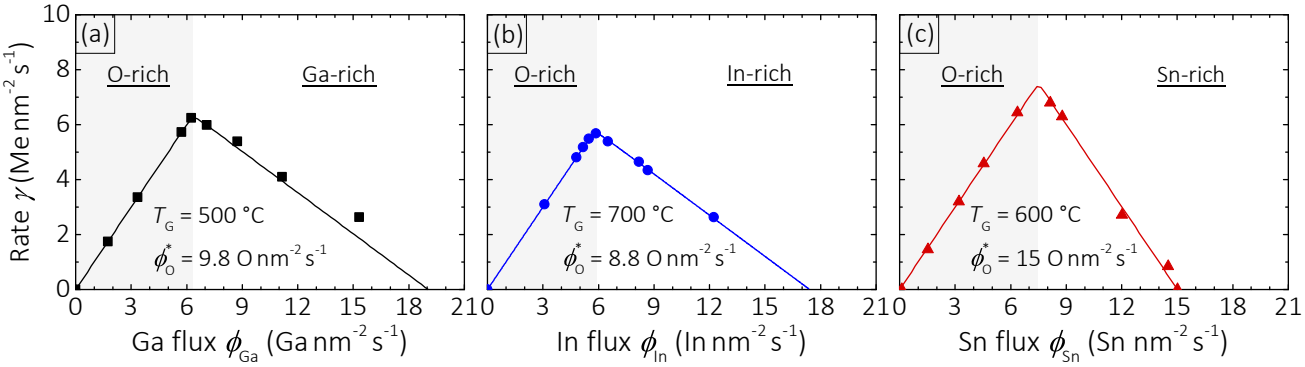

Figure 5.1.: (a), (b), and (c) depict the binary growth rates γ as a function of the respective Me flux ϕ_{Me} of Ga_2O_3, In_2O_3, and SnO_2, respectively. The lines are model fits according to Eqs. (5.65) and (5.67).

Figs. 3.6 (a), (b), and (c) for O flux calibration, but now plotted in particle flux units. Henceforth, all γ and ϕ_j^{des} are discussed in particle or molecular flux units (unless otherwise stated). Two distinct regimes are evidenced: O-rich and Me-rich growth regimes. In the O-rich regime (Me-limited growth), i.e. $\phi_{\mathrm{Ga,In,Sn}} \leq a\phi_{\mathrm{O}}^*$, all compounds show a proportional increase of $\gamma = \sigma_{\text{O-rich}}\,\phi_{\mathrm{Me}}$, with increasing ϕ_{Me} and slope $\sigma_{\text{O-rich}} = 1$. The pre-factor a is 2/3 for Ga_2O_3 and In_2O_3, 1/2 for SnO_2 growth, and due to the different Me-to-O stoichiometries of these compounds. During growth in the O-rich regime, the ϕ_{Me} supplied did not result in any appreciable desorbed species flux measured by QMS, as shown for Ga_2O_3 growth in Fig. 5.2 (a) (gray area). These results confirm full incorporation of the Me into the oxide film, corresponding to a Me sticking coefficient of unity in the O-rich regime. The proportional increase of γ with ϕ_{Me} reaches a maximum at stoichiometric growth conditions, corresponding to $\phi_{\mathrm{Ga,In,Sn}} = a\phi_{\mathrm{O}}$, where all available Me and O atoms are incorporated into the film. A further increase of ϕ_{Me} pushes the growth domain into the Me-rich regime, i.e. for $\phi_{\mathrm{Ga,In,Sn}} > a\phi_{\mathrm{O}}^*$. Here, γ linearly decreases immediately and reaches zero at a strong excess of ϕ_{Me} of $\phi_{\mathrm{Ga,In}} = 2\phi_{\mathrm{O}}^*$ for Ga_2O_3 and In_2O_3 growth, and $\phi_{\mathrm{Sn}} = \phi_{\mathrm{O}}^*$ for SnO_2 growth. In the Me-rich regime, the slope $\sigma_{\text{Me-rich}}$ of the decreasing γ is

$$\frac{\partial\gamma}{\partial\phi_{\mathrm{Ga,In}}} = \sigma_{\text{Ga-,In-rich}} = -\frac{1}{2} \tag{5.1}$$

for Ga_2O_3, In_2O_3, and

$$\frac{\partial\gamma}{\partial\phi_{\mathrm{Sn}}} = \sigma_{\text{Sn-rich}} = -1 \tag{5.2}$$

for SnO_2. A similar behavior during Ga_2O_3 [114] and SnO_2 [117, 134] MBE has been already reported in literature by Tsai *et al.* [114, 117] and White *et al.* [134].

Detection of desorbing species from the growth surface by QMS

A first explanation for the decreasing γ in the Sn-rich regime during SnO_2 MBE was given by Tsai *et al.* [117]. Here, due to multiple oxidation states of Sn, the tin suboxide SnO was observed in the Sn-rich regime and identified as the origin of the decreasing γ. For Ga_2O_3

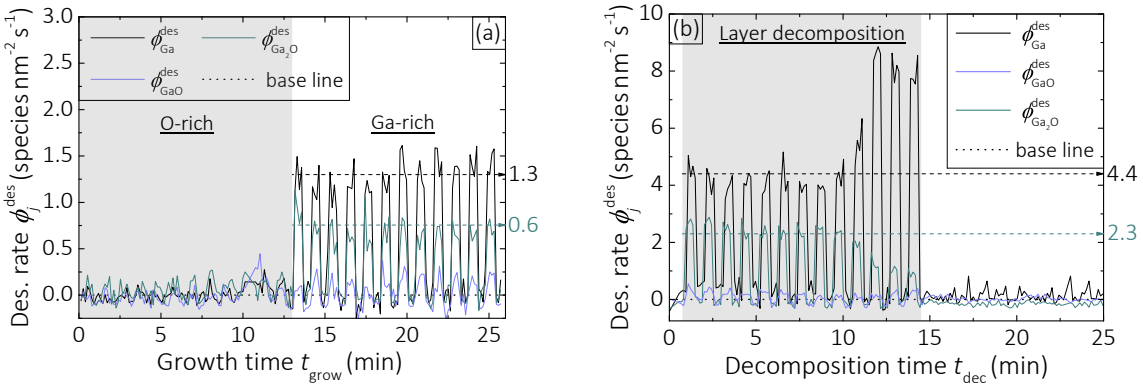

Figure 5.2.: (a) Ga (ϕ_{Ga}^{des}) and suboxide (ϕ_{Ga_2O}, ϕ_{GaO}) signals measured by QMS during Ga_2O_3 growth. To correct for the background signal, the QMS shutter is periodically opened such that the amplitude of the rapidly oscillating signal represents the desorbing flux. Two scenarios are depicted: growth in the O-rich and Ga-rich regime. The growth temperature was $T_G = 500\,°C$ and the Ga flux $\phi_{Ga} = 4.9\,Ga\,nm^{-2}\,s^{-1}$. The O flux ϕ_O^* in the O-rich and Ga-rich regime was $9.8\,O\,nm^{-2}\,s^{-1}$and $4.9\,O\,nm^{-2}\,s^{-1}$, respectively. (b) Detected QMS signal while decomposing a previously grown Ga_2O_3 layer by Ga adatoms at $\phi_{Ga} = 6\,Ga\,nm^{-2}\,s^{-1}$ and $T_G = 700\,°C$.

MBE the same qualitative γ-evolution as for SnO_2 was observed and also reported by Tsai *et al.* [114]. For the same argument as for SnO_2, the suboxide Ga_2O was suggested to be the cause of the decreasing γ in the Ga-rich regime. Based on the results published in Refs. [114, 117] and taking all oxidation states of Ga into account, the selected species to be observed by QMS were elemental Ga, the first suboxide GaO, and the second suboxide Ga_2O.

It will be shown in this chapter, that due to the existence of suboxides for all investigated (binary) compounds, their γ-evolution in the Me-rich regime differs, from other oxides such as ZnO [64] or group-III/V semiconductors, like GaAs [99], GaN [41, 54], or InN [65]. These compounds do not posses suboxides, subarsenides, or subnitrides, respectively.

Figure 5.2 (b) shows the detected QMS signal during Ga_2O_3 growth in the Ga-rich regime (white area). Three species are detected: Ga ϕ_{Ga}^{des} (black), GaO ϕ_{GaO}^{des} (pale blue), and $\phi_{Ga_2O}^{des}$ Ga_2O (turquois). The ratio r_{QMS} of the detected signal between Ga and Ga_2O of $r_{QMS} = \phi_{Ga}^{des}/\phi_{Ga_2O}^{des} \sim 2$ may be referred to a dissociation of Ga_2O into Ga in the quadrupole. A quantitative explanation of the γ-evolutions presented in Figs. 5.1 (a)–(c) and its origin, that also explains r_{QMS}, is given in subsection 5.1.3. The signal of ϕ_{GaO}^{des} is negligible and can be referred to the background signal of this species or also due to the dissociation of a small amount of Ga_2O into GaO molecules in the quadrupole. During SnO_2 growth, Sn and the suboxide SnO were detected (not shown). For In_2O_3 growth, only In could be measured by QMS, which is likely due to low sensitivity to In_2O (large mass of 246 atomic mass units (amu)) and its dissociation in the quadrupole.

Due to the low sensitivity on the desorbing species (e.g. Ga_2O), a reliable evaluation of the used QMS data was very difficult (calibration given in the appendix A.5). Therefore, the origin of the decreasing γ in the Me-rich regime has to be further analyzed. In order to do so, the decomposition of the metal-oxide layers by their respective Me is discussed now and will allow conclusions on the desorbing species.

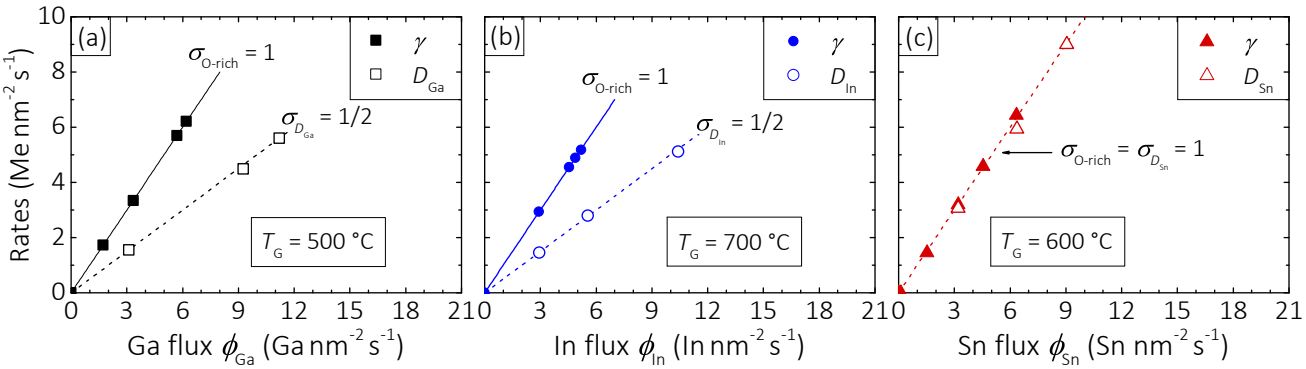

Figure 5.3.: (a), (b), and (c) depict the decomposition rates D_{Me} of Ga_2O_3, In_2O_3, and SnO_2 as a function of ϕ_{Me} with $\phi^*_{\text{O}} = 0$, respectively. γ, measured in the O-rich regime of the corresponding compound, is plotted to compare the increase of D_{Me} and γ with ϕ_{Me}. The lines are guides to the eye.

5.1.2. Decomposition of metal-oxide layers by their respective metal

This subsection deals with the feasible decomposition of Ga_2O_3, In_2O_3, and SnO_2. In this experiment, previously grown Ga_2O_3, In_2O_3, and SnO_2 layers were exposed to ϕ_{Ga}, ϕ_{In}, and ϕ_{Sn} (without ϕ^*_{O}), respectively. The decomposition rate D_{Me} was measured `in-situ` by laser reflectometry. Species occurring and desorbing during decomposition are detected `in-situ` by QMS.

Figures (a), (b), and (c) depict D_{Me} as a function of ϕ_{Me} of Ga_2O_3, In_2O_3, and SnO_2, respectively. The proportional increase of D_{Me} with ϕ_{Me}, i.e. $D_{\text{Me}} = \sigma_{D_{\text{Me}}} \phi_{\text{Me}}$, implies that impinging Me adatoms decompose the oxide layer, resulting in a reduction of the layer thickness. This can be seen by the discontinuity of the reflected laser signal during layer decomposition in Fig. 3.2 (b) at point (iii) (chapter 3, section 3.2), and the resulting QMS signal as shown in Fig. 5.2 (b) for Ga_2O_3 decomposition. This QMS signal also shows a contribution of Ga atoms and Ga_2O molecules with $r_{\text{QMS}} \sim 2$. The layers could even be decomposed until the substrate was exposed as detected by a vanishing suboxide signal and increasing Ga signal (Fig. 5.2 (b), for $t_{\text{dec}} > 10\,\text{min}$), as well as the appearance of the streaky RHEED pattern of the c-plane sapphire substrate (not shown). The slopes of the increasing decomposition rates $\sigma_{D_{\text{Me}}}$ with increasing ϕ_{Me} in the case of Ga_2O_3 and In_2O_3 are

$$\sigma_{D_{\text{Ga,In}}} = \frac{\partial D_{\text{Ga,In}}}{\partial \phi_{\text{Ga,In}}} = \frac{1}{2} = -\sigma_{\text{Ga,In-rich}} \ , \tag{5.3}$$

which modulus corresponds to the half of the slope of γ in the O-rich regime. In the case of SnO_2 the slope is

$$\sigma_{D_{\text{Sn}}} = \frac{\partial D_{\text{Sn}}}{\partial \phi_{\text{Sn}}} = 1 = -\sigma_{\text{Sn-rich}} \ , \tag{5.4}$$

which modulus corresponds to the same slope as the one of γ in the O-rich regime.

5.1.3. Common origin of the decreasing growth rate and decomposition of the layer

Based on the data plotted in Figs. 5.1, 5.2, and 5.3, the compound formed during layer decomposition and the origin of the decreasing γ is systematically investigated by comparing γ in the O-rich regime with D_{Me} at same ϕ_{Me}.

In the case of Ga_2O_3 and In_2O_3, both materials show the same behavior due to their common Me-to-O ratio of 2/3 (Me=Ga,In). The net reaction for growth reads as

$$2\,\mathrm{Me}\,(a) + 3\,\mathrm{O}\,(a) \longrightarrow \mathrm{Me_2O_3}\,(s)\ . \tag{5.5}$$

Possible reactions for decomposition are

$$4\,\mathrm{Me}\,(a) + 1\,\mathrm{Me_2O_3}\,(s) \longrightarrow 3\,\mathrm{Me_2O}\,(g) \tag{5.6}$$

and

$$1\,\mathrm{Me}\,(a) + 1\,\mathrm{Me_2O_3}\,(s) \longrightarrow 3\,\mathrm{MeO}\,(g) \tag{5.7}$$

depending on the stoichiometry of the suboxide (MeO and Me_2O are known suboxides [19]). All Me is consumed during growth in the O-rich regime, thus, taking the ratio of the Me coefficients for the growth, Eq. (5.5), with the ones for decomposition, Eqs. (5.6) and (5.7), reveals which compound is indeed formed during decomposition. That means,

$$\frac{2\mathrm{Me}}{4\mathrm{Me}} = \frac{1}{2} = \sigma_{D_{\mathrm{Me}}} = -\sigma_{\text{Ga-,In-rich}} \tag{5.8}$$

taking twice as many Me to decompose one Me_2O_3, and

$$\frac{2\mathrm{Me}}{1\mathrm{Me}} = 2 \neq \sigma_{D_{\mathrm{Me}}}\ , \tag{5.9}$$

taking half of Me to decompose one Me_2O_3 unit than growing it, respectively. Only decomposition reaction (5.6) leads to the experimentally observed ratio of growth and decomposition rate of

$$D_{\mathrm{Ga,In}} = -\sigma_{\text{Ga-,In-rich}}\gamma = \frac{1}{2}\,\gamma\ , \tag{5.10}$$

as plotted in Figs. 5.3 (a) and (b) for Ga_2O_3 and In_2O_3, respectively. A significant mixture of both decomposition reactions, Eqs. (5.6) and (5.7), can be ruled out on the basis of the measured γ, D_{Me}, and the QMS signal shown in Fig. 5.2 for Ga_2O_3. Theoretically, a 1 : 1 mixture of GaO formation and desorption (Eq. (5.7)), plus Ga desorption (which would lead to the same γ-evolution in the Me-rich regime), can also be ruled out based on the measured QMS signals. Therefore, the compounds Ga_2O and In_2O are identified to be the formed volatile suboxides in the cases of Ga_2O_3 and In_2O_3 decomposition, respectively. This result is confirmed by QMS measurements during Ga_2O_3 growth in the Ga-rich regime (Fig. 5.2 (a)) and its decomposition by Ga (Fig. 5.2 (b)). The other contributions in the detected QMS signal (Ga and GaO) are attributed to the dissociation of Ga_2O in the quadrupole and based on the analysis of reactions for γ, Eq. (5.5), and D_{Me}, Eq. (5.6), that lead to the measured γ- and D_{Me}-evolutions.

In the case of Sn the equations for growth and decomposition of SnO_2 are

$$\mathrm{Sn}\,(a) + 2\,\mathrm{O}\,(a) \longrightarrow \mathrm{SnO_2}\,(s) \tag{5.11}$$

product	educt$_1$	educt$_2$	G^{prod} (eV/f.u.)	G^{ed_1} (eV/f.u.)	G^{ed_2} (eV/f.u.)	ΔG (eV)	Eq. (n)
3 Ga_2O	4 Ga	Ga_2O_3	-3.94	1.13	-12.30	-4.02	(5.6)
3 GaO	1 Ga	Ga_2O_3	-0.87	1.13	-12.30	8.54	(5.7)
3 In_2O	4 In	In_2O_3	-3.74	0.81	-10.79	-3.67	(5.6)
2 SnO	1 Sn	SnO_2	-3.00	0.86	-6.82	-0.05	(5.12)

Table 5.1.: Determined changes in the Gibbs free energies of formation ΔG according to Eq. (4.10), chapter 4, for possible decomposition reactions of the investigated oxides. The single values to determine ΔG can be found in the appendix in Tab. B.1. All Gibbs free energies G are given per formula unit (f.u.).

and

$$\text{Sn}\,(a) + \text{SnO}_2\,(s) \longrightarrow 2\,\text{SnO}\,(g)\;, \tag{5.12}$$

respectively. Comparing the Sn coefficient for growth and decomposition of the same amount of SnO_2 in Eqs. (5.11) and (5.12), gives the ratio

$$1\text{Sn}/1\text{Sn} = 1 = \sigma_{D_{\text{Sn}}} = -\sigma_{\text{Sn-rich}}\;. \tag{5.13}$$

The responsible volatile suboxide is tin-monoxide SnO.

The relation of slopes for decomposition of the layer and growth in the Me-rich regime (Eqs. (5.8) and (5.13)) may lead to the interpretation that the decreasing γ can be considered as decomposition of the films by excess Me after all available oxygen has been used for film formation. Arguments against this explanation are given in section 5.2.

Thermochemical calculations according to Eq. (4.10), chapter 4, were performed in order to confirm the thermodynamic feasibility of the decompositions reactions, determined under the present MBE conditions. The data to determine ΔG was taken from Ref. [19]. The results are collected in Tab. 5.1 and are in qualitative agreement with published experimental equilibrium results for Ga_2O_3 [45], In_2O_3 [118] (decomposition by respective Me into Me_2O), and SnO_2 [29] (thermal decomposition into SnO). This favorable comparison indicates reactions under non-equilibrium MBE conditions can have a tendency towards thermodynamic equilibrium. Only reactions (5.6) and (5.12) are thermodynamically feasible, confirming the results of the last paragraph, that only Ga_2O, In_2O, and SnO are the suboxides formed during Ga_2O_3, In_2O_3, and SnO_2 MBE, respectively.

In order to specify at which ϕ_{Me} the film growth stops, the stoichiometries of ϕ_{Me} for growth reaction and suboxide formation are analyzed in the case when no film is formed. These reactions for Me_2O_3 and SnO_2 are

$$6\,\text{Me}\,(a) + 3\,\text{O}\,(a) \longrightarrow 3\,\text{Me}_2\text{O}\,(a \text{ or } g) \tag{5.14}$$

and

$$2\,\text{Sn}\,(a) + 2\,\text{O}\,(a) \longrightarrow 2\,\text{SnO}\,(a \text{ or } g)\;, \tag{5.15}$$

respectively.

In the case of Ga_2O_3 and In_2O_3, the comparison of the Me coefficients in Eqs. (5.5) and (5.14) suggests the layer growth ceases at three times the stoichiometric ϕ_{Me} and two times

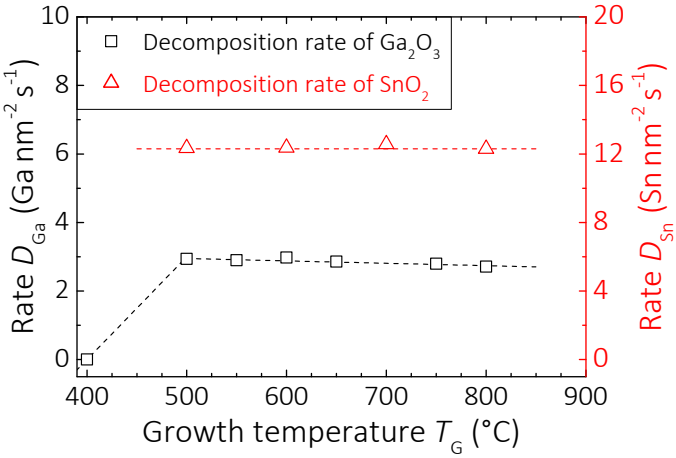

Figure 5.4.: Decomposition rates $D_{\mathrm{Ga,Sn}}$ of Ga_2O_3 and SnO_2 as a function of growth temperature T_{G}. The set Me fluxes were $\phi_{\mathrm{Ga}} = 6.0\,\mathrm{Ga\,nm^{-2}\,s^{-1}}$and $\phi_{\mathrm{Sn}} = 12.3\,\mathrm{Sn\,nm^{-2}\,s^{-1}}$. The lines are guides to the eye.

ϕ_{O}^{*} (i.e. at $\phi_{\mathrm{Ga,In}} = 2\phi_{\mathrm{O}}^{*}$) due to the complete formation of suboxides. In the case of SnO_2 and comparing the growth and decomposition reactions Eqs. (5.11) and (5.12), respectively, the growth stops at $\phi_{\mathrm{Sn}} = \phi_{\mathrm{O}}^{*}$. These are exactly the result as plotted in Figs. 5.3 (a) for Ga_2O_3, (b) for In_2O_3, and (c) for SnO_2. Here, the growth (extrapolated) of all compounds stops at these growth conditions, again confirming that only Ga_2O, In_2O, and SnO are the formed suboxides. A further increase of ϕ_{Me}, i.e. for $\phi_{\mathrm{Ga,In}} > 2\phi_{\mathrm{O}}^{*}$ and $\phi_{\mathrm{Sn}} > \phi_{\mathrm{O}}^{*}$, the remaining Me adatoms would decompose the previously grown oxide layer until the substrate is exposed. Once the substrate is revealed, the impinging Me atoms either adsorb or desorb depending on T_{G}. For all investigated compounds, D_{Me} remains constant at same ϕ_{Me} for all investigated T_{G} above the Me adsorption temperature T_{ads}. The feasible decomposition reactions (5.6) and (5.12) are fast enough for all $T_{\mathrm{G}} > T_{\mathrm{ads}}(\phi_{\mathrm{Me}})$, i.e., kinetically activated. In the example of Ga_2O_3 decomposition and given ϕ_{Ga} this is the case for all $T_{\mathrm{G}} > 500\,^{\circ}\mathrm{C} > T_{\mathrm{ads}}(\phi_{\mathrm{Ga}} = 6.0\,\mathrm{Ga\,nm^{-2}\,s^{-1}})$. The functional dependencies of D_{Ga} and D_{Sn} on T_{G} are plotted in Fig. 5.4. Both rates are almost independent on T_{G}. The slight decrease of D_{Ga} with increasing T_{G}, might be referred to a small increase of Ga desorption with increasing T_{G} (since less Ga adatoms are available on the growth surface to decompose Ga_2O_3). This is not the case for D_{Sn} since the vapor pressure of Sn from the SnO_2 growth surface is lower than the one of Ga from the Ga_2O_3 growth surface. Detailed discussions about the vapor pressures of all possible species from their respective growth surfaces are given in subsection 5.1.6.

Figure 5.5 shows three conceivable γ-evolutions in the Me-rich regime for Me_2O_3 growth: (i) no suboxide is formed and the remaining Me atoms that cannot be oxidized are either adsorbed or desorbed depending on T_{G}. In this case, γ plateaus due to the O-limited Me incorporation as it is the case for ZnO [64], GaN [41], or InN [48] growth, for instance. (ii) Once the Me-rich regime is entered only the suboxide Me_2O is formed and γ decreases due to Me_2O desorption and the growth stops at $\phi_{\mathrm{Me}} = 2\phi_{\mathrm{O}}^{*}$. The slope of the decreasing γ taken from Eq. (5.8). (iii) Only the suboxide MeO is formed and γ decreases because of

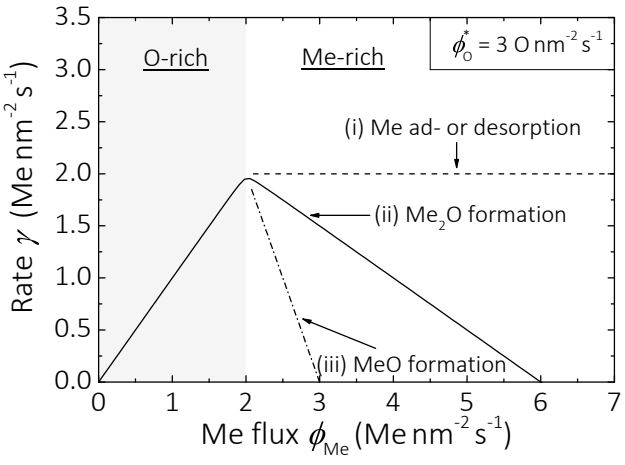

Figure 5.5.: Hypothetical evolutions of the Me incorporation rates, i.e. γ, as a function of Me flux ϕ_{Me}, exemplarily shown for sesquioxides.

its desorption and the growth stops at $\phi_{\mathrm{Me}} = \phi_{\mathrm{O}}^*$. The slope of the decreasing γ in the Me-rich regime in this case was taken from Eq. (5.9).

This example demonstrates that only by analyzing the slopes of the decreasing γ in the Me-rich regime and comparing it with the growth reactions (Eq. (5.5)) and decomposition reactions (Eqs. (5.6) and (5.7)), it is possible to identify the formed suboxide. Which is in the case of sesquioxides Me_2O, i.e. scenario (ii).

5.1.4. Metal incorporation and desorption as a function of all MBE growth parameters

In order to fully understand the reaction kinetics of the binary grown metal-oxide layers, the Me incorporation at different T_{G} was extensively studied. The following figures show one of the key and main experimental results in this thesis.

Figure 5.6 (a) shows γ of Ga_2O_3 when varying ϕ_{Ga} at constant ϕ_{O}^* and different T_{G}. Compared to low-$T_{\mathrm{G}} = 500\,^{\circ}\mathrm{C}$, a different γ-evolution at identical ϕ_{Ga} is observed at high-$T_{\mathrm{G}} = 560\,^{\circ}\mathrm{C}$ and $610\,^{\circ}\mathrm{C}$. The maximum γ is decreased and a plateau of it in the O-rich regime is present, resembling the γ-evolutions shown in Refs. [90] and [87] for the MBE growth of Ga_2O_3 on $Al_2O_3(0001)$ and $Ga_2O_3(010)$, respectively. In Ref. [87], it is stated that the plateau arises in the Ga-rich regime due to O-limited Ga incorporation and its desorption. In Ref. [90] no explanation about the origin of the plateau is given. It will be shown in this section, that the findings reported in Refs. [90] and [87] have another origin and that the growth took place in the O-rich and quasi O-rich regime (darker gray area in Fig. 5.6 (a), explanation in subsection 5.1.6).

Figure 5.6 (b) shows the γ-evolution of Ga_2O_3 when varying T_{G} at constant r_{Ga} ranging from 0.11 to 1.09. For all r_{Ga} γ decreases with increasing T_{G} and the decrease is stronger at larger r_{Ga}. That means, increasing ϕ_{O}^* enables the formation of Ga_2O_3 at higher T_{G}. The kinetic origin of the data plotted in these two figures is given in subsection 5.1.6.

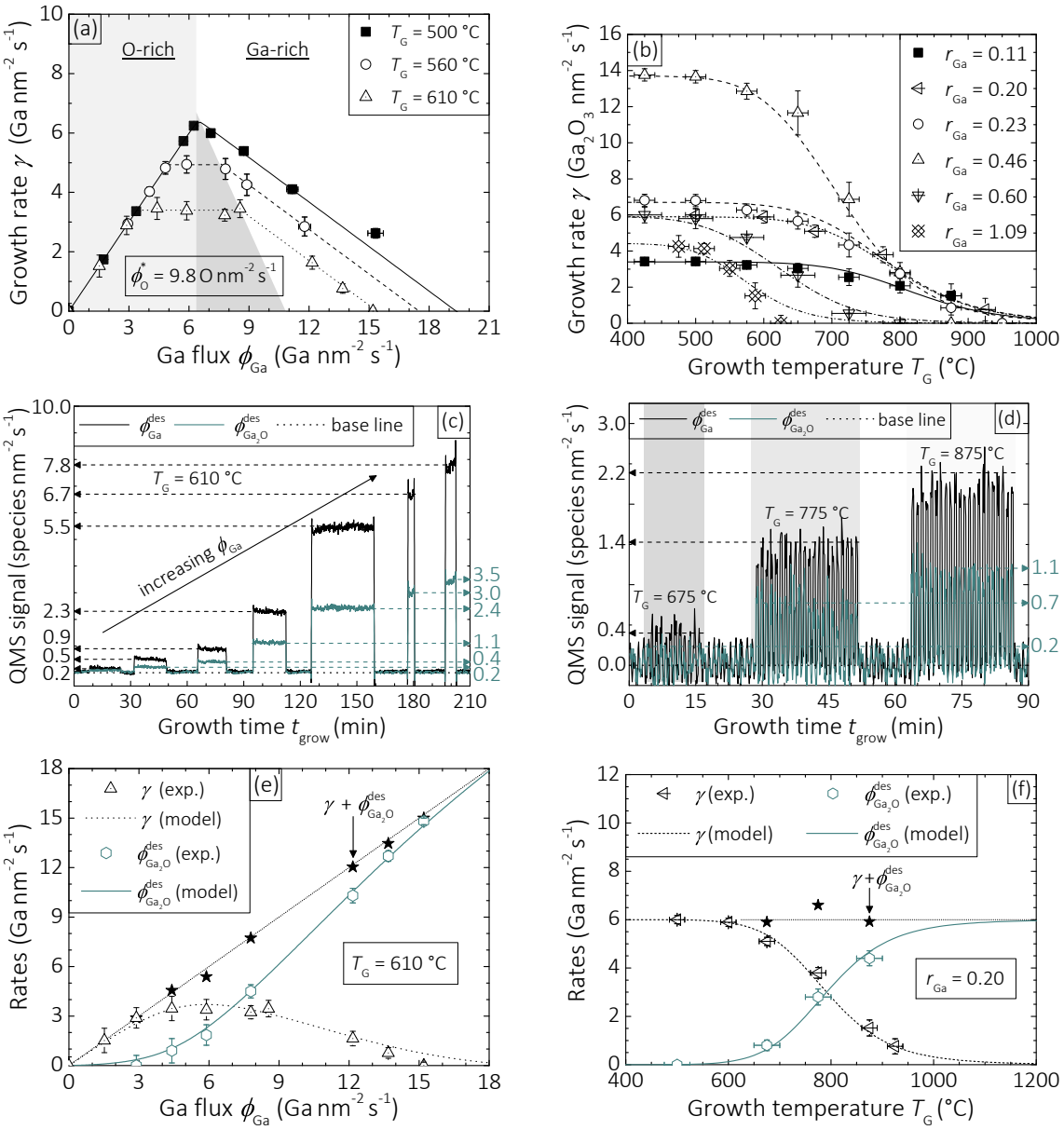

Figure 5.6.: (a) Growth rate γ as a function of Ga flux ϕ_{Ga} for different growth temperatures T_{G}. (b) γ as a function of T_{G} for different Ga-to-O flux ratios r_{Ga}. The O flux ϕ_{O}^{*} for $r_{\mathrm{Ga}} = 0.11$ to 0.46 was 29.4 O nm^{-2} s^{-1}and 9.8 O nm^{-2} s^{-1} for $r_{\mathrm{Ga}} = 0.60$ and 1.09. (c) and (d) Plot the detected QMS signal during growth when varying ϕ_{Me} at $T_{\mathrm{G}} = 610\,^{\circ}\mathrm{C}$ (γ plotted as triangles in (a)) and when varying T_{G} for $r_{\mathrm{Ga}} = 0.20$ (γ plotted as left arrows in (b)), respectively, as a function of growth time t_{grow}. (e) and (f) Show the combined Me incorporation and desorption data as extracted from (a) and (c) for the left panel (e) at $T_{\mathrm{G}} = 610\,^{\circ}\mathrm{C}$, as well as (b) and (d) for the right panel (f) at $r_{\mathrm{Ga}} = 0.20$. The lines are model predictions according to Eqs. (5.65) and (5.66), section 5.2. The error is calculated by Eq. (5.69), section 5.2.

The desorbing fluxes at $T_G = 610\,°C$, while changing ϕ_{Ga} (corresponding γ-data in Fig. 5.6 (a)) and at $r_{Ga} = 0.20$ while varying T_G (corresponding γ-data in Fig. 5.6 (b)), are plotted in Figs. 5.6 (c) and (d), respectively. Only ϕ^{des}_{Ga} and $\phi^{des}_{Ga_2O}$ could be measured with $r_{QMS} \sim 2$. This in combination with the decreasing γ in the Ga-rich regime (Fig. 5.6 (a)) suggests Ga_2O dissociates in the quadrupole. A final explanation that Ga_2O is the only desorbing species for all growth conditions can be drawn from the geometry of the plateau. A detailed explanation of the surface kinetics determining the geometry of the plateau is given in subsection 5.1.6 for In_2O_3, and holds also true for Ga_2O_3 as published in Ref. [127].

The normalization factor between the measured raw QMS signal in $10^{-12}\,A$ and the one depicted in $Ga\,nm^{-2}\,s^{-1}$ or $Ga_2O\,nm^{-2}\,s^{-1}$ (in figure written as species $nm^{-2}\,s^{-1}$) was obtained by comparing the maximum desorption rate, where $\gamma = 0$ (triangles in Fig. 5.6 (a) at $\phi_{Ga} = 15.2\,Ga\,nm^{-2}\,s^{-1}$). Here, all supplied Ga is converted into Ga_2O, which now can be used as a reference of $\phi^{des}_{Ga_2O}$ at lower ϕ_{Ga}. The desorption of $\phi^{des}_{Ga_2O}$ increases in both cases, i.e., when increasing r_{Ga} and T_G.

No Ga desorption was detected by QMS during growth for all $T_G \leq 900\,°C$ and $r_{Ga} \leq 2$. In a separate experiment (not shown), Ga desorption instead of Ga_2O desorption when $\phi_{Ga} = 6.0\,Ga\,nm^{-2}\,s^{-1}$ and $\phi^*_O = 9.8\,O\,nm^{-2}\,s^{-1}$ were supplied to a blank $Al_2O_3(0001)$ surface at similarly high T_G between 900 °C and 500 °C. The set ϕ_{Ga} and ϕ^*_O are usual fluxes for Ga_2O_3 growth and nucleation. Total Ga desorption was detected down to T_G = 550 °C. Below 550 °C the measured Ga signal decreased and Ga_2O_3 nucleated at these fluxes (measured `in-situ` by laser reflectometry). The different Ga species desorbing from Al_2O_3 and Ga_2O_3 surfaces suggest that the Ga_2O_3 surface is required as a catalyst for Ga_2O formation.

Figures 5.6 (e) and (f) present the combination of the Ga incorporation and desorption rates, i.e. γ, $\phi^{des}_{Ga_2O}$, and their sum, as a function of ϕ_{Me} at $T_G = 610\,°C$, and as a function of T_G at $r_{Ga} = 0.20$, respectively. Both figures show that the loss of Ga incorporation (within the error limits) in the Ga-rich regime and at elevated T_G is always caused by the formation and desorption of Ga_2O. This is the fundamental difference of oxides possessing suboxides grown by MBE as compared to nitride or arsenide semiconductors, which would show Me desorption. The lines in Figs. 5.6 (e) and (f) for Me incorporation and desorption γ and $\phi^{des}_{Ga_2O}$, respectively, are predictions of the kinetic binary growth model that is developed in section 5.2, and mainly based on the data presented here.

5.1.5. MBE growth domain of $Ga_2O_3/Al_2O_3(0001)$

Figure 5.7 collects all measured γ for $Ga_2O_3/Al_2O_3(0001)$ MBE growth in this thesis, and are plotted in a two-dimensional (2D) phase-space with three growth parameters ϕ_{Ga} and ϕ^*_O (reduced to r_{Ga}) and T_G. All obtained γ are projected onto the 2D r_{Ga}-T_G phase-diagram to show different growth and no growth regimes. The data points depicted do not give information about the value of γ, but reveal in which growth regime the Ga_2O_3 growth takes place. The white and black symbols present growth and no growth, respectively. Based on the data, the Ga_2O_3 MBE growth domain could be identified and divided in two major growth regimes, O-rich and Ga-rich, as well as subdivided in four minor growth regimes, (i)–(iv) as indicated in Fig. 5.7. These four minor growth regimes are defined

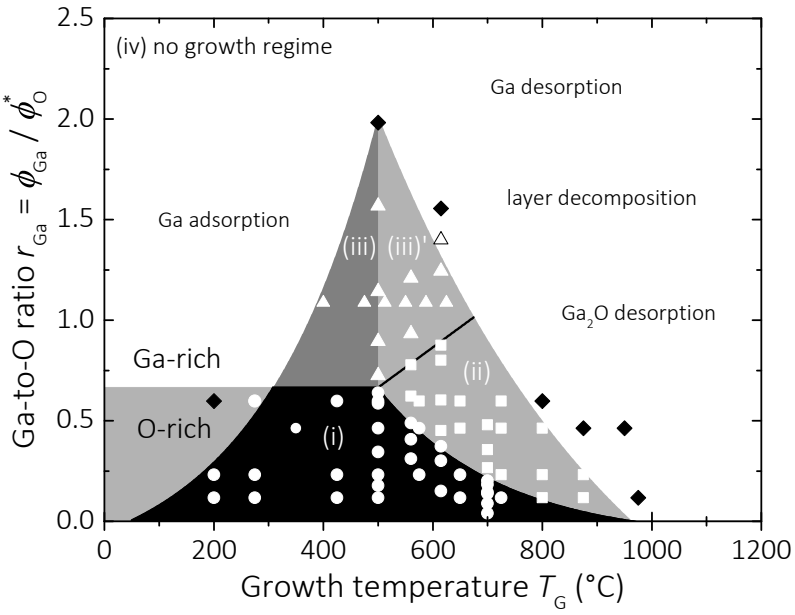

Figure 5.7.: MBE growth domain of $Ga_2O_3/Al_2O_3(0001)$ depicting the measured γ projected onto the two-dimensional parameter space spanned by the Ga-to-O flux ratio r_{Ga} and growth temperature T_G. The growth domain is divided in two major growth regimes: O-rich and Ga-rich regime. The different symbols define four minor growth regimes: (i) discs — complete Ga incorporation, (ii) squares — plateau of γ, (iii) triangles — decreasing γ in Me-rich regime, (iv) rhombs — no growth regime.

as follows: (i) Ga transport limited O-rich growth regime with full Ga incorporation (the linear increase of γ with ϕ_{Ga}, plotted as discs). (ii) Ga_2O desorption limited O-rich or surface O-rich (subsection 5.1.6) growth regime with partial Ga incorporation (plateau of γ, plotted as squares). (iii) O transport limited Ga-rich growth regime with partial Ga incorporation (the linear decrease of γ with ϕ_{Ga}, plotted as upward triangles). Regime (iii)′ is similar to (iii), since the origin of the decrease of γ is induced by O-deficiency on the growth surface. But here, O desorption is additionally taken into account at elevated T_G, that even further reduces the O surface density at same ϕ^*_O, and so γ. Regime (iv) defines the `no` growth regime, which includes all possible no growth scenarios (plotted as rhombs): full Ga adsorption, full Ga desorption, and layer decomposition by the remaining Ga adatoms that could not be converted into Ga_2O (for $\phi_{Ga} > 2\phi^*_O$).

This MBE growth diagram for Ga_2O_3 growth may serve as a guidance for the improvement of γ, crystal quality, and electronic structure of Ga_2O_3. For example, a higher γ on all Ga_2O_3 surfaces may be realized by lower T_G or higher ϕ^*_O that suppress Ga_2O desorption. In order to improve crystal quality, high-T_G growth is needed, and the results shown in Fig. 5.7 reveal that an increased ϕ^*_O helps maintaining reasonable γ. Finally, growth in regime (ii) and more in the Ga-rich regime (iii) may suppress the formation of Ga vacancies, which are responsible for the compensation of electrical donors [67, 119].

5.1.6. Suboxide vapor pressure limiting metal incorporation during oxide MBE

The previous subsection dealt with the Ga incorporation into Ga_2O_3 as a function of all MBE growth parameters limited by the r_{Me} and T_G-driven desorption of its suboxide Ga_2O. In this subsection the growth kinetics of In_2O_3 and SnO_2 as a function of T_G for different Me-to-O flux ratios is presented. By comparing all three γ-evolutions conclusions about the kinetic differences of oxides possessing suboxides are given.

Figures 5.8 (a)–(d) show γ of In_2O_3 and SnO_2 as a function ϕ_{Me} ((a) and (c)) and T_G ((b) and (d)), respectively. The decreasing γ plotted in (a) and (c) in the Me-rich regime (Me=In,Sn) is due to suboxide desorption as explained in subsection 5.1.3. In the case of In_2O_3, a plateau in the O-rich regime is present at elevated T_G, similar to Ga_2O_3 growth as plotted in Fig. 5.6 (a). However, the plateau for In_2O_3 growth is much less pronounced and appears at much higher T_G as compared to Ga_2O_3. A quantitative measurement of In_2O was not possible by means of the QMS used for these studies due to its large mass of 246 amu. Therefore, another approach was chosen in order to experimentally confirm that the plateau is caused by In_2O desorption. For this purpose, the geometry of the plateau was carefully analyzed, i.e., summing up all impinging, incorporating, and desorbing fluxes. The same approach was applied for Ga_2O_3 MBE and is discussed in Ref. [127].

But first, the explanation of the plateau is the following: for $T_G > 700\,°C$ a plateau of γ in the O-rich regime (and quasi O-rich regime, explained in the next paragraph) is present; followed by the known decreasing γ in the In-rich regime. The maximum growth rate γ_{max} (position of the plateau in Fig. 5.8 (a), black dashed line) decreases with increasing T_G. The maximum O flux ϕ'_O, that may react with In to In_2O and In_2O_3, is calculated by extending the γ-evolution from the In-rich regime until it intersects the O-rich regime (indicated as dotted black line in Fig. 5.8 (a) for $T_G = 900\,°C$). This intersection is the obtained stoichiometric flux condition for this T_G reduced by O desorption. The available O flux on the growth surface in this case is $\phi'_O = 8.0\,O\,nm^{-2}\,s^{-1}$ (the value of ϕ'_O shown in Fig. 5.8 needs to be multiplied by 3/2 since the γ-axis is scaled according to In incorporation). This value may be subtracted from the supplied ϕ^*_O, giving the number of desorbing (or recombining[1]) O atoms,

$$N^{des}_O(T_G) = \phi^*_O - \phi'_O(T_G)\ . \tag{5.16}$$

Values can be found in Tab. 5.2. The maximum number of desorbing suboxides $N^{des}_{In_2O}$ at given T_G in the O-rich regime at the end of the plateau is determined by

$$N^{des}_{In_2O}(T_G) = \phi'_O(T_G) - \gamma_{max}(T_G)\ , \tag{5.17}$$

and reflect the number of O atoms that are not incorporated into the In_2O_3 layer but can react to In_2O. Since only one O atom is needed for In_2O formation, instead of two In atoms, the width of the plateau λ when varying ϕ_{In} is

$$\lambda(T_G) = N^{des}_{In_2O}(T_G) = \phi^{end}_{In}(T_G) - \phi^{start}_{In}(T_G)\ . \tag{5.18}$$

The quantities are indicated in Fig. 5.8 (a) and all values are tabulated in Tab. 5.2. By comparing all impinging, incorporation, and desorption rates, this calculation evidences

[1] If the O atoms desorb, recombine, or both could no be investigated.

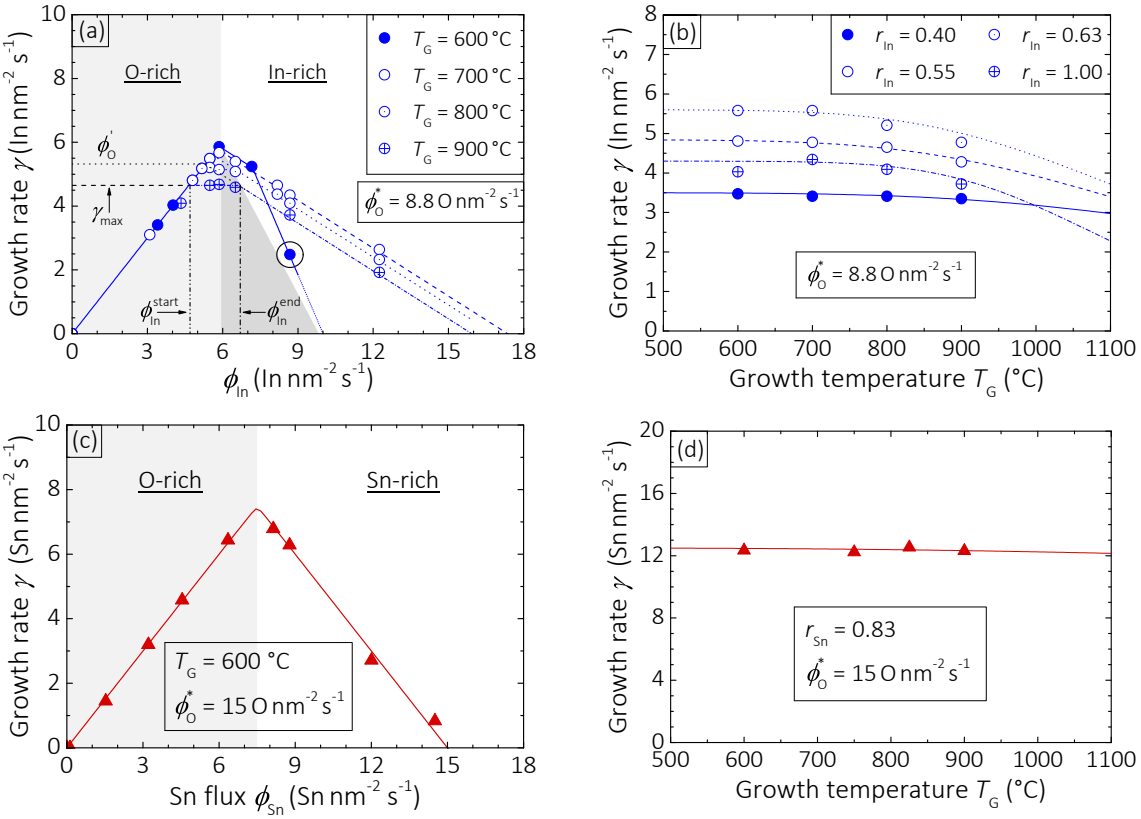

Figure 5.8.: (a) and (c) Growth rate γ as a function of In flux ϕ_{In} for different growth temperatures T_{G} and Sn flux ϕ_{Sn}, respectively. (b) and (d) γ as a function of T_{G} at different In-to-O ratios r_{In} and one Sn-to-O flux ratio r_{Sn}, respectively. The lines are model predictions according to Eqs. (5.65) for In_2O_3 and (5.67) for SnO_2 (in panel (c)). No error bars are shown for the sake of clarity.

that In_2O is formed and desorbed at elevated T_{G} causing the plateau in γ. If In desorption was the reason for it, the plateau would shift towards higher ϕ_{In} (i.e. increasing λ), because more O adatoms would be available on the growth surface and incorporated into In_2O_3.

This description already implies the explanation of the quasi O-rich growth regime, as indicated as dark gray area in Figs. 5.6 (a) and 5.8 (a). Here, the `growth surface` remains O-rich, even if according to the In-to-O flux ratio of $r_{\mathrm{In}} > 2/3$ (or $r_{\mathrm{Ga}} > 2/3$ in the case of Ga_2O_3 growth) the growth already takes place in the In-rich regime (Ga-rich regime). This is because during suboxide desorption not only one O but also `two` In atoms are removed from the growth surface. As an example, the values for In_2O_3 growth at $T_{\mathrm{G}} = 900\,^{\circ}\mathrm{C}$ are taken to compare the impinging In and O atoms with the ones incorporated and desorbed at the end of the plateau. For this example, 'effective' In and O fluxes on the growth surface that are not desorbed are defined as $\phi_{\mathrm{In}}^{\star}$ and $\phi_{\mathrm{O}}^{\star}$, respectively, and calculated as (values written in Tab. 5.2)

$$\phi_{\mathrm{In}}^{\star} = \phi_{\mathrm{In}}^{\mathrm{end}} - N_{\mathrm{In_2O}}^{\mathrm{des}} = 6.70 - 2.04 = 4.66\,\mathrm{In\,nm^{-2}\,s^{-1}} \tag{5.19}$$

and

$$\phi_{\mathrm{O}}^{\star} = \phi_{\mathrm{O}}' - N_{\mathrm{In_2O}}^{\mathrm{des}} = 8.00 - 1.02 = 6.98\,\mathrm{In\,nm^{-2}\,s^{-1}}\,. \tag{5.20}$$

compound	T_G (°C)	ϕ'_O $\left(\frac{O}{nm^2\,s}\right)$	γ_{max} $\left(\frac{O}{nm^2\,s}\right)$	ϕ_{Me}^{start} $\left(\frac{Me}{nm^2\,s}\right)$	ϕ_{Me}^{end} $\left(\frac{Me}{nm^2\,s}\right)$	N_O^{des} $\left(\frac{O}{nm^2\,s}\right)$	$N_{Me_2O}^{des}$ $\left(\frac{Me}{nm^2\,s}\right)$	λ $\left(\frac{Me}{nm^2\,s}\right)$
In_2O_3	600	8.80	8.80	0	0	0	0	0
In_2O_3	700	8.68	8.50	5.66	6.02	0.12	0.36	0.36
In_2O_3	800	8.40	7.76	5.14	6.42	0.40	1.28	1.28
In_2O_3	900	8.00	6.98	4.66	6.70	0.80	2.04	2.04
Ga_2O_3	500	9.80	9.80	0	0	0	0	0
Ga_2O_3	560	8.70	7.40	4.96	7.56	1.10	2.60	2.60
Ga_2O_3	610	7.70	5.13	3.44	8.58	2.10	5.14	5.14

Table 5.2.: Data collection of the impinging, incorporating, and desorbing fluxes corresponding to the geometry of the plateaus in the O-rich regime during In_2O_3 and Ga_2O_3 growth as plotted in Figs. 5.8 (a) and 5.6 (a), respectively. The O fluxes for In_2O_3 and Ga_2O_3 growth were $\phi_O^* = 8.8\,O\,nm^{-2}\,s^{-1}$ and $9.8\,O\,nm^{-2}\,s^{-1}$, respectively.

Taking the ratio of both values gives

$$\frac{\phi_{In}^{\star}}{\phi_O^{\star}} = \frac{4.66}{6.98} = \frac{2}{3} \tag{5.21}$$

and reveals that the growth surface is still O-rich (or stoichiometric at this growth condition). A further increase of ϕ_{In} also pushes the growth surface into the In-rich regime and γ decreases due to O-deficiency on the growth surface. The underlying mechanism that fully explains this γ-evolution is given in section 5.2.

The same formalism was applied to Ga_2O_3 (and serves as justification for the QMS calibration in Fig. 5.6 (c) in the former subsection) and is published for Ga_2O_3 [127] and In_2O_3 [126].

Another qualitative explanation that In_2O desorption and `not` In desorption is responsible for the plateau in γ in the O-rich and quasi O-rich regime is: the decreasing γ with increasing ϕ_{In} in the In-rich regime for all investigated $T_G > 700\,°C$ is due to the O-deficiency-induced In_2O formation and `not` because of In desorption, as explained in subsection 5.1. For this reason, In desorption instead of In_2O formation and its desorption at even lower ϕ_{In} in the O-rich regime (i.e., in the excess of O) is unphysical. Indium desorption, in turn, would lead to a plateau in the In-rich regime (as demonstrated for hypothetical γ-evolution (i) in Fig. 5.5) and not to a decrease of γ as plotted in Figs. 5.1 (c) and 5.8 (a). The same arguments can be applied for Ga_2O_3 and SnO_2 and are used in this thesis. In the case of SnO_2 MBE, Tsai *et al.* [117] and White *et al.* [134] have interpreted a plateau in γ when varying ϕ_{Sn} and keeping ϕ_O^* and T_G constant. Based on the findings in this section it is suggested that the origin of the plateau in the case of SnO_2 MBE is due to SnO desorption and that it appears in the O-rich and quasi O-rich growth regime.

The functional dependence of $N_{Ga_2O}^{des}$ and $N_{In_2O}^{des}$ on T_G obtained by Arrhenius-plots (not shown) is depicted in Fig. 5.9. In addition, the vapor pressures of Ga ($p_{Ga}^{lit.}$), In ($p_{In}^{lit.}$), Sn ($p_{Sn}^{lit.}$), Ga_2O ($p_{Ga_2O}^{lit.}$), In_2O ($p_{In_2O}^{lit.}$), and SnO ($p_{SnO}^{lit.}$) taken from literature are shown for

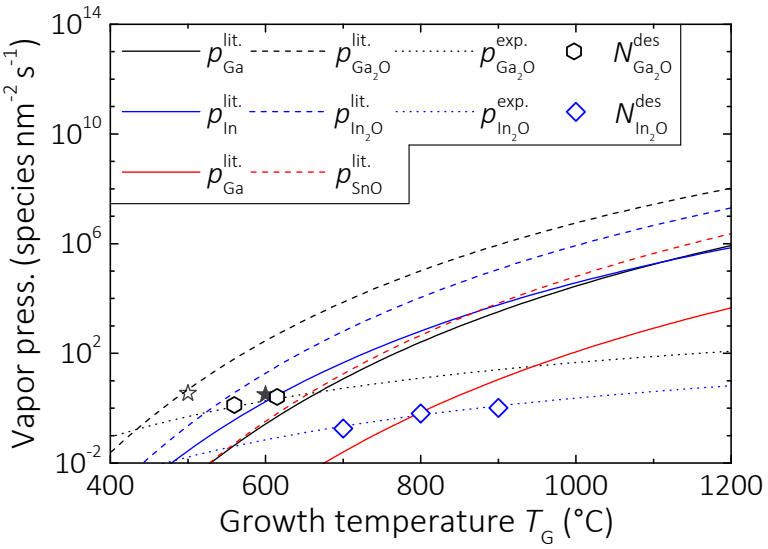

Figure 5.9.: Vapor pressures taken from literature and converted into species nm^{-2} s^{-1} for Ga $p^{\text{lit.}}_{\text{Ga}}$ [3] (solid black), In $p^{\text{lit.}}_{\text{In}}$ [3] (solid blue), Sn $p^{\text{lit.}}_{\text{Sn}}$ [3] (solid red), Ga_2O $p^{\text{lit.}}_{Ga_2O}$ [45] (dashed black), In_2O $p^{\text{lit.}}_{In_2O}$ [118] (dashed blue), and SnO $p^{\text{lit.}}_{\text{SnO}}$ [29] (dashed red). The experimentally obtained values at the end of the plateau for the Ga_2O and In_2O desorption rates N_{Ga_2O} (open diamonds) and N_{In_2O} (open rhombs) (values given in Tab. 5.2) with their corresponding experimentally determined vapor pressures $p^{\text{exp.}}_{Ga_2O}$ (dotted black) and $p^{\text{exp.}}_{In_2O}$ (dotted blue) are plotted, respectively.

comparison. All curves may be described by the exponential function

$$p^k_j(T_G) = A^k_j \exp\left(-\frac{E^k_{a,j}}{k_B\, T_G}\right) , \tag{5.22}$$

with j = Ga, In, Sn, Ga_2O, In_2O, SnO, k = lit., exp., the activation energy for desorption $E^k_{a,j}$, and pre-exponential factor A^k_j. The corresponding values are summarized in Tab. 5.3.

The experimental vapor pressures $p^{\text{exp.}}_{Ga_2O}$ and $p^{\text{exp.}}_{In_2O}$ qualitatively describe the desorption of Ga_2O from the Ga_2O_3 and In_2O from the In_2O_3 growth surface, respectively, but differ quantitatively from the vapor pressures obtained from literature $p^{\text{lit.}}_{Ga_2O}$ and $p^{\text{lit.}}_{In_2O}$. However, $p^{\text{exp.}}_{Ga_2O} > p^{\text{exp.}}_{In_2O}$ and $p^{\text{lit.}}_{Ga_2O} > p^{\text{lit.}}_{In_2O}$ confirming the experimental results plotted in Figs. 5.6 (a) and 5.8 (a). Here, the decrease of γ for Ga_2O_3 with increasing T_G and r_{Ga} is much more pronounced than for In_2O_3 with increasing T_G and r_{In}. Taking the ratio of the activation energies for both suboxide vapor pressures obtained, i.e.

$$\frac{E^{\text{exp.}}_{a,Ga_2O}}{E^{\text{exp.}}_{a,In_2O}} = 0.918 \approx \frac{E^{\text{lit.}}_{a,Ga_2O}}{E^{\text{lit.}}_{a,In_2O}} = 0.923 , \tag{5.23}$$

suggest the same origin for the decrease of $E^{\text{exp.}}_{a,Ga_2O}$ and $E^{\text{exp.}}_{a,In_2O}$ compared to $E^{\text{lit.}}_{a,Ga_2O}$ and $E^{\text{lit.}}_{a,In_2O}$, respectively. The origin might be that the binding energies between the adatoms, admolecules (Me, O, and Me_2O), and the Me_2O_3 growth surface influence the desorption of Me_2O and strongly depends on ϕ_{Me}, ϕ^*_O, and T_G. Furthermore, as shown in Tab. 5.3, the order of activation energies for suboxide desorption taken from literature and obtained by experiment in this thesis for Ga_2O_3, In_2O_3, and SnO_2 growth (Figs. 5.6 (b), 5.8 (b) and

(d)) are consistent, i.e.

$$E^{\text{lit.}}_{\text{a,Ga}_2\text{O}} < E^{\text{lit.}}_{\text{a,In}_2\text{O}} < E^{\text{lit.}}_{\text{a,SnO}} \, . \tag{5.24}$$

On the other hand, comparing the pre-exponential factors obtained from literature and experiment, i.e.

$$\frac{A^{\text{exp.}}_{\text{Ga}_2\text{O}}}{A^{\text{exp.}}_{\text{In}_2\text{O}}} \approx 1 \neq \frac{A^{\text{lit.}}_{\text{Ga}_2\text{O}}}{E^{\text{lit.}}_{\text{In}_2\text{O}}} \approx 13.5 \, , \tag{5.25}$$

does not lead to the same ratio. However, $A^{\text{exp.}}_{\text{Ga}_2\text{O}} > A^{\text{exp.}}_{\text{In}_2\text{O}}$ in agreement with the experimental data, i.e., a higher Ga_2O desorption rate at same r_{Me} and T_{G} as compared to In_2O desorption. The discrepancy between experimental and literature pre-exponential factors might originate form the different symmetries of monoclinic Ga_2O_3 and bixbyite In_2O_3 (i.e. different symmetries in oxidation sites). These different symmetries might lead to different steric factors $\mathcal{P}$ (chapter 4, 4.3) describing the ratio between the cross section of reactive collisions and the cross section of total collisions. That means, the probability that In_2O reacts with an O adatom after an In_2O-O collision is higher than for Ga_2O to react with an O adatom after a Ga_2O-O collision. This, in turn, leads a higher Ga_2O desorption rate which is reflected by $A^{\text{exp.}}_{\text{Ga}_2\text{O}} > A^{\text{exp.}}_{\text{In}_2\text{O}}$. A similar argumentation is applied for the discussion of the kinetic parameters for Ga_2O_3 and In_2O_3 MBE obtained by the derived kinetic growth model in subsection 5.2.2.

In summary, these differences in the suboxide vapor pressures of Ga_2O, In_2O, and SnO on their respective growth surface explain the different sensitivities of γ on T_{G} and $r_{\text{Ga,In,Sn}}$ quantitatively. This sensitivity is the highest for Ga_2O_3 and lowest for SnO_2 MBE.

Me droplet formation at low growth temperature and high Me flux

In the In-rich regime at $T_{\text{G}} \leq 600\,^{\circ}\text{C}$, In forms droplets on the In_2O_3 surface and further decreases γ in the In-rich regime (indicated as black circle in Fig. 5.8 (a)). On the contrary, no Ga droplet formation (SEM measurements by Anne-Kathrin Bluhm, PDI, Berlin, not shown) was observed at similar growth conditions for Ga_2O_3 growth down to $T_{\text{G}} = 500\,^{\circ}\text{C}$ (Fig. 5.6 (a)). In order to understand this difference the vapor pressures of the suboxides obtained experimentally and taken from literature are compared with the loss of γ in the Me-rich regime. Exemplarily, $N^{\text{des}}_{\text{In}_2\text{O}} = \phi_{\text{In}} - \gamma = 6.2\,\text{In}\,\text{nm}^{-2}\,\text{s}^{-1}$ (filled star in Fig. 5.9 and black circle in Fig. 5.8 (a) at $\phi_{\text{In}} = 8.7\,\text{In}\,\text{nm}^{-2}\,\text{s}^{-1}$) and $N^{\text{des}}_{\text{Ga}_2\text{O}} = \phi_{\text{Ga}} - \gamma = 7.0\,\text{Ga}\,\text{nm}^{-2}\,\text{s}^{-1}$ (open star in Fig. 5.9 and Fig. 5.6 (a) at $\phi_{\text{Ga}} = 11\,\text{Ga}\,\text{nm}^{-2}\,\text{s}^{-1}$) for the loss in γ of In_2O_3 and Ga_2O_3 are compared, respectively. In both cases, $p^{\text{lit.}}_{\text{In}_2\text{O}}$ and $p^{\text{lit.}}_{\text{Ga}_2\text{O}}$ are in excess and $p^{\text{exp.}}_{\text{In}_2\text{O}}$ and $p^{\text{exp.}}_{\text{Ga}_2\text{O}}$ are below the loss of γ. This means that In droplet or In_2O droplet formation might be because of limited In_2O formation or desorption, respectively. A potential explanation is that the oxidation velocity of In to In_2O_3 at low-T_{G} and high-ϕ_{In} is slower than one of Ga to Ga_2O_3 at low-T_{G} and high-ϕ_{Ga}. This idea is reasonable, since for Ga_2O_3 all Ga could be oxidized even at lower T_{G} and $p_{\text{Ga}_2\text{O}}$. Comparing p_{In} and p_{Ga} with the corresponding suboxide vapor pressures $p_{\text{In}_2\text{O}} > p_{\text{In}}$ and $p_{\text{Ga}_2\text{O}} > p_{\text{Ga}}$, respectively, shows that Me desorption for both materials is not the reason for the decreasing γ in the Me-rich regime, as explained in subsection 5.1.4 for Ga desorption.

parameters	$p_{\mathrm{Ga}}^{\mathrm{lit.}}$ [3]	$p_{\mathrm{In}}^{\mathrm{lit.}}$ [3]	$p_{\mathrm{Sn}}^{\mathrm{lit.}}$ [3]	$p_{\mathrm{Ga_2O}}^{\mathrm{lit.}}$ [45]	$p_{\mathrm{In_2O}}^{\mathrm{lit.}}$ [118]	$p_{\mathrm{SnO}}^{\mathrm{lit.}}$ [29]	$p_{\mathrm{Ga_2O}}^{\mathrm{exp.}}$	$p_{\mathrm{In_2O}}^{\mathrm{exp.}}$
$E_{\mathrm{a},j}^{k}$ (eV)	2.71	2.40	3.0	2.39	2.59	2.90	0.79	0.86
$A_j^k \left(\frac{\mathrm{species}}{\mathrm{nm^2\,s}}\right)$	e^{19}	$e^{32.4}$	$e^{32.0}$	$e^{37.2}$	$e^{37.4}$	$e^{37.4}$	$e^{11.3}$	$e^{8.7}$

Table 5.3.: Kinetic parameters for Me and suboxide vapor pressures. Literature values were converted from atmospheric pressures into species $\mathrm{nm^{-2}\,s^{-1}}$.

Since the suboxide vapor pressures are in all cases much higher than the vapor pressures of the respective Me finally confirms the QMS measurements during Ga_2O_3 growth (Figs. 5.6 (c) and (d), for instance). Here, no Ga desorption could be detected for any growth condition down to $T_{\mathrm{G}} = 550\,^{\circ}\mathrm{C}$. It also supports the γ-evolutions for all investigated compounds.

5.2. Kinetic binary growth model for oxide MBE

Based on the findings in the previous section, it is stated that oxides grow via a two-step-oxidation process (TOP). That means the oxidation of the Me to the suboxide and a possibly further oxidation from the suboxide to the solid metal-oxide. Based on this TOP, a semi-empirical, kinetic growth model for binary oxide MBE is developed. The oxidation mechanism this model is based on and the mathematics needed are introduced and described. Other (hypothetical) scenarios of oxide growth are discussed in order to verify the derived model. The results of the model, i.e., the model parameters and their physical significance for the growth kinetics of oxides possessing suboxides is given.

The derived model allows the prediction of the macroscopic Me incorporation and desorption during MBE and largely explains all experimental results obtained in this thesis. In addition, by the help of this kinetic model the macroscopic In and Ga incorporation x and $(1-x)$, respectively, as a function of ϕ_{In}, ϕ_{Ga}, $\phi_{\mathrm{O}}^{*,\mathrm{eff}}$, and T_{G} during $(\mathrm{In}_x\mathrm{Ga}_{1-x})_2\mathrm{O}_3$ MBE growth can be modeled as presented in chapter 6.

5.2.1. Two-step-oxidation nature of oxides possessing suboxides

One of the key findings in this thesis is that oxides possessing at least one suboxide grow via a TOP. This TOP reads for sesquioxides as

$$2\,\mathrm{Me}\,(a) + \mathrm{O}\,(a) \xrightarrow{k_3} \mathrm{Me_2O}\,(a \text{ or } g) \tag{5.26}$$

$$\mathrm{Me_2O}\,(a) + 2\mathrm{O}\,(a) \xrightarrow{k_6} \mathrm{Me_2O_3}\,(s)\,. \tag{5.27}$$

During reaction (5.26) the suboxide is formed which can either be incorporated into the layer through reaction (5.27) or desorbed off the growth surface via reaction

$$\mathrm{Me_2O}\,(a) \xrightarrow{k_5} \mathrm{Me_2O}\,(g)\,. \tag{5.28}$$

The incorporation reaction (5.27) can take place, if, after the first oxidation step, O is still available on the growth surface and suboxide desorption is not dominant. The reaction scheme with corresponding reaction rate constants k_3, k_5, and k_6 is drawn in Fig. 5.10 and explained stepwise in subsection 5.2.2. For other Me-to-O stoichiometries of the compound, the stoichiometric coefficients in reactions (5.26) and (5.27) are different, as it is the case for SnO_2, for example.

Both reactions (5.26) and (5.27) are trimolecular, and therefore, rather unlikely to proceed directly. It is much more probable that both processes react through one or several bimolecular processes. For reaction (5.26) possible first bimolecular processes are

$$\mathrm{Me}\,(a) + \mathrm{O}\,(a) \longrightarrow \mathrm{MeO}\,(a) \tag{5.29}$$

$$2\,\mathrm{Me}\,(a) \longrightarrow \mathrm{Me_2}\,(a) \tag{5.30}$$

and then forming the suboxide by second bimolecular reactions

$$\mathrm{MeO}\,(a) + \mathrm{Me}\,(a) \longrightarrow \mathrm{Me_2O}\,(a \text{ or } g) \tag{5.31}$$

$$\mathrm{Me_2}\,(a) + \mathrm{O}\,(a) \longrightarrow \mathrm{Me_2O}\,(a \text{ or } g)\ . \tag{5.32}$$

For reaction (5.27) (sesquioxide formation) possible bimolecular intermediate reactions are

$$\mathrm{Me_2O}\,(a) + \mathrm{O}\,(a) \longrightarrow \mathrm{Me_2O_2}\,(a) \tag{5.33}$$

$$2\,\mathrm{O}\,(a) \longrightarrow \mathrm{O_2}\,(a) \tag{5.34}$$

and then reacting to the sesquioxides via second bimolecular reactions

$$\mathrm{Me_2O_2}\,(a) + \mathrm{O}\,(a) \longrightarrow \mathrm{Me_2O_3}\,(s) \tag{5.35}$$

$$\mathrm{Me_2O}\,(a) + \mathrm{O_2}\,(a) \longrightarrow \mathrm{Me_2O_3}\,(s)\ . \tag{5.36}$$

All these mechanisms, i.e., intermediate bimolecular reactions (5.29)–(5.36), are possible but with different reaction probabilities. All reactions are written without reaction rate constants since they may only be determined (in this thesis) for thermodynamically stable reactants and products as written for reactions (5.26) and (5.27). From a kinetic point of view a bimolecular reaction is faster than a trimolecular one since just two instead of three reactants need to meet and react. Therefore, it is assumed that reactions (5.26) and (5.27) are `not` elementary even if these reactions may still take place directly, but with a lower probability than one or more of reactions (5.29)–(5.36). In order to fully understand the underlying reaction mechanisms for all possible reactions, i.e. through which reaction channels the oxides are indeed formed, each reaction (5.29)–(5.36) needed to be investigated. This was not possible during this thesis. Hence, it is not possible to determine the total reaction orders $\mathcal{O}$ of reactions (5.26) and (5.27) needed for the

derivation of the binary kinetic growth model presented in the next subsection. For this reason, two different models are introduced: the first one has $\mathcal{O} = 2$ in both reactions ((5.26) and (5.27)) and the second one has $\mathcal{O} = 3$ in both reactions (model given in the appendix B.2).

Before these models are introduced, is it shown, how the decreasing growth rate γ can be explained by the suggested TOP.

Decreasing growth rate due to suboxide formation

By means of TOP (reactions (5.26) and (5.27)) the decrease of γ in the Me-rich regime can be naturally explained. As an example, Figs. 5.6 (a) and 5.8 (a) plot the low-T_G γ-evolution of Ga_2O_3 and In_2O_3 when varying ϕ_Me. Here, the growth stops at $\phi_\mathrm{Me} = 2\phi_\mathrm{O}^*$ since all O is consumed for Me_2O formation, and no O adatoms are available to oxidize the Me_2O to Me_2O_3.

For SnO_2 the growth stops at $\phi_\mathrm{Sn} = \phi_\mathrm{O}^*$, as shown in Fig. 5.8 (c), which is due to a different O stoichiometry of SnO and SnO_2 as compared to Me_2O and Me_2O_3. The TOP for SnO_2 reads as

$$\mathrm{Sn}\,(a) + \mathrm{O}\,(a) \xrightarrow{k_3} \mathrm{SnO}\,(a \text{ or } g) \tag{5.37}$$

$$\mathrm{SnO}\,(a) + \mathrm{O}\,(a) \xrightarrow{k_6} \mathrm{SnO_2}\,(s)\,. \tag{5.38}$$

These reactions are indeed `elementary` and the total reaction order in both reactions is $\mathcal{O} = 2$.

By means of TOP, during the first oxidation step from the Me to the suboxide (reactions (5.26) and (5.37)) all Me is oxidized. If, after this first oxidation step O adatoms are still available the suboxide can be further oxidized to Me_2O_3 or SnO_2.

In order to find the γ-evolution for Me_2O_3 and SnO_2, derived by the stated TOP, reactions (5.26) and (5.27) in the case of Me_2O_3, as well as (5.37) and (5.37) in the case of SnO_2, may be combined and re-written. With flux parameters ϕ_Me, ϕ_Sn, and ϕ_O^* being the new 'stoichiometric flux' coefficients. In the O-rich regime, i.e. for $\phi_\mathrm{Me} \leq a\phi_\mathrm{O}^*$ (with $a = 2/3$ for Me_2O_3 and $a = 1/2$ for SnO_2), the re-written TOP reads for Me_2O_3 and SnO_2 as

$$\phi_\mathrm{Me}\,\mathrm{Me}\,(a) + \phi_\mathrm{O}^*\,\mathrm{O}\,(a) \xrightarrow{k_3} \frac{\phi_\mathrm{Me}}{2}\,\mathrm{Me_2O}\,(a) \;+ \left(\phi_\mathrm{O}^* - \frac{\phi_\mathrm{Me}}{2}\right)\,\mathrm{O}\,(a \text{ or } g) \tag{5.39}$$

$$\xrightarrow{k_6} \frac{\phi_\mathrm{Me}}{2}\,\mathrm{Me_2O_3}\,(s) + \left(\phi_\mathrm{O}^* - \frac{3}{2}\phi_\mathrm{Me}\right)\,\mathrm{O}\,(g) \tag{5.40}$$

and

$$\phi_\mathrm{Sn}\,\mathrm{Sn}\,(a) + \phi_\mathrm{O}^*\,\mathrm{O}\,(a) \xrightarrow{k_3} \phi_\mathrm{Sn}\,\mathrm{SnO}\,(a) \;+ (\phi_\mathrm{O}^* - \phi_\mathrm{Sn})\,\mathrm{O}\,(a \text{ or } g) \tag{5.41}$$

$$\xrightarrow{k_6} \phi_\mathrm{Sn}\,\mathrm{SnO_2}\,(s) + (\phi_\mathrm{O}^* - 2\,\phi_\mathrm{Sn})\,\mathrm{O}\,(g)\,, \tag{5.42}$$

respectively. Now, with ϕ_{Me} and γ given in $\mathrm{Me\,nm^{-2}\,s^{-1}}$ gives $\gamma_{\mathrm{Me_2O_3}} = 2(\phi_{\mathrm{Me}}/2)$ (for $\mathrm{Me_2O_3}$ due to two Me) and $\gamma_{\mathrm{SnO_2}} = \phi_{\mathrm{Sn}}$. Regarding the written consecutive reactions as mathematical equations and comparing the impinging Me fluxes with the Me incorporation rates (i.e., γ), the slopes of γ in the O-rich regime for $\mathrm{Me_2O_3}$ and $\mathrm{SnO_2}$ may be obtained by taking the partial derivative of γ with respect to the corresponding Me flux, i.e.

$$\frac{\partial \gamma_{\mathrm{Me_2O_3}}}{\partial \phi_{\mathrm{Me}}} = \frac{\partial \gamma_{\mathrm{SnO_2}}}{\partial \phi_{\mathrm{Sn}}} = 1 = \sigma_{\text{O-rich}} \,. \tag{5.43}$$

The slope $\sigma_{\text{O-rich}}$ for γ in the O-rich regime is the same as already introduced in subsection 5.1.1.

In the Me-rich regime the first oxidation step to the suboxide, reactions (5.39) and (5.41) for $\mathrm{Me_2O_3}$ and $\mathrm{SnO_2}$, respectively, remains the same. Inserting $\phi_{\mathrm{Me}} = a\phi_{\mathrm{O}}^*$ ($a = 2$ for Eq. (5.39) and $a = 1$ for Eq. (5.41)) in the parentheses gives zero, i.e., no growth at these conditions. For the sake of clarity, the re-written TOP for both reactions steps is still given in the case of Me-rich growth and reads for $\mathrm{Me_2O_3}$ and $\mathrm{SnO_2}$ as

$$\phi_{\mathrm{Me}}\,\mathrm{Me}\,(a) + \phi_{\mathrm{O}}^*\,\mathrm{O}\,(a) \xrightarrow{k_3} \frac{\phi_{\mathrm{Me}}}{2}\,\mathrm{Me_2O}\,(a) + \left(\phi_{\mathrm{O}}^* - \frac{\phi_{\mathrm{Me}}}{2}\right)\,\mathrm{O}\,(a \text{ or } g) \tag{5.44}$$

$$\xrightarrow{k_6} \left(\frac{\phi_{\mathrm{O}}^*}{2} - \frac{\phi_{\mathrm{Me}}}{4}\right)\,\mathrm{Me_2O_3}\,(s) + \left(\frac{3}{4}\phi_{\mathrm{Me}} - \frac{\phi_{\mathrm{O}}^*}{2}\right)\,\mathrm{Me_2O}\,(g) \tag{5.45}$$

and

$$\phi_{\mathrm{Sn}}\,\mathrm{Sn}\,(a) + \phi_{\mathrm{O}}^*\,\mathrm{O}\,(a) \xrightarrow{k_3} \phi_{\mathrm{Sn}}\,\mathrm{SnO}\,(a) \;+ (\phi_{\mathrm{O}}^* - \phi_{\mathrm{Sn}})\;\mathrm{O}\,(a \text{ or } g) \tag{5.46}$$

$$\xrightarrow{k_6} (\phi_{\mathrm{O}}^* - \phi_{\mathrm{Sn}})\,\mathrm{SnO_2}\,(s) + (2\phi_{\mathrm{Sn}} - \phi_{\mathrm{O}}^*)\;\mathrm{O}(g)\;, \tag{5.47}$$

respectively. Here, γ of $\mathrm{Me_2O_3}$ and $\mathrm{SnO_2}$ are $\gamma_{\mathrm{Me_2O_3}} = \phi_{\mathrm{O}}^*/2 - \phi_{\mathrm{Me}}/4$ and $\gamma_{\mathrm{SnO_2}} = \phi_{\mathrm{O}}^* - \phi_{\mathrm{Sn}}$, respectively. This gives a slope of γ in the Me-rich for $\mathrm{Me_2O_3}$ (taking the two Me in $\mathrm{Me_2O_3}$ into account) and $\mathrm{SnO_2}$ of

$$\frac{\partial \gamma_{\mathrm{Me_2O_3}}}{\partial \phi_{\mathrm{Me}}} = -\frac{1}{2} = \sigma_{\text{Ga-,In-rich}} \tag{5.48}$$

and

$$\frac{\partial \gamma_{\mathrm{SnO_2}}}{\partial \phi_{\mathrm{Sn}}} = -1 = \sigma_{\text{Sn-rich}}\;, \tag{5.49}$$

respectively, as already derived in subsection 5.1.1. Based on these calculations, the introduced TOP explains the decreasing γ of oxides possessing suboxides, and the growth condition at which the growth stops.

However, this is exactly the same result as obtained in subsection 5.1.3 when comparing ϕ_{Me} used for growth and decomposition (reactions (5.8) for $\mathrm{Me_2O_3}$ and (5.13) for $\mathrm{SnO_2}$). Here, it is assumed that first all O is consumed for $\mathrm{Me_2O_3}$ and $\mathrm{SnO_2}$ formation and the remaining Me decomposes the layer while forming suboxides resulting in exactly the same

γ-evolution as predicted by the TOP. In the case of decomposition, the consecutive reaction for Me_2O_3 Me-rich growth (following the same formal procedure as for TOP) reads as

$$\phi_{\mathrm{Me}}\,\mathrm{Me}\,(g) + \phi_{\mathrm{O}}^{*}\,\mathrm{O}\,(a) \xrightarrow{k} \frac{\phi_{\mathrm{O}}^{*}}{3}\,\mathrm{Me_2O_3}\,(s) + \frac{\phi_{\mathrm{Me}}}{2}\,\mathrm{Me}\,(a) \tag{5.50}$$

$$\xrightarrow{k_4} \left(\frac{\phi_{\mathrm{O}}^{*}}{2} - \frac{\phi_{\mathrm{Me}}}{4}\right)\mathrm{Me_2O_3}\,(s) + \left(\frac{3}{4}\phi_{\mathrm{Me}} - \frac{\phi_{\mathrm{O}}^{*}}{2}\right)\mathrm{Me_2O}\,(g)\,. \tag{5.51}$$

The reaction rate constant k is arbitrarily chosen and k_4 is drawn in Fig. 5.10. Inserting $\phi_{\mathrm{Me}} = 2\phi_{\mathrm{O}}^{*}$ in the first parenthesis in (5.51) also gives zero γ since all Me_2O_3 is decomposed into Me_2O. Here, the second step is the decomposition of the layer as introduced in subsection 5.1.3 and gives exactly the same outcome as the stated TOP. That means a slope of the decreasing γ in the Me-rich regime of $\sigma_{\text{Ga-,In-rich}} = -1/2$ and a growth stop at $\phi_{\mathrm{Me}} = 2\phi_{\mathrm{O}}^{*}$. For SnO_2 the same procedure can be applied yielding the same slope as derived by TOP, i.e., $\sigma_{\text{Sn-rich}} = -1$ and a growth stop at $\phi_{\mathrm{Sn}} = \phi_{\mathrm{O}}^{*}$ (not shown).

Based on this analysis of possible reaction mechanisms of oxides, two reaction channels for suboxide formation are feasible. For convenience, for sesquioxides the net reactions are repeated here:

$$2\,\mathrm{Me}\,(a) + \mathrm{O}\,(a) \xrightarrow{k_3} \mathrm{Me_2O}\,(a \text{ or } g) \tag{5.52}$$

$$4\,\mathrm{Me}\,(a) + \mathrm{Me_2O_3}\,(s) \xrightarrow{k_4} 3\,\mathrm{Me_2O}\,(a \text{ or } g)\,. \tag{5.53}$$

The latter reaction is also drawn in Fig. 5.10 with reaction rate constant k_4. As proven in section 5.1, the loss of γ is always caused by suboxide desorption. That means, experimentally, it cannot be distinguished through which reaction channel the suboxide is indeed formed, i.e., whether $k_3 \gg k_4$, $k_3 \sim k_4$, or $k_4 \gg k_3$.

In order to get an idea which reaction channel is preferred, kinetic arguments are given for Me_2O_3 growth (similar to the arguments applied for bimolecular and trimolecular reactions). (i) Considering the minimum number of reactants needed for suboxide reactions to proceed, gives three reactants for reaction (5.52). Five reactants are needed for reaction (5.53) to occur since the reaction takes place on the Me_2O_3 growth surface and Me_2O_3 has to be formed first, before being decomposed. That means reaction (5.52) is kinetically much more preferred than reaction (5.53). (ii) On the other hand, it is conceivable (even if extremely unlikely) that in the highly O-rich regime 2Me and 3O immediately react to Me_2O_3. But, for the same reason — that Me_2O_3 may be directly formed in the excess of O — decomposition of Me_2O_3 is kinetically suppressed by the excess of O. This scenario contradicts the results plotted, for example, in Fig. 5.6 where Ga_2O desorption was detected despite an excess of O causing the decreasing γ. For example, γ plotted in Fig. 5.6 (b) (left arrows) for $r_{\mathrm{Ga}} = 0.20$ (strong excess of O) decreases and the corresponding Ga_2O signal detected by QMS (Fig. 5.6 (d)) increases with increasing T_{G}. That means, if 2Me and 3O immediately form Me_2O_3, there is no Me available anymore (in the excess of O) in order to decompose Me_2O_3 and cause the decrease of γ. This behavior, i.e. a decreasing γ with increasing T_{G} in the excess of O caused by suboxide desorption, strongly confirms the

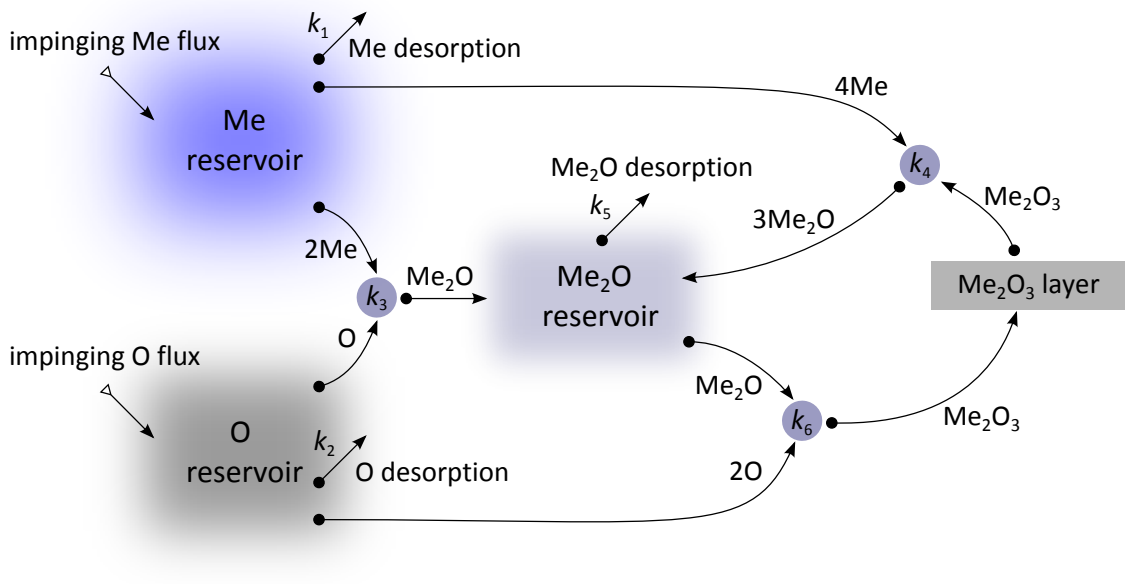

Figure 5.10.: Growth scheme for sesquioxide MBE showing impinging fluxes, resulting reservoirs, and a Me_2O_3 layer. The possible reactions that may occur during growth are shown and characterized by reaction rate constants k_i.

suggested TOP. According to the given arguments and experimental observations reaction

$$2\,\mathrm{Me}\,(a) + 3\,\mathrm{O_3}\,(a) \xrightarrow{k} \mathrm{Me_2O_3}\,(s) \tag{5.54}$$

with arbitrary reaction rate constant k is excluded. Figure 5.10 depicts a schematic of all possible reactions on the growth surface during Me_2O_3 MBE growth[2].

Now, the kinetic growth model is introduced quantitatively. It might be generalized for all oxides that posses at least one suboxide and is explicitly shown for Me_2O_3. Since oxides grow via a complex consecutive reaction process, the surface lifetimes of Me_2O (τ_{Me_2O}) and O (τ_O) on the Me_2O_3 growth surface could not be identified, thus, the reaction orders for reactions (5.26) and (5.27).

For elementary reactions the partial reaction order equals the stoichiometric coefficients. Considering sesquioxides likely do `not` grow via elementary reactions but intermediate reaction steps (reactions (5.29)–(5.36)), and that τ_{Me_2O} and τ_O are unknown, o and $\mathcal{O}$ for reactions (5.26) and (5.27) cannot be determined experimentally. Therefore, two models are presented: (i) a model were the the total reaction order is $\mathcal{O} = 2$ (subsection 5.2.2) and (ii) one with total reaction order $\mathcal{O} = 3$ (appendix B.2). The solution of the first model can be given analytically, hence, is shown in detail. For the model with $\mathcal{O} = 3$, the complete mathematical formalism is presented. Its solution can be only given numerically.

[2]The growth diagram for SnO_2 looks exactly the same just with different stoichiometric coefficients.

5.2.2. Model with total reaction order of two in oxide formation

During oxide MBE, impinging Me and plasma-activated O species adsorb on the growth surface (below a critical T_G), producing the Me and O adsorbate reservoirs (Fig. 5.10) with adatom surface densities θ_{Me} and θ_O, respectively. No Me desorption has been observed for $\phi_{Me} \leq 2\phi_O^*$. Therefore, in the derived model the related reaction rate constant is assumed to be zero, i.e. $k_1 = 0$ (Fig. 5.10). For the sake of simplicity, only O desorption — no O recombination — is taken into account and described by one reaction rate constant k_2 with rate equation

$$-\dot{\theta}_O^{des} = k_2\,\theta_O = \tau_O^{-1}\,\theta_O\ . \tag{5.55}$$

The partial derivative due to desorption of θ_O with respect to time $\partial_t\theta_O = \dot{\theta}_O^{des}$ gives the desorption rate of O from the Me_2O_3 growth surface with $k_2 = \tau_O^{-1}$. The first oxidation step to Me_2O (suboxide formation, 'SoF') is characterized by reaction rate constant k_3 with rate equation

$$\dot{\theta}_{Me_2O}^{SoF} = -\frac{1}{2}\dot{\theta}_{Me}^{SoF} = -\dot{\theta}_O^{SoF} = k_3\,\theta_{Me}\,\theta_O\ . \tag{5.56}$$

For this reaction $\mathcal{O} = 2$. The time derivatives of θ_{Me}, θ_O, and their use for Me_2O formation are described by $\dot{\theta}_{Me}^{SoF}$ and $\dot{\theta}_O^{SoF}$, respectively. The suboxide molecule surface density is denoted as θ_{Me_2O} and its formation as $\dot{\theta}_{Me_2O}^{SoF}$. In this model, due to the kinetic reasons mentioned above (comparison of reactions (5.52) and (5.53)), it is assumed that decomposition during growth can be neglected. For this reason, the reaction rate constant for decomposition reaction (5.53) is set to zero, i.e.

$$D_{Me} = \dot{\theta}_{Me_2O}^{dec} = -\frac{1}{4}\dot{\theta}_{Me}^{dec} = k_4\,\theta_{Me}\;\theta_{Me_2O_3} = 0 \quad\Longleftrightarrow\quad k_4 = 0\ , \tag{5.57}$$

with $\dot{\theta}_{Me_2O}^{dec}$ and $\dot{\theta}_{Me}^{dec}$ the formation of Me_2O and use of Me by layer decomposition, respectively. The constant Me_2O_3 surface density is denoted as $\theta_{Me_2O_3}$. For the same argument as for Me desorption, where $k_1 = 0$, $k_3 \gg 0$ since the oxidation to Me_2O is expected to proceed 'instantaneously' and all Me is consumed for Me_2O formation in the first oxidation step (cf. previous subsection). The resulting filling of the Me_2O reservoir corresponds to the half of the supplied Me flux, i.e. $\dot{\theta}_{Me_2O}^{SoF} = 1/2\phi_{Me}$. The decreasing γ with increasing T_G for all Me-to-O ratios and the plateau of γ at elevated T_G when changing ϕ_{Me} caused by Me_2O desorption is characterized by reaction rate constant k_5 with rate equation

$$-\dot{\theta}_{Me_2O}^{des} = k_5\,\theta_{Me_2O} = \tau_{Me_2O}^{-1}\,\theta_{Me_2O}\ . \tag{5.58}$$

The reciprocal of k_5 equals τ_{Me_2O}. The flux of Me_2O desorbing off the growth surface is denoted as $\dot{\theta}_{Me_2O}^{des}$. As described by reactions (5.26) and (5.27), the Me_2O may be further oxidized to Me_2O_3 for $r_{Me} < 2$ in a T_G-regime where k_5 is not too large, i.e., not all Me_2O desorbs before being oxidized to Me_2O_3. This final oxidation step to the desired sesquioxide is governed by reaction rate constant k_6 with rate equation

$$\gamma = -\dot{\theta}_{Me_2O}^{growth} = -\frac{1}{2}\dot{\theta}_O^{growth} = k_6\,\theta_{Me_2O}\,\theta_O \tag{5.59}$$

and $\mathcal{O} = 2$. The Me_2O and O consumption for growth is given by $-\dot{\theta}_{Me_2O}^{growth}$ and $-1/2\,\dot{\theta}_O^{growth}$, respectively.

Under steady state growth conditions the sums of all time derivatives of θ_{Me_2O} and θ_O are zero, i.e.,

$$\begin{aligned}\sum_i \dot{\theta}^i_{Me_2O} = 0 &= \dot{\theta}^{SoF}_{Me_2O} - \dot{\theta}^{growth}_{Me_2O} - \dot{\theta}^{des}_{Me_2O} \\ &= \frac{1}{2}\phi_{Me} - \gamma - \left(\frac{\theta_{Me_2O}}{\tau_{Me_2O}}\right)\end{aligned} \tag{5.60}$$

and

$$\begin{aligned}\sum_j \dot{\theta}^j_O = 0 &= \phi^*_O - \dot{\theta}^{SoF}_O - \frac{1}{2}\dot{\theta}^{growth}_O - \dot{\theta}^{des}_O \\ &= \phi^*_O - \frac{1}{2}\phi_{Me} - 2\gamma - \left(\frac{\theta_O}{\tau_O}\right) ,\end{aligned} \tag{5.61}$$

respectively.

Since the vapor pressures of Me_2O and O from the Me_2O_3 growth surface are unknown, the surface densities θ_{Me_2O} and θ_O cannot be calculated. Therefore, a special approach that allowed the solving of this model analytically was used: the right-hand side in Eq. (5.59) was multiplied by unity two times, i.e., $\tau_{Me_2O}/\tau_{Me_2O} = 1$ and $\tau_O/\tau_O = 1$. Equation (5.59) now reads as

$$\gamma = \mathcal{K}\left(\frac{\theta_{Me_2O}}{\tau_{Me_2O}}\right)\left(\frac{\theta_O}{\tau_O}\right) \tag{5.62}$$

with new reaction rate constant $\mathcal{K} = k_6\,\tau_{Me_2O}\,\tau_O$ in $Me_2O^{-1}\,nm^2\,s$. This approach has two advantages: (i) the Me_2O and O desorption rates, expressed by Eqs. (5.60) and (5.61), respectively, can be inserted into Eq. (5.62) and the resulting quadratic equation in γ be solved. (ii) The number of unknown model parameters is reduced from six to two. The new reaction rate constant (chapter 4, section 4.3) reads in detail as,

$$\begin{aligned}\mathcal{K} &= k_6\,\tau_{Me_2O}\,\tau_O \\ &= \frac{k_6}{k_5\,k_2} \\ &= \prod_{m=6,5,2} B_m \exp\left(-\frac{E^m_a}{k_B T_G}\right) \\ &= \left(\frac{B_6}{B_5\,B_2}\right)\exp\left(-\frac{\left(E^6_a - E^5_a - E^2_a\right)}{k_B T_G}\right) \\ &= B\exp\left(-\frac{E_a}{k_B T_G}\right) .\end{aligned} \tag{5.63}$$

The resulting `two` model parameters are the total energy of activation E_a, a sum of the activation energies for Me_2O_3 formation E^6_a, Me_2O desorption E^5_a, and O desorption E^2_a. The second parameter, the pre-exponential factor B (chapter 4, section 4.3), reads explicitly

as

$$
\begin{aligned}
B &= \frac{\left(\frac{k_\mathrm{B}\,T_\mathrm{G}}{h}\right)\,\exp\left(\frac{\Delta S_6^\ddagger}{k_\mathrm{B}}+1\right)\,\mathcal{M}^{-1}}{\left(\frac{k_\mathrm{B}\,T_\mathrm{G}}{h}\right)\,\exp\left(\frac{\Delta S_5^\ddagger}{k_\mathrm{B}}+1\right)\,\mathcal{M}^{0}\,\left(\frac{k_\mathrm{B}\,T_\mathrm{G}}{h}\right)\,\exp\left(\frac{\Delta S_2^\ddagger}{k_\mathrm{B}}+1\right)\,\mathcal{M}^{0}} \\
&= \left(\frac{h}{k_\mathrm{B}\,T_\mathrm{G}}\right)\,\exp\left(\left(\frac{\Delta S_6^\ddagger-\Delta S_5^\ddagger-\Delta S_2^\ddagger}{k_\mathrm{B}}\right)-1\right)\mathcal{M}^{-1} \\
&= \left(\frac{h}{k_\mathrm{B}\,T_\mathrm{G}}\right)\,\exp\left(\left(\frac{\Delta S^\ddagger}{k_\mathrm{B}}\right)-1\right)\mathcal{M}^{-1}\,,
\end{aligned}
\tag{5.64}
$$

with total entropy of activation $\Delta S^\ddagger = \Delta S_6^\ddagger - \Delta S_5^\ddagger - \Delta S_2^\ddagger$. Due to the various numbers of unknown activation energies and pre-exponential factors included in the final E_a and B a quantitative physical evaluation of them is not possible. However, a qualitative discussion of these values is given in the next paragraph.

The solution of γ for this model with $\mathcal{O}=2$ in rate equation (5.62), reads as

$$
\begin{aligned}
&\gamma_{\mathrm{Me_2O_3}}(T_\mathrm{G},\phi_\mathrm{Me},\phi_\mathrm{O}^*) = \left(\frac{1}{8B}\right)\left(2\,e^{-\frac{E_\mathrm{a}}{k_\mathrm{B}T_\mathrm{G}}}+B\,(\phi_\mathrm{Me}+2\phi_\mathrm{O}^*)-\right. \\
&\left.-\frac{1}{2}\left(32\,B^2\,\phi_\mathrm{Me}(\phi_\mathrm{Me}-2\phi_\mathrm{O}^*)+\left(4\,e^{-\frac{E_\mathrm{a}}{k_\mathrm{B}T_\mathrm{G}}}+2\,B\,(\phi_\mathrm{Me}+2\,\phi_\mathrm{O}^*)\right)^2\right)^{\frac{1}{2}}\right)
\end{aligned}
\tag{5.65}
$$

with the corresponding $\mathrm{Me_2O}$ desorption rate $\phi_{\mathrm{Me_2O}}^{\mathrm{des}}$,

$$
\phi_{\mathrm{Me_2O}}^{\mathrm{des}}(T_\mathrm{G},\phi_\mathrm{Me},\phi_\mathrm{O}^*) = \frac{\phi_\mathrm{Me}}{2}-\gamma_{\mathrm{Me_2O_3}}(T_\mathrm{G},\phi_\mathrm{Me},\phi_\mathrm{O}^*)\,.
\tag{5.66}
$$

The factor 1/2 in the latter expression is because of the two Me atoms in $\mathrm{Me_2O}$. The model was solved using the computer algebra software Wolfram Mathematica[3].

The solution of this model for $\mathrm{SnO_2}$ reads as

$$
\begin{aligned}
&\gamma_{\mathrm{SnO_2}}(T_\mathrm{G},\phi_\mathrm{Sn},\phi_\mathrm{O}^*) = \left(\frac{1}{2B}\right)\left(e^{-\frac{E_\mathrm{a}}{k_\mathrm{B}T_\mathrm{G}}}+B\,\phi_\mathrm{O}^*-\right. \\
&\left.-\left(4\,B^2\,\phi_\mathrm{Sn}(\phi_\mathrm{Sn}-\phi_\mathrm{O}^*)+\left(e^{-\frac{E_\mathrm{a}}{k_\mathrm{B}T_\mathrm{G}}}+B\,\phi_\mathrm{O}^*\right)^2\right)^{\frac{1}{2}}\right)
\end{aligned}
\tag{5.67}
$$

with the corresponding SnO desorption rate ϕ_SnO

$$
\phi_\mathrm{SnO}(T_\mathrm{G},\phi_\mathrm{Sn},\phi_\mathrm{O}^*) = \phi_\mathrm{Sn}-\gamma_{\mathrm{SnO_2}}(T_\mathrm{G},\phi_\mathrm{Sn},\phi_\mathrm{O}^*)\,.
\tag{5.68}
$$

For $\mathrm{SnO_2}$ the total reaction orders in reactions (5.37) and (5.38) are $\mathcal{O}=2$, and the reactions are `elementary`.

[3] Wolfram Research, 100 Trade Center Drive, Champaign, Illinois, USA

The uncertainty of the model used for the error calculation of the measured γ and $\phi^{\mathrm{des}}_{\mathrm{Me_2O}}$ is calculated by the standard deviations of the growth σ_γ and desorption rate $\sigma_{\phi^{\mathrm{des}}_{\mathrm{Me}_i\mathrm{O}}}$ (using Eqs. (5.65)–(5.68)), i.e.,

$$\sigma_\gamma = \sqrt{\sum_{v\,=\,T_\mathrm{G},\,\phi_\mathrm{Me},\,\phi^*_\mathrm{O}} \left(\frac{\partial\gamma}{\partial v}\right)^2 \sigma_v^2} \tag{5.69}$$

and

$$\sigma_{\phi^{\mathrm{des}}_{\mathrm{Me}_i\mathrm{O}}} = \sqrt{\sum_{v\,=\,T_\mathrm{G},\,\phi_\mathrm{Me},\,\phi^*_\mathrm{O}} \left(\frac{\partial\phi^{\mathrm{des}}_{\mathrm{Me}_i\mathrm{O}}}{\partial v}\right)^2 \sigma_v^2} \quad , \tag{5.70}$$

respectively. With Me = Ga, In, Sn, $i = 2$ for Me_2O_3 and $i = 1$ for SnO_2. The standard deviations σ_v of the variables $v = T_\mathrm{G}$, ϕ_Me, and ϕ^*_O are given in chapter 3, section 3.3.

Model applied for Ga_2O_3 MBE

The solution of the kinetic growth model, Eq. (5.65), is applied for Ga_2O_3 growth using four different model approaches.

Model 0 — In this model, E_a and B are constant. Here, the data-fits according to Eq. (5.65) do not converge. However, in Figs. 5.12 (a) and (b) model predictions with $E_\mathrm{a} = 2.0\,\mathrm{eV}$ and $B = 2 \times 10^{-10}\,\mathrm{Me_2O^{-1}\,nm^2\,s}$ according to Eq. (5.65) are exemplarily demonstrated.

Model 1 — In this model the T_G-dependence of γ for different r_Ga is fitted by Eq. (5.65) using two free fitting parameters, E_a and B.

Model 2 — Here, E_a is the only free model parameter for fitting the T_G-dependence of γ. The pre-exponential factor B is kept constant and estimated using Eq. (5.64) at an average growth temperature of $T_\mathrm{G} = 1000\,\mathrm{K}$ yielding

$$B = \frac{e^{-1}\,h}{k_\mathrm{B}\,T_\mathrm{G}}\,\mathcal{M}^{-1} \sim 10^{-14}\,\mathrm{Ga_2O^{-1}\,nm^2\,s} \quad . \tag{5.71}$$

In this approach, it is assumed that the change in total entropy of activation is zero and does not depend on r_Ga, i.e., $\Delta S^\ddagger = 0$ for all r_Ga.

Model 3 — In model 3, $E_\mathrm{a} \stackrel{!}{=}$ constant, and B is the only free model parameter. Since all activation energies in this model are unknown, as a first approach an arbitrary intermediate total activation energy of $E_\mathrm{a} = 2.0\,\mathrm{eV}$ is used. A systematic procedure to find a correct value of E_a is given the next paragraph.

Model results:

The fitting results of model 1, 2, and 3 are plotted in Figs. 5.11 (a) and (b), (c) and (d), as well as (e) and (f), respectively. On the left-hand side, γ as a function of T_G is shown with corresponding model fits at different r_Ga. On the right-hand side, the resulting fitting parameters E_a and B as a function of r_Ga are plotted.

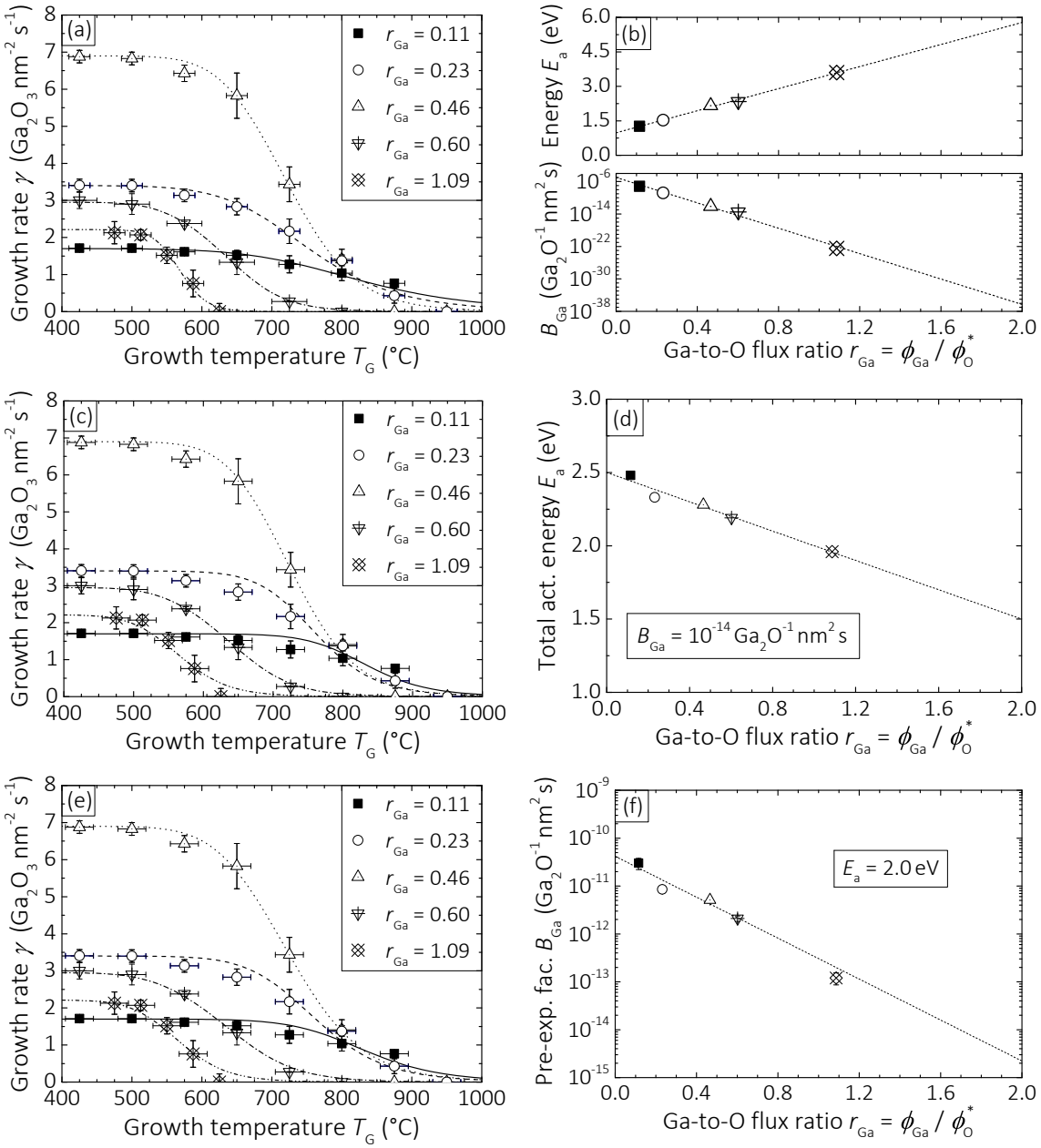

Figure 5.11.: (a), (c), (e) show the measured growth rate γ of Ga_2O_3 as a function of growth temperature T_G for different Ga-to-O flux ratios r_{Ga}, and corresponding model fits (drawn as lines) according to Eq. (5.65) for model 1, 2, and 3, respectively. (b) Model 1: plots the free model parameters E_a and B as a function of r_{Ga}. (d) Model 2: depicts E_a as a function of r_{Ga} at constant B. (f) Model 3: shows B as a function of r_{Ga} with constant E_a. The parameters on the right-hand side were obtained by fitting the data-sets on the left-hand side and are plotted with the same symbols as the fitted data-set.

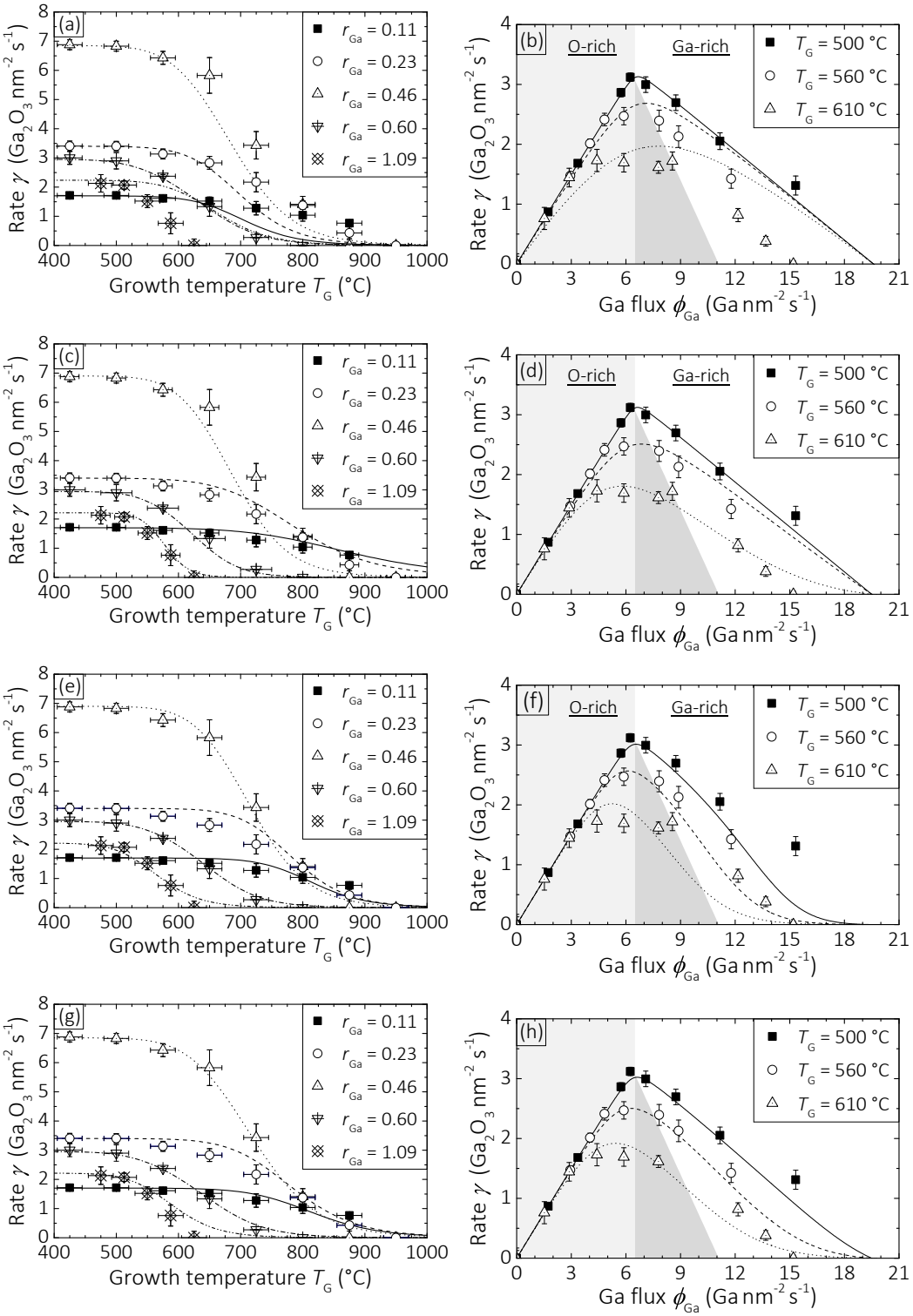

Figure 5.12.: (a), (c), (e), (g) and (b), (d), (e), (h) depict the model predictions according to Eqs. (5.65), (5.72), and (5.73) as a function of T_G and ϕ_{Me}, respectively. The measured γ is plotted for comparison. Upper, top middle, low middle, and lower panels present model 0, 1, 2, and 3, respectively.

The functional dependence of E_a on $r_{Ga} = \phi_{Ga}/\phi^*_O$ can be expressed by a linear function as

$$E_a(\phi_{Ga}, \phi^*_O) = \alpha^i_0 + \alpha_i \left(\frac{\phi_{Ga}}{\phi^*_O} \right) \tag{5.72}$$

with $\alpha^1_0 = (0.98 \pm 0.09)\,\text{eV}$, $\alpha_1 = (2.40 \pm 0.08)\,\text{eV}$ (model 1), $\alpha^2_0 = (2.50 \pm 0.03)\,\text{eV}$, and $\alpha_2 = (-0.50 \pm 0.05)\,\text{eV}$ (model 2). The pre-exponential factor follows an exponential behavior depending on r_{Ga} reading as

$$B(\phi_{Ga}, \phi^*_O) = \beta^j_0 \exp\left(-\beta_j \left(\frac{\phi_{Ga}}{\phi^*_O} \right) \right) \tag{5.73}$$

with $\beta^1_0 = (1.03 \pm 0.09) \times 10^{-5}\,Ga_2O^{-1}\,nm^2\,s$, and $\beta_1 = (36.03 \pm 1.96)$ (model 1), as well as $\beta^3_0 = (4.09 \pm 0.02) \times 10^{-11}\,Ga_2O^{-1}\,nm^2\,s$ and $\beta_3 = (4.92 \pm 0.76)$ (model 3).

Using the functional dependencies of E_a (Eq. (5.72)) and B (Eq. (5.73)) on r_{Ga}, and the expressions for γ (Eq. (5.65)) and $\phi^{des}_{Me_2O}$ (Eq. (5.66)), the growth rates and desorption rates as a function all MBE growth parameters can be predicted. The γ predictions of models 1, 2, and 3 are plotted in Figs. 5.12 (c), (e), (g) as a function of T_G as well as a function of ϕ_{Me} in (d), (f) and (h), respectively. The measured γ are plotted for comparison.

Discussion of physical significance of the obtained model parameters

The data cannot be described when E_a and B_{Ga} are kept constant demonstrated by `model 0` in Figs. 5.12 (a) and (b). Different sets of parameters were applied yielding qualitatively the same result. This indicates that either E_a, B_{Ga}, or both parameters depend on r_{Ga}. `Models 1, 2`, and `3` yield an adequate prediction of the measured γ as a function of T_G for all r_{Ga} as depicted in Figs. 5.12 (c), (e), and (g), respectively. As a function of ϕ_{Me} (Figs. 5.12 (d), (f), and (h)) all three models allow a qualitative description of the measured γ. The measured plateau in γ, however, is not quantitatively reflected by either model. Modeling γ by including decomposition of the layer, i.e. $k_4 \neq 0$, could not reflect the measured plateau in γ either. An example when decomposition is taken into account is shown in the appendix B.2 in Fig. B.1 (a) for the model with $\mathcal{O} = 3$. In order to chose one final model with $\mathcal{O} = 2$ the physical significance of E_a and B obtained as well as their dependence on r_{Ga} is discussed now.

In `model 1`, E_a is increasing, whereas E_a decreases in `model 2`, with increasing r_{Ga}. Since $\mathcal{K}$ is a product of k_6, τ_{Ga_2O}, and τ_O the total energy of activation is a sum of all three activation energies, Eq. (5.63). This activation energy can be expressed as

$$E_a = E^6_a - E^5_a - E^2_a = E^{Ga_2O_3}_{a,reac} - E^{tot}_{a,des} \tag{5.74}$$

with the activation energy for Ga_2O_3 formation $E^6_a \equiv E^{Ga_2O_3}_{a,reac} \stackrel{!}{=}$ constant. It is assumed that $E^{Ga_2O_3}_{a,reac}$ does `not` depend on the reactant concentration but is an intrinsic property of the reacting elements and determined by their electronic configurations, for instance. The total activation energy of desorption of Ga_2O plus that of O from the Ga_2O_3 growth surface is re-written as $E^5_a + E^2_a \equiv E^{tot}_{a,des}$. According to Eq. (5.74), `model 2` can be excluded. Its E_a dependence on r_{Ga} is in contradiction with the assumption that $E^{Ga_2O_3}_{a,reac} \stackrel{!}{=}$ constant. The

experimental data show that the loss of Ga_2O is larger at larger r_{Ga} and same T_G. That means a lower γ at higher r_{Ga} and same T_G. Regarding $\mathcal{K}$ in reaction rate (5.62) either B or E_a has to increase, following that $E_{a,des}^{tot}$ needs to decrease (minus sign in Eq. (5.74)), in order to physically describe the experimental data. For this reason, `model 2` can be ruled out, since here, B = constant and E_a decreases (i.e., $E_{a,des}^{tot}$ increases) with increasing r_{Ga}. In model 1, the pre-exponential factor B decreases about 30 orders of magnitude from $10^{-8}\,Ga_2O^{-1}\,nm^2\,s$ at $r_{Ga} = 0$ to $10^{-38}\,Ga_2O^{-1}\,nm^2\,s$ at $r_{Ga} = 2$, as plotted in Fig. 5.12 (b). This decrease seems unphysical and suggests that E_a and B might be correlated. That means, the strong decrease of B with r_{Ga}, compensates a decrease of E_a with r_{Ga} so that E_a increases with increasing r_{Ga}. For this reason, model 1 is `not` considered for further discussions, although it cannot totally be ruled out.

After this discussion, `model 3` is the only one left. As mentioned above, the problem for this model is that E_a is completely unknown. To overcome this problem, an iterative approach is applied in order to find E_a.

The result with $E_a = 2.0\,eV$ (Figs. 5.12 (g) and (h)) yielded a good prediction of the measured data. For this reason, the same data-sets were fitted with different fixed activation energies in the proximity of 2 eV, i.e., additionally for $E_a = 1.0\,eV$, $1.5\,eV$, $2.5\,eV$, and $3.0\,eV$. To give an idea about this approach the different model results are plotted in Figs 5.13 (a) and (b), as a function of T_G and ϕ_{Me}, respectively. For the sake of clarity, only three data-sets are shown at constant ϕ_O^*. Each value of E_a leads to a different prediction of γ.

The advantage of this approach is that by means of the different dependencies of B on r_{Ga}, obtained by fitting the data at different E_a, a functional dependence of B on E_a can be found, i.e.

$$B(\phi_{Me}, \phi_O^*) \rightarrow B(\phi_{Me}, \phi_O^*, E_a)\ . \tag{5.75}$$

The fitting results, i.e, the different B-evolutions on r_{Ga} for different E_a are depicted in Fig. 5.13 (c). The intersection with the B-axis (i.e β_0^3 in Eq. (5.73)) and the slope of B (i.e. β_3 in Eq. (5.73)) depending on E_a are plotted in Fig. 5.13 (d). This functional dependence of β_0^3 and β_3 on E_a can be used to find the best matching E_a to the experimental data. Which is found to be: $E_a \equiv E_a^{Ga} = 1.85\,eV$.

Final model for Ga_2O_3

The final model with total reaction order $\mathcal{O} = 2$ obtained, predicting γ and $\phi_{Me_2O}^{des}$, has the parameters $E_a^{Ga} = 1.85\,eV$ and $B_{Ga}(\phi_{Ga}, \phi_O^*, E_a = 1.85\,eV)$. The evolution of B_{Ga} with r_{Ga} is described by Eq. (5.73) with parameters:

$$\beta_0^3 \equiv \beta_{0,Ga} = (8.9 \pm 0.7) \times 10^{-10}\,Ga_2O^{-1}\,nm^2\,s \tag{5.76}$$

$$\beta_3 \equiv \beta_{Ga} = 4.1 \pm 0.3\ . \tag{5.77}$$

With these E_a and $B_{Ga}(\phi_{Ga}, \phi_O^*)$, all γ and $\phi_{Ga_2O}^{des}$ may be predicted as a function of all MBE growth parameters using Eqs. (5.65), (5.66), and (5.73). The result compared to the measured data is plotted in Fig. 5.14.

Since the growth kinetics studies were performed on $Al_2O_3(0001)$, the derived model parameters might need to be adjusted for different growth surfaces due to their different

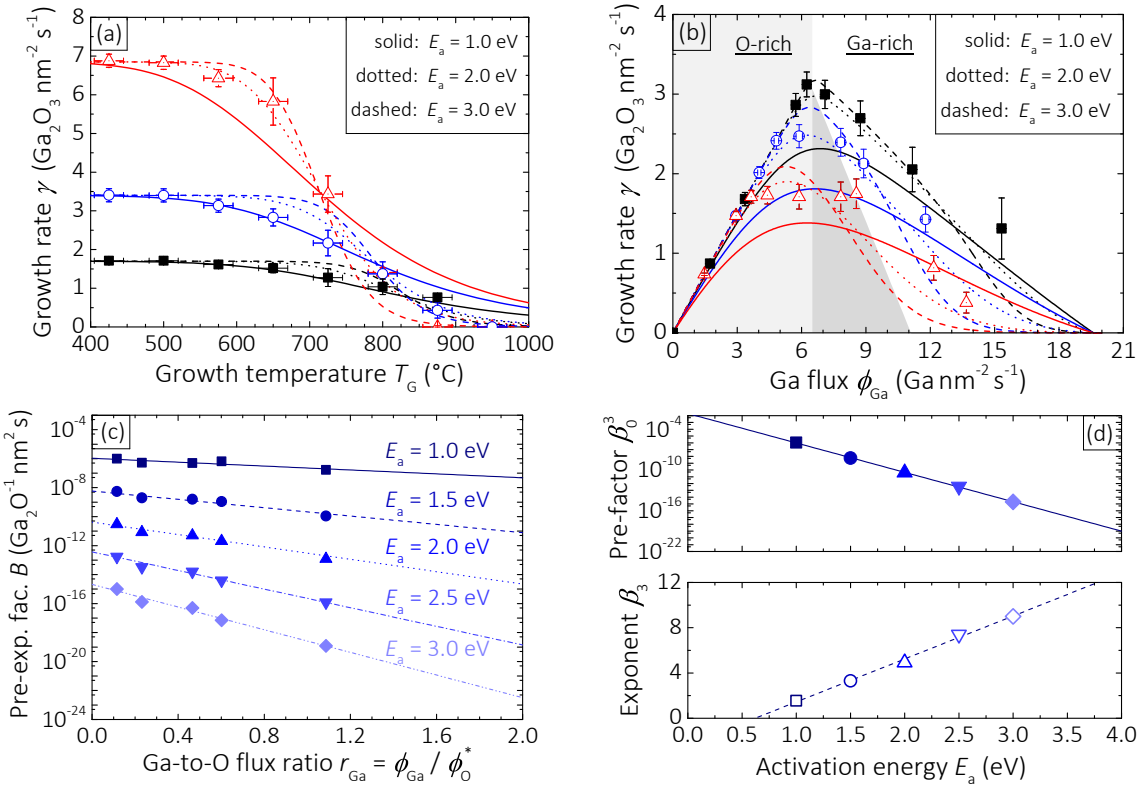

Figure 5.13.: Predictions of model 3 as function of T_G (left panel) and ϕ_{Me} (right panel) for different fixed E_a. The O flux was kept constant at $\phi_O^* = 29.4\,O\,nm^{-2}\,s^{-1}$and $\phi_O^* = 9.8\,O\,nm^{-2}\,s^{-1}$ for graph (a) and (b), respectively. (c) Obtained dependence of the pre-exponential factor B using model 3 on the Ga-to-O ratio r_{Ga} for different constant activation energies E_a. (d) Functional dependence of the parameters of B, Eq. (5.73), on E_a extracted from the data plotted in graph (a).

vapor pressures. For example, Sasaki *et al.* have found that for homoepitaxially grown Ga_2O_3 a relation between γ and the Ga_2O_3 growth surface orientation exists [104]. They show that at same growth conditions γ of Ga_2O_3 grown on Ga_2O_3(100) is approximately ten times lower than γ of Ga_2O_3 grown on Ga_2O_3(010). They attribute this effect to the lower adhesion energy between Ga adatoms and the (100) surface as compared to the adhesion energy between Ga adatoms and the (010) surface. Based on the stated TOP and the catalytic effect of the Ga_2O_3 surface on Ga_2O formation (section 5.1.4), it is suggested that the adhesion energies between Ga_2O admolecules and different Ga_2O_3 orientations diverge. This difference in adhesion energy is the cause for the different kinetics of Ga_2O_3 grown on different Ga_2O_3 orientations as observed by Sasaki *et. al.* That means, that the adhesion energy between Ga_2O admolecules and the Ga_2O_3(100) surface is lower than the adhesion energy between Ga_2O admolecules and the Ga_2O_3(010) surface. According to the model presented here, this leads to a higher E_a^{Ga}, i.e. lower $E_{a,des}^{tot}$, for the model applied for Ga_2O_3 grown on Ga_2O_3(100) as compared to Ga_2O_3 grown on Ga_2O_3(010).

Figures 5.15 (a) and (b) present the three-dimensional (3D) model predictions as a function of T_G and ϕ_{Ga}, respectively. They illustrate the dependence on γ on T_G and ϕ_{Ga}. For these model predictions an arbitrarily O flux of $\phi_O^* = 9.0\,O\,nm^{-2}\,s^{-1}$ (corresponding to

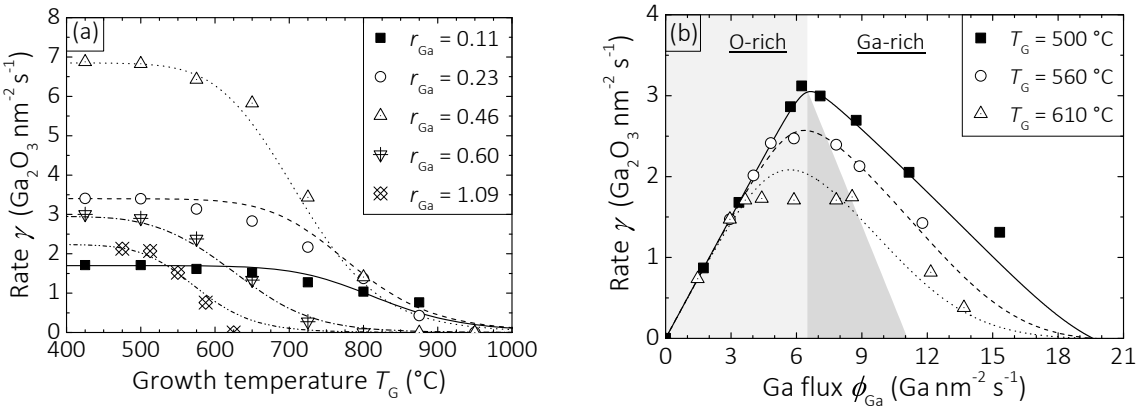

Figure 5.14.: (a) and (b) Predictions of growth rate γ by means of the finally chosen model with parameters $E_a^{Ga} = 1.85\,\text{eV}$ and $B_{Ga}(T_G, \phi_{Ga}, E_a^{Ga} = 1.85\,\text{eV})$ as a function of growth temperature T_G and Ga flux ϕ_{Ga}, respectively. In right panel (b), the best model result was obtained for a fixed model temperature of $T_{mod} = T_G - 20\,°C$. No error bars are shown for the sake of clarity.

$\sim 1.0\,\text{SCCM}$ and $P_{rf} = 300\,\text{W}$ for the used O plasma source) was chosen. The envelopes of the Ga_2O_3 MBE growth domain, i.e., its borders are defined as the region once γ is $< 0.01\,Ga_2O_3\,\text{nm}^{-2}\,\text{s}^{-1}$.

Discussion of the pre-exponential factor B in the final model

Now, a qualitative discussion of the functional dependence of B on r_{Ga} is given. The derived B in the modified Arrhenius-equation Eq. (4.18) and explicitly written in Eq. (5.64) may give conclusions about the reaction mechanism of Ga_2O_3, In_2O_3, and SnO_2.

Comparing the exponential factors in B_{Ga} obtained by the model, Eq. (5.73), with the one accessed from transition state theory, Eq. (5.64), gives[4]

$$B \sim \exp\left(-\beta_3\left(\frac{\phi_{Me}}{\phi_O^*}\right)\right) \sim \exp\left(\frac{\Delta S^\ddagger}{k_B}\right) = \mathcal{P} \tag{5.78}$$

The steric factor $\mathcal{P}$ has already been introduced in chapter 4 in the framework of collision theory Eq. (4.14) and equals the entropy factor, i.e $\mathcal{P} = e^{\Delta S^\ddagger/k_B}$ [6]. That means, the origin of $\mathcal{P} < 1$ in collision theory may be identified as a reduction in entropy during a reaction. Comparing the exponents in the latter expression gives a negative entropy of activation depending on ϕ_{Me} and ϕ_O^*, i.e.,

$$\frac{\Delta S^\ddagger(\phi_{Me}, \phi_O^*)}{k_B} = -\beta_3\left(\frac{\phi_{Me}}{\phi_O^*}\right) . \tag{5.79}$$

This negative $\Delta S^\ddagger$, implying a decrease in entropy while forming the transition state, indicates an associative reaction mechanism [37, 135]. This means, that single reaction partners form a single intermediate state, e.g., through reactions (5.29)–(5.36).

[4]The constant pre-factors in Eqs. (5.73) and (5.64) are not discussed. Only the dependence of B_{Ga} on the reactant concentrations is described.

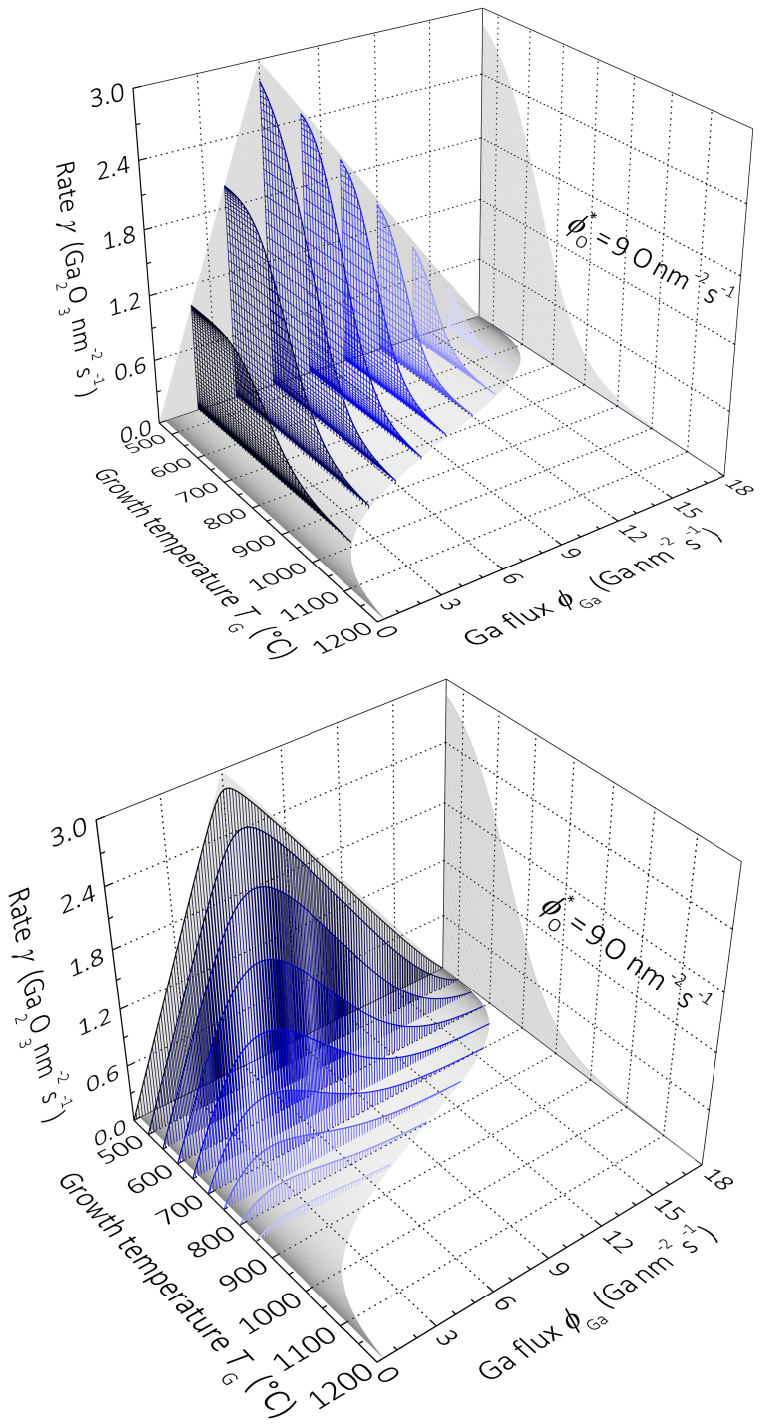

Figure 5.15.: Three-dimensional illustration of the Ga_2O_3 MBE growth domain. It shows the growth rate γ when varying the growth temperature T_G at different constant Ga fluxes ϕ_{Me} (upper panel) and when varying ϕ_{Me} at different constant T_G (lower panel). The envelopes plotted as a function of T_G and ϕ_{Me} are projected on the γ-T_G-plane and γ-ϕ_{Me}-plane, respectively. The projection of the model onto the T_G-ϕ_{Me}-plane gives the parameter space where Ga_2O_3 MBE growth is feasible at this set ϕ^*_O on $Al_2O_3(0001)$.

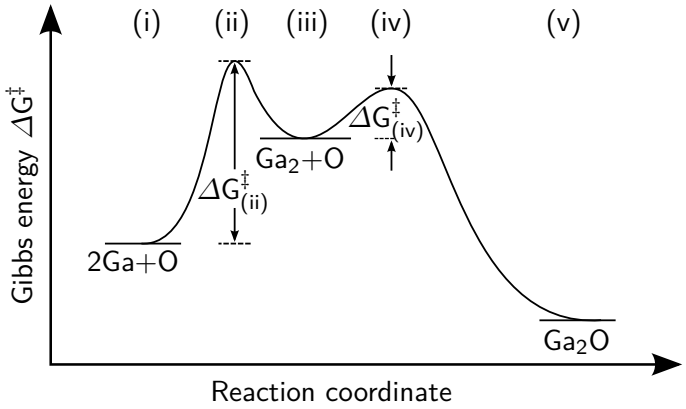

Figure 5.16.: Sketch of the reaction profile for an associative reaction mechanism for the suboxide Ga_2O showing five different reaction states. The Gibbs free energies of activation for transition states (ii) and (iv) are denoted as $\Delta G^{\ddagger}_{(ii)}$ and $\Delta G^{\ddagger}_{(iv)}$, respectively, and arbitrarily chosen.

This idea shall be explained by the example when the suboxide reaction (5.26) goes through the intermediate bimolecular reaction (5.30), for instance. The respective consecutive reaction is

$$2\,\mathrm{Ga}\,(a) + \mathrm{O}\,(a) \xrightarrow{k_{(ii)}} \mathrm{Ga_2}\,(a) + \mathrm{O}\,(a) \xrightarrow{k_{(iv)}} \mathrm{Ga_2O}\,(a\,\mathrm{or}\,g)\ . \tag{5.80}$$

The arbitrary intermediate reaction rate constants $k_{(ii)}$ and $k_{(iv)}$ describe the transition states (ii) and (iv), respectively, as indicated in Fig. 5.16. In this figure, five different states (i)–(v) based on the latter reaction are shown at different reaction coordinates. (i) Defines the thermodynamically stable ground state of the reactants (2Ga + O). (ii) Describes the first transition state forming the intermediate product — the `activated complex` Ga_2 + O — occurring in a local minimum of the potential energy surface indicated as (iii). While forming the activated complex the number of reactants decreases (from three to two). Hence, the entropy of the activated complex is lower than the one of the reactants and $\Delta S^{\ddagger}$ is decreased. The local minimum of the activated complex Ga_2 + O is thermodynamically unstable and small perturbations (e.g. collisions) lead to the formation of the final thermodynamically stable product through the second transition state (iv): the suboxide Ga_2O (v).

That $\Delta S^{\ddagger}$ decreases with increasing ϕ_{Ga} might be explained by the bond distances between nearest Ga adatoms. This distance might decrease at increasing r_{Ga}, hence, further decreases $\Delta S^{\ddagger}$. This, in turn, might affect the rate constant k_5 for Ga_2O desorption, which is included in the entropic term ($\Delta S^{\ddagger} = \Delta S^{\ddagger}_6 - \Delta S^{\ddagger}_5 - \Delta S^{\ddagger}_2$). This change in $\Delta S^{\ddagger}$ might again lead to an increased Ga_2O desorption rate at higher r_{Ga}. However, due to the diverse number of unknown parameters in Eq. (5.64) this is a very speculative explanation, and therefore, not further discussed.

Nevertheless, the explanation of an associative reaction mechanism of the investigated oxides, based on the result of the model (i.e. negative $\Delta S^{\ddagger}$), is consistent with the kinetic arguments given in subsection 5.2.1 suggesting that reactions (5.26) and (5.27) are not elementary. Other possible reaction mechanisms are dissociative where the reactants dissociate while undergoing a reaction or interchanged where no intermediate state is formed. The dissociative mechanism for the oxides investigated can be ruled out due to the atomic reactants supplied for growth. The interchange mechanism describing, for example, the direct formation of suboxides (e.g. $2\mathrm{Me} + \mathrm{O} \rightarrow \mathrm{Me_2O}$) cannot be totally ruled out, but, is based on the kinetic arguments given in subsection 5.2.1 rather unlikely to proceed. The explanation of an associative reaction mechanism is not in conflict with the experimental results either, i.e., an increased suboxide desorption at higher r_{Ga} at given T_{G}. Nonetheless, through which intermediate reaction channels the suboxides and 'full' oxides are indeed formed, cannot be extracted from the experimental data and derived model in this thesis.

Model applied for In_2O_3 MBE

Following the same procedure and arguments as given in the last paragraph, the growth domain of In_2O_3 was modeled in this thesis. The model parameters are the total energy of activation for In_2O_3 growth, $E_{\mathrm{a}}^{\mathrm{In}} = (2.03 \pm 0.05)\,\mathrm{eV}$ and the pre-exponential factor B_{In} depending on the In-to-O flux ratio r_{In}. In the case of In_2O_3 growth B_{In} reads as

$$B_{\mathrm{In}}(\phi_{\mathrm{In}}, \phi_{\mathrm{O}}^{*}) = \beta_{0,\mathrm{In}} \exp\left(-\beta_{\mathrm{In}}\left(\frac{\phi_{\mathrm{In}}}{\phi_{\mathrm{O}}^{*}}\right)\right) \tag{5.81}$$

with parameters $\beta_{0,\mathrm{In}} = (2.01 \pm 0.06) \times 10^{-7}\,\mathrm{In_2O}^{-1}\,\mathrm{nm^2\,s}$ and $\beta_{\mathrm{In}} = 1.95 \pm 0.05$. This dependency of B_{In} on r_{In} is plotted in Fig. 5.17 (a). Due to the same Me-to-O stoichiometry of In_2O_3 and Ga_2O_3, the same kinetic arguments as used for Ga_2O_3 MBE can be applied for In_2O_3 growth. The behavior of B_{In} is qualitatively the same as the one for Ga_2O_3 growth, suggesting an associative reaction mechanism for In_2O_3.

Using the parameters $E_{\mathrm{a}}^{\mathrm{In}}$ and B_{In}, Figs. 5.17 (b) and (c) depict the model predictions according to Eq. (5.65) as a function of T_{G} for different r_{In} and as a function of ϕ_{In} at different T_{G}, respectively. In both cases model predictions are in fair agreement with the measured γ.

Comparison of model parameters obtained for Ga_2O_3 and In_2O_3 growth

A quantitative comparison between the obtained model parameters for Ga_2O_3 and In_2O_3 MBE is not possible. In particular, the obtained total activation energies with $E_{\mathrm{a}}^{\mathrm{Ga}} = 1.85\,\mathrm{eV} < 2.03\,\mathrm{eV} = E_{\mathrm{a}}^{\mathrm{In}}$. This is because the individual activation energies for Me_2O_3 formation $E_{\mathrm{a,reac}}^{\mathrm{Me_2O_3}}$ and total activation energies of desorption $E_{\mathrm{a,des}}^{\mathrm{tot}}$ are unknown. Consequently, the values of $E_{\mathrm{a}}^{\mathrm{Ga}}$ and $E_{\mathrm{a}}^{\mathrm{In}}$ for Ga_2O_3 and In_2O_3, respectively, cannot be compared.

However, the parameters for the pre-exponential factor B can be qualitatively analyzed. The single values are $\beta_0^{\mathrm{Ga}} = 8.9 \times 10^{-10}\,\mathrm{Ga_2O}^{-1}\,\mathrm{nm^2\,s} < 2.0 \times 10^{-7}\,\mathrm{In_2O}^{-1}\,\mathrm{nm^2\,s} = \beta_0^{\mathrm{In}}$ and $\beta_{\mathrm{Ga}} = 4.1 < 1.95 = \beta_{\mathrm{In}}$. Inserting these values into Eqs. (5.73) for Ga_2O_3 and Eq. (5.81)

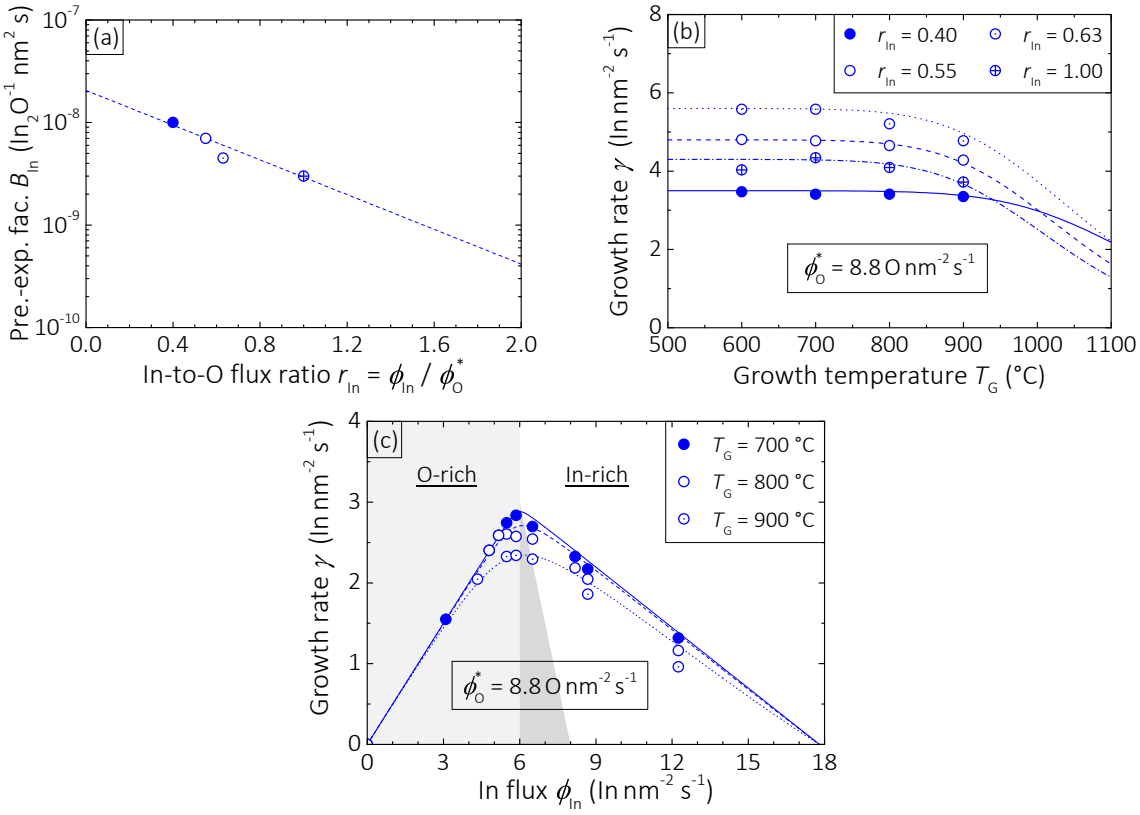

Figure 5.17.: (a) Depicts the obtained pre-exponential factor described by Eq. (5.73) for In_2O_3 growth B_{In} as a function of the In-to-O flux ratio r_{In}. (b) and (c) Plot the model predictions according to Eq. (5.65) as a function of T_G and ϕ_{In}, respectively. The measured γ are shown for comparison. No error bars are depicted, for the sake of clarity.

for Ga_2O_3 yields at same r_{Me} that

$$B_{In}(\Phi_{In}, \phi_O^*) > B_{Ga}(\Phi_{Ga}, \phi_O^*) \, . \tag{5.82}$$

This means the decrease of B_{Ga} with increasing r_{Ga} is more pronounced as the decrease of B_{In} with increasing r_{In}, reflecting the measured growth kinetics. As introduced in Eq. (5.63), $B = B_6 \, B_5^{-1} \, B_2^{-1} \sim B_5^{-1}$ with B_5^{-1} the pre-exponential factor for the reaction rate constant describing Me_2O desorption, Eq. (5.58). The pre-exponential factor for Me_2O_3 formation B_6 described by reaction rate constant k_6, Eq. (5.59), is assumed to be independent on r_{Me}. These results indicate a higher Ga_2O desorption at same Me-to-O flux ratio as compared to In_2O desorption. For this reason, the model parameters reflect the kinetic behavior of the investigated oxides suggesting that the used model approach and its solutions give an adequate description of their growth.

In addition, the entropic factor in rate equation (5.62) (included in $\mathcal{K}$) may be related with the steric factor $\mathcal{P}$ from collision theory (chapter 4, section 4.3). Applied to the results for Ga_2O_3 and In_2O_3, and comparing them, yields

$$e^{-\beta_{Ga}\left(\frac{\phi_{Ga}}{\phi_O^*}\right)} \sim \mathcal{P}_{Ga} = e^{\frac{\Delta s_{Ga}^{\ddagger}}{k_B}} < e^{\frac{\Delta s_{In}^{\ddagger}}{k_B}} = \mathcal{P}_{In} \sim e^{-\beta_{In}\left(\frac{\phi_{In}}{\phi_O^*}\right)} \, . \tag{5.83}$$

In words of collision theory, this result suggests that the probability for a reaction to proceed when two or more reactants collide is higher for In_2O_3 than for Ga_2O_3 (same argument as employed in subsection 5.1.6). This comparison might kinetically explain the different oxidation efficiencies that the oxides posses, which is larger for In_2O_3 than for Ga_2O_3, as obtained by O flux calibration and plotted in Fig. 3.6 (chapter 3). The difference in $\mathcal{P}$ might be related with the different crystal symmetries of bixbyite In_2O_3 (Fig. 2.3, chapter 2) and monoclinic Ga_2O_3 (Fig. 2.1, chapter 2). The higher symmetry in octahedral oxidation sites in the In_2O_3 crystal compared to the lower symmetry in octahedral and tetrahedral oxidation sites in the Ga_2O_3 crystal potentially explains the higher oxidation efficiency during In_2O_3 growth as compared to Ga_2O_3 growth. These different oxidation efficiencies of the Me or Me_2O lead to different effective O fluxes $\phi_O^{*,\text{eff}}$on the growth surface, determining the surface reaction kinetics during ternary oxide growth (chapter 6).

5.3. Summary

This chapter presented a comprehensive study of the MBE growth kinetics of the binary transparent semiconducting oxide Ga_2O_3, In_2O_3, and SnO_2.

In section 5.1, the growth rates γ and desorption rates were measured `in-situ` by laser relflectometry and line-of-sight OMS, respectively, as a function of Me flux ϕ_{Me}, active O flux ϕ_O^*, and growth temperature T_G. The measured γ-evolutions depending on ϕ_{Me} can be basically divided in two major growth regimes: O-rich regime (linear increase of γ with increasing ϕ_{Me}) and Me-rich regime (linear decrease of γ with increasing ϕ_{Me}). It was shown that decomposition of the oxide layers by their respective Me is feasible and measured `in-situ` by laser reflectometry and QMS. Combining the Me incorporation rates and desorption rates as well as the layer decomposition rates, the key finding in this section is the formation and desorption of `suboxides` during Ga_2O_3, In_2O_3, and SnO_2 MBE. The found suboxides Ga_2O (for Ga_2O_3), In_2O (for In_2O_3), and SnO (for SnO_2) determine the growth kinetics of the respective metal-oxide. This property differs from other semiconductors like group-III nitrides or arsenides, which do not posses subnitrides or subarsenides. Consequently, their growth kinetics are determined by other factors (not discussed).

Besides the kinetic similarity of Ga_2O_3, In_2O_3, and SnO_2 (i.e. that the growth is governed by suboxide desorption) their kinetic differences were investigated. Meaning the sensitivity of γ on T_G for different Me-to-O flux ratios r_{Me}. Increasing ϕ_O^*, i.e. decreasing r_{Me}, enables the growth at higher T_G for all compounds. The sensitivity of γ on T_G and r_{Me} is the highest for Ga_2O_3 and the lowest for SnO_2. The reason for this divergence is the difference between the respective suboxide vapor pressures, i.e. that $p_{SnO} < p_{In_2O} < p_{Ga_2O}$. This means, in turn, that Ga_2O_3 has the narrowest growth domain (above the Me adsorption temperature) followed by In_2O_3 and SnO_2. In the case of Ga_2O_3, its MBE growth domain was quantitatively determined by the measured γ. The γ-evolutions of Ga_2O_3 and In_2O_3 show a plateau in the O-rich and quasi O-rich regime. By analyzing the geometry of the plateau the cause of the constant γ when varying ϕ_{Me} is attributed to suboxide desorption. The plateaus measured of Ga_2O_3 and In_2O_3 are differently pronounced and because of the different Ga_2O and In_2O vapor pressures, respectively. It is suggested that the plateau

in the case of SnO_2 MBE observed by Tsai *et al.* [117] and White *et al.* [134] is due to the desorption of SnO. No Me desorption for all growth conditions and all investigated compounds was detected.

Based on the findings presented in section 5.1, in section 5.2, a general semi-empirical kinetic growth model for binary oxide MBE was developed. This model predicts the macroscopic Me incorporation and desorption for all MBE growth parameters. It is a first quantitative growth model for oxides possessing suboxides. Different reaction mechanisms and reaction paths were discussed on which this model is based. By data analysis, kinetic arguments, and model results, it was found that oxides grow via a two-step-oxidation process (TOP), from the Me to the suboxide and the suboxide to the thermodynamically stable metal-oxide. Since the vapor pressures of the suboxides and O on the respective growth surfaces are unknown, a special approach that reduced the unknown kinetic model parameters was used in order to solve this model analytically. This, in turn, did not allow a quantitative evaluation of the obtained model parameters. However, it is suggested by the results of the model and kinetic arguments, that oxides grow via an associative reaction mechanism. The model predicts the γ-evolution as a function of T_G quantitatively and r_Me qualitatively. The plateau of γ when varying ϕ_Me is not quantitatively reflected by the model. An explanation might be that microscopic effects such as surface diffusion or nucleation are not considered in this model. However, the benefit of this model is that it can be used to set desired growth conditions. For example, in order to grow high quality oxide layers, this model is capable of predicting growth conditions where layer growth is still feasible at high-T_G and high-ϕ_Me. It can also predict the growth regime in which the growth takes place, e.g., in the O-rich or Me-rich regime which are expected to reduce the number of O or Me vacancies, respectively.

Furthermore, this model gives a deeper understanding of the surface reaction kinetics of these oxides. Since no Me desorption for all growth conditions was observed, based on the derived TOP, an increased γ at increased ϕ_O^* and same T_G (as found in section 5.1) can be kinetically explained as follows: the reaction to the suboxide proceeds extremely fast and the suboxide is likely diffusing on the growth surface before being further oxidized to the film material. This, in turn, suggests the suboxides either experience a higher diffusion barrier at higher ϕ_O^* or the probability an O adatom meets a suboxide (in the case suboxides do not or hardly diffuse) increases. This leads to a decreased oxidation time from the suboxide to the solid metal-oxide leading to a higher Me incorporation at same T_G for higher ϕ_O^*, i.e. lower r_Me.

The understanding of the reaction kinetics during oxide MBE and its developed model can be transferred and applied to other growth techniques, such as MOVPE or PLD. Here, the same qualitative behavior in the reaction kinetics of Ga_2O_3 was found, e.g., a decreasing γ with increasing T_G during MOVPE [129], or an increasing γ with increasing O partial pressure during PLD [83]. The observed effects in both growth methods can be qualitatively explained and described by the findings and derived model in this chapter.

6. Growth kinetics and thermodynamics of MBE grown $(In_xGa_{1-x})_2O_3$

This chapter presents studies on the growth kinetics and thermodynamics of the ternary oxide $(In_xGa_{1-x})_2O_3$. Based on these investigations a kinetic ternary growth model is developed predicting the macroscopic In and Ga incorporation into $(In_xGa_{1-x})_2O_3$.

In section 6.1, the total growth rate Γ_{InGaO} of the alloy is measured `in-situ` by laser reflectometry. Species which were not incorporated into $(In_xGa_{1-x})_2O_3$, and desorbed off the growth surface during growth, are identified `in-situ` by QMS monitoring. The macroscopic In and Ga incorporation is measured as a function of growth temperature T_G, different effective (In+Ga)-to-O flux ratios $r_{InGa} = (\phi_{In} + \phi_{Ga})/\phi_O^{*,eff}$ ranging from 0.07 to 1.77, and In-to-(In+Ga) flux ratios X ranging from 0 to 1. The effective active O flux $\phi_O^{*,eff}$ is determined by the empirically found relation, Eq. (3.20) (chapter 3). The results are discussed in terms of kinetic and thermodynamic limitations and compared to the binary growth kinetics of In_2O_3 as well as Ga_2O_3. Growth conditions to force Me incorporation are demonstrated. The results presented in this section are published in large parts in Ref. [127].

Depending on T_G, r_{InGa}, and X the $(In_xGa_{1-x})_2O_3$ layers were either amorphous, polycrystalline, or crystalline. The average In concentration x was measured `ex-situ` in a macroscopic volume of the epilayer of $\sim 4\,\mu m^3$ in a SEM by means of EDX with an electron beam energy of 7.0 keV and beam tilt of zero degrees. In order to investigate whether x depends on the substrate material and orientation, different cleaved substrates of Al_2O_3((0001),(11$\bar{2}$0),(10$\bar{1}$2)) and YSZ((111),(100)) were In-bonded on a Si carrier wafer enabling the simultaneous $(In_xGa_{1-x})_2O_3$ growth on different substrates under identical growth conditions. It turned out that at a scale of a macroscopic volume x neither depends on the used substrate material and orientation the layers were grown, nor on the crystallinity of the film. The crystallinity and structure of the alloys were identified `in-situ` by RHEED and `ex-situ` by XRD ω-2θ wide-range scans. Structural data are presented in chapter 7 and in the masters thesis of Anjneya Verma [121].

Section 6.2 presents a catalytic-surfactant effect of In on the formation of Ga_2O_3. It is shown and explained how Ga_2O_3 incorporation is enhanced in the presence of In as compared to binary grown Ga_2O_3. In contrast, the In incorporation is decreased in the presence of Ga as compared to binary grown In_2O_3.

Section 6.3 introduces the ternary kinetic growth model that was developed in this thesis which is based on the findings presented in sections 6.1 and 6.2. It predicts the macroscopic In, Ga, and total Me (i.e., In + Ga) incorporation and desorption as a function of T_G for all $r_{InGa} \leq 2$, and X ranging from 0 to 1. The Ga_2O desorption for this model is

Figure symbols	ϕ_{In} $\left(\frac{In}{nm^2\,s}\right)$	ϕ_{Ga} $\left(\frac{Ga}{nm^2\,s}\right)$	$\phi_O^{*,eff}$ $\left(\frac{O}{nm^2\,s}\right)$	$\phi_O^{*,In}$ $\left(\frac{O}{nm^2\,s}\right)$	$\phi_O^{*,Ga}$ $\left(\frac{O}{nm^2\,s}\right)$	X	r_{InGa}
Squares (inset in Figs.)	1.6	1.9	51.8	79.2	29.4	0.46	0.07
Discs	4.3	1.7	18.8	26.4	9.8	0.71	0.27
Up triangles	6.2	6.1	33.0	52.8	19.6	0.50	0.36
Down triangles	3.4	4.2	11.9	26.4	9.8	0.45	0.43
Rhombs	3.6	1.7	10.5	26.4	9.8	0.68	0.50
Left triangles	2.0	6.1	14.0	26.4	9.8	0.25	0.57
Right triangles	3.2	6.6	5.9	13.4	4.9	0.31	1.77

Table 6.1.: Growth parameters and corresponding figure symbols as depicted in Figs. 6.1, 6.2, 6.3, 6.7, 6.8, and 6.9 for $(In_xGa_{1-x})_2O_3$ growth. Available O reservoirs in the case of binary In_2O_3 and Ga_2O_3 growth are shown in columns $\phi_O^{*,In}$ and $\phi_O^{*,Ga}$, respectively.

predicted by the kinetic binary model (chapter 5). It is a first quantitative growth model for $(In_xGa_{1-x})_2O_3$ MBE and can be transferred to other ternary oxides when their binary compounds posses suboxides, such as $(Al_xGa_{1-x})_2O_3$.

6.1. Metal incorporation and desorption during $(In_xGa_{1-x})_2O_3$ MBE

The total macroscopic Me incorporation rate Γ_{InGaO} is presented. Actual layer concentrations x and pseudo-binary growth rates for In ($\rho_{In_2O_3}$) and Ga ($\rho_{Ga_2O_3}$) were extracted in order to compare them to the binary growth rates of In_2O_3 ($\gamma_{In_2O_3}$) and Ga_2O_3 ($\gamma_{Ga_2O_3}$). Decomposition experiments were performed in order to understand the underlying reaction mechanisms leading to the measured $\rho_{In_2O_3}$ and $\rho_{Ga_2O_3}$.

Figure 6.1 depicts Γ_{InGaO} in Å/s as a function of T_G. Plotting Γ_{InGaO} in Å/s is an exception here. This is because x is not known at this point, thus, the atomic incorporation rate of In and Ga. However, the growth conditions for the growth data presented are tabulated in particle flux units in Tab. 6.1. In Fig. 6.1, Γ_{InGaO} decreasaes for $X = 0.25$, 0.46, 0.50, and 0.68 with increasing T_G and increasing r_{InGa}. This means, increasing $\phi_O^{*,eff}$ enables the growth of $(In_xGa_{1-x})_2O_3$ at higher T_G, similar to the growth of the binary oxides (chapter 5). This effect can be seen by comparing Γ_{InGaO}, e.g., for $r_{InGa} = 0.07$ (highly O-rich) and 1.77 (highly Me-rich). Particularly, for the lowest $r_{InGa} = 0.07$ (inset, Fig. 6.1) no decrease of Γ_{InGaO} up to $T_G = 800\,°C$ is detected.

The average Me concentration x in the films are plotted in Fig. 6.2 as a function of T_G. Under O-rich growth conditions and $T_G = 500\,°C$ the nominal equals the actual In concentration, i.e. $x = X$. For $T_G > 500\,°C$ x decreases with increasing T_G. Only under extremely O-rich conditions ($r_{InGa} \leq 0.07$), x does not depend on T_G up to 800 °C (inset, Fig. 6.2). Under Me-rich growth conditions ($r_{InGa} = 1.77$) $\phi_O^{*,eff} \approx 1.5\,\phi_{Ga}$ and $\phi_{Ga} \approx 2\,\phi_{In}$, $x = 0$ for all measured T_G, i.e., only Ga_2O_3 is incorporated. SEM measurements revealed that In accumulated as droplets on the growth surface for the sample grown at $T_G = 500\,°C$ (not shown). Similar In accumulation has been observed under In-rich conditions at low-

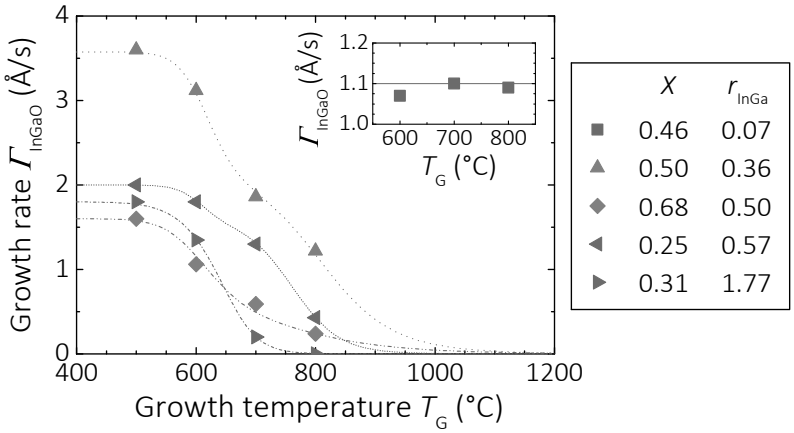

Figure 6.1.: Total growth rate Γ_{InGaO} of $(In_xGa_{1-x})_2O_3$ in Å/s as a function of growth temperature T_G for different In-to-(In+Ga) flux ratios X and effective (In+Ga)-to-O flux ratios r_{InGa}. For the sake of clarity, the growth parameters corresponding to the plotted symbols are collected in Tab. 6.1. The lines are guides to the eye.

T_G for binary In_2O_3, but not for binary Ga_2O_3 (chapter 5, subsection 5.1.6). This finding suggests preferential incorporation of Ga over In.

The pseudo-binary growth rates $\rho_{In_2O_3}$ and $\rho_{Ga_2O_3}$ are defined as

$$\rho_{In_2O_3} = x\,\Gamma_{InGaO} \tag{6.1}$$

and

$$\rho_{Ga_2O_3} = (1-x)\,\Gamma_{InGaO} \quad . \tag{6.2}$$

Figures 6.3 (a) and (b) depict the variation of $\rho_{In_2O_3}$ and $\rho_{Ga_2O_3}$, respectively, as a function of T_G for different r_{InGa} and X. The evolution of $\rho_{Ga_2O_3}$ follows qualitatively the trend of binary grown Ga_2O_3 (e.g., as plotted in Fig. 5.6 (a)). In contrast, $\rho_{In_2O_3}$ is strongly reduced for $T_G > 500\,°C$ and $r_{Me} > 0.07$ compared to the binary $\gamma_{In_2O_3}$ (e.g., as depicted in Fig. 5.8 (a)). In Figs. 6.3 (a) and (b), the blue dashed-dotted and black dashed-dotted lines for ternary Me incorporation of In_2O_3 and Ga_2O_3 in the highly Me-rich regime, respectively, are guides to the eye and correspond to the data-sets plotted as right triangles (i.e., for $X = 0.31$). For comparison, the red short-dashed lines in both figures depict the binary model predictions, Eq. (5.65), for In_2O_3 and Ga_2O_3 for the same growth conditions (as the data obtained for $X = 0.31$). All values are collected in Tab. 6.1. This comparison evidences, when both Me (i.e. In and Ga) are present on the $(In_xGa_{1-x})_2O_3$ growth surface, the In incorporation is decreased (in this case zero) and the Ga incorporation is increased, as compared to their binary growth kinetics. This behavior is discussed in detail in section 6.2.

However, the inset shows a constant $\rho_{In_2O_3}$ and $\rho_{Ga_2O_3}$ at $r_{Me} = 0.07$ up to $T_G = 800\,°C$. Based on the data plotted in Figs. 6.1–6.3, the maximum range defined of r_{InGa} where x decreases with T_G is:

$$0.07 < r_{InGa} < 1.77 \quad . \tag{6.3}$$

Under extremely O-rich growth conditions ($r_{InGa} \leq 0.07$, inset in Figs. 6.1–6.3) all In is incorporated, whereas, under highly Me-rich conditions (right triangles in Figs. 6.1–6.3

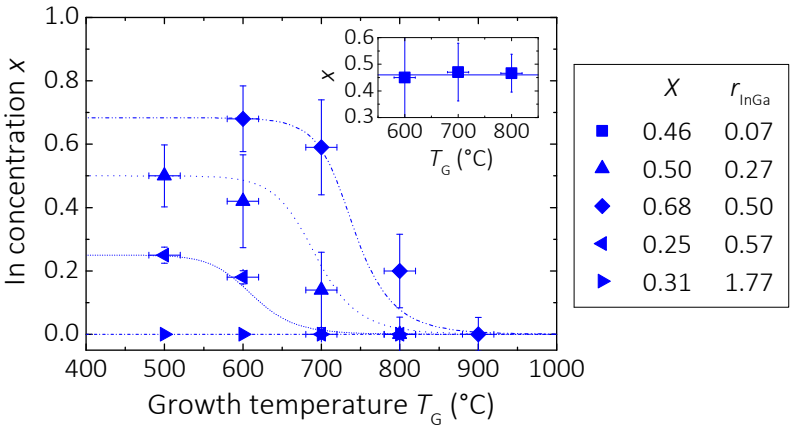

Figure 6.2.: Extracted In concentration x by EDX measurements as a function of growth temperature T_G. Growth parameters corresponding the plotted symbols can be found in Tab. 6.1. The lines for $x > 0$ are model predictions corresponding to Eq. (6.15). The error of x is calculated by Eq. (6.18).

for $r_{InGa} = 1.77$) no In incorporation is detected. These results strongly suggest that the presence of Ga inhibits the incorporation of In whereas the presence of In increases the Ga incorporation. In chapter 5 it was shown, that the In incorporation is kinetically favored over the Ga incorporation. Therefore, a kinetic origin as explanation for the reciprocal results between γ and ρ can be excluded. This means that the origin of the different In and Ga incorporations during binary and ternary growth should be a thermodynamic one.

6.1.1. Origin of the suppressed In incorporation

In amorphous indium-gallium-zinc-oxide (a-IGZO) the Ga–O bond energy is higher than the In–O bond energy as calculated by first-principles density functional calculations [85]. According to the growth rate data shown in the previous subsection it is suggested that the Ga–O bonds in $(In_xGa_{1-x})_2O_3$ are also stronger than the In–O bonds, i.e. Ga is preferentially incorporated. In order to verify this idea, (i) complementary decomposition experiments, i.e., trying to decompose the In–O and Ga–O bonds with Ga and In, respectively, and (ii) thermochemical calculations were performed.

Decomposition experiments

The decomposition experiments conducted are similar to the ones shown in chapter 5, subsection 5.1.2, but here, a In_2O_3 layer is exposed to ϕ_{Ga}, and reciprocally, a Ga_2O_3 layer to ϕ_{In}. Potential decomposition reactions are:

$$2Ga\,(a) + In_2O_3\,(s) \xrightarrow{k_\alpha} Ga_2O_3\,(s) + 2In\,(a \text{ or } g) \tag{6.4}$$

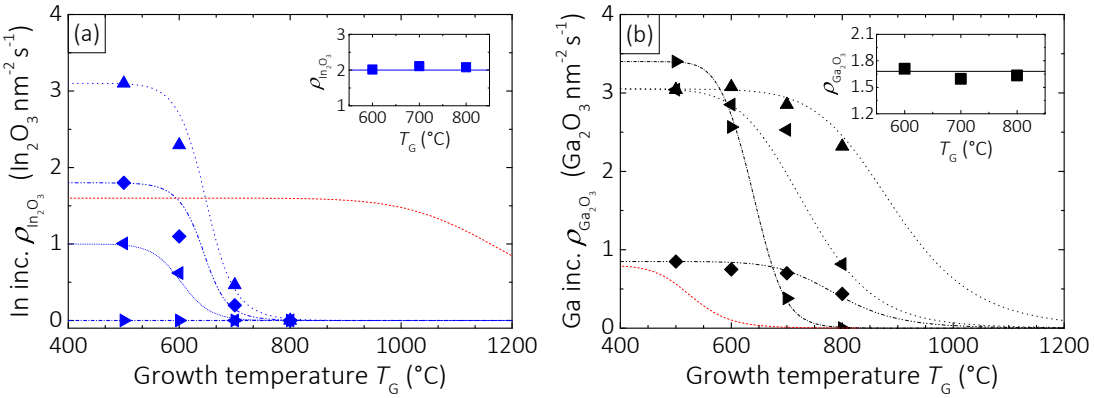

Figure 6.3.: Extracted pseudo-binary In and Ga incorporation rates $\rho_{In_2O_3}$ (a) and $\rho_{Ga_2O_3}$ (b), respectively, as a function of growth temperature T_G for growth parameters given in Tab. 6.1. The lines in (a) and (b) are ternary model fits according to Eqs. (6.21) and (5.65), respectively. The red short-dashed lines in both figures are model predictions, Eq. (5.65), for binary grown In_2O_3 and Ga_2O_3 at same growth conditions as the data depicted as right triangles with $X = 0.31$. Error bars are left for the sake of clarity.

$$2\mathrm{In}\,(a) + \mathrm{Ga_2O_3}\,(s) \xrightarrow{k_\beta} \mathrm{In_2O_3}\,(s) + 2\mathrm{Ga}\,(a \text{ or } g) \tag{6.5}$$

$$4\mathrm{Ga}\,(a) + \mathrm{In_2O_3}\,(s) \xrightarrow{k_\gamma} 2\mathrm{Ga_2O}\,(a \text{ or } g) + \mathrm{In_2O}\,(a \text{ or } g) \tag{6.6}$$

$$4\mathrm{In}\,(a) + \mathrm{Ga_2O_3}\,(s) \xrightarrow{k_\delta} 2\mathrm{In_2O}\,(a \text{ or } g) + \mathrm{Ga_2O}\,(a \text{ or } g) \tag{6.7}$$

$$6\mathrm{Ga}\,(a) + \mathrm{In_2O_3}\,(s) \xrightarrow{k_\epsilon} 3\mathrm{Ga_2O}\,(a \text{ or } g) + 2\mathrm{In}\,(a \text{ or } g) \tag{6.8}$$

$$6\mathrm{In}\,(a) + \mathrm{Ga_2O_3}\,(s) \xrightarrow{k_\zeta} 3\mathrm{In_2O}\,(a \text{ or } g) + 2\mathrm{Ga}\,(a \text{ or } g) \tag{6.9}$$

with reaction rate constants k_α–k_ζ. During the exposure of Ga_2O_3 and In_2O_3 layers to ϕ_{In} and ϕ_{Ga}, respectively, the desorbing species were monitored by QMS in order to study which of the decomposition reactions (6.4)–(6.9) take place.

Note — A new QMS built by Hiden Analytical[1], has been installed in the MBE growth chamber in November 2016. Its mass and operating range is up to 500 amu and a background pressure in the growth chamber of 5×10^{-6} Torr. For this reason, the sensitivity on the In_2O suboxide signal is higher than the one of the previous `Stanford` QMS (calibration given in the appendix A.5). In a calibration experiment (not shown), binary In_2O_3 was grown in the In-rich regime (where only In_2O desorbs). Here, In as well as In_2O with a ratio of ~ 2 was detected due to the dissociation of In_2O into In in the quadrupole; similar to Ga_2O dissociation occurred in the Stanford QMS (chapter 5). The `Hiden` QMS was installed in the final stage of this thesis and only used for experiments being essential for the understanding of $(In_xGa_{1-x})_2O_3$ MBE.

Figure 6.4, regime (i), depicts the QMS calibration of ϕ_{In} and ϕ_{Ga} by total desorption of

[1]Hiden Analytical, 420 Europa Boulevard, Warrington, United Kingdom.

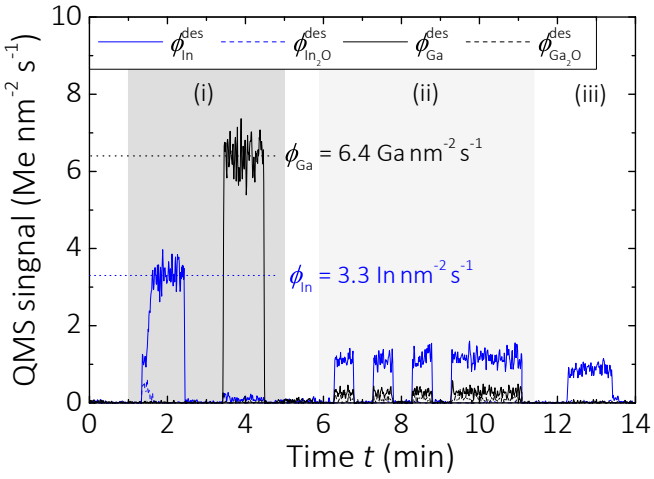

Figure 6.4.: (i) Total reflection of In and Ga from an $Al_2O_3(0001)$ growth surface without O flux. (ii) Signal detected exposing an In_2O_3 layer to ϕ_{Ga}. (iii) QMS signal while exposing an Ga_2O_3 layer to ϕ_{In}. The substrate surface temperature was 700 °C. In regime (ii) the QMS shutter was pulsed.

In and Ga, respectively, from an $Al_2O_3(0001)$ surface. Regime (ii) shows the QMS signal while exposing In_2O_3 to ϕ_{Ga}. Only In, Ga, and Ga_2O is detected. The measured Ga and Ga_2O is likely due to the dissociation of Ga_2O in the QMS. Ga_2O might be formed through exchange reaction (6.8) Regime (iii) depicts the QMS signal while exposing a Ga_2O_3 layer to ϕ_{In}. In this experiment, only In desorption is detected suggesting that In cannot decompose Ga–O and that reactions (6.5), (6.7), and (6.9) do not take place.

That the In signal in (ii) and (iii) is much lower than the one in (i) indicates that the remaining In accumulates as droplets on the Ga_2O_3 and In_2O_3 surface which might be due to the lower T_G and different In vapor pressures on the respective growth surfaces.

Thermochemical calculations

Thermochemical calculations were performed to confirm the results shown in Fig. 6.4. The change of the Gibbs free energy ΔG (Eq. (4.10), chapter 4) as function of T_G for reactions (6.4)–(6.9) is depicted in Fig. 6.5. For reactions (6.4), (6.6), and (6.8) ΔG is negative for all T_G. For reactions (6.5), (6.7), and (6.9) ΔG is positive for all T_G (used in this thesis). Therefore, reactions (6.4), (6.6), and (6.8) should be thermodynamically feasible whereas reactions (6.5), (6.7), and (6.9) should be thermodynamically hindered.

The thermochemical calculations combined with the reference decomposition experiments prove that the Ga–O bonds are stronger than the In–O bonds during $(In_xGa_{1-x})_2O_3$ MBE. These results reveal that the incorporation of Ga into $(In_xGa_{1-x})_2O_3$ is thermodynamically favored over the incorporation of In.

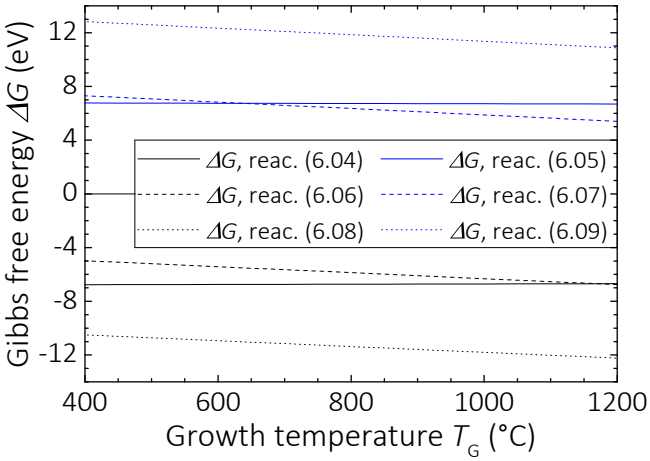

Figure 6.5.: Calculated Gibbs free energy ΔG as a function of growth temperature T_G for reactions (6.4)–(6.9) using Eq. (4.10).

6.2. Indium — a catalyst for Ga_2O_3 formation

That Ga exchanges In in In_2O_3 or decomposes In_2O_3 into In_2O and Ga_2O does not only lead to a decreased In incorporation into $(In_xGa_{1-x})_2O_3$ but also leads to an enhanced Ga incorporation, as compared to binary Ga_2O_3. This can be seen by comparing $\rho_{In_2O_3}$ and $\rho_{Ga_2O_3}$ with their binary γ (red short-dashed lines) as presented in Figs. 6.3 (a) and (b), respectively. These results suggest that In acts as a catalyst for Ga_2O_3 incorporation. In order to verify this idea, a reference growth experiment was performed using In to control the Ga_2O_3 growth. In this experiment a low-T_G β-$Ga_2O_3(\bar{2}01)/Al_2O_3(0001)$ nucleation layer of thickness $\approx 20\,\text{nm}$ was grown first to exclude effects of nucleation.

Figure 6.6 (a), regime (i), shows the QMS signal for binary Ga_2O_3 growth, i.e. when only ϕ_{Ga} and ϕ_O^* are supplied. At these growth conditions, no Ga_2O_3 is formed, i.e. $\gamma = 0$ (as proven in a separate experiment, not shown). Hence, the resulting QMS signal corresponds to desorbing Ga_2O (which dissociates in the QMS). In regime (ii), additionally to ϕ_{Ga} and ϕ_O^*, ϕ_{In} is supplied. Once the In shutter is open the Ga and Ga_2O signals decrease indicating the formation Ga_2O_3 (as also measured `in-situ` by laser reflectometry). In contrast, In desorbs off the growth surface. `Ex-situ` EDX measurements revealed `no` In was incorporated but only Ga. The resulting Ga_2O_3 growth rate was $\gamma = 4.9\,\text{Ga}\,\text{nm}^{-2}\,\text{s}^{-1}$ (measured `in-situ` by laser reflectometry and `ex-situ` by SEM). That means the presence of In allows the growth of Ga_2O_3 at conditions where binary Ga_2O_3 formation is not feasible. The growth rate indicates that (at these growth conditions) also in the presence of In not all Ga supplied was incorporated since $\gamma < \phi_{Ga}$, thus, the Ga_2O_3 growth was still Ga-rich. Which exchange reactions, i.e. Eqs. (6.4) and/or (6.8), indeed take place — leading to the formation of Ga_2O_3 — cannot be concluded from this experiment.

Another consequence of the catalytic effect of In on Ga_2O_3 incorporation is the formation of the metastable hexagonal ε-$Ga_2O_3(0001)$ phase. The structural data for the same layer as presented in Fig. 6.6 are shown in chapter 7, section 7.3.

To further analyze the impact of In on the formation of Ga_2O_3, Fig. 6.6 (b) plots the

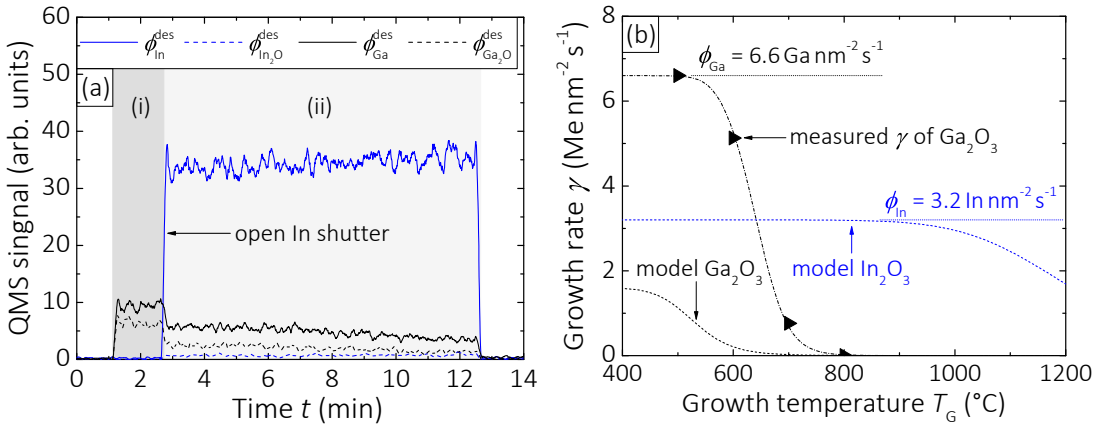

Figure 6.6.: (a) QMS signal measured during Ga_2O_3 growth without (regime (i)) and with In flux ϕ_{In} supplied (regime (ii)). Growth parameters were $T_G = 650\,°C$, $\phi_{Ga} = 6.8\,Ga\,nm^{-2}\,s^{-1}$, $\phi_{In} = 6.1\,In\,nm^{-2}\,s^{-1}$, and $\Phi_{O_2}(P_{rf} = 300\,W) = 0.75\,SCCM$, resulting in $\phi_O^{*,In} = 19.8\,O\,nm^{-2}\,s^{-1}$ and $\phi_O^{*,Ga} = 6.4\,O\,nm^{-2}\,s^{-1}$ (binary active O fluxes). (b) Growth rate γ as a function of growth temperature T_G. Black and blue short-dashed lines show the γ-evolution for binary grown Ga_2O_3 and In_2O_3 predicted by Eq. (5.65), respectively. Binary active O fluxes for Ga and In were $\phi_O^{*,Ga} = 4.9\,O\,nm^{-2}\,s^{-1}$ and $\phi_O^{*,In} = 13.4\,O\,nm^{-2}\,s^{-1}$, respectively. The black dashed-dotted line is a guide to the eye. The data shown in (a) and (b) do not correspond to the same experiment.

measured γ with $X = 0.31$ as a function of T_G. The data-set depicted as right arrows shows the same data as plotted in Fig 6.3, but now in $Me\,nm^{-2}\,s^{-1}$. The supplied O flux was 0.5 SCCM at a plasma power of 300 W. This results in an maximum O particle flux of $\phi_O^{BEP} = 51\,O\,nm^{-2}\,s^{-1}$ (Eq. (3.18), chapter 3). With the oxidation efficiencies for Ga, $J_O^{Ga} = 0.096$, and In, $J_O^{In} = 0.263$, the available ϕ_O^* for binary Ga_2O_3 and In_2O_3 growth is (also given in Tab. 6.1)

$$\phi_O^{*,Ga} = \phi_O^{BEP}\,J_O^{Ga} = 4.9\ O\,nm^{-2}\,s^{-1} \tag{6.10}$$

and

$$\phi_O^{*,In} = \phi_O^{BEP}\,J_O^{In} = 13.4\ O\,nm^{-2}\,s^{-1} \quad , \tag{6.11}$$

respectively. For this set $\Phi_{O_2}(P_{rf} = 300\,W)$, ϕ_{Ga}, and ϕ_{In} binary Ga_2O_3 growth would be Ga-rich whereas the binary In_2O_3 growth O-rich. The respective binary γ-evolutions are drawn as short-dashed lines. The measured γ showed no In incorporation for all T_G. In addition, the maximum γ is much larger than physically feasible when Ga_2O_3 or In_2O_3 are binary grown (low $T_G = 500\,°C$) and equals the supplied ϕ_{Ga}. That means not only Ga may exchange or decompose In_2O_3, but also, the resulting In or In_2O may be re-oxidized to In_2O_3, which, in turn, may be exchanged or decomposed again by other Ga adatoms. The rate how often In or In_2O may be re-oxidized depends on their $(In_xGa_{1-x})_2O_3$ surface lifetimes τ_{In} and τ_{In_2O}, respectively, and decreases exponentially with increasing T_G. At these growth conditions the re-oxidation rate $\mathscr{R}$ of In at $T_G = 500\,°C$ is $\mathscr{R} = \gamma/\phi_{In} = \phi_{Ga}/\phi_{In} \approx 2$ (with γ in $Me\,nm^{-2}\,s^{-1}$), in the case only reaction (6.4) takes place. If only reaction (6.8) occurs $\mathscr{R} \approx 6$ and due to the factor of three in O atoms between In_2O_3 and In_2O. If both reactions take place $2 < \mathscr{R} < 6$.

Combining the data presented in Figs. 6.6 (a) and (b) as well as the decomposition experi-

ments shown in subsection 6.1.1 the effect of In on the formation of Ga_2O_3 can be explained by a sequence of four other effects found in this thesis: (i) the In oxidation to In_2O_3 remains kinetically favored (chapter 5). (ii) The higher oxidation efficiency of In compared to Ga (chapter 3) enhances the Ga_2O_3 formation. This is because the 'effective' O reservoir on the growth surface for Ga is increased by In_2O_3 or In_2O. (iii) After In_2O_3 is formed Ga exchanges the In in In–O and uses the O consumed by In. (iv) Indium segregates on the growth surface and can be re-oxidized or desorbs off depending on ϕ_{In} and T_G.

This finding is not in conflict with the kinetical limits of Ga incorporation by Ga_2O desorption during $(In_xGa_{1-x})_2O_3$ growth. All possible reactions for Ga_2O_3 or Ga_2O formation, i.e the exchange reactions (6.4) and (6.8) as well as the stated TOP for binary growth with reactions (5.26) and (5.27), have different reaction rate constants which different Boltzmann- (i.e, different activation energies) and pre-exponential factors. That means that all reaction paths are still feasible but with different probabilities. Based on the findings that no Ga desorption was detected for binary Ga_2O_3 it is suggested that the Ga incorporation remains kinetically limited by Ga_2O desorption also in the ternary case. However, this is not the only limiting factor for Ga incorporation as shown in Fig. 6.6 (b). Increasing T_G decreases τ_{In}, which reduces $\mathscr{R}$ and as consequence γ. Nevertheless, the Ga species that (likely) desorbs off the growth surface is the suboxide Ga_2O. If also Ga may desorb off can neither be confirmed nor excluded by the experiments presented.

The phenomenon that Me segregates on the growth surface during ternary or quaternary epitaxial growth for semiconducting systems like $In_xGa_{1-x}N$ [32], $In_xGa_{1-x}As$ [84], or $CuIn_xGa_{1-x}Se_2$ [75], for instance, is not new. That the segregated Me may serve as a catalyst, e.g. by increasing the relative arsenic (As) incorporation with catalyst bismuth in an $In_xGa_{1-x}Sb$ system [4], or as a surfactant, e.g. by inhibiting islanding in a Si/Ge quantum-well structure with surfactant As leading to an improved surface morphology of Si and Ge layers [30], has also been reported. During Ga_2O_3 MOVPE, the concentration of structural defects, such as stacking faults and twins, decreases by the presence of In on the growth surface [8].

Nonetheless, the effect of In described in this section (and chapter 7) in the case of $(In_xGa_{1-x})_2O_3$ MBE, i.e. the combination of different binary reaction kinetics of In_2O_3 and Ga_2O_3, plus the different oxidation efficiencies of In and Ga, plus the exchange of In in In_2O_3 by Ga, plus the re-oxidation rate of In species (leading to a higher γ than physically possible when In_2O_3 and Ga_2O_3 are binary grown), seems unique.

Therefore, In can be considered as a surfactant-catalyst on the formation of Ga_2O_3.

6.3. Kinetic ternary growth model

Based on the findings in the former sections, a phenomenological kinetic growth model for In and Ga incorporation during $(In_xGa_{1-x})_2O_3$ growth is developed. This model takes advantage of the binary model derived in chapter 5 to predict the Ga_2O desorption rate $\phi^{des}_{Ga_2O}$.

Under the assumption that only In and Ga_2O desorbs from the $(In_xGa_{1-x})_2O_3$ surface (section 6.2), the macroscopic In layer concentration x can be modeled as

$$x = \frac{\phi_{\mathrm{In}} - \phi_{\mathrm{In}}^{\mathrm{des}}}{(\phi_{\mathrm{In}} - \phi_{\mathrm{In}}^{\mathrm{des}}) + (\phi_{\mathrm{Ga}} - \phi_{\mathrm{Ga_2O}}^{\mathrm{des}})} \,, \tag{6.12}$$

with

$$\begin{aligned} x &= x(T_{\mathrm{G}}, \phi_{\mathrm{In}}, \phi_{\mathrm{Ga}}, \phi_{\mathrm{O}}^{*,\mathrm{eff}}) \,, \\ \phi_{\mathrm{In}}^{\mathrm{des}} &= \phi_{\mathrm{In}}^{\mathrm{des}}(T_{\mathrm{G}}, \phi_{\mathrm{In}}, \phi_{\mathrm{Ga}}, \phi_{\mathrm{O}}^{*,\mathrm{eff}}) \,, \\ \phi_{\mathrm{Ga_2O}}^{\mathrm{des}} &= \phi_{\mathrm{Ga}}(T_{\mathrm{G}}, \phi_{\mathrm{Ga}}, \phi_{\mathrm{O}}^{*,\mathrm{eff}}) \quad . \end{aligned} \tag{6.13}$$

The In desorption rate $\phi_{\mathrm{In}}^{\mathrm{des}}$, i.e. the In loss from the $(In_xGa_{1-x})_2O_3$ surface, is assumed to be describable by an exponential function since thermally activated as

$$\phi_{\mathrm{In}}^{\mathrm{des}} = C\, x \exp\left(-\frac{E_{\mathrm{a,des}}^{\mathrm{In}}}{k_{\mathrm{B}}\, T_{\mathrm{G}}}\right) \tag{6.14}$$

with constant C in $\mathrm{In\,nm^{-2}\,s^{-1}}$. A similar approach to model the In loss during $In_xGa_{1-x}N$ MBE has already been shown by Averbeck and Riechert [7]. Combining Eqs. (6.12), (6.14), and solving the resulting function with respect to x yields

$$\boxed{x = \frac{\mathcal{C} + \phi_{\mathrm{In}} + \phi_{\mathrm{Ga}} - \phi_{\mathrm{Ga_2O}}^{\mathrm{des}} - \sqrt{\left(\mathcal{C} + \phi_{\mathrm{In}} + \phi_{\mathrm{Ga}} - \phi_{\mathrm{Ga_2O}}^{\mathrm{des}}\right)^2 - 4\,\mathcal{C}\,\phi_{\mathrm{In}}}}{2\mathcal{C}}} \tag{6.15}$$

with

$$\boxed{\mathcal{C}(T_{\mathrm{G}}) = C \exp\left(-\frac{E_{\mathrm{a,des}}^{\mathrm{In}}}{k_{\mathrm{B}}\, T_{\mathrm{G}}}\right)} \quad , \tag{6.16}$$

and $\phi_{\mathrm{Ga_2O}}^{\mathrm{des}}$ determined by Eq. (5.66). The uncertainty of x is calculated using Gaussian error propagation and inserting Eq. (5.66) (i.e. substituting $\phi_{\mathrm{Ga_2O}}^{\mathrm{des}}$) in (6.15) for independent variables as

$$\sigma_x = \sqrt{\sum_{v\,=\,T_{\mathrm{G}},\,\phi_{\mathrm{In}},\,\phi_{\mathrm{Ga}},\,\phi_{\mathrm{O}}^{*,\mathrm{eff}}} \left(\frac{\partial x}{\partial v}\right)^2 \sigma_v^2} \quad . \tag{6.17}$$

The standard deviations σ_v for the variables v are defined in chapter 3. This is a simplified error calculation since $\phi_{\mathrm{O}}^{*,\mathrm{eff}}$ is calculated by Eq. (3.20), hence, covariant with ϕ_{In} and ϕ_{Ga}. For the sake of simplicity, the total error of x, σ_x^{tot}, is conservatively estimated by adding a systematic error σ_{sys} originating from the `ex-situ` EDX measurements, i.e,

$$\sigma_x^{\mathrm{tot}} = \left(\sigma_{\mathrm{sys}}^2 + \sigma_x^2\right)^{\frac{1}{2}} \quad . \tag{6.18}$$

The systematic error is assumed to be $\sigma_{\mathrm{sys}} = \pm 0.02$ and considers the resolution limit of the device by which the layer concentrations have been measured.

The model parameters for the ternary grown Ga_2O_3 are obtained using a similar approach as presented in chapter 5, i.e., by fitting $\rho_{\mathrm{Ga_2O_3}}$ as a function of T_{G} for different $r_{\mathrm{Ga}}^{\mathrm{ter}} = \phi_{\mathrm{Ga}}/\phi_{\mathrm{O}}^{*,\mathrm{eff}}$. The actual O reservoir available for Ga during $(In_xGa_{1-x})_2O_3$ growth is

unknown so far (due to the unknown $\mathscr{R}$, section 6.2). Therefore, using $\phi_{\mathrm{O}}^{*,\mathrm{eff}}$ for modeling the ternary Ga_2O_3 incorporation is a first approximation and based on the empirically derived formula Eq. (3.20). Only for the data-set depicted as right triangles (e.g. in Fig. 6.6 (b)) $\mathscr{R}$ can be determined (since here no In was incorporated) and equals 2 in the case if only reaction (6.4) takes place. Considering $\mathscr{R}$ for the determination of $\phi_{\mathrm{O}}^{*,\mathrm{eff}}$ for all $r_{\mathrm{Ga}}^{\mathrm{ter}} = \phi_{\mathrm{Ga}} / \phi_{\mathrm{O}}^{*,\mathrm{eff}}$ (i.e. a different available O reservoir for Ga than estimated by Eq. (3.20)) might change the kinetic parameters. The γ-fits corresponding to Eq. (5.65) are plotted in Fig. 6.7 (a). The obtained pre-exponential factor $B_{\mathrm{Ga}}^{\mathrm{ter}}$ for ternary Ga_2O_3 follows the same functional dependence as introduced for Eq. (5.73), chapter 5. Its dependence on $r_{\mathrm{Ga}}^{\mathrm{ter}}$ is shown in Fig. 6.7 (b) with parameters:

$$\begin{aligned} \beta_{0,\mathrm{Ga}}^{\mathrm{ter}} &= (7.3 \pm 0.2) \times 10^{-10}\,\mathrm{Ga_2O^{-1}\,nm^2\,s} \\ \beta_{\mathrm{Ga}}^{\mathrm{ter}} &= 5.74 \pm 0.93 \quad . \end{aligned} \tag{6.19}$$

The value of $E_{\mathrm{a}}^{\mathrm{ter}} = 1.85\,\mathrm{eV}$ was obtained by the same iterative approach as explained for the binary growth model in chapter 5. The lines shown in Fig. 6.7 (a) are model predictions according to Eqs. (5.65) and (5.73) with parameters given in Eq. (6.19).

The total energy of activation of Ga_2O_3 when ternary and binary grown are the same, i.e. that $E_{\mathrm{a}}^{\mathrm{ter}} = 1.85\,\mathrm{eV} = E_{\mathrm{a}}^{\mathrm{Ga}}$. This suggests that the average total activation energy of desorption for Ga_2O and O from an $(In_xGa_{1-x})_2O_3$ growth surface (consisting of crystallites with different In and Ga concentrations), and the one from a Ga_2O_3 surface, are similar. This result, in turn, indicates that the adhesion energy between Ga_2O admolecules, O adatoms, and Ga_2O_3 and $(In_xGa_{1-x})_2O_3$ surfaces are similar. The difference between $B_{\mathrm{Ga}}^{\mathrm{ter}}$ (ternary Ga_2O_3) and B_{Ga} (binary Ga_2O_3, chapter 5) originates from the larger O reservoir available for Ga since $\phi_{\mathrm{O}}^{*,\mathrm{eff}} > \phi_{\mathrm{O}}^{*,\mathrm{Ga}}$. Furthermore, the difference between $B_{\mathrm{Ga}}^{\mathrm{ter}}$ and B_{Ga} might be due to the difference in reaction kinetics because of the additional reaction paths for Ga_2O_3 and Ga_2O formation (i.e. reactions (6.4) and (6.8)), respectively, as compared to binary Ga_2O_3. Because of the large number of reaction paths for Ga_2O_3 during $(In_xGa_{1-x})_2O_3$ growth a quantitative analysis of $B_{\mathrm{Ga}}^{\mathrm{ter}}$ is not possible.

With ϕ_{Ga}, ϕ_{In}, $\phi_{\mathrm{O}}^{*,\mathrm{eff}}$, and $\phi_{\mathrm{Ga_2O}}^{\mathrm{des}}$ the only remaining unknown parameters in Eq. (6.15) are $E_{\mathrm{a,des}}^{\mathrm{In}}$ and C. To further reduce the free parameters, $C = 1.2 \times 10^{14}\,\mathrm{In\,nm^{-2}\,s^{-1}}$ is taken from literature [3] and kept constant. The functional dependence of $E_{\mathrm{a,des}}^{\mathrm{In}}$ on the nominal In-to-(In+Ga) flux ratio X is obtained by fitting x as a function of T_{G} for different X and reads as

$$E_{\mathrm{a,des}}^{\mathrm{In}}(X) = \varepsilon_0 + \varepsilon\, X \quad , \tag{6.20}$$

with $\varepsilon_0 = (2.10 \pm 0.14)\,\mathrm{eV}$ and $\varepsilon = (0.8 \pm 0.3)\,\mathrm{eV}$. The model fit results are depicted in Fig. 6.8 (a). Its predictions for x according to Eqs. (6.15) and (6.20) are shown in Fig. 6.8 (b).

Discussion of In desorption energy

The energy required to remove one In atom from an In reservoir is 2.4 eV [3]. This value is in the proximity of the obtained model values for $E_{\mathrm{a,des}}^{\mathrm{In}}$. For $(In_xGa_{1-x})_2O_3$ growth, a potential explanation for the increasing $E_{\mathrm{a,des}}^{\mathrm{In}}$ with increasing X is that the bond strength between In–In adatoms increases due to a decrease in separation length between them (i.e.,

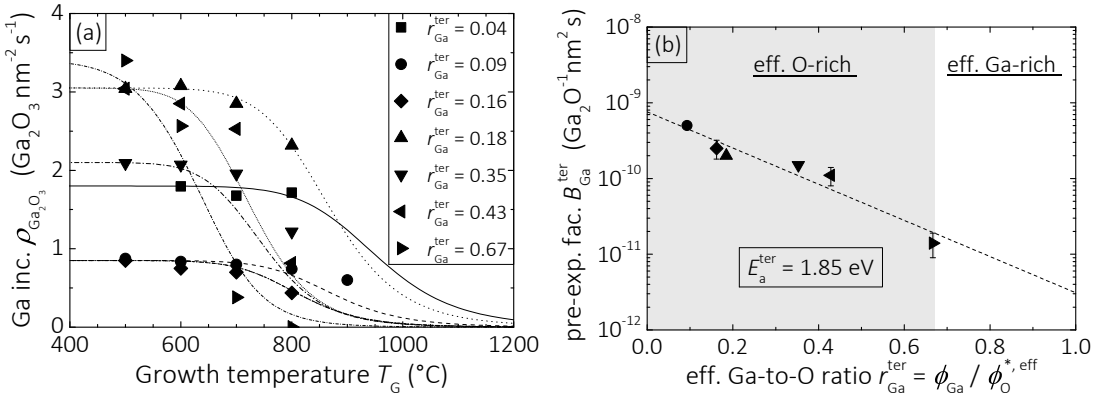

Figure 6.7.: (a) Pseudo-binary growth rate of Ga_2O_3($\rho_{Ga_2O_3}$) as function of growth temperature T_G for different effective Ga-to-O ratios r^{ter}_{Ga}. The lines are model predictions according to Eq. (5.65). No error bars are shown for the sake of clarity. (b) Obtained pre-exponential factor B^{ter}_{Ga} as a function of r^{ter}_{Ga} by fitting the data plotted in (a) with constant total energy of activation E^{ter}_a. The symbols for B^{ter}_{Ga} correspond to the symbols of the fitted data-set in (a). The line is an exponential fit corresponding to Eq. (5.73). The set ϕ_{Ga} and $\phi^{*,eff}_O$ are collected in Tab. 6.1.

increasing In surface coverage), thus, $E^{In}_{a,des}$ increases. The observation that the activation energy for Me desorption changes with Me flux concentration has already been reported in literature for Ga desorption from a GaN growth surface [52], for instance. Here, a similar effect was measured by investigating the Ga desorption kinetics on a GaN(0001) growth surface during MBE. The activation energy for Ga desorption increases with increasing Ga-to-N flux ratio (i.e. Ga surface coverage) since the in-plane separation between Ga–Ga adatoms decreases. This, in turn, leads to an increase of the cohesive energy between the Ga–Ga adatoms based on the Madelung model [52]. For a highly Ga-rich surface with Ga surface coverage of 100 % the activation energy of Ga desorption equals the cohesive energy of Ga desorbing from a Ga reservoir (which is 2.71 eV [3]).

A modified explanation might be applied for $(In_xGa_{1-x})_2O_3$ growth. Here, the cohesive energy between In–In adatoms may also change and increase with increasing In surface coverage. But, the maximum cohesive energy for In–In adatoms, i.e, the energy required to remove one In atom from an In reservoir is 2.4 eV [3]. The result of the model gives $E^{In}_{a,des}$ which is larger than the literature value for $X > 0.375$, i.e. $E^{In}_{a,des}(X > 0.375) > 2.4$ eV. That means, in turn, that the obtained activation energy for In desorption from an $(In_xGa_{1-x})_2O_3$ growth surface cannot only be explained by the cohesive energy between In adatoms. Another energy added to the cohesive energy contributing to $E^{In}_{a,des}$ might be the adhesion energy between In adatoms and the $(In_xGa_{1-x})_2O_3$ growth surface. This idea is supported by the QMS data shown in Fig. 6.4 and comparing the In signal shown in regimes (i), (ii), and (iii). Here, the Al_2O_3, Ga_2O_3, and In_2O_3 surfaces cause a different In desorption rate. The vapor pressure caused by the respective surface depends on the adhesion (or cohesive energy) between In adatoms and the surface. The specific adhesion energy between In adatoms and the $(In_xGa_{1-x})_2O_3$ surface (a mixture of $(In_xGa_{1-x})_2O_3$, Ga_2O_3, and In_2O_3 crystallites) might explain the higher $E^{In}_{a,des}$ obtained by the model than the cohesive energy between In–In adatoms given in literature above a critical $X > 0.375$.

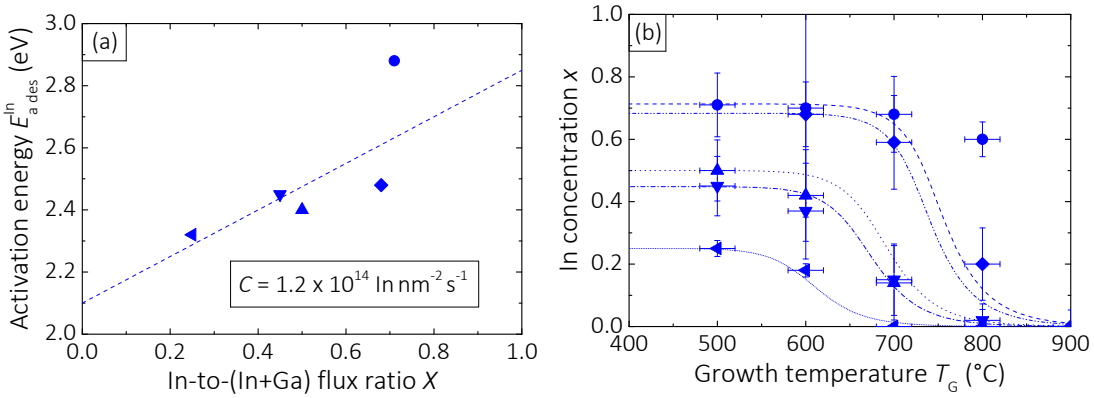

Figure 6.8.: (a) Activation energy of In desorption from the $(In_xGa_{1-x})_2O_3$ growth surface $E^{In}_{a,des}$ as a function of the nominal In-to-(In+Ga) flux ratio X obtained by fitting the data plotted in (b) with Eq. (6.15). (b) Lines are model predictions of In layer concentration x as a function of T_G according to Eqs. (6.15) and (6.20) based on the functional dependence of $E^{In}_{a,des}$ on X depicted in (a). Measured data are shown for comparison. Growth conditions are given in Tab. 6.1. Data symbols in (a) correspond to the symbols of the fitted data-set in (b).

6.3.1. Model absolute Me incorporation

Using the solution of the model for x, Eq. (6.15), its obtained parameters given in Eq. (6.20), $\phi^{des}_{Ga_2O}$ predicted by the binary growth model Eq. (5.66), and its parameters given in Eq. (6.19), $\rho_{In_2O_3}$ can be predicted by the expression:

$$\rho_{In_2O_3} = \frac{x}{(1-x)}\,\rho_{Ga_2O_3} = \frac{x}{(1-x)}\left(\frac{\phi_{Ga}}{2} - \phi^{des}_{Ga_2O}\right) \quad . \tag{6.21}$$

The predictions of $\rho_{In_2O_3}$ are drawn as lines in Fig. 6.3 (a).

Now, the total growth rate of $(In_xGa_{1-x})_2O_3$ in particle fluxes γ_{InGaO} can also be predicted by summing Eqs. (6.21) for $\rho_{In_2O_3}$ and (5.65) for $\rho_{Ga_2O_3}$, i.e.,

$$\gamma_{InGaO} = \rho_{In_2O_3} + \rho_{Ga_2O_3} \; . \tag{6.22}$$

The model predictions are depicted as lines in Fig. 6.9 and are in good agreement with the measured data.

By Eqs. (5.65), (6.15), (6.21) and obtained ternary model parameters, Eqs. (6.19) and (6.20), `all` Me incorporation rates and desorption rates, as a function of T_G for all Me-to-O and In-to-(In+Ga) flux ratios, during $(In_xGa_{1-x})_2O_3$ MBE can be predicted.

The benefit of this model is that the macroscopic In and Ga incorporation into $(In_xGa_{1-x})_2O_3$ can be systematically controlled and changed. In addition, it predicts growth conditions where In incorporation is still feasible. This, in turn, may lead to the growth of high-quality $(In_xGa_{1-x})_2O_3$ layers with desired x enabling systematic band gap engineering of this material, for instance.

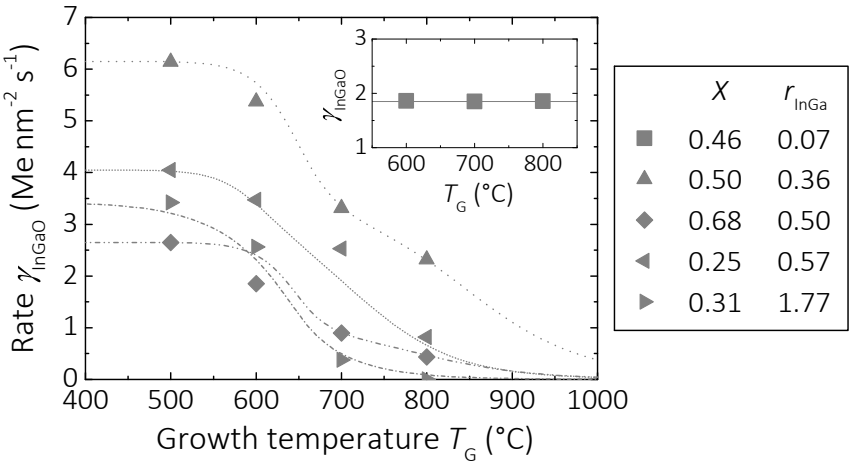

Figure 6.9.: Model predictions of the total growth rate γ_{InGaO} of $(In_xGa_{1-x})_2O_3$ as a function of growth temperature T_G according to Eq. (6.22). No error bars are shown for the sake of clarity.

6.4. Summary

This chapter presented a systematic study of the macroscopic In and Ga incorporation rates during $(In_xGa_{1-x})_2O_3$ MBE. It was found, that the macroscopic In (and Ga) concentration x (and $(1-x)$) neither depends on the crystal structure of the layer nor on the substrate on which the layers are grown.

In section 6.1, the total growth rate Γ_{InGaO} (obtained `in-situ` by laser reflectometry) as a function of growth temperature T_G, for different nominal In-to-(In+Ga) flux ratios X and (In+Ga)-to-O flux ratios r_{InGa} was presented. Pseudo-binary growth rates of In_2O_3 ($\rho_{In_2O_3}$) and Ga_2O_3 ($\rho_{Ga_2O_3}$) were extracted by measuring x in the $(In_xGa_{1-x})_2O_3$ layers `ex-situ` using EDX. Comparing $\rho_{In_2O_3}$, $\rho_{Ga_2O_3}$, $\gamma_{In_2O_3}$ (binary In_2O_3 growth rate), and $\gamma_{Ga_2O_3}$ (binary Ga_2O_3 growth rate) reveals that the kinetics of ternary grown Ga_2O_3 is qualitatively the same as the one for binary grown Ga_2O_3. In contrast, ternary In_2O_3 formation is strongly reduced as compared to binary In_2O_3 formation. However, it was demonstrated that the In and Ga incorporation into $(In_xGa_{1-x})_2O_3$ can be kinetically controlled by the supplied O flux.

Decompositions experiments and thermochemical calculations were performed which reveal that the Ga–O bonds in $(In_xGa_{1-x})_2O_3$ are stronger than the In–O bonds. This finding explains the difference in reaction kinetics and thermodynamics between binary and ternary grown Ga_2O_3 and In_2O_3, resulting that the Ga incorporation is thermodynamically favored over that of In. It was found that Ga exchanges In in In_2O_3 and/or decomposes In_2O_3 into Ga_2O and In. The Ga incorporation likely remains kinetically limited by Ga_2O desorption whereas In incorporation is thermodynamically suppressed by Ga and desorbs off at elevated T_G.

In section 6.2, a new catalytic effect of In on the formation of Ga_2O_3 is presented. This effect is a combination of the kinetic preference of In to be oxidized, its higher oxidation efficiency compared to Ga, and the thermodynamically preferred exchange of In in the

In–O bonds by Ga leading to a strong increase of Ga incorporation. Furthermore, this effect enables the growth of Ga_2O_3 at much higher T_G and ϕ_{Ga} as compared to Ga_2O_3 grown without In. The enhanced Ga incorporation is associated with the total suppression of In incorporation in the highly Me-rich regime.

In summary, In acts as a `surfactant-catalyst` on the formation of Ga_2O_3.

Based on the findings presented in sections 6.1 and 6.2, in section 6.3, a kinetic macroscopic ternary growth model for $(In_xGa_{1-x})_2O_3$ MBE is developed. By means of this model x, $\rho_{In_2O_3}$, $\rho_{Ga_2O_3}$, and total $(In_xGa_{1-x})_2O_3$ growth rate γ_{InGaO} can be predicted for all MBE growth conditions. This model may serve as a guidance in order to engineer the band gap of $(In_xGa_{1-x})_2O_3$, for example, which is expected to depend on x.

The findings in this chapter can describe the results published for (i) $(Al_xGa_{1-x})_2O_3$ MBE [91], (ii) $(In_xGa_{1-x})_2O_3$ PLD [131], and (iii) $(In_xGa_{1-x})_2O_3$ MOVPE [8]:

(i) The kinetics and thermodynamics found for $(In_xGa_{1-x})_2O_3$ MBE can be transferred to other ternary oxide systems which binary compounds posses suboxides. For example, for monoclinic $(Al_xGa_{1-x})_2O_3/Ga_2O_3(010)$ grown by MBE, Oshima *et al.* have observed by pulsed laser atom probe tomography that the average Al concentrations in the $(Al_xGa_{1-x})_2O_3$ layers are significantly higher than those expected from the nominal Al-to-(Al+Ga) flux ratios [91]. Here, the decreased Ga incorporation was attributed to the low incorporation efficiency of Ga because of the formation of Ga_2O. Based on the findings in this chapter, another explanation is suggested: Al inhibits the Ga incorporation — analogous to Ga that inhibits In incorporation into $(In_xGa_{1-x})_2O_3$. This is because the Al–O bonds are stronger than the Ga–O bonds as measured by their bond dissociation energy [31]. Therefore, it is proposed that Al incorporation is thermodynamically favored over Ga incorporation leading to the significantly higher measured Al concentration in the $(Al_xGa_{1-x})_2O_3$ layers as published in Ref. [91].

(ii) Kranert *et al.* [68], Wenckstern *et al.* [131], and (iii) Baldini *et al.* [8] have found that the In incorporation during $(In_xGa_{1-x})_2O_3$ PLD and MOVPE, respectively, is increased at higher O pressures as compared to lower O pressures in the growth chamber. This is the same behavior as observed for $(In_xGa_{1-x})_2O_3$ MBE. That means, the kinetics and thermodynamics during $(In_xGa_{1-x})_2O_3$ PLD and MOVPE can be qualitatively described by the findings presented in this chapter.

7. Phase formation during $(In_xGa_{1-x})_2O_3$ MBE

This chapter briefly presents studies about crystal phases and surface morphologies of $(In_xGa_{1-x})_2O_3$ as well as a method to determine the `microscopic` In incorporation χ into different $(In_\chi Ga_{1-\chi})_2O_3$ structures.

A large number of $(In_xGa_{1-x})_2O_3$ films were simultaneously grown under identical growth conditions on Al_2O_3((0001),(11$\bar{2}$0),(10$\bar{1}$2)) and YSZ((111),(001)). In the framework of this research, Anjeya Verma carried out his masters thesis in which parts of the structural and electrical data obtained by post-growth XRD, AFM, I-V, and C-V measurements are presented [121]. In the present chapter, reference examples grown on Al_2O_3(0001) are shown.

Section 7.1 introduces a first macroscopic approach to determine χ in possible $(In_\chi Ga_{1-\chi})_2O_3$ phases by a combination of `Bragg's law` [25] (assuming full layer relaxation) and Vegard's law [120] (assuming linear dependence of the lattice parameter on the Me concentration).

Section 7.2 presents studies on the crystal phases occurring during $(In_xGa_{1-x})_2O_3$ MBE at different growth temperatures T_G, effective O fluxes $\phi_O^{*,eff}$, and nominal In-to-(In+Ga) flux ratios X. The microscopic In concentration χ is determined by analyzing the out-of-plane diffraction peak position obtained by ω-2θ XRD wide-range scans and using Eq. (7.5), derived in section 7.1.

Section 7.3 presents crystal data on the metastable hexagonal ε-Ga_2O_3(0001) phase. The occurrence of the ε-phase is a consequence of the `catalytic-surfactant` of In on the formation of Ga_2O_3 (as presented in chapter 6).

Shannon and Prewitt [106] have found that $(In_\chi Ga_{1-\chi})_2O_3$ may condense into a monoclinic (space-group: C2/m, lattice parameters: $a = 12.84$ Å, $b = 3.20$ Å, $c = 5.97$ Å, $\beta = 102.4°$) and hexagonal (space-group: P3$_6$/mmc, lattice parameters: $a = b = 3.31$ Å, $c = 12.04$ Å) phase with $\chi = 0.5$. Theoretical reports have predicted the miscibility of In_2O_3 and Ga_2O_3 [76–78, 94]. Peelaers *et al.* predicted a solubility limit of In in β-Ga_2O_3 of 50 %. For an In content larger than 50 % the bixbiyte In_2O_3 phase shall become thermodynamically more stable [94]. A low In solubility in monoclinic $(In_xGa_{1-x})_2O_3$, a low Ga solubility in bixbyite $(In_xGa_{1-x})_2O_3$, and a 50 : 50 mixture of In and Ga in the hexagonal $(In_xGa_{1-x})_2O_3$ phase have been predicted by Maccioni *et al.* [76].

7.1. Indium incorporation χ into $(In_\chi Ga_{1-\chi})_2O_3$

The microscopic In incorporation χ into $(In_\chi Ga_{1-\chi})_2O_3$ can be determined by the peak shift of the diffraction angle θ using a combination of `Bragg's law` [25] and `Vegard's law` [120].

The Bragg equation for any Bravais lattice and lattice spacing reads as

$$a_{(hkl)} = n \left(\frac{\lambda_{\text{X-ray}}}{2} \right) \sin^{-1}(\theta) \ , \tag{7.1}$$

with $a_{(hkl)}$ the lattice spacing between two diffracting lattice planes for a given (hkl)-growth direction, diffraction order n, diffraction angle θ (angle between lattice plane and incident X-ray beam), and wavelength of the used X-rays, $\lambda_{\text{X-ray}}$. For a cubic and monoclinic crystal $a_{(hkl)}$ can be determined as [70]

$$a_{(hkl)} = a \left(h^2 + k^2 + l^2 \right)^{-\frac{1}{2}} \tag{7.2}$$

and

$$a_{(hkl)} = \sin(\beta) \left(\left(\frac{h}{a} \right)^2 + \left(\frac{k \sin(\beta)}{b} \right)^2 + \left(\frac{l}{c} \right)^2 + \left(\frac{2\,h\,l \cos(\beta)}{a\,c} \right) \right)^{-\frac{1}{2}} \ , \tag{7.3}$$

respectively. With a, b, and c, the lattice parameters of the respective unit cell, and β the angle between the (100) and (001) lattice planes of the monoclinic unit cell.

The lattice parameter a_i for a ternary crystal with specific atomic concentration can be determined by Vegard's law [120] as

$$a_i = \chi\, a_j + (1 - \chi)\, a_k \quad , \tag{7.4}$$

with a_j and a_k the lattice constants of the respective binary crystals. The linear dependence of a_i on χ is due to the different sizes of the atoms the alloy consists of. Rearranging Eq. (7.4) with respect to χ, inserting Eq. (7.1) for a_i, a_j, a_k, and transforming gives

$$\boxed{\chi = \left(\frac{n_i - n_k \sin(\theta_i) \sin^{-1}(\theta_k)}{n_j - n_k \sin(\theta_j) \sin^{-1}(\theta_k)} \right) \left(\frac{\sin(\theta_j)}{\sin(\theta_i)} \right)} \quad . \tag{7.5}$$

At same diffraction orders, i.e. $n_i = n_j = n_k$, the latter equation simplifies. In this case it allows a direct calculation of χ in the respective ternary crystal only by measuring the out-of-plane growth directions (i.e., the diffraction angles $\theta_{i,j,k}$) of the alloy and the binary compounds. The diffraction angles of the binary compounds θ_j and θ_k can be (usually) taken from crystal data bases or determined experimentally. By means of Eq. (7.5), χ in possible $(In_\chi Ga_{1-\chi})_2O_3$ phases as plotted in Figs. 7.2 and 7.3 is determined.

For all ω-2θ scans presented, an area of the sample of $A_{\text{X-ray}} \sim 10\,\text{mm}^2$ is scanned. That means all crystallites in a volume of $V_{\text{X-ray}} = A_{\text{X-ray}} \times d$ (with layer thickness d) contribute to the detected X-ray signal. The error of χ is obtained by fitting the measured diffraction peak by Gaussian distribution $\mathcal{G}$,

$$\mathcal{G}(\theta) = \frac{\mathcal{A}}{\sigma\sqrt{2\pi}} \exp\left(-\frac{(\theta - \theta_0)^2}{2\sigma^2} \right) \ , \tag{7.6}$$

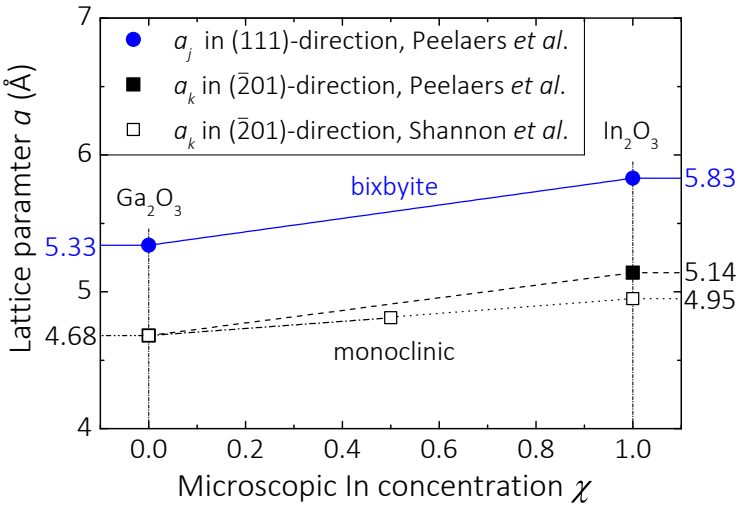

Figure 7.1.: Lattice parameters for cubic $a_{(111)}$ and monoclinic $a_{(\bar{2}01)}$ Ga_2O_3 as well as In_2O_3 as a function of the In content χ. Solid and dashed lines are linear interpolations of $a_{(111)}$ and $a_{(\bar{2}01)}$ according to Peelaers *et al.* [94]. Dashed-dotted line is a linear interpolation between $a_{(\bar{2}01)}$ for pure Ga_2O_3 obtained by the ω-2θ scan as plotted in Fig. 7.2 (a) and the literature value for monoclinic $InGaO_3(\bar{2}01)_m$ according to Shannon and Prewitt [106]. The dotted line is a linear extrapolation according to the measured and published data.

with amplitude $\mathcal{A}$, mean value θ_0 (i.e., maximum X-ray intensity at given diffraction peak), and standard deviation σ. The standard deviation at given growth conditions, i.e. the full-width-at-half-maximum (FWHM) of the measured peak, due to occurring point, line or planar defects as well as from the experimental set-up is obtained by fitting the binary In_2O_3 and Ga_2O_3 peaks serving as a reference for the analysis of the cubic and monoclinic $(In_\chi Ga_{1-\chi})_2O_3$ phases.

The lattice parameter for bixbyite In_2O_3 is $a_j = 10.11\,\text{Å}$ [79] with $j = In_2O_3(100)_c$. Bixbyite Ga_2O_3 has not been synthesized yet, and so, a theoretical prediction of hypothetical bixbyite Ga_2O_3 is used [94]. The lattice parameter for (predicted) bixbyite Ga_2O_3 is $a_k = 9.38\,\text{Å}$ with $k = Ga_2O_3(100)_c$. The same procedure can be applied for the peak shift caused by In incorporation into monoclinic Ga_2O_3. Figure 7.1 plots the evolution of the bixbyite (balls) and monoclinic (squares) lattice parameters for Ga_2O_3 and In_2O_3 on the In content χ. Two evolutions of the monoclinic parameters are shown. One obtained by Peelaers *et al.* [94] assuming a pseudo-cubic lattice constant for the monoclinic phase and one obtained by the crystal data published by Shannon and Prewitt [106]. Both evolutions can be used to determine the In incorporation into the monoclinic $(In_\chi Ga_{1-\chi})_2O_3$ phase.

7.2. $(In_xGa_{1-x})_2O_3$ growth in the O-rich regime

Net O flux $\Phi_{O_2}(P_{rf} = 300\,W) = 3.0\,SCCM$

Figures 7.2 (a)–(e) show ω-2θ XRD wide-range scans of the films grown at $\Phi_{O_2}(P_{rf} = 300\,W) = 3.0\,SCCM$. At this Φ_{O_2}, x remains constant and equals the nominal flux concentration, i.e $X = x$, at least up to $T_G = 800\,°C$ (chapter 6). The total growth rate,

Figures	ϕ_{In} $\left(\frac{In}{nm^2\,s}\right)$	ϕ_{Ga} $\left(\frac{Ga}{nm^2\,s}\right)$	$\phi_O^{*,eff}$ $\left(\frac{O}{nm^2\,s}\right)$	X
7.2 (a)	0	3.8	29.4	0
7.2 (b)	0.6	3.0	37.8	0.17
7.2 (c)	2.1	1.6	57.9	0.55
7.2 (d)	2.4	1.2	62.9	0.67
7.2 (e)	3.4	0	79.5	1.00
7.3 $(a)_1$–$(a)_4$	4.3	1.8	18.8	0.71

Table 7.1.: Set In (ϕ_{In}) and Ga fluxes (ϕ_{Ga}) with resulting nominal In-to-(In+Ga) flux ratio X as well as the effective active O flux $\phi_O^{*,eff}$ for the structural data plotted in Figs. 7.2 (a)–(e) and 7.3 $(a)_1$–$(a)_4$.

i.e. the sum of In and Ga flux, for all data shown in this figure was $\Gamma \approx 1.0\,\text{Å}\,s^{-1}$. The set T_G, ϕ_{In}, ϕ_{Ga}, and resulting $\phi_O^{*,eff}$ for the data shown in Figs. 7.2 (a)–(e) are collected in Tab. 7.1. Data in order to identify the diffraction peaks of Ga_2O_3, In_2O_3, and hexagonal $(In_\chi Ga_{1-\chi})_2O_3$ were taken from Refs. [44], [20], and [106], respectively. The Me concentration in the cubic and monoclinic $(In_\chi Ga_{1-\chi})_2O_3$ phases are determined by Eq. (7.5).

Figure 7.2 (a) depicts the XRD pattern for pure Ga_2O_3, i.e. $x = 0$. It shows the β-phase in $(\bar{2}01)$-growth direction. (b) Depicts the crystal phases occurring at $x = 0.17$ and three different T_G. At low-$T_G = 600\,°C$ no X-ray signal originating from the layer was measured suggesting that the layer is amorphous or polycrystalline. Increasing T_G up to 800 °C leads to a more crystalline layer by emerging cubic $(In_\chi Ga_{1-\chi})_2O_3(111)_c$ with $\chi = 0.13 \pm 0.05$, hexagonal $InGaO_3(0001)_h$, and monoclinic $(In_\chi Ga_{1-\chi})_2O_3(\bar{2}01)_m$ with $\chi = 0.11 \pm 0.01$ phases. Conversely, the binary β-Ga_2O_3 phase disappeared and all In and Ga supplied is incorporated in one of the $(In_\chi Ga_{1-\chi})_2O_3$ phases. (c) Shows the out-of-plane orientation for $x = 0.55$. The $(In_{0.87}Ga_{0.13})_2O_3(111)_c$ and $InGaO_3(0001)_h$ phases become more pronounced for $T_G > 600\,°C$. At $T_G = 800\,°C$ the Ga content in the cubic phase decreases to 10 %, i.e. $(In_{0.9}Ga_{0.1})_2O_3(111)_c$. (d) Shows the crystal phases at $x = 0.67$. The hexagonal $(In_\chi Ga_{1-\chi})_2O_3$ phase almost completely disappears for all T_G and $(In_{0.87}Ga_{0.13})_2O_3(111)_c$ becomes more pronounced. The monoclinic $(In_\chi Ga_{1-\chi})_2O_3(\bar{4}02)_m$ phase is detected at $2\theta = 37.0\,°$. The diffraction angles for monoclinic In_2O_3 obtained using Peelaers and Shannons approach are $2\theta_j^{Peel} = 34.8\,°$ and $2\theta_j^{Shan} = 36.1\,°$, respectively. Applying Eq. (7.5) gives an In incorporation into monoclinic $(In_\chi Ga_{1-\chi})_2O_3$ of 37 % according to Peelaers and 60 % according to Shannon. Thermodynamic calculations by Peelaers *et al.* [94] suggest an In solubility limit of 50 % in β-Ga_2O_3. For higher In concentrations they found the bixbyite phase to be thermodynamically more stable than the monoclinic one. For this reason, based on the results by Peelaers *et al.*, it is suggested that the In content in the detected monoclinic $(In_\chi Ga_{1-\chi})_2O_3$ phase is $\chi = 0.37 \pm 0.04$. (e) Plots the XRD pattern for binary In_2O_3 with $x = 1.0$ grown in (111) and (001)-direction.

These experiments suggest a maximum Ga incorporation of 13 % in bixbyite $(In_\chi Ga_{1-\chi})_2O_3$. Neither an increase of ϕ_{Ga} nor an increase of T_G lead to a higher Ga concentration. On the other hand, increasing T_G lead to a decrease of Ga concentration in cubic $(In_\chi Ga_{1-\chi})_2O_3$ (highlighted by a circle in the middle panel (c)). This can be seen by a peak shift towards lower θ at higher T_G.

Net O flux $\Phi_{O_2}(P_{rf} = 300\,W) = 1.0\,SCCM$

Figure 7.3 shows the crystal phases occurred during $(In_xGa_{1-x})_2O_3$ growth on $Al_2O_3(0001)$ at a lower O flux of $\Phi_{O_2}(P_{rf} = 300\,W) = 1.0\,SCCM$, fixed ϕ_{In}, and ϕ_{Ga} (values given in Tab. 7.1). At identical growth conditions $(In_xGa_{1-x})_2O_3$ was grown on co-loaded $Al_2O_3(10\bar{1}2)$ and YSZ(111) (not shown).

Figures $(a)_1$–$(a)_4$ depict ω-2θ XRD scans at different T_G. Comparing the diffraction pattern in $(a)_3$ with the one shown in Fig. 7.2 (d) at similar $x = 0.67$ reveals more crystalline phases and higher crystallinity at lower O flux even at lower T_G. At $T_G = 500\,°C$ cubic $(In_{0.87}Ga_{0.13})_2O_3((111)_c,(001)_c)$ with maximum Ga concentration is measured. Only a small shoulder of the hexagonal $InGaO_3(0001)_h$ phase is detected. With increasing T_G $(In_xGa_{1-x})_2O_3$ becomes more crystalline and has the highest crystallinity at $T_G = 800\,°C$. For $T_G \geq 600\,°C$ $(In_\chi Ga_{1-\chi})_2O_3(001)_c$ phase becomes more apparent with $\chi < 0.13$ and decreasing with T_G. The hexagonal $InGaO_3((0001)_h,(01\bar{1}1)_h)$ phase becomes more pronounced. The same effect was measured in Fig. 7.2 where the hexagonal $(In_\chi Ga_{1-\chi})_2O_3$ phase was strongest at $x = 0.55$ and the cubic phase decreased as indicated by a circle. At $T_G = 700\,°C$ a small shoulder of $(In_{0.37}Ga_{0.63})_2O_3(\bar{4}02)_m$ appears.

Figures $(b)_1$–$(b)_4$ show the surface morphology of the same layers measured by SEM. The higher their crystallinity the rougher their surface. At $T_G = 800\,°C$ (graph b_4) large triangle-shaped cubic $(In_\chi Ga_{1-\chi})_2O_3(111)_c$ with $\chi = 0.95 \pm 0.02$ (framed by a dashed line) and hexagon-shaped $InGaO_3(0001)_h$ crystallites (framed by a dotted line) are formed. The increase in χ from 0.87 to 0.95, i.e. decreasing Ga concentration in the cubic $(In_\chi Ga_{1-\chi})_2O_3$ phase can be seen, e.g., in the shift of the $(222)_c$-peak towards lower 2θ between $T_G = 500\,°C$ ('high' $2\theta = 30.9\,°$) and $T_G = 800\,°C$ ('low' $2\theta = 30.7\,°$).

The root mean square (rms) of the surface roughness was measured by AFM and increases exponentially with T_G as plotted in (c). The strong increase in surface roughness might be due to the higher mobility of the adatoms at higher T_G allowing the adatoms to diffuse to their thermodynamically favored ground state, i.e., either the cubic or hexagonal $(In_\chi Ga_{1-\chi})_2O_3$ crystallite. Depending on the growth mode this leads to a lateral and vertical growth of the formed islands (island growth) resulting in a higher rms at higher T_G.

Due to the low $\phi_O^{*,eff} = 1.0\,SCCM$, x decreases with increasing T_G as plotted as blue balls in Fig. 7.3 (d). The dotted blue line is its model prediction according to Eq. (6.15). Only at $T_G = 500\,°C$, $X = x$. The total growth rate γ_{InGaO} also decreases with increasing T_G as plotted as gray open discs. Its model prediction according Eq. (6.22) is drawn as gray dashed line. In Fig. 7.3 (d) the model predictions of x and γ_{InGaO} underestimate the In content at $T_G = 800\,°C$. This outlier may originate from an unknown experimental error, e.g., that T_G was lower than expected due to a poor heat contact between the Si carrier wafer and the $Al_2O_3(0001)$ substrate or due to non-uniform heat distribution on the growth surface.

Comparing the data shown in Figs. 7.2 and 7.3 reveals that a higher O flux leads to a higher or constant macroscopic In and Ga concentration (chapter 6) but to a lower crystallinity. The results for the maximum Ga and In incorporation into cubic and monoclinic $(In_\chi Ga_{1-\chi})_2O_3$ of 0.13 ± 0.05 and 0.37 ± 0.04, respectively, are in fair agreement with

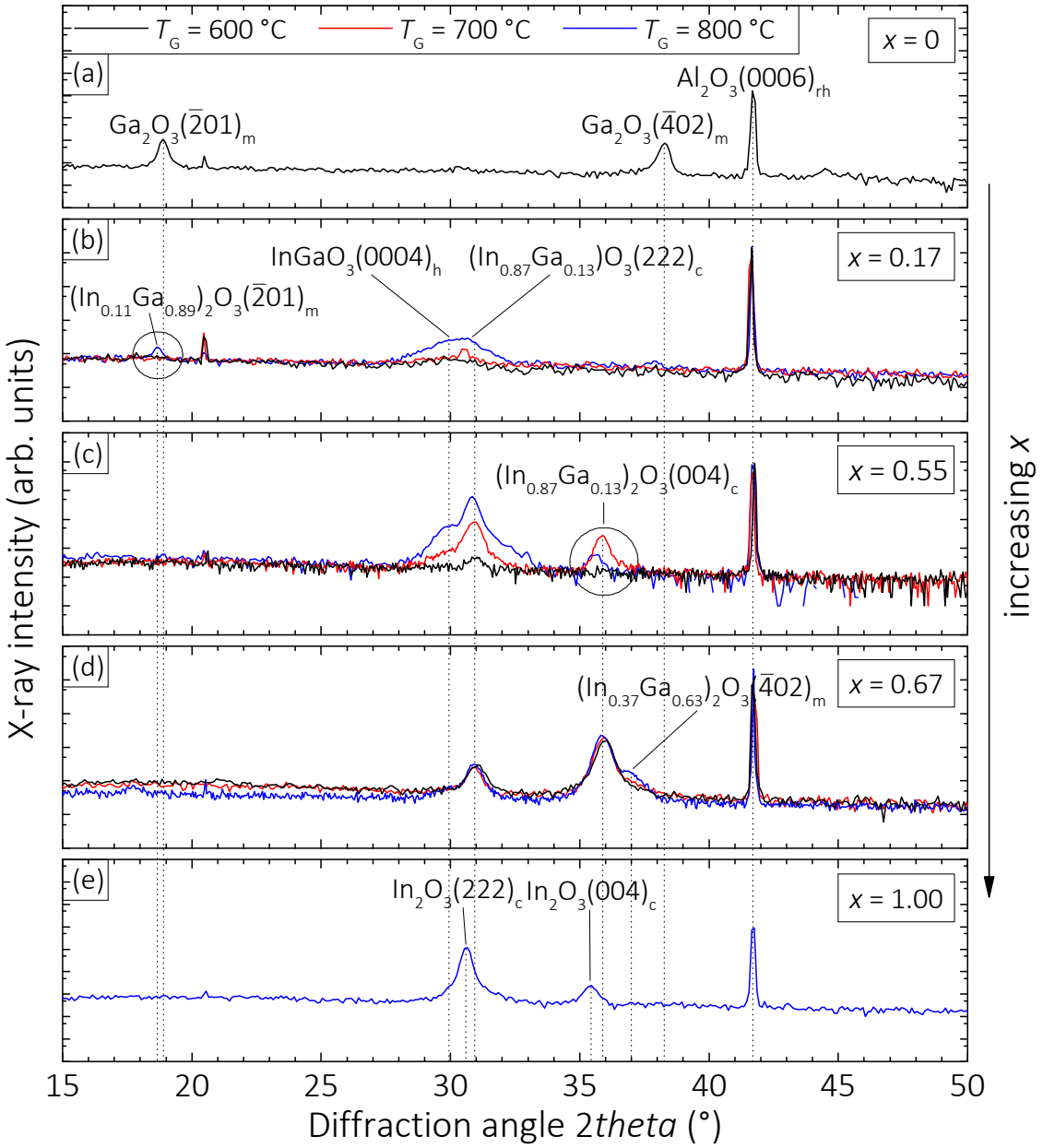

Figure 7.2.: X-ray diffraction pattern obtained by ω-2θ scans as a function of the diffraction angle 2θ for $(In_xGa_{1-x})_2O_3$ grown on $Al_2O_3(0001)$. (a) Shows pure Ga_2O_3 with $x = 0$. Middle panels (b), (c), and (d) depict $(In_xGa_{1-x})_2O_3$ phases occurring at $x = 0.17$, 0.55, and 0.67, respectively. (e) Depicts In_2O_3 phases with $x = 1.0$. Five crystal structures could be identified: (i) monoclinic Ga_2O_3, (ii) bixbyite In_2O_3, (iii) bixbyite $(In_\chi Ga_{1-\chi})_2O_3$, (iv) hexagonal $(In_\chi Ga_{1-\chi})_2O_3$, and (v) monoclinic $(In_\chi Ga_{1-\chi})_2O_3$. The subscripts written at the parentheses 'm', 'c', 'h' refer to the monoclinic, bixbyite (i.e. cubic), and hexagonal crystal structure, respectively.

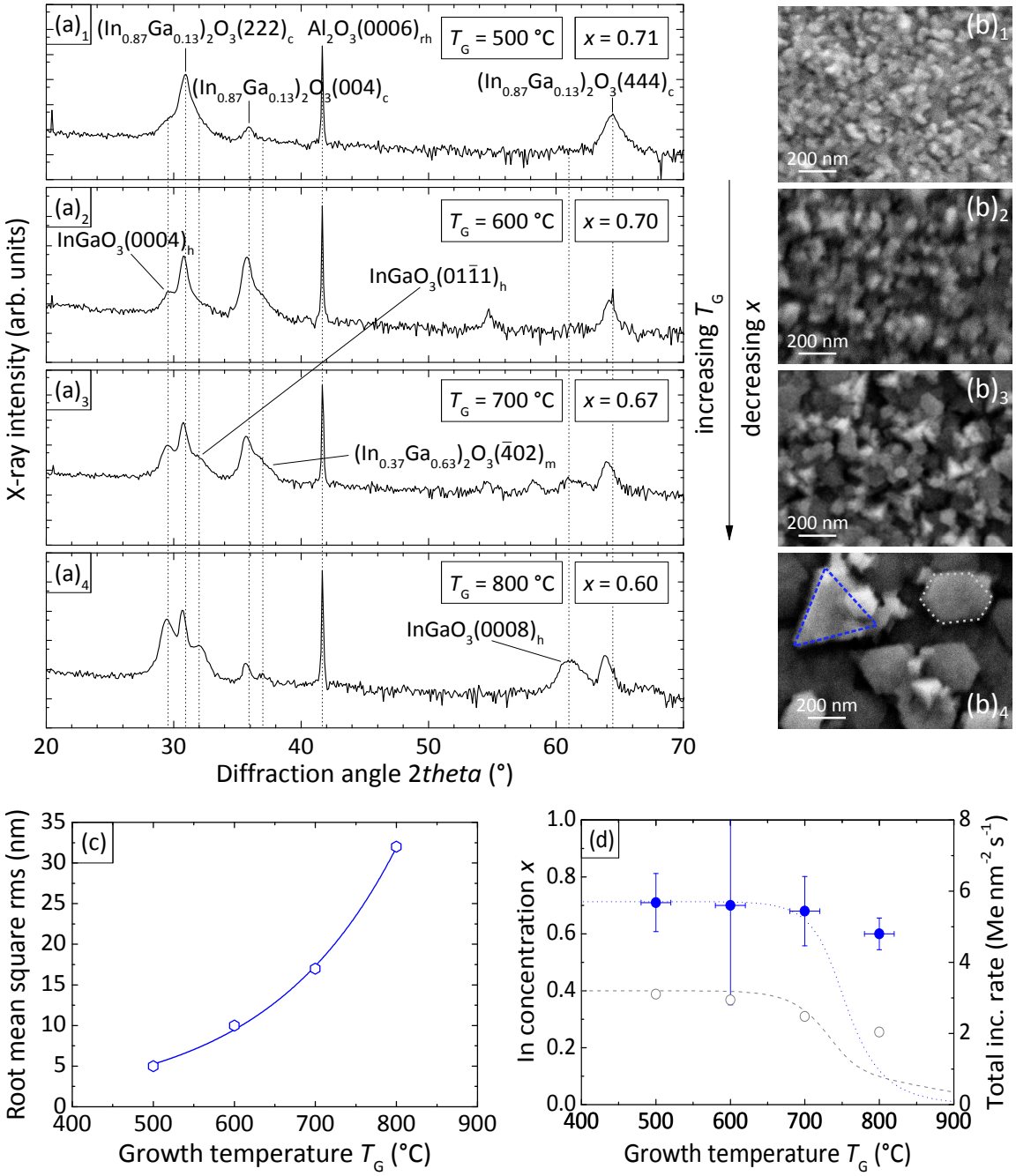

Figure 7.3.: (a) X-ray intensity as a function of the diffraction angle 2θ of $(In_xGa_{1-x})_2O_3/Al_2O_3(0001)$ measured by ω-2θ scans. (b) Surface morphology measured by SEM of the same layers as depicted in (a), i.e., $(b)_i$ corresponds to $(a)_i$. The lower panel $(b)_4$ shows a triangle-shaped crystallite of $(In_{0.95}Ga_{0.05})_2O_3(111)_c$ and a hexagon-shaped $InGaO_3(001)_h$ crystallite, which are indicated as blue dashed and gray dotted lines, respectively.. (c) Root mean square (rms) of the same layers as a function of T_G obtained by AFM measurements (morphologies obtained by AFM not shown). The line is a guide to the eye. (d) Macroscopic In concentration x and total Me incorporation rate γ as a function of T_G of the same layers. The dotted blue and dashed gray lines are model predictions according to Eqs. (6.15) and (6.22), respectively.

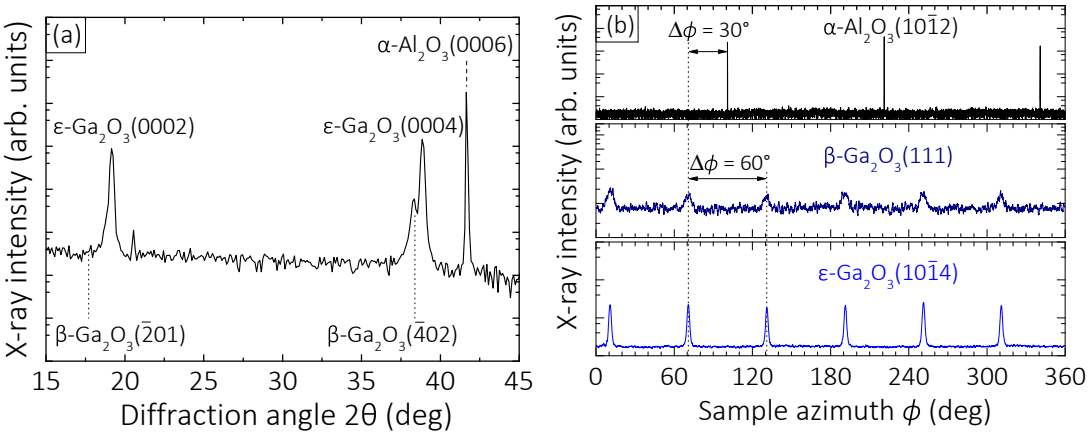

Figure 7.4.: (a) X-ray intensity as a function of the diffraction angle 2θ obtained by a ω-2θ scan showing phase-pure ε-$Ga_2O_3(0001)$/β-$Ga_2O_3(\bar{2}01)$/$Al_2O_3(0001)$. (b) X-ray intensity as function of the sample azimuth ϕ of the asymmetric $(10\bar{1}2)$-peak of the substrate, (111)-peak of the β-Ga_2O_3 nucleation layer, and $(10\bar{1}4)$-peak of the ε-Ga_2O_3 film. Same sample as depicted in Fig. 6.6 (a), chapter 6, with growth parameters $T_G = 650\,°C$, $\phi_{Ga} = 6.8\,Ga\,nm^{-2}\,s^{-1}$, $\phi_{In} = 6.1\,In\,nm^{-2}\,s^{-1}$, $\Phi_{O_2}(P_{rf} = 300\,W) = 0.75\,SCCM$, and a low-$T_G$ β-$Ga_2O_3(\bar{2}01)$ nucleation layer.

powder samples prepared under equilibrium conditions by Edwards *et al.* [36]. Kranert *et al.* reported an In solubility in β-$Ga_2O_3(\bar{2}01)$ grown by PLD of $\sim 40\,\%$ [68]; similar to the In solubility in monoclinic $(In_\chi Ga_{1-\chi})_2O_3$ grown by MBE described in this section.

7.3. Indium — a surfactant for ε-Ga_2O_3 formation

As a consequence of the catalytic effect of In on the formation of Ga_2O_3 (chapter 6), it also serves as `surfactant` on the crystal quality and phase of Ga_2O_3.

Figures 7.4 (a) and (b) show the out-of-plane and in-plane epitaxial relationship of ε-Ga_2O_3/β-Ga_2O_3/α-Al_2O_3 as

$$\varepsilon\text{-}Ga_2O_3(0001)\,||\,\beta\text{-}Ga_2O_3(\bar{2}01)\,||\,\alpha\text{-}Al_2O_3(0001) \quad \text{and} \tag{7.7}$$

$$\varepsilon\text{-}Ga_2O_3(\bar{1}100)\,||\,\beta\text{-}Ga_2O_3(010)\,||\,\alpha\text{-}Al_2O_3(\bar{1}210) \quad , \tag{7.8}$$

respectively. The ε-Ga_2O_3 reflexes were chosen and analyzed based on the structural model proposed by Mezzadri *et al.* as given in the supplement of Ref. [82].

Figure 7.5 (a) plots the full-widths-at-half-maximum (FWHM) of the on-axis ((0001)-direction) and off-axis ((10$\bar{1}$4)-direction) rocking curves (RCs) $\omega^{FWHM}_{(0004)} = 0.24\,°$ and $\omega^{FWHM}_{(10\bar{1}4)} = 0.97\,°$, respectively. The crystal quality in growth direction of heteroepitaxially grown ε-$Ga_2O_3(0001)$ (this work) is comparable to homoepitaxially grown ε-$Ga_2O_3(0001)$ by means of HVPE with $\omega^{FWHM}_{(0004)} = 0.21\,°$ (Ref. [92]). No studies on the crystal quality and morphology of ε-$Ga_2O_3(0001)$ grown by MBE are reported in literature. The crystal quality in in-plane direction of $\omega^{FWHM}_{(10\bar{1}4)} = 0.97\,°$ is poorer, than the one in out-of-plane direction, but still comparable with homoepitaxially grown ε-Ga_2O_3 by HVPE with $\omega^{FWHM}_{(10\bar{1}1)} = 0.87\,°$ [92]. The poor in-plane crystal quality might arise due to the poor crystal quality of the

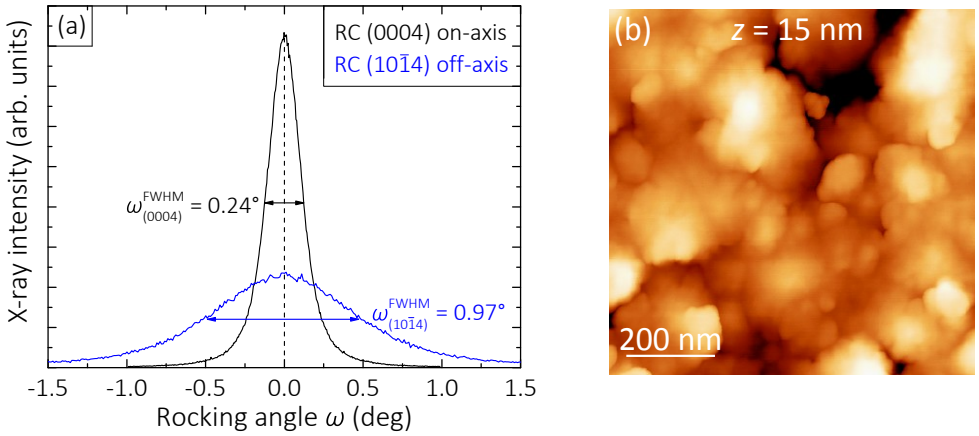

Figure 7.5.: (a) X-ray intensity as a function of the rocking angle ω of ε-Ga_2O_3(0002) and ε-Ga_2O_3(10$\bar{1}$4) measured in symmetric and skew-symmetric geometry, respectively. (b) Surface morphology obtained by AFM of the same layer as depicted in (a) with rms = 3.9 nm.

β-Ga_2O_3($\bar{2}$01) nucleation layer. This can be seen by the surface morphology of this layer obtained by AFM as depicted in Fig. 7.5 (b) with rms = 3.9 nm. This β-Ga_2O_3($\bar{2}$01) nucleation layer may cause the randomly in-plane oriented ε-Ga_2O_3(0001) crystallites resulting in a large in-plane mosaicity (i.e. large $\omega^{\mathrm{FWHM}}_{(10\bar{1}4)}$) and surface roughness (i.e. large rms).

The data presented in Figs. 7.4 and 7.5 show that the presence of In stabilizes the ε-Ga_2O_3(0001) phase with highest crystal quality achieved for heteroepitaxially MBE grown Ga_2O_3/Al_2O_3(0001). The out-of-plane and in-plane crystal quality might be further improved by growing a high crystal quality nucleation layer using In as a surfactant.

The stabilization of the metastable ε-Ga_2O_3 phase by In might be explained by one of the two reasons: (i) In kinetically enables the growth of Ga_2O_3 at high-T_G and high-ϕ_{Ga} where binary Ga_2O_3 MBE growth is not feasible anymore (chapter 6). This high-T_G and high-ϕ_{Ga} migth set growth conditions where the metastable ε-phase becomes thermodynamically stable. (ii) On Al_2O_3(0001) bixbyite In_2O_3 usually grows (phase-pure) in (111)-direction [33, 81, 101]. Due to the exchange reactions occurring, i.e. that Ga exchanges In in In_2O_3 (chapter 6), it might be that condensed In_2O_3 determines the growth direction of Ga_2O_3.

7.4. Summary

This chapter presented crystal phases (measured by post-growth XRD scans) and morphologies (measured by post-growth SEM and AFM) occurring during $(In_xGa_{1-x})_2O_3$ MBE. The surfactant effect of In on the stabilization of hexagonal ε-Ga_2O_3 was introduced.

In section 7.1, a macroscopic method using Bragg's law and Vegard's law to determine the microscopic In incorporation χ into possible $(In_\chi Ga_{1-\chi})_2O_3$ phases was derived. This method allows the calculation of χ only by measuring the peak shift of the out-of-plane

diffraction angle θ obtained by symmetric ω-2θ XRD scans. This peak shift can occur due to different In and Ga concentrations in $(In_\chi Ga_{1-\chi})_2O_3$.

In section 7.2, the XRD pattern for $(In_xGa_{1-x})_2O_3$ layers grown in the excess of O on $Al_2O_3(0001)$ at different T_G were presented, with x ranging from 0 to 1. The method derived in section 7.1 to determine χ was applied to the measured data and χ in possible $(In_\chi Ga_{1-\chi})_2O_3$ phases extracted. A hexagonal $(In_\chi Ga_{1-\chi})_2O_3$ phase with $\chi = 0.50$ was measured. A maximum In and Ga solubility in monoclinic and cubic $(In_\chi Ga_{1-\chi})_2O_3$ of $\chi = 0.37 \pm 0.04$ and $1 - \chi = 0.13 \pm 0.05$, respectively, is examined. These results are in agreement with theoretical predictions by Peelaers *et al.* [94].

Section 7.3 introduced the surfactant effect of In on the formation of the hexagonal ε-$Ga_2O_3(0001)$, which is a consequence of the catalytic effect of In on the incorporation of Ga (chapter 6). The catalytic-surfactant effect of In on the formation of Ga_2O_3 kinetically sets growth conditions that stabilize the ε-Ga_2O_3 phase. The crystal quality of ε-$Ga_2O_3(0001)$ using In as a surfactant is the highest obtained for heteroepitaxially MBE grown $Ga_2O_3/Al_2O_3(0001)$ thin films.

8. Conclusions

The purpose of this work was to systematically explore the growth of the transparent semiconducting oxides Ga_2O_3, In_2O_3, $(In_xGa_{1-x})_2O_3$, and SnO_2, synthesized by oxygen (O) plasma-assisted molecular beam epitaxy (MBE). This work provides a first, comprehensive understanding of the reaction mechanisms of these materials, and explains them in the framework of kinetic and thermodynamic limitations. Semi-empirical, quantitative growth models for binary and ternary oxide MBE are developed. A new catalytic-surfactant effect for ternary oxide material systems is discovered and explained.

The MBE growth processes were studied with extensive use of `in-situ` characterization: the metal (Me = Ga, In, Sn) incorporation rates γ and decomposition rates are measured `in-situ` by laser reflectometry. The species that are not incorporated during growth are detected `in-situ` by line-of-sight quadrupole mass spectrometry (QMS).

The growth kinetics of the binary oxides shows a linear decrease in γ in the Me-rich growth regime with increasing Me flux ϕ_{Me}. It is known that these oxides posses suboxides, and therefore, the decreasing γ in the Me-rich regime is attributed to the O-deficiency-induced desorption of suboxides. At high growth temperatures T_{G}, a plateau in γ when varying ϕ_{Me} in the O-rich growth regime becomes present. A decreasing γ with increasing T_{G} for all compounds and Me-to-O flux ratios is observed. Decomposition of the oxide layers by their respective Me is demonstrated. The decomposition rate linearly increases with increasing ϕ_{Me} and is almost independent on T_{G}. Combining the growth rate and decomposition rate evolutions, with measured desorption data, it is found that the growth kinetics of the binary oxides is governed by the formation and desorption of suboxides. These suboxides are identified as Ga_2O for Ga_2O_3, In_2O for In_2O_3, and SnO for SnO_2. For all MBE growth conditions used here, `no` Me desorption is detected. The loss in γ is `always` caused by the desorption of suboxides that remove Me and O atoms from the growth surface. Due to the different Me-to-O stoichiometries between Me_2O_3 and SnO_2, combined with their same qualitative growth kinetics, it is proposed that the growth of `all` binary oxides possessing suboxides is determined by the kinetics of their respective suboxide. This is a fundamental difference in reaction kinetics, e.g., as compared to group-III nitride (N) or arsenide (As) semiconductors. Here, γ saturates in the Me-rich regime because of N- or As-deficiency-induced Me droplet formation or Me desorption. These materials do not posses subnitrides or subarsenides.

The quantitative difference in the reaction kinetics of binary oxides is investigated. Analyzing the Me incorporation rates and desorption rates, as well as their equilibrium suboxide vapor pressures p taken from literature, the vapor pressure of SnO on the SnO_2 growth surface is identified to be the lowest whereas the one of Ga_2O on the Ga_2O_3 growth surface is the highest. That means that $p_{\mathrm{Ga_2O}} > p_{\mathrm{In_2O}} > p_{\mathrm{SnO}}$, and defines the quantitative disparity in the reaction kinetics of Ga_2O_3, In_2O_3, and SnO_2. For this reason, SnO_2 has

the widest and Ga_2O_3 the narrowest MBE growth domain. In the case of Ga_2O_3, the MBE growth domain is quantitatively determined by experimental growth rate data. The different oxidation efficiencies of the Me J_O^{Me} are examined, i.e. the fraction of maximum available O adatoms for Me oxidation at given net active O flux. These efficiencies are quantified as $J_O^{Sn} = 0.296 > J_O^{In} = 0.263 > J_O^{Ga} = 0.096$. Their differences are explained in the framework of kinetic effects originating, e.g., from the different symmetries of the ground-state crystal structures of Ga_2O_3 and In_2O_3.

Based on these growth rate studies, the fundamental reaction paths of oxides possessing suboxides are established. Since the loss in γ can always be referred to suboxide desorption it is concluded that, for all growth conditions where oxide layer growth takes place, suboxides are `always` formed. Therefore, a two-step oxidation process is stated: the oxidation of the elemental Me to the suboxide and a further oxidation from suboxide to the solid metal-oxide compound. This two-step oxidation nature is the basis for the development of a general, semi-empirical kinetic growth model for oxide MBE. The derivation of this model is a significant step towards the understanding of the fundamental reaction mechanisms of transparent semiconducting oxides. The practical use of this model is the prediction of growth and desorption rates as a function of T_G, ϕ_{Me}, and O flux. It allows to systematically control the material properties by adjusting the growth parameters prior to growth. For example, the model predicts high-T_G regimes, that are expected to lead to higher crystal qualities of the oxide layers, with reasonable γ. It also predicts the Me-to-O flux regime in which the growth takes place, including, the O-rich and Me-rich growth regimes which are expected to reduce the number of O vacancies and Me vacancies acting as donors or compensating acceptors, respectively.

The growth kinetics and thermodynamics of the ternary oxide $(In_xGa_{1-x})_2O_3$ was systematically studied. The individual In and Ga layer concentrations were measured `ex-situ` by energy dispersive X-ray spectroscopy. As a result, the detected In incorporation is drastically reduced in the presence of Ga, as compared to binary grown In_2O_3 at comparable growth conditions. In contrast, the Ga incorporation is increased in the presence of In, as compared to binary grown Ga_2O_3 at comparable growth conditions. It likely remains kinetically limited by Ga_2O desorption. Decomposition and exchange experiments of Ga_2O_3 and In_2O_3 layers by impinging In and Ga, respectively, revealed that the Ga–O bonds in $(In_xGa_{1-x})_2O_3$ are stronger than the In–O bonds. This difference in the O-bond energies leads to a thermodynamic suppression of In by Ga, and explains the discrepancy between the measured binary and ternary Me incorporation rates into In_2O_3 and Ga_2O_3. Thermochemical calculations have been performed and support this finding. The strength of thermodynamic suppression of In incorporation by Ga can be kinetically controlled by the supplied O flux. In the strong excess of O complete In and Ga incorporation is observed. On the contrary, in the excess of Me (i.e., In + Ga) only Ga incorporation is detected.

In this context, a new catalytic effect of In on the formation of Ga_2O_3 is found. This effect allows the growth of Ga_2O_3 at much higher T_G and higher ϕ_{Ga} than possible without the presence of In. This catalytic effect can be explained by a combination of four other effects found in this thesis. (i) The favorable reaction kinetics of In_2O_3 compared to Ga_2O_3. (ii) The higher oxidation efficiency of In compared to Ga. (iii) The thermodynamically stronger Ga–O bonds than the In–O bonds in $(In_xGa_{1-x})_2O_3$. (iv) The segregation of In on the growth surface (minimizing the surface free energy), and its desorption. An

intuitive explanation of this effect is the following: the In oxidation to In_2O and In_2O_3 remains kinetically favored, also in the case when In, Ga, and O are present. After In is oxidized to In_2O_3, by means of the two-step oxidation process, Ga replaces the In in the In–O bonds and uses the O reacted to In_2O_3 as a 'quasi' O reservoir. This leads to an enhanced Ga incorporation since In or In_2O posses a higher oxidation efficiency than Ga or Ga_2O. Depending on the surface lifetime of In, it may be re-oxidized to In_2O_3, and the In in the In–O is again replaced by other Ga adatoms. This re-oxidation step enables a Ga incorporation rate which is even larger than the supplied In flux, which determines the 'quasi' O reservoir for Ga.

In the highly Me-rich regime, a surfactant effect of In on the formation of Ga_2O_3 is observed. The metastable hexagonal ε-Ga_2O_3 phase is formed in the presence of In (without In being incorporated). The crystal structure of this ε-Ga_2O_3 layers posses the best crystal quality of MBE grown Ga_2O_3 on *c*-plane sapphire. The crystallinity of these films was verified `in-situ` by reflection high-energy electron diffraction and post-growth X-ray diffraction (XRD) analysis. The stabilization of ε-Ga_2O_3 might be a consequence of thermodynamic and kinetic conditions set by In, i.e., the formation of Ga_2O_3 at growth temperatures and Ga-to-O flux ratios where binary Ga_2O_3 growth is not feasible anymore.

In summary, In has a `catalytic-surfactant effect` on the formation of Ga_2O_3.

A phenomenological, kinetic growth model for ternary oxide systems is explicitly developed for $(In_xGa_{1-x})_2O_3$ MBE. This model is based on the thermodynamically induced reaction kinetics, i.e., the exchange of In in In_2O_3 by Ga adatoms, the segregation of In on the $(In_xGa_{1-x})_2O_3$ growth surface, and its desorption.

This phenomenological model serves as a first quantitative description of $(In_xGa_{1-x})_2O_3$ MBE. It predicts the macroscopic In and Ga incorporation rates, the total Me incorporation rates, the `macroscopic` In concentration x, and all Me desorption rates, as a function of all growth parameters. In this ternary model, the Ga_2O desorption is predicted by the embedded growth model developed for binary oxide MBE. One benefit of this model is that it predicts x for all growth conditions allowing to engineer the band gap of $(In_xGa_{1-x})_2O_3$. Furthermore, due to the low miscibility of Ga_2O_3 and In_2O_3 into $(In_xGa_{1-x})_2O_3$ this ternary model may predict thermodynamic settings with desired x that enable a better miscibility of both materials.

The miscibility of Ga_2O_3 and In_2O_3 and their solubility limits in different polymorphs of $(In_\chi Ga_{1-\chi})_2O_3$ with `microscopic` In concentration χ were systematically investigated. The crystal structures and surface morphologies were analyzed by post-growth XRD, atomic force microscopy, and scanning electron microscopy. A first macroscopic approach using Bragg's law and Vegard's law to determine χ is derived. By means of this approach, the microscopic Me concentration in the crystal structure can be extracted by measuring a macroscopic volume of the $(In_xGa_{1-x})_2O_3$ layers. The crystal structure is measured utilizing XRD, and analyzing the diffraction peak positions obtained by ω-2θ wide-range scans. A hexagonal $(In_\chi Ga_{1-\chi})_2O_3$ phase with $\chi = 0.50$ is observed. Cubic and monoclinic $(In_\chi Ga_{1-\chi})_2O_3$ phases with maximum Ga and In solubility of $(13 \pm 5)\,\%$ and $(37 \pm 4)\,\%$, respectively, are identified.

8.1. Outlook

The studies, findings, and models presented in this thesis can serve as a basis for the development of more sophisticated growth models including microscopic growth effects, such as surface diffusion or nucleation. Furthermore, they can be transferred to other epitaxial growth techniques, such as pulsed laser deposition and metal-organic vapor phase epitaxy.

The microscopic reaction mechanisms of oxides possessing suboxides can be further investigated by using a suboxide source material for growth. The growth kinetics between elementary (e.g., Ga) and molecular (e.g., Ga_2O) source materials can be compared and should give a deeper insight into the reaction paths of these materials (e.g., Ga_2O_3). For example, the measured plateau in γ in the O-rich regime should still be present utilizing a suboxide source and finally confirm the stated two-step oxidation process, in all growth regimes. In contrast, no decrease in γ in the Me-rich regime is expected when growing the oxides with a suboxide source. Instead, a plateau in γ as it is the case for group-III nitride semiconductors, for instance, is anticipated. Furthermore, using a suboxide source can reveal at which oxidation step of the Me the oxidation efficiency is different. In this thesis, only the 'average' oxidation efficiency J_O^{Me} from the Me to the solid compound could be investigated.

The suppression of In incorporation by Ga during $(In_xGa_{1-x})_2O_3$ MBE can be transferred to other ternary oxide compounds, such as $(Al_xGa_{1-x})_2O_3$. In the case of $(Al_xGa_{1-x})_2O_3$ MBE, it is expected that the Ga incorporation is suppressed by the presence of Al because of the stronger Al–O bonds compared to the Ga–O bonds. In the case that Al indeed suppresses the Ga incorporation, it is conceivable that the segregating Ga (minimizing the surface free energy) has an effect on the Al incorporation and its crystal structures, similar as In on the formation of Ga_2O_3 during $(In_xGa_{1-x})_2O_3$ growth. This effect might depend on the relation between the oxidation efficiencies of Al and Ga. In case the oxidation efficiency of Ga is larger than the one of Al, the Al incorporation would be increased at equal growth conditions as compared when Al_2O_3 is grown without Ga.

In case Ga indeed segregates on the growth surface during $(Al_xGa_{1-x})_2O_3$ MBE, the same model for Ga desorption from the $(Al_xGa_{1-x})_2O_3$ growth surface with embedded Al_2O desorption rate predicted by the kinetic binary growth model (developed in this thesis) can be applied; the same as the modeling of In and Ga_2O desorption from an $(In_xGa_{1-x})_2O_3$ growth surface in this thesis.

A. Supplement to: Growth of group-III and IV oxides by MBE

A.1. Technical drawing of the MBE growth chamber

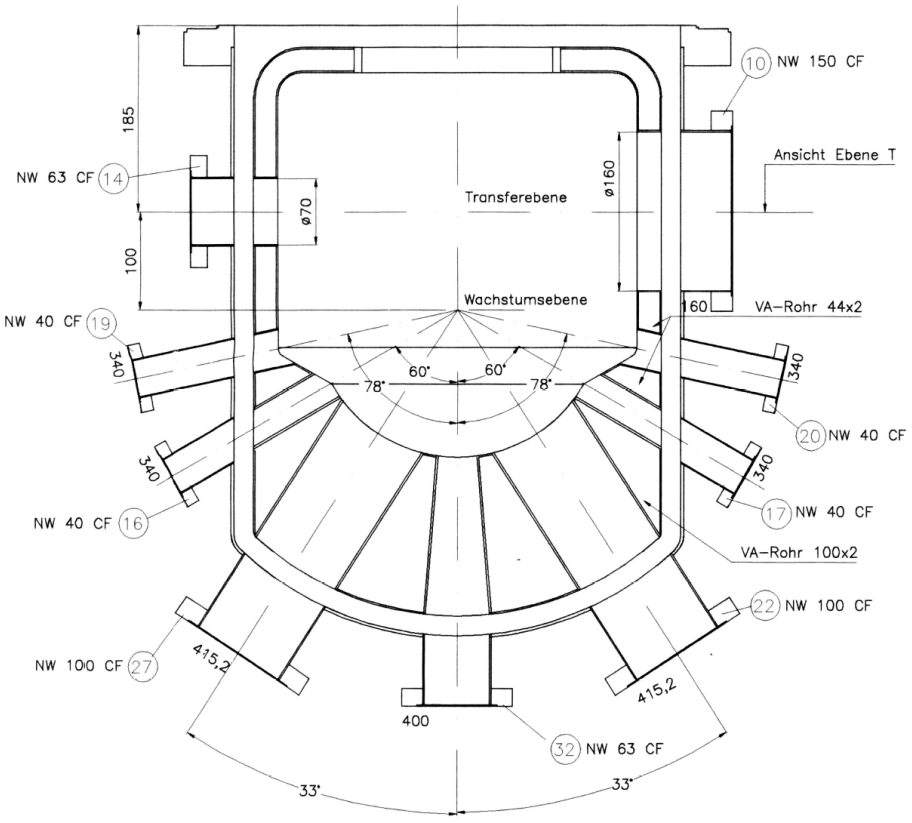

Figure A.1.: Cross-sectional technical drawing of the MBE growth chamber used for this thesis delivered from *Createc GmbH*, the company that built this chamber. Adress: Createc GmbH, Industriestraße 9, 74391 Erligheim, Germany

A.2. Drawings for the laser leflectometry set-up

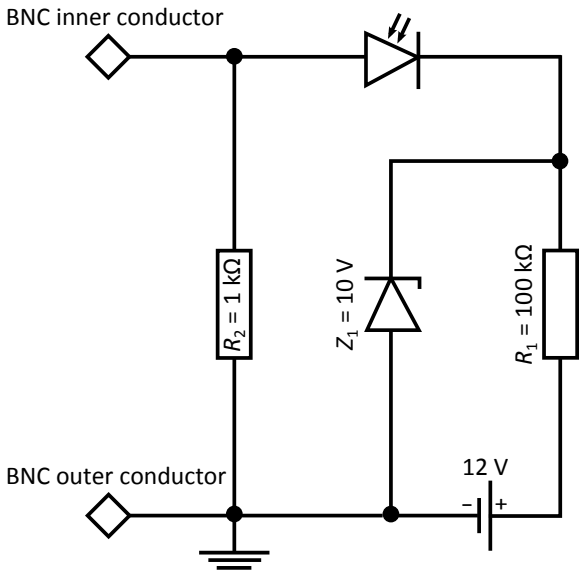

Figure A.2.: Sketch of the voltage-divider circuit for the photodiode of the laser reflectometry set-up installed at the growth chamber. This circuit enables a distribution of the input voltage $U_{\mathrm{in}} = 12\,\mathrm{V}$ among the components.

A.3. EPIC-code for BEP calibration of the metal effusion cells

```
Global Standby_Me = x1
Global Standby_MeHL = y2

Local T_Me = x2
Local T_MeHL = y2
Local numsteps = u1
Local stepsize = v1
Local step = 0
Local deltaT = 0
Local fluxopen = 0
Local fluxclosed = 0
Local flux = 0

While(step < numsteps)

deltaT = step*stepsize-10
Ramp(Me, T_Me-deltaT, 0.5)
Ramp(MeHL, T_MeHL-deltaT, 0.5)
WaitRampEnd(Me, MeHL)

Wait(10:00)

deltaT = step*stepsize
Ramp(Me, T_Me-deltaT, 0.0833)
Ramp(MeHL, T_MeHL-deltaT, 0.0833)
WaitRampEnd(Me, MeHL)

Wait(5:00)

ReadAvgGauge(FLUX IG, 5, fluxclosed)
Open(Me)
Wait(1:00)
ReadAvgGauge(FLUX IG, 5, fluxopen)
flux = fluxopen - fluxclosed
SaveFluxToFile(Me, Me.MV, flux)
Close(Me)

step = step + 1

End While

Ramp(Me, Standby_Me, 1)
Ramp(MeHL, Standby_MeHL, 1)
```

A.4. X-ray diffraction characterization

In order to determine the crystal structure and orientation of the grown layers X-ray diffraction (XRD) was used. X-ray diffraction takes advantage of the periodic ordered atomic or molecular structure of crystals and was first described by W. Bragg [25]. A schematic of the set-up as used for this thesis is drawn in Fig. A.3.

The device used for XRD measurements was a X'Pert Pro MRD built and sold by PANalytical[1]. The X-rays are produced by a copper K_α-source with wavelength $\lambda_{\text{X-ray}} = 1.54\,\text{Å}$. Two X-rays may experience constructive interference when the optical path difference equals an multiple integer of $\lambda_{\text{X-ray}}$, i.e.

$$a_{(hkl)} = n \left(\frac{\lambda_{\text{X-ray}}}{2} \right) \sin^{-1}(\theta) \; . \tag{A.1}$$

The distance between two lattice planes is denoted as $a_{(hkl)}$[2], the angle between incidence X-ray beam and sample is tagged as ω. The condition written in the former equation is called Bragg condition (same as introduced in chapter 7, Eq. (7.1)).

Four different XRD-scanning modes were used in order to investigate the crystal structure of the grown samples. (i) ω-2θ scan: here, the source is fixed. The sample and the detector rotate around ω and 2θ (the angle between incident beam and detector). The tilt of the sample with respect to the impinging beam is $\psi = 90\,^\circ$ and the in-plane rotation around the azimuth ϕ is arbitrary. This scan allows the spacing of lattice planes along the growth direction of the sample to be measured and gives information about its crystal phase(s). (ii) ω-scan: here, the source and detector are fixed. The sample is rocked around a chosen $\omega = 2\theta/2$ angle that fulfills condition (A.1). This angle is usually found by a previous ω-2θ scan. An ω-scan gives information about the tilt contribution to mosaicity. The smaller the mosaicity the higher the crystal quality of the grown layer. (iii) ϕ-scan: here the sample is tilted by ψ and rotated around the center of the sample by ϕ from $0\,^\circ$ to $360\,^\circ$ at a constant lattice spacing, i.e., constant ω and 2θ. By a ϕ-scan one gets information about possible rotational domains, for instance, or the epitaxial relation between substrate and epilayer. (iv) Pole-figure scan: here the sample is measured at a fixed scattering angle 2θ, i.e. a fixed lattice plane distance, accessing tilted lattice planes. A Pole-figure scan consists of a series of ϕ-scans at different ψ ranging from $0\,^\circ$ to $90\,^\circ$ (for the data shown in in Ref. [128]). This scan gives insights about the texture of the sample.

[1] PANalytical B.V, Lelyweg 1, 7602 EA Almelo, Netherlands.
[2] For a given crystal structure a for each lattice plane described by the Miller indices hkl may be calculated.

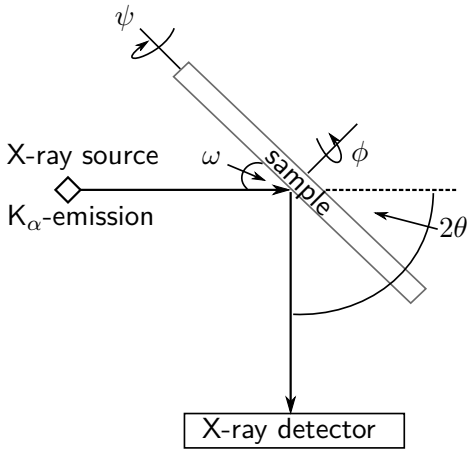

Figure A.3.: Schematic of the experimental set-up for X-ray diffraction as used for this thesis. The used X-ray tubes have a wavelength of $\lambda_{\text{X-ray}} = 1.54\,\text{Å} < a$, with a the lattice spacing between two atomic or molecular planes. The meaning of the angles ω, 2θ, ϕ, and ψ are explained in the text.

A.5. Line-of-sight quadrupole mass spectrometer

The amplitude of the signal detected by QMS strongly depends on the background pressure in the growth chamber p_{GC}. This dependence is described by Φ_{O_2} (no plasma) and Ga flux Φ_{Ga}. The used QMS was a residual gas analyzer SRS RGA-300 built by Stanford Research Systems[3] with mass range up to 300 atomic mass units (amu). The operating range of this device is up to 10^{-6} Torr. The background pressure during oxide layer growth in this thesis ranged from 1×10^{-6} Torr to 2×10^{-5} Torr. Therefore, it was very difficult to get reliable quantitative data measured by this QMS.

Figure A.4 (a) shows the maximum Ga flux $\Phi_{\text{Ga}}^{\text{des}}$ desorbing from an $Al_2O_3(0001)$ surface at $T_{\text{G}} = 800\,^{\circ}\text{C}$ for three different Φ_{Ga} of $4.0\,\text{Å}\,\text{s}^{-1}$, $2.0\,\text{Å}\,\text{s}^{-1}$, and $1.0\,\text{Å}\,\text{s}^{-1}$, as a function of time t_{meas}. The maximum $\Phi_{\text{Ga}}^{\text{des}}$ is used to calibrate the QMS signal according to the impinging Φ_{Ga} on the substrate. With increasing Φ_{O_2} the detected $\Phi_{\text{Ga}}^{\text{des}}$ QMS signal systematically decreases. The numbers written at the peaks denote Φ_{O_2} at 0 SCCM, 0.5 SCCM, 1.0 SCCM, and 3.0 SCCM. (b) Plots the evaluated $\Phi_{\text{Ga}}^{\text{des}}$ as function of Φ_{Ga} at different constant pressure in the growth chamber, i.e., at different constant Φ_{O_2}. The inset depicts the dependence of the slopes σ_{Ga} on Φ_{O_2}, obtained by linear data-fits in Fig. A.4 (b).

With the results from Fig. A.4 (a) and (b) the QMS signal can be parameterized depending on Φ_{Ga} and Φ_{O_2}. The equation reads as

$$\Phi_{\text{Ga}}^{\text{des}}(\Phi_{\text{Ga}}, \Phi_{\text{O}_2}) = A\,\sigma_{\text{Ga}}(\Phi_{\text{O}_2})\,\Phi_{\text{Ga}} = A\,(1 - a\,\sigma_{\text{O}}\,\Phi_{\text{O}})\,\Phi_{\text{Ga}} \tag{A.2}$$

with $\sigma_{\text{O}} = (0.16 \pm 0.01)\,\text{SCCM}^{-1}$, obtained by fitting the data plotted in the inset of Fig. A.4 (b). The active O flux is denoted as Φ_{O}. The dimensionless geometric factor A takes the size of the aperture into account which is unity for this study. Here, the diameter

[3] Stanford Research Systems, Inc., 1290-D Reamwood Avenue, Sunnyvale, CA 94089, USA.

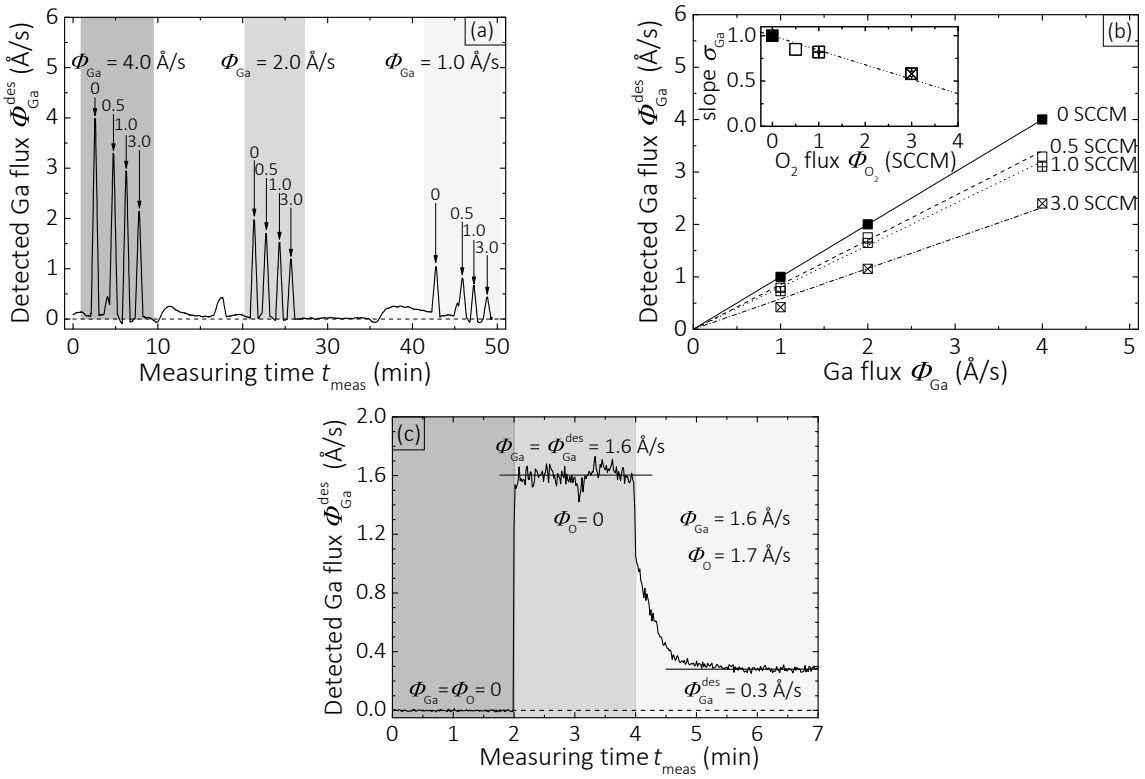

Figure A.4.: (a) Detected Ga flux $\Phi_{\mathrm{Ga}}^{\mathrm{des}}$ by line-of-sight QMS for three different impinging Ga fluxes Φ_{Ga} as a function of time t_{meas}. The numbers written at the peaks refer to different supplied O_2 fluxes $\Phi_{O_2} = 0\,\mathrm{SCCM} \mathrel{\hat{\sim}} 1 \times 10^{-9}$ Torr, $0.5\,\mathrm{SCCM} \mathrel{\hat{\sim}} 1 \times 10^{-6}$ Torr, $1.0\,\mathrm{SCCM} \mathrel{\hat{\sim}} 5 \times 10^{-6}$ Torr, and $3.0\,\mathrm{SCCM} \mathrel{\hat{\sim}} 2 \times 10^{-5}$ Torr. (b) Plots $\Phi_{\mathrm{Ga}}^{\mathrm{des}}$ as a function of Φ_{Ga} for different Φ_{O_2} as denoted in (a). The lines are linear fits with slopes σ_{Ga}. Inset: Plots σ_{Ga} obtained by fitting the data in the main graph as a function of Φ_{O_2}. (c) Shows the drop of the QMS signal detected with O plasma at set $\Phi_{O_2}(P_{\mathrm{rf}} = 300\,\mathrm{W}) = 1.0\,\mathrm{SCCM}$.

of the aperture in front of the ionizer was 15 mm. The dimensionless factor a includes a further signal drop when the O plasma is on, as indicated in the lower panel (c) of Fig. A.4.

Using Eq. (A.2), a can be calculated. In this example, the active O flux is $\Phi_{\mathrm{O}} = 1.7\,\text{Å/s} \mathrel{\hat{=}} \Phi_{O_2}(P_{\mathrm{rf}} = 300\,\mathrm{W}) = 1.0\,\mathrm{SCCM}$ the pre-factor a is

$$\Phi_{\mathrm{Ga}}^{\mathrm{des}}(\Phi_{\mathrm{Ga}} = 1.6\,\text{Å/s},\, \Phi_{\mathrm{O}} = 1.7\,\text{Å/s}) = 0.3\,\text{Å/s} = \tag{A.3}$$

$$= (1 - 0.16\,a)\,1.6\,\text{Å/s} \quad \Longleftrightarrow \quad a = 5.07\,. \tag{A.4}$$

The detected QMS signal is five times smaller when the O plasma is on — at same background pressure. A further increase Φ_{O} does not lead to a further decrease of the QMS signal (not shown). The signal of the desorbing Ga flux decreases with increasing Φ_{O_2} because all O atoms or molecules reaching the ionizer of the quadrupole are ionized. The relative change of the Ga signal in the quadrupole decreases with increasing impinging O rate. The drop of the signal is even larger when the O plasma is on. This might be because Ga and O atoms react in the ionizer which results in a further decrease of the detected Ga signal.

B. Supplement to: Reaction kinetics and thermodynamics of binary group-III and IV oxides in MBE

B.1. Thermochemical data to Ga_2O_3, In_2O_3, and SnO_2

	ΔH_{T_0} $\left(\frac{\text{eV}}{\text{f.u.}}\right)$	ΔS_{T_0} $\left(\frac{\text{eV}}{\text{f.u.}}\frac{1}{\text{K}}\right)$	C_P $\left(\frac{\text{meV}}{\text{f.u.}}\frac{1}{\text{K}}\right)$	a $\left(\frac{\text{meV}}{\text{f.u.}}\frac{1}{\text{K}}\right)$	b $\left(\frac{\mu\text{eV}}{\text{f.u.}}\frac{1}{\text{K}^2}\right)$	c $\left(\frac{\mu\text{eV K}}{\text{f.u.}}\right)$	d $\left(\frac{\mu\text{eV}}{\text{f.u.}}\frac{1}{\text{K}^3}\right)$
Ga	2.71	1.65	0.26	0.24	13.8	2.5	0
In	2.41	1.69	0.24	0.22	23.6	2.4	0
Sn	3.00	1.64	0.30	0.31	20.3	-11.3	-13.7
GaO	1.37	2.25	0.36	0.36	0	0	0
SnO	0.20	2.26	0.35	0.34	13.4	-3.5	0
Ga_2O	-0.96	2.77	0.47	0.47	0	0	0
In_2O	-0.65	2.91	0.49	0.48	0	0	0
Ga_2O_3	-10.62	0.93	1.24	1.10	154.4	-21.0	0
In_2O_3	-9.03	1.01	1.26	1.20	81.0	-22.0	0
SnO_2	-5.66	0.61	0.77	0.65	166.4	-16.7	0

Table B.1.: Values for the enthalpy and entropy at room temperature ΔH_{T_0} and ΔS_{T_0}, respectively, the heat capacity at constant pressure C_P as well as the pre-factors a, b, c, and d were taken from Ref. [19]. These values are needed to determine the Gibbs free energy of formation, ΔG, for the chemical reactions given in this thesis by Eq. (4.10), chapter 4. All energies are given per formula unit (f.u.).

B.2. Model with total reaction order of three in oxide formation

In this paragraph, the kinetic binary growth model with total reaction order of $\mathcal{O} = 3$ in reactions (5.26) and (5.27) is briefly introduced. The basic structure is the same as for the model with $\mathcal{O} = 2$ (presented in detail in section 5.2, chapter 5). It includes all reactions found occurring during growth of the investigated oxides. This model can only be solved numerically, hence, just demonstrative examples of it are given and compared to the results of the model with $\mathcal{O} = 2$.

The reactions found for sesquioxide MBE are drawn in Fig. 5.10 (chapter 5) and are re-written here for convenience:

$$\mathrm{O}\,(a) \xrightarrow{k_2} \mathrm{O}\,(g) \qquad \text{(O desorption)} \tag{B.1}$$

$$2\,\mathrm{Me}\,(a) + \mathrm{O}\,(a) \xrightarrow{k_3} \mathrm{Me_2O}\,(a \text{ or } g) \qquad (\mathrm{Me_2O} \text{ formation}) \tag{B.2}$$

$$4\,\mathrm{Me}\,(a) + \mathrm{Me_2O_3}\,(s) \xrightarrow{k_4} 3\,\mathrm{Me_2O}\,(a \text{ or } g) \qquad (\mathrm{Me_2O} \text{ formation}) \tag{B.3}$$

$$\mathrm{Me_2O}\,(a) \xrightarrow{k_5} \mathrm{Me_2O}\,(g) \qquad (\mathrm{Me_2O} \text{ desorption}) \tag{B.4}$$

$$\mathrm{Me_2O}\,(a) + 2\,\mathrm{O}\,(a) \xrightarrow{k_6} \mathrm{Me_2O_3}\,(s) \qquad (\mathrm{Me_2O_3} \text{ formation}) \tag{B.5}$$

For a constant rate of arrival Me and O adatoms on the growth surface the system of equations for dynamic equilibrium (i.e. steady state growth regime) assuming elementary reactions reads as

$$0 = \underbrace{\dot{\theta}_{\mathrm{Me}}}_{=\phi_{\mathrm{Me}}} - \underbrace{k_3\,\theta_{\mathrm{Me}}^2\,\theta_{\mathrm{O}}}_{=\dot{\theta}^{\mathrm{SoF}}_{\mathrm{Me_2O}}} - \underbrace{k_4\,\theta_{\mathrm{Me}}^4\,\theta_{\mathrm{Me_2O_3}}}_{=\dot{\theta}^{\mathrm{dec}}_{\mathrm{Me_2O}}} \tag{B.6}$$

$$0 = \underbrace{\dot{\theta}_{\mathrm{O}}}_{=\phi^{*}_{\mathrm{O}}} - \underbrace{k_2\,\theta_{\mathrm{O}}}_{=\dot{\theta}^{\mathrm{des}}_{\mathrm{O}}} - \underbrace{\frac{1}{2}\,k_3\,\theta_{\mathrm{Me}}^2\,\theta_{\mathrm{O}}}_{=\dot{\theta}^{\mathrm{SoF}}_{\mathrm{O}}} - \underbrace{k_6\,\theta_{\mathrm{Me_2O}}\,\theta_{\mathrm{O}}^2}_{=\dot{\theta}^{\mathrm{growth}}_{\mathrm{O}}} \tag{B.7}$$

$$0 = \underbrace{k_3\,\theta_{\mathrm{Me}}^2\,\theta_{\mathrm{O}}}_{=\dot{\theta}^{\mathrm{SoF}}_{\mathrm{Me_2O}}} + \underbrace{k_4\,\theta_{\mathrm{Me}}^4\,\theta_{\mathrm{Me_2O_3}}}_{=\dot{\theta}^{\mathrm{dec}}_{\mathrm{Me_2O}}} - \underbrace{k_6\,\theta_{\mathrm{Me_2O}}\,\theta_{\mathrm{O}}^2}_{=\dot{\theta}^{\mathrm{growth}}_{\mathrm{Me_2O}}} - \underbrace{k_5\,\theta_{\mathrm{Me_2O}}}_{=\dot{\theta}^{\mathrm{des}}_{\mathrm{Me_2O}}} \tag{B.8}$$

All symbols have been already defined in chapter 5, subsection 5.2.2 for the model with $\mathcal{O} = 2$. The only difference in rate equations written are the powers in the surface densities (i.e. the partial reaction orders o) of the species, which now, equal the stoichiometric coefficients as written in reactions (B.1)–(B.5).

In the case all reactions are taken into account, the approach to reduce the number of unknown model parameters cannot be applied. When decomposition is considered, i.e. $k_4 \neq 0$, k_3 cannot assumed to be very large as in the model with $\mathcal{O} = 2$. Therefore, the number of unknown reaction rate constants is increased from one for model with $\mathcal{O} = 2$ (i.e. $\mathcal{K}$) to five: k_2, k_3, k_4, k_5, and k_6. This makes a semi-quantitative analysis, like for the

model with $\mathcal{O} = 2$, impossible. Here, the total suboxide formation is a combination of direct Me_2O formation by reaction rate constant k_3 (reaction (B.2)) and layer decomposition by reaction rate constant k_4 (reaction (B.3)). Therefore, γ is a sum of Me_2O_3 formation and decomposition, i.e.,

$$\gamma = k_6\,\theta_{Me_2O}\,\theta_O^2 - k_4\,\theta_{Me}^4\,\theta_{Me_2O_3}\ . \tag{B.9}$$

Figure B.1 plots the solution of this model as applied for Ga_2O_3 growth. The upper panel (a) depicts the growth rate prediction of Ga_2O_3 when varying ϕ_{Ga} at different ratios of suboxide formation by reaction (B.2) and layer decomposition reaction (B.3), i.e. k_4/k_3. For $k_4 \ll k_3$ the model predicts the low-T_G γ-evolution as experimentally obtained. At higher k_4, that means, faster decomposition of the layer by Ga adatoms and slower direct suboxide formation, the chosen kinetic parameters cannot describe the measured data anymore. Other values of k_2–k_6 (not shown) did not result in an adequate description of the measured data either. The peaks in the model functions are due to discontinuities in its solution. The middle panel (b) shows the model prediction with $k_4 = 0$. Compared to the data this approach yields a much better result than shown in Fig. **??** (a) with $k_4 > 0$. The reaction rate constants k_2–k_6 were arbitrarily chosen to qualitatively describe the data. Even when all reaction rate constants were not systematically investigated, together with the kinetic arguments given in subsection 5.2.2 and the result of the model in Fig. B.1 (a), it is concluded that layer decomposition during oxide MBE does not play (or if, a minor role), i.e. $k_4 \approx 0$.

For this reason, Fig. B.1 (c) depicts the γ prediction when varying T_G for three different r_{Ga} using the same approach as for model with $\mathcal{O} = 2$, i.e, reducing the number of unknown reaction rate constants from four (k_2, k_3, k_5, k_6) to one ($\mathcal{K}$). The measured data follows the model prediction. For comparison with the previous model with $\mathcal{O} = 2$, the parameters chosen are the total energy of activation $E_a = 1.7\,\text{eV}$ and the obtained dependence of B_{Ga} on r_{Ga}. The parameters for B are $\beta_{0,Ga} = (4.1 \pm 0.3) \times 10^{-11}\,Ga_2O^{-1}\,nm^2\,s$ and $\beta_{Ga} = 3.6 \pm 0.9$. These model parameters compared to the ones obtained for the model with $\mathcal{O} = 2$ in chapter 5 show that the different powers o in the surface densities of the species i, i.e. θ_i^o, does not significantly change the values of the kinetic parameters.

In summary, both derived models with $\mathcal{O} = 2$ and $\mathcal{O} = 3$ yield the same qualitative result and allow a description of the measured γ-data. Further studies need to be performed in order to unveil through which reaction channels the oxides, that posses suboxides, are indeed formed. That means if reactions (5.26) and (5.27) can be considered as elementary reactions or if several intermediate bimolecular reaction steps occur (as introduced in chapter 5).

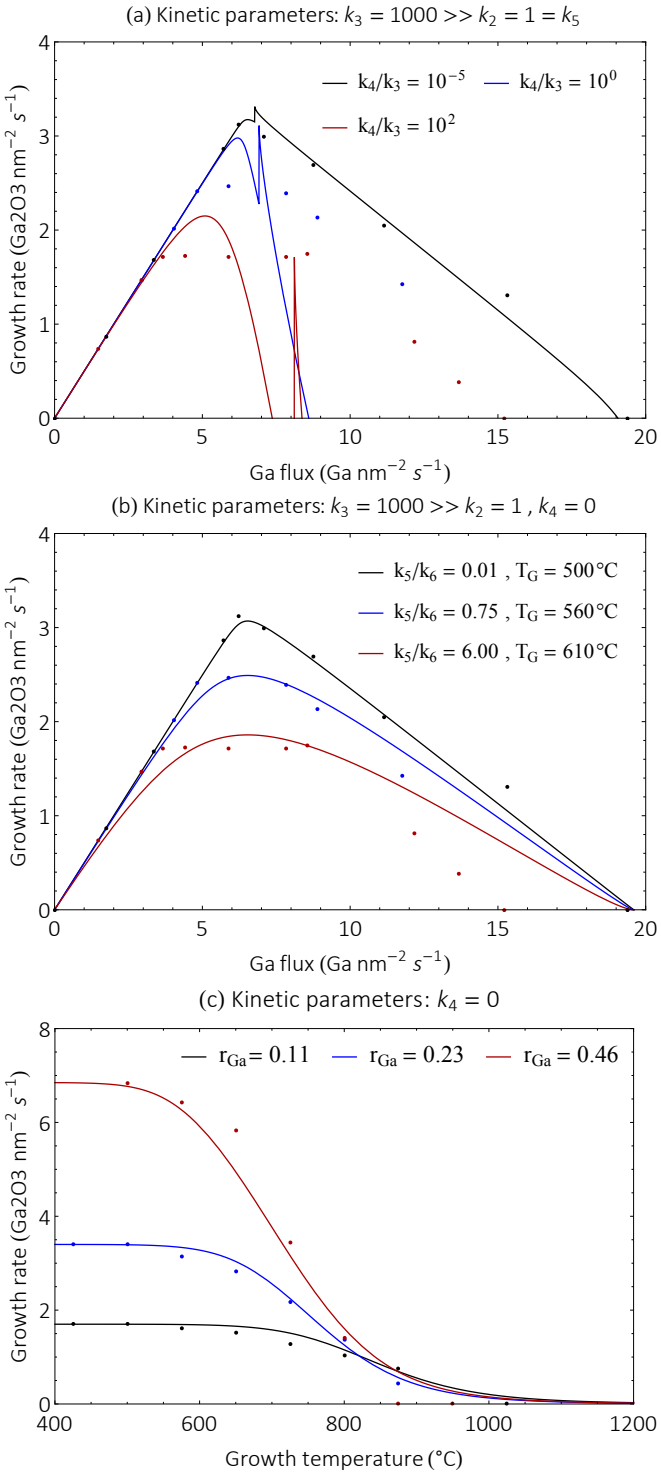

Figure B.1.: Numeric solution of the kinetic growth model solved with `Wolfram Mathematica` with $\mathcal{O} = 3$ in reactions (5.56) and (5.59). The used O flux was $9.8\,\mathrm{O\,nm^{-2}\,s^{-1}}$. (a) Shows the γ prediction of Ga_2O_3 as a function of the Ga flux ϕ_{Ga} for different ratios of k_3 and k_4. (b) Depicts γ as a function of ϕ_{Ga} with $k_4 = 0$ and varying the ratio of k_5 and k_6 at three different T_G. (c) Plots the model prediction as a function of T_G for three different r_{Ga} with $k_4 = 0$. The measured γ of Ga_2O_3 in (c) are shown for comparison.

References

[1] Åhman, J., Svensson, G., and Albertsson, J. A Reinvestigation of β-Gallium Oxide. *Acta Cryst. C* ***52*** (1996), 1336.

[2] Aida, H., Nishiguchi, K., Takeda, H., Natsuko, A., Sunakawa, K., and Yaguchi, Y. Growth of β-Ga_2O_3 Single Crystals by the Edge-Defined, Film Fed Growth Method. *Jpn. J. Appl. Phys.* ***47*** (2008), 8506.

[3] Alcock, C. B., Itkin, V. P., and Horrigan, M. K. Vapor Pressure of the Metallic Elements. *Can. Metall. Q.* ***309*** (1984), 23.

[4] Anderson, E. M., Lundquist, A. M., Sarney, W. L., Svensson, S. P., Carrington, P. J., Pearson, C., and Millunchick, J. M. Influence of a Bi surfactant on Sb incorporation in InAsSb alloys. *J. Appl. Phys.* ***116*** (2014), 014901.

[5] Arrhenius, S. A. Über die Reaktionsgeschwindigkeit bei der Inversion von Rohrzucker durch Säuren. *Z. Phys. Chem.* ***4*** (1889), 226.

[6] Atkins, P. *Physical Chemistry.* Oxford University Press, 10$^{\text{th}}$ Edition, United Kingdom, 2010.

[7] Averbeck, R., and Riechert, H. Quantitative Model for the MBE-Growth of Ternary Nitrides. *Phys. Stat. Sol. (a)* ***176*** (1999), 301.

[8] Baldini, M., Albrecht, M., Gogova, D., Schewski, R., and Wagner, G. Effect of indium as a surfactant in $(Ga_{1-x}In_x)_2O_3$ epitaxial growth on β-Ga_2O_3 by metal-organic vapour phase epitaxy. *Semicond. Sci. Technol.* ***30*** (2015), 024013.

[9] Baldini, M., Gogova, D., Irmscher, K., Schmidbauer, M., Wagner, G., and Fornari, R. Heteroepitaxy of $Ga_{2(1-x)}In_{2x}O_3$ layers by MOVPE with two different oxygen sources. *Cryst. Res. Technol.* ***49*** (2014), 552.

[10] Barsan, N., and Weimar, U. Conduction Model of Metal Oxide Gas Sensors. *J. Electroceram.* ***7*** (2001), 143.

[11] Batzill, M., and Diebold, U. The surface and materials science of tin dioxide. *Prog. Surf. Sci.* ***79*** (2005), 47.

[12] Bellitto, V. *Atomic Force Microscopy — Imaging, Measuring and Manipulating Surfaces at the Atomic Scale.* InTech (open source), 2012.

[13] Bierwagen, O. Indium oxide — a transparent, wide-band gap semiconductor for (opto)electronic applications. *Semicond. Sci. Technol.* ***30*** (2015), 024001.

[14] Bierwagen, O., Nagata, T., White, M. E., Tsai, M.-Y., and Speck, J. S. Electron transport in semiconducting SnO_2: Intentional bulk donors and acceptors, the interface, and the surface. *J. Mater. Res.* ***27*** (2012), 2232.

[15] Bierwagen, O., Rombach, J., and Speck, J. S. Faceting control by the stoichiometry influence on the surface free energy of low-index bcc-In_2O_3 surfaces. *J. Phys. Condens. Matter* ***28*** (2016), 224006.

[16] Bierwagen, O., and Speck, J. S. Mg acceptor doping of In_2O_3 and overcompensation by oxygen vacancies. *Appl. Phys. Lett.* ***101*** (2012), 102107.

[17] Bierwagen, O., and Speck, J. S. Plasma-assisted molecular beam epitaxy of Sn-doped In_2O_3: Sn incorporation, structural changes, doping limits, and compensation. *Phys. Status Solidi (a)* ***211*** (2014), 48.

[18] Bierwagen, O., White, M. E., Tsai, M.-Y., and Speck, J. S. Plasma-assisted molecular beam epitaxy of high quality $In_2O_3(001)$ thin films on Y-stabilized $ZrO_2(001)$ using In as an auto surfactant. *Appl. Phys. Lett.* ***95*** (2009), 262105.

[19] Binnewies, M., and Mielke, E. *Thermochemical Data of Elements and Compounds.* Wiley-VCH Verlag GmbH, Weinheim, 2nd Edition, 2002.

[20] Bizo, L., Choisnet, J., Retoux, R., and Raveau, B. The great potential of coupled substitutions in In_2O_3 for the generation of bixbyite-type transparent conducting oxides, $In_{2-2x}M_xSn_xO_3$. *Solid State Commun.* ***136*** (2008), 163.

[21] Bloembergen, N., and Pershan, P. S. Light Waves at the Boundary of Nonlinear Media. *Phys. Rev. B* ***128***, 2 (1962).

[22] Boehler, R., and Ross, M. Melting curve of aluminum in a diamond cell to 0.8 mbar: implications for iron. *Earth Planet. Sci. Lett.* ***153*** (1997), 223.

[23] Bolzan, A. A., Fong, C., Kennedy, B. J., and Howard, C. J. Structural Studies of Rutile-Type Metal Dioxides. *Acta Cryst. B****53*** (1997), 373.

[24] Boschi, F., Bosi, M., Berzina, T., Buffagni, E., Ferrari, C., and Fornari, R. Hetero-epitaxy of ε-Ga_2O_3 layers by MOCVD and ALD. *J. Cryst. Growth* ***443*** (2016), 25.

[25] Bragg, W. L. The Diffraction of Short Electromagnetic Waves by a Crystal. *Proc. Cambridge Philos. Soc.* ***XVII*** (1913), Part I.

[26] Braun, W. *Applied RHEED — Reflection High-Energy Electron Diffraction During Crystal Growth.* Springer-Verlag Berlin Heidelberg New York, 1999.

[27] Chae, G. S. A Modified Transparent Conducting Oxide for Flat Panel Displays. *Jpn. J. Appl. Phys.* ***40*** (2001), 1282.

[28] Chern, M. Y., Huang, Y. C., and Xu, W. L. A-plane sapphire: A well-matched substrate for epitaxial growth of indium tin oxide. *Thin Solid Films* ***515*** (2007), 7866.

[29] Colin, R., Drowart, J., and Verhaegen, G. Mass-spectrometric study of the vaporization of tin oxides. Dissociation energy of SnO. *Trans. Faraday Soc.* ***61*** (1965), 1364.

[30] Copel, M., Reuter, M. C., Kaxiras, E., and Tromp, R. M. Surfactants in Epitaxial Growth. *Phys. Rev. Lett.* ***63*** (1989), 632.

[31] Dean, J. A. *Lange's Handboock of Chemistry.* Mc-Graw Hill, 15th Edition, New York, United States of America, 1956.

[32] Deng, Z., Jiang, Y., Wang, W., Cheng, L., Li, W., Lu, W., Jia, H., Liu, W., Zhou, J., and Chen, H. Indium segregation measured in InGaN quantum well layer. *Sci. Rep.* ***4*** (2014), 6734.

[33] Dixit, A., Sudakar, C., Naik, R., Naik, V. M., and Lawes', G. Undoped vacuum annealed In_2O_3 thin films as a transparent conducting oxide. *Appl. Phys. Lett..* ***95*** (2009), 192105.

[34] Du, X., Mi, W., Luan, C., Li, Z., Xia, C., and Ma, J. Characterization of homoepitaxial β-Ga_2O_3 films prepared by metal-organic chemical vapor deposition. *J. Cryst. Growth* ***404*** (2014), 75.

[35] Editer-in-chief Lide, D. R. *CRC Handbook of Chemistry and Physics.* CRC Press, 71st Edition, Boca Raton, United States of America, 1990.

[36] Edwards, D. D., Folkins, P. E., and Mason, O. M. Phase Equilibria in the Ga_2O_3-In_2O_3 System. *J. Am. Ceram. Soc.* ***80*** (1997), 253.

[37] Espenson, J. H. *Chemical Kinetics and Reaction Mechanisms.* McGraw-Hill, Inc., 2nd Edition, United States of America, 1995.

[38] Eyring, H. The Activated Complex in Chemical Reactions. *J. Chem. Phys.* ***3*** (1935), 107.

[39] Feneberg, M., Lidig, C., Lange, K., Goldhahn, R., Neumann, M. D., Esser, N., Bierwagen, O., White, M. E., Tsai, M.-Y., and Speck, J. S. Ordinary and extraordinary dielectric functions of rutile SnO_2 up to 20 eV. *Appl. Phys. Lett.* ***104*** (2014), 231106.

[40] Feneberg, M., Nixdorf, J., Lidig, C., Bierwagen, O., and Speck, J. S. Many-electron effects on the dielectric function of cubic In_2O_3: Effective electron mass, band nonparabolicity, band gap renormalization, and Burstein-Moss shift Momentum. *Phys. Rev B* ***93*** (2016), 045203.

[41] Fernández-Garrido, S., Koblmüller, G., Calleja, E., and Speck, J. S. *In-situ* GaN decomposition analysis by quadrupole mass spectrometry and reflection high-energy electron diffraction. *J. Appl. Phys.* ***104*** (2008), 1.

[42] Fleischer, M. Advances in application potential of adsorptive-type solid state gas sensors: high-temperature semiconducting oxides and ambient temperature GasFET devices. *Meas. Sci. Technol.* ***19*** (2008), 042001.

[43] Fortunato, E., Ginley, D., Hosono, H., and Paine, D. C. Transparent Conducting Oxides for Photovoltaics. *MRS Bull.* ***32*** (2007), 242.

[44] Foster, L. M., Chandrashekhar, G. V., Scardefield, J. E., and Bradford, R. B. Phase Diagram of the System Na_2O, Ga_2O_3-Ga_2O_3 and its Relation to the System Na_2O, Al_2O_3-Al_2O_3. *J. Am. Ceram. Soc.* ***63*** (1980), 509.

[45] Frosch, C.-J., and Thurmond, C.-D. The pressure of Ga_2O over gallium-Ga_2O_3 mixtures. *J. Phys. Chem.* ***66*** (1962), 877.

[46] Fujita, S., and Kaneko, K. Epitaxial growth of corundum-structured wide band gap III-oxide semiconductor thin film. *J. Cryst. Growth* ***401*** (2014), 588.

[47] Galazka, Z., Uecker, R., Irmscher, K., Albrecht, M., Klimm, D., Pietsch, M., Brützam, M., Bertram, R., Ganschow, S., and Fornari, R. Czochralski growth and characterization of β-Ga_2O_3 single crystals. *Cryst. Res. Technol.* ***45*** (2010), 1229.

[48] Gallinat, C. S., Koblmüller, G., Brown, J. S., and Speck, J. S. A growth diagram for plasma-assisted molecular beam epitaxy of In-face InN. *J. Appl. Phys.* ***102***, 6 (2007).

[49] Gottschalch, V., Mergenthaler, K., Wagner, G., Bauer, J., Paetzelt, H., Sturm, C., and Teschner, U. Growth of β-Ga_2O_3 on Al_2O_3 and GaAs using metal-organic vapor-phase epitaxy. *Phys. Stat. Solidi (a)* ***206*** (2009), 243.

[50] Green, A. J., Chabak, K. D., ller, E. R., Fitch, R. C., Baldini, M., Fiedler, A., Irmscher, K., Wagner, G., Galazka, Z., Tetlak, S. E., Crespo, A., Leedy, K., and Jessen, G. H. 3.8 MV/cm Breakdown Strength of MOVPE-Grown Sn-Doped β-Ga_2O_3 MOSFETs. *IEEE Electr. Device Lett.* ***37*** (2016), 902.

[51] Harvey, T. E., Bertness, K. A., Hickernell, R. K., Wang, C. M., and Splett, J. D. Accuracy of AlGaAs growth rates and composition determination using RHEED oscillations. *J. Cryst. Growth* ***251*** (2003), 73.

[52] He, L., Moon, Y. T., Xie, J., Muñoz, M., Johnstone, D., and Morkoç, H. Gallium desorption kinetics on (0001) GaN surface during the growth of GaN by molecular beam epitaxy. *Appl. Phys. Lett.* ***88*** (2006), 071901.

[53] Held, R., Crawford, D. E., Johnston, A. M., Dabiran, A. M., and Cohen, P. I. N-limited versus Ga-limited growth on GaN(000$\bar{1}$) by MBE using NH_3. *Surf. Rev. Lett.* ***5*** (1998), 913.

[54] Heying, B., , R., Chen, L. F., Haus, E., Riechert, H., and Speck, J. S. Control of GaN surface morphologies using plasma-assisted molecular beam epitaxy. *J. Appl. Phys.* ***88*** (2000), 1855.

[55] Higashiwaki, M., Sasaki, K., Kuramata, A., Masui, T., and Yamakoshi, S. Gallium oxide (Ga_2O_3) metal-semiconductor fiel-effect transistors on single-crystal β-Ga_2O_3 (010) substrates. *Appl. Phys. Lett.* ***100*** (2012), 013504.

[56] Higashiwaki, M., Sasaki, K., Kuramata, A., Masui, T., and Yamakoshi, S. Development of gallium oxide power devices. *Phys. Stat. Solidi (a)* ***211*** (2014), 21.

[57] Higashiwaki, M., Sasaki, K., Murakami, H., Kumagai, Y., Koukitu, A., Kuramata, A., Masui, T., and Yamakoshi, S. Recent progress in Ga_2O_3 power devices. *Semicond. Sci. Technol.* ***31*** (2016), 034001.

[58] Hu, Y.-L., Rind, E., and Speck, J. S. Antiphase boundaries and rotation domains in In_2O_3(001) films grown on yttria-stabilized zirconia (001). *J. Appl. Cryst.* ***47*** (2014), 443.

[59] Hughes, O. H., Cheng, T. S., Novikov, S. V., Foxon, C. T., Korakakis, D., and Je, N. J. RHEED studies of the GaN surface during growth by molecular beam epitaxy. *J. Cryst. Growth* ***202*** (1999), 388.

[60] Ichimiya, A., and Cohen, C. *Reflection High-Energy Electron Diffraction.* Cambridge University Press, United Kingdom, 2004.

[61] John, C. R., Ashby Frs., M., Kiessling, R., and Charles, J. *Fundamentals of Energy Dispersive X-ray Analysis.* Elsevier Ltd., Amsterdam, Netherlands, 1984.

[62] Jousten, K. *Handbook of Vacuum and Technology.* WILEY-VCH Verlag GmbH and Co. KGaA., Weinheim, 2008.

[63] Kaneko, S., Torii, H., Soga, M., Akiyama, K., Iwaya, M., Yoshimoto, M., and Amazawa, T. Epitaxial Indium Tin Oxide Film Deposited on Sapphire Substrate by Solid-Source Electron Cyclotron Resonance Plasma. *Jpn. J. Appl. Phys.* ***51*** (2012), 01AC02.

[64] Kato, H., Sano, M., Miyamoto, K., and Yao, T. Effect of O/Zn Flux Ratio on Crystalline Quality of ZnO Films Grown by Plasma-Assisted Molecular Beam Epitaxy. *Jpn. J. Appl. Phys.* ***42*** (2003), 2241.

[65] Koblmüller, G., Fernández-Garrido, S., Calleja, E., and Speck, J. S. *In-situ* investigation of growth modes during plasma-assisted molecular beam epitaxy of (0001) GaN. *Appl. Phys. Lett.* ***91*** (2007), 161904.

[66] Koblmüller, G., Pongratz, P., Averbeck, R., and Riechert, H. Nucleation Phenomena during Molecular Beam Epitaxy of GaN Observed by Line-of-Sight Quadrupole Mass Spectrometry. *Phys. Stat. Sol. (a)* ***194*** (2002), 515.

[67] Korhonen, E., Tuomisto, F., Gogova, D., Wagner, G., Baldini, M., Galazka, Z., Schewski, R., and Albrecht, M. Electrical compensation by Ga vacancies in Ga_2O_3 thin films. *Appl. Phys. Lett.* ***106*** (2015), 242103.

[68] Kranert, C., Lenzner, J., Jenderka, M., Lorenz, M., Wenckstern, H. v., Schmidt-Grund, R., and Grundmann, M. Lattice parameters and raman-active phonon modes of $(In_xGa_{1-x})_2O_3$ for $x < 0.4$. *J. Appl. Phys.* ***116*** (2014), 013505.

[69] Kumaran, R., Tiedje, T., Webster, S. E., Penson, S., and Li, W. Epitaxial Nd-doped α-$(Al_{1-x}Ga_x)_2O_3$ films on sapphire for solid-state waveguide lasers. *Opt. Lett.* ***35*** (2010), 22.

[70] Ladd, M. F. C., and Palmer, R. A. *Structure Determination by X-ray Crystallography.* Plenum Press, 3rd Edition, New York, United States of America, 1993.

[71] Leidler, K. J., and King, M. C. The Deveopment of Transition State Theory. *J. Phys. Chem.* ***87*** (1983), 2657.

[72] Lewis, W. C. M. The Calculation in Absolute Measure of Velocity Constants and Equilibrium Constants in Gaseous Systems. *J. Chem. Soc. Trans.* ***113*** (1918), 471.

[73] Low, P. S., Bada, J. L., and Somero, G. N. Temperature Adaption of Enzymes: Roles of the Free Energy, the Enthalpy, and the Entropy of Activation. *Proc. Nat. Acad. Sci.* ***70*** (1973), 430.

[74] Lu, Y. M., Jiang, J., Xia, C., Kramm, B., Polity, A., He, Y. B., Klar, P. J., and Meyer, B. K. The influence of oxygen flow rate on properties of SnO_2 thin films grown epitaxially on *c*-sapphire by chemical vapor deposition. *Thin Solid Films* ***594*** (2015), 270.

[75] Ludwig, C. D. R., Gruhn, T., Felser, C., Windeln, J., and Kratzer, P. Indium-Gallium Segregation in $CuIn_xGa_{1-x}Se_2$: An *Ab Initio*-Based Monte Carlo Study. *Phys. Rev. Lett.* ***105*** (2010), 025702.

[76] Maccioni, M. B., and Fiorentini, V. Phase diagram and polarization of stable phases of $(Ga_{1-x}In_x)_2O_3$. *Appl. Phys. Express* ***9*** (2016), 041102.

[77] Maccioni, M. B., Ricci, F., and Fiorentini, V. Properties of $(Ga_{1-x}In_x)_2O_3$ over the whole x-range. *J. Phys. Conf. Ser.* ***566*** (2014), 012016.

[78] Maccioni, M. B., Ricci, F., and Fiorentini, V. Low In solubility and band offsets in the small-x β-$Ga_2o_3/(Ga_{1-x}In_x)_2O_3$ system. *Appl. Phys. Express* ***8*** (2015), 021102.

[79] Marezio, M. Refinement of the Crystal Structure of In_2O_3 at two Wavelengths. *Acta Cryst.* ***20*** (1966), 723.

[80] Massa, W. *Crystal Structure Determination.* Springer-Verlag Berlin Heidelberg, Germany, 2004.

[81] Mei, Z. X., Wang, Y., Du, X. L., Zeng, Z. Q., Ying, M. J., Zheng, H., Jia, J. F., Xue, Q. K., and Zhang, Z. Growth of In_2O_3 single-crystalline film on sapphire (0001) substrate by molecular beam epitaxy. *J. Cryst. Growth* ***289*** (2006), 686.

[82] Mezzadri, F., Calestani, G., Boschi, F., Delmonte, D., Bosi, M., and Fornari, R. Crystal Structure and Ferroelectric Properties of ε-Ga_2O_3 Films Grown on (0001)-Sapphire. *Inorg. Chem.* ***55*** (2016), 12079.

[83] Müller, S., Wenckstern, H. v., Splith, D., Schmidt, F., and Grundmann, M. Control of the conductivity of Si-doped β-Ga_2O_3 thin films via growth temperature and pressure. *Phys. Stat. Sol. (a)* ***211*** (2014), 34.

[84] Muraki, K., Fukatsu, S., Shiraki, Y., Ito, R., Muraki, K., Fukatsu, S., and Shiraki, Y. Surface segregation of In atoms during molecular beam epitaxy and its influence on the energy levels in InGaAs / GaAs quantum wells. *Appl. Phys. Lett.* ***61*** (1992), 557.

[85] Noh, H. K., Chang, K. J., Ryu, B., and Lee, W. J. Electronic structure of oxygen-vacancy defects in amorphous In-Ga-Zn-O semiconductors. *Phys. Rev. B* ***84*** (2011), 115205.

[86] Okumura, H., Balakrishnan, K., Hamaguchi, H., Koizumi, T., Chichibu, S., Nakanishi, H., Nagatomo, T., and Yoshida, S. Analysis of MBE growth mode for GaN epilayers by RHEED. *J. Cryst. Growth* ***190*** (1998), 364.

[87] Okumura, H., Kita, M., Kuramata, A., Higashiwaki, M., and Speck, J. S. Systematic investigation of the growth rate of β-Ga_2O_3(010) by plasma-assisted molecular beam epitaxy. *Appl. Phys. Express* ***7*** (2014), 095501.

[88] Orita, M., Ohta, H., and Hosono, M. H. Deep-ultraviolet transparent conductive β-Ga_2O_3 thin films. *Appl. Phys. Lett.* ***77*** (2000), 4166.

[89] Oshima, T., Nakazono, T., Mukai, A., and Ohtomo, A. Epitaxial growth of γ-Ga_2O_3 films by mist chemical vapor deposition. *J. Cryst. Growth* ***359*** (2012), 60.

[90] Oshima, T., Okuno, T., and Fujita, S. Ga_2O_3 Thin Film Growth on *c*-Plane Sapphire Substrates by Molecular Beam Epitaxy for Deep-Ultraviolet Photodetectors. *Jpn. J. Appl. Phys.* ***46*** (2007), 7217.

[91] Oshima, Y., Ahmadi, E., Badescu, S. C., Wu, F., and Speck, J. S. Composition determination of β-$(Al_xGa_{1-x})_2O_3$ layers coherently grown on (010) β-Ga_2O_3 substrates by high-resolution X-ray diffraction. *Appl. Phys. Express* ***9*** (2016), 061102.

[92] Oshima, Y., Víllora, E. G., Matsushita, Y., Yamamoto, S., and Shimamura, K. Epitaxial growth of phase-pure ε-Ga_2O_3 by halide vapor phase epitaxy. *J. Appl. Phys.* ***118*** (2015), 085301.

[93] Papadogianni, A., White, M. E., Speck, J. S., Galazka, Z., and Bierwagen, O. Hall and Seebeck measurements estimate the thickness of a (buried) carrier system: identifying interface electrons in In-doped SnO_2 films. *Appl. Phys. Lett.* ***107*** (2016), 252105.

[94] Peelaers, H., Steiauf, D., Varley, J. B., Janotti, A., and Van-de Walle, C. G. $(In_xGa_{1-x})_2O_3$ alloys for transparent electronics. *Phys. Rev. B* ***92*** (2015), 085206.

[95] Peev, N. S. The Collision Frequency of Adsorbed Particles. *Bulg. J. Phys.* ***40*** (2013), 214.

[96] Pfeiffer, G. *The Vacuum Technology Book: Volume II.* Pfeiffer Vacuum GmbH, Asslar, Germany, 2008.

[97] Pilling, M. J., and Seakins, P. W. *Reaction Kinetics.* Oxford University Press, 2nd Edition, United States of America, 1996.

[98] Preissler, N., Bierwagen, O., Ashok, T. R., and Speck, J. S. Electrical transport, electrothermal transport, and effective electron mass in single-crystalline In_2O_3 films. *Phys. Rev. B* ***88*** (2013), 085305.

[99] Ralston, J., Wicks, G. W., and Eastman, L. F. Reflection high-energy electron diffraction intensity oscillation study of Ga desorption from molecular beam epitaxially grown $Al_xGa_{1-x}As$. *J. Vac. Sci. Technol. B* ***4*** (1986), 594.

[100] Reimer, L. *Scanning Electron Microscopy.* Springer-Verlag Berlin Heidelberg, Germany, 1998.

[101] Rombach, J., Papadogianni, A., Mischo, M., Cimalla, V., Kirste, L., Ambacher, O., Berthold, T., Krischok, S., Himmerlich, M., Selve, S., and Bierwagen, O. The role of surface electron accumulation and bulk doping for gas-sensing explored with single-crystalline In_2O_3 thin films. *Sens. Actuators, B* ***236*** (2016), 909.

[102] Roy, R., Hill, V. G., and Osborn, E. F. Polymorphism of Ga_2O_3 and the System Ga_2O_3-H_2O. *J. Am. Chem. Soc.* ***74*** (1952), 719.

[103] Sasaki, K., Higashiwaki, M., Kuramata, A., Masui, T., and Yamakoshi, S. Growth temperature dependences of structural and electrical properties of Ga_2O_3 epitaxial films grown on β-Ga_2O_3(010) substrates by molecular beam epitaxy. *J. Cryst. Growth* ***392*** (2014), 30.

[104] Sasaki, K., Kurumata, A., Masui, T., Víllora, E. G., Shimamura, K., and Yamakoshi, S. Device-Quality β-Ga_2O_3 Epitaxial Films Fabricated by Ozone Molecular Beam Epitaxy. *Appl. Phys. Express* ***5*** (2012), 035502.

[105] Schewski, R., Wagner, G., Baldini, M., Gogova, D., Galazka, Z., Schulz, T., Remmele, T., Markurt, T., Wenckstern, H. v., Grundmann, M., Biwerwagen, O., Vogt, P., and Albrecht, M. Epitaxial stabilization of pseudomorphic α-Ga_2O_3 on sapphire (0001). *Appl. Phys. Express* ***8*** (2015), 011101.

[106] Shannon, R. D., and Prewitt, C. T. Synthesis and Structure of Phases in the In_2O_3-Ga_2O_3 System. *J. Inorg. Nucl. Chem.* ***30*** (1968), 1389.

[107] Sharp, K., and Matschinsky, F. Translation of Ludwig Boltzmann's paper "On the Relationship between the Second Fundamental Theorem of the Mechanical Theory of Heat and Probability Calculations Regarding the Conditions for Thermal Equilibrium". *Entropy* ***17*** (2015), 1971.

[108] Shinohara, D., and Fujita, S. Heteroepitaxy of Corundum-Structured α-Ga_2O_3 Thin Films on α-Aa_2O_3 Substrates by Ultrasonic Mist Chemical Vapor Deposition. *Jpn. J. Appl. Phys.* ***47*** (2008), 7311.

[109] Siekacz, M. *PhD Thesis.* Unipress, Warsaw, Poland, 2012.

[110] Sturm, C., Furthmüller, J., Bechstedt, F., and Grundmann, M. Dielectric tensor of monoclinic Ga_2O_3 single crystals in the spectral range 0.5–8.5 eV. *APL Mater.* ***3*** (2015), 106106.

[111] Tarsa, E. J., English, J. H., and Speck, J. S. Pulsed laser deposition of oriented In_2O_3 on (001) InAs, MgO, and yttria-stabilized zirconia. *Appl. Phys. Lett.* ***62*** (1993), 2332.

[112] Tiwari, A. N., Khrypunov, G., Kurdzesau, F., Bätzner, D. L., Romeo, A., and Zogg, H. CdTe Solar Cell in a Novel ConïňĄguration. *Prog. Photovolt.: Res. Appl.* ***12*** (2004), 33.

[113] Tomm, Y., Reiche, P., Klimm, D., and Fukuda, T. Czochralski grown Ga_2O_3 crystals. *J. Cryst. Growth* ***220*** (2000), 510.

[114] Tsai, M.-Y., Bierwagen, O., White, M. E., and Speck, J. S. β-Ga_2O_3 growth by plasma-assisted molecular beam epitaxy. *J. Vac. Sci. Technol., A* ***28*** (2010), 354.

[115] Tsai, M.-Y., White, M. E., and Speck, J. S. Plasma-assisted molecular beam epitaxy of SnO_2 on TiO_2. *J. Cryst. Growth* ***310*** (2008), 4256.

[116] Tsai, M.-Y., White, M. E., and Speck, J. S. Plasma-assisted molecular beam epitaxy of SnO_2 on TiO_2. *J. Cryst. Growth* ***310*** (2008), 4256.

[117] Tsai, M.-Y., White, M. E., and Speck, J. S. Investigation of (110) SnO_2 growth mechanisms on TiO_2 substrates by plasma-assisted molecular beam epitaxy. *J. Appl. Phys.* ***106*** (2009), 024911.

[118] Valderrama-N, J., and Jacob, K. T. Vapor pressure and dissociation energy of In_2Ojournal = Jpn. J. Appl. Phys.,. *Thermochim. Acta* ***21*** (1977), 215.

[119] Varley, J. B., Weber, J. R., Janotti, a., and Van de Walle, C. G. Oxygen vacancies and donor impurities in β-$Ga2_2O_3$. *Appl. Phys. Lett.* ***97*** (2010), 142106.

[120] Vegard, L. Die Konstitution der Mischkristalle und die Raumfüllung der Atome. *Z. Phys* ***5*** (1921), 17.

[121] Verma, A. *Investigating epitaxial* $(In_xGa_{1-x})_2O_3$ *as potential transparent contact on GaN based UV-LEDs.* Paul-Drude-Institut für Festkörperelektronik, Berlin, Germany, 2016.

[122] Víllora, E. G., Shimamura, K., Kitamura, K., Aoki, K., and Takekazu, U. Epitaxial relationship between wurtzite GaN and Epitaxial relationship between wurtzite GaN and β-Ga_2O_3. *Appl. Phys. Lett.* ***90*** (2007), 234102.

[123] Víllora, E. G., Shimamura, K., Yoshikawa, Y., Aoki, K., and Ichinose, N. Large-size β-Ga_2O_3 single crystals and wafers. *J. Cryst. Growth* ***270*** (2004), 420.

[124] Víllora, E. G., Shimamura, K., Yoshikawa, Y., and Ujiie, T. Electrical conductivity and carrier concentration control by Si doping. *Appl. Phys. Lett.* ***92*** (2008), 202120.

[125] Vogt, P., and Bierwagen, O. The competing oxide and sub-oxide formation in metal-oxide molecular beam epitaxy. *Appl. Phys. Lett.* ***106*** (2015), 081910.

[126] Vogt, P., and Bierwagen, O. Comparison of the growth kinetics of In_2O_3 and Ga_2O_3 and their suboxide desorption during plasma-assisted molecular beam epitaxy. *Appl. Phys. Lett.* ***109*** (2016), 062103.

[127] Vogt, P., and Bierwagen, O. Reaction kinetics and growth window for plasma-assisted molecular beam epitaxy of Ga_2O_3: Incorporation of Ga vs. Ga_2O desorption. *Appl. Phys. Lett.* ***108*** (2016), 072101.

[128] Vogt, P., Trampert, A., Ramsteiner, M., and Bierwagen, O. Domain matching epitaxy of cubic In_2O_3 on *r*-plane sapphire. *Phys. Stat. Solidi (a)* ***212*** (2015), 1433.

[129] Wagner, G., Baldini, M., Gogova, D., Schmidbauer, M., Schewski, R., Albrecht, M., Galazka, Z., Klimm, D., and Fornari, R. Homoepitaxial growth of β-Ga_2O_3 layers by metal-organic vapor phase epitaxy. *Phys. Stat. Sol. (a)* ***211*** (2014), 27.

[130] Wang, C. Y., Dai, Y., Pezoldt, J., Lu, B., Kups, T., Cimalla, V., and Ambacher, O. Phase Stabilization and Phonon Properties of Single Crystalline Rhombohedral Indium Oxide. *Cryst. Growth Des.* ***8*** (2008), 1257.

[131] Wenckstern, H. v., Splith, D., Purfürst, M., Zhang, Z., Kranert, C., Müller, S., Lorenz, M., and Grundmann, M. Structural and optical properties of $(In,Ga)_2O_3$ thin films and characteristics of Schottky contacts thereon. *Semicond. Sci. Technol.* ***30*** (2015), 024005.

[132] White, M. E., Bierwagen, O., Tsai, M.-Y., and Speck, J. S. Electron transport properties of antimony doped SnO_2 single crystalline thin films grown by plasma-assisted molecular beam epitaxy. *J. Appl. Phys.* ***106*** (2009), 093704.

[133] White, M. E., Bierwagen, O., Tsai, M.-Y., and Speck, J. S. Synthesis and Characterization of Highly Resistive Epitaxial Indium-Doped SnO_2. *Appl. Phys. Express* ***3*** (2010), 051101.

[134] White, M. E., Tsai, M.-Y., Wu, F., and Speck, J. S. Plasma-assisted molecular beam epitaxy and characterization of SnO_2 (101) on *r*-plane sapphire. *J. Vac. Sci. Technol., A* ***26*** (2008), 1300.

[135] Wilkins, R. G. *Substitution Reactions in Kinetics and Mechanism of Reactions of Transition Metal Complexes.* Wiley-VCH Verlag GmbH, 2nd Edition, Weinheim, Germany, 1991.

[136] Yao, H., and Yan, C. H. Anisotropic optical responses of sapphire (α-Al_2O_3) single crystals. *J. Appl. Phys.* ***85***, 4 (1999).

[137] Yoshioka, S., Hayashi, H., Kuwabara, A., Oba, F., Matsunaga, K., and Tanaka, I. Structures and energetics of Ga_2O_3 polymorphs. *J. Phys.: Condens. Matter* ***19*** (2007), 346211.

[138] Zhang, K. H. L., Lazarov, V. K., Galindo, P. L., Oropeza, F. E., Payne, D. J., Lai, H. H.-C., and Egdell, R. G. Domain Matching Epitaxial Growth of In_2O_3 Thin Films on α-Al_2O_3(0001). *Cryst. Growth Des.* ***12*** (2012), 1000.

[139] Zhao, C., Li, Z., Mi, W., Luan, C., and Feng, X. Structure and Optical Properties of Epitaxial Indium Oxide Films Deposited on Y-Stabilized ZrO_2(111) by MOCVD. *J. Electron. Mater.* ***44*** (2015), 8.

C. Acknowledgements

My gratitude goes to all who contributed to this work and made my time at the Paul-Drude-Institut für Festkörperelektronik (PDI) scientifically and personally fulfilling.

I am grateful to my professor Prof. Dr. Henning Riechert who gave me the opportunity to carry out my PhD at the PDI. The last three years have been a great scientific experience to me.

Special thanks go to Dr. Oliver Bierwagen who introduced me into the world of molecular beam epitaxy. I appreciate the fruitful discussions and his constant supervision of my research.

My thank goes to the department head of the epitaxy department Dr. Lutz Geelhaar for his valuable advices and suggestions.

I would like to thank Hans-Peter Schönherr for technical MBE support and kindly answering technical questions.

I gratitude to Dr. Uwe Jahn for his permanent support and help with EDX and SEM measurements.

Many people contributed to this work by valuable discussions and sharing their experience with me. For this purpose I would like to thank Dr. Vladimir Kaganer, Dr. Oliver Brandt, Dr. Segio Fernández-Garrido, and Dr. Caroline chèz.

I want to thank Anjneya Verma who carried out his Master's thesis at the PDI in the framework of $(In_xGa_{1-x})_2O_3$ research, for his assistance during XRD, EDX, and AFM measurements.

I would like to thank Dr. Bernd Jenichen for XRD introduction, Anne-Kathrin Bluhm for SEM measurements, and Claudia Herrmann for support with the AFM.

I thank my colleagues and office mates Julius Rombach and Carsten Stemmler for creating a nice working atmosphere and their help whenever it was needed.

Last but not least, I would like to express my gratitude to Prof. Dr. W. Ted Masselink and Prof. Dr. James S. Speck for refereeing my thesis.

Erklärung:

Ich erkläre, dass ich die Dissertation selbständig und nur unter Verwendung der von mir gemäß §7 Abs. 3 der Promotionsordnung der Mathematisch-Naturwissenschaftlichen Fakultät, veröffentlicht im Amtlichen Mitteilungsblatt der Humboldt-Universität zu Berlin Nr. 126/2014 am 18.11.2014 angegebenen Hilfsmittel angefertigt habe.

Berlin, den 14.März 2017 .....